GENETIC ENGINEERING OF HYDROGENASE AND RELATED ENZYMES IN THE HYPERTHERMOPHILIC ARCHAEON *PYROCOCCUS FURIOSUS*

by

CHANG-HAO WU

(Under the Direction of Michael W. W. Adams)

ABSTRACT

The model hyperthermophilic archaeon, *Pyrococcus furiosus*, grows optimally at 100 °C by fermenting carbohydrates and peptides. In the absence of elemental sulfur (S^0), the reduced ferredoxin (Fd) generated from the glycolysis pathway transfers electrons to a membrane-bound hydrogenase (MBH) for H_2 production and Na^+ gradient generation, which is used by ATP synthase for energy production. Two soluble hydrogenases termed SHI and SHII are thought to recycle the H_2 for nicotinamide cofactor generation. SHI has been extensively studied and is widely used in several applications, such as *in vitro* H_2 production. To scale up these applications, large amounts of purified SHI are required. Herein, we engineered *P. furiosus* to overproduce SHI by increasing the expression of the genes encoding the maturation accessory proteins and devised a 500-g wet wt. cell-scale purification procedure. In the presence of S^0, the expression of the genes encoding MBH, SHI and SHII decreases dramatically and MBH is replaced by a membrane-bound oxidoreductase of unknown function. Herein we show that this enzyme is a sulfane reductase (MBS). Like MBH, MBS is proposed to oxidize Fd and generate a Na^+ gradient but it reduces sulfane sulfur derived from S^0. A sulfane-containing substrate was discovered for MBS and the enzyme was purified in membrane-associated and soluble forms and these were biochemically

characterized. *P. furiosus* was also utilized as a platform for the heterologous expression of enzymes to study respiratory systems from other hyperthermophiles. An arsenate respiratory reductase (Arr) was heterologously-expressed from the archaeon *Pyrobaculum aerophilum* in *P. furiosus*. This is the first archaeal Arr to be purified and biochemically characterized and a novel type of arsenite resistance was observed in the Arr-expressing *P. furiosus* strain. In addition, this strain was able to use arsenate as the terminal electron acceptor to support growth. This represents the first example of *P. furiosus* using a non-native substrate as a terminal electron acceptor other than S^0 and protons.

INDEX WORDS: *Pyrococcus furiosus*, hydrogenases, hydrogen, purification, respiration, sulfur metabolism, bioenergetics, evolution, *Pyrobaculum aerophilum*, arsenate reductase, arsenic detoxification, Cryo-EM

GENETIC ENGINEERING OF HYDROGENASE AND RELATED ENZYMES IN THE HYPERTHERMOPHILIC ARCHAEON *PYROCOCCUS FURIOSUS*

by

CHANG-HAO WU

B.S., Chung Shan Medical University, 2008

A Dissertation Submitted to the Graduate Faculty of The University of Georgia in Partial Fulfillment of the Requirements for the Degree

DOCTOR OF PHILOSOPHY

ATHENS, GEORGIA

2018

GENETIC ENGINEERING OF HYDROGENASE AND RELATED ENZYMES IN THE HYPERTHERMOPHILIC ARCHAEON *PYROCOCCUS FURIOSUS*

by

CHANG-HAO WU

Major Professor:	Michael W. W. Adams
Committee:	Michael K. Johnson
	Robert J. Maier
	William N. Lanzilotta

Electronic Version Approved:

Suzanne Barbour
Dean of the Graduate School
The University of Georgia
August 2018

DEDICATION

This dissertation is dedicated to my family in Taiwan that has been extremely supportive throughout my years at UGA. I would also like to thank my wife, Yi-Jung Lee, for her loving support and being with me all the time.

ACKNOWLEDGEMENTS

I would like to thank Dr. Michael W. W. Adams for his support, guidance and optimism, which helped me obtain valuable results from the challenging projects. I would also like to thank my committee members (Dr. Michael Johnson, Dr. Robert Maier and Dr. William Lanzilotta) for their suggestions and help in my committee meetings. In addition, I would like to express my gratitude to members of Adams lab for their support throughout my graduate career. In particular, I thank Dr. Sanjeev Chandrayan and Dr. Patrick McTernan for their advice and training that contributed greatly to my accomplishments.

TABLE OF CONTENTS

Page

LIST OF TABLES

Page

LIST OF FIGURES

Page

CHAPTER 1

INTRODUCTION AND LITERATURE REVIEW

Archaea

All living organisms are classified into three domains: Eukarya, Bacteria, and Archaea (1-3). Archaea were formerly classified within Bacteria as Archaebacteria, and then re-categorized to Archaea (4). These three domains have been further phylogenetically analyzed based on the sequence of small-subunit ribosomal RNA, as shown in Figure 1.1 (1). In contrast to Eukarya, Bacteria and Archaea are prokaryotes, lacking nuclei or organelles. According to phylogenetic analysis, the relationship between Archaea and Eukarya is closer than that between Archaea and Bacteria.

Archaea have similarities to both Bacteria and Eukarya. Morphology, genome organization, gene regulation systems, and the majority of operational proteins, such as metabolic enzymes and transporters, are similar in Bacteria and Archaea (5-7). However, the mechanisms of DNA replication, transcription and translation have more in common between Archaea and Eukarya (6, 8, 9). Despite the similarities between Archaea and the two other domains of life, a major distinction of Archaea is that their membranes contain isoprenoid tetraether lipids (10). Archaea may also represent the most ancient form of life and many have been isolated from extreme environments, such as extremes of salt, pH, and temperature, although they are also widespread in more "common" environments like lakes, oceans or soil (3, 5, 11).

Based on phylogenetic analyses, Archaea contains two major phyla - *Euryarchaeota* and *Crenarchaeota* (4). *Euryarchaeota* includes methanogens (*Methanococcales* and *Methanopyrales*), sulfate reducers (*Archaeoglobales*), and sulfur reducers (*Thermococcales*) (1). *Thermococcales* includes three genera, *Pyrococcus, Thermococcus* and *Paleococccus*. All of these were isolated from shallow marine thermal springs or deep-sea hydrothermal vents. *Thermococcales* are heterotrophic anaerobes that can use peptides and carbohydrates to reduce elemental sulfur or protons to produce H_2S or H_2 as the end-products.

Pyrococcus furiosus

Hyperthermophiles are typically referred to as organisms that grow optimally at a temperature of 80 °C and above (12). They include members of both the Archaea and Bacteria domains. Some of these organisms can survive temperatures higher than 100 °C in the deep sea, where water does not boil owing to the pressure. For example, *Methanopyrus kandleri* can grow up to 122 °C with increased pressure (13). The work presented in this thesis focuses on *Pyrococcus furiosus* (DSM 3638), which is a hyperthermophilic *Euryarchaeota* that belongs to the order, *Thermococcales*. It was isolated from marine sediments in Italy (Figure 1.2) (14) and is a strict anaerobic heterotroph that grows optimally at 100 °C with a growth temperature ranging from 70 to 103 °C. *P. furiosus* can use a wide range of substrates, such as starch, maltose, cellobiose, chitin, and peptides as carbon sources. It utilizes both intracellular and extracellular enzymes to hydrolyze large polysaccharides into shorter sugar units that can be incorporated into the cell (15-18). However, *P. furiosus* is unable to metabolize monosaccharide sugars, such as glucose, fructose, or galactose (14). Extracellular hydrolases, such as α-amylase, pullulanase, and amylopullulanase,

have been characterized from *P. furiosus* (19). These hydrolases only cleave α-1, 4 and α-1, 6 glycosidic bonds, so they are unable to completely digest many polysaccharides into their monomeric forms. The partially digested polysaccharides are transported into the cell and further digested by intracellular hydrolases (20). This might explain the observation that *P. furiosus* cannot grow with monosaccharides because the sugar transporters are specific to partially digested polymeric sugars. The genome of *P. furiosus* (1.91 Mb) was sequenced in 2000 and encodes 2,196 open reading frames (21). The genetically traceable variant, COM1, was also sequenced and a dynamic genome was revealed (22).

Elemental sulfur (S^0) plays a key role in regulating expression of the respiratory systems of *P. furiosus*. As shown in Figure 1.3 (14, 23), in the absence of S^0, reduced ferredoxin (Fd) generated from glycolysis is the electron donor to a membrane-bound hydrogenase (MBH) for H_2 production and this also generates a Na^+-gradient. The Na^+ gradient is used by ATP synthase for ATP generation (24). Two soluble hydrogenases, SHI and SHII, are predicted to use the H_2 to generate reduced nicotinamide cofactors, although the exact physiological functions of these enzymes are still unknown due to the lack of growth phenotype in mutational studies (25). In the presence of S^0, the expression of MBH dramatically decreases and a membrane-bound oxidoreductase (MBX) was predicted to replace MBH. MBX was proposed to use electrons from Fd to reduce S^0 to H_2S and generate a Na^+-gradients (23). For example, a transcriptional analysis was carried out to investigate the genome-wide response to the addition of S^0 (26). The expression changes within 10 minutes were referred to as the primary response, and those changes within 30 minutes were termed the secondary response. In the primary response, the expression of the gene encoding NADPH sulfur reductase (NSR) increased 3.7-fold while those encoding MBX increased 12-fold. All three hydrogenases, MBH, SHI, and SHII, are also featured in the primary response,

where the expression of their genes decreased up to 11-fold. These results are consistent with the scheme of H_2 and S^0 metabolism depicted in Figure 1.3 (26). The genes responsive to S^0 are regulated by a sulfur-response regulator (SurR) (27). SurR binds to the motif, $GRRn_3AAC$, and functions as an activator for its own gene and those genes downregulated in the primary S^0 response, such as those of the hydrogenases. SurR also functions as a repressor for those genes upregulated in the primary S^0 response, such as the genes of NSR and MBX. SurR-binding motifs appear upstream of most of the genes identified in the primary S^0 response. Structural studies revealed that SurR harbors helix-turn-helix DNA-binding domains and a CxxC motif adjacent to the recognition helix (28). In the absence of S^0, the cysteine residues stay in the reduced state, thereby enabling SurR to bind to target DNA. In the presence of S^0, oxidation of its cysteine residues cause a conformational change that disrupts the helical bundle of the helix-turn-helix domain and prevents DNA binding, controlling the regulation of the expression between H_2 and S^0 metabolism (28). In addition, the results from the SurR mutants suggest that it is a master regulator of electron flow in *P. furiosus*, affecting the pools of NAD(P)H and reduced and oxidized Fd, metabolic pathways, and thiol/disulfide redox balance (29).

In the absence of S^0, the overall end-products from the fermentation of a C_6 glucose unit by *P. furiosus* are 1.2 equivalents of acetate, 1.2 equivalents of CO_2, 2.6 equivalents of H_2, and 0.5 equivalents of alanine (30, 31). *P. furiosus* utilizes a modified Embden-Meyerhof pathway to metabolize glucose to meet the needs of growth (Figure 1.4) (32). The pathway commences with the phosphorylation of glucose to glucose-6-phosphate catalyzed by glucokinase (GK) using ADP as a cofactor. *P. furiosus* GK is a dimer of 47 kDa, and its activity is dependent on ADP rather than ATP (32, 33). Glucose-6-phosphate is isomerized to fructose-6-phosphate by phosphoglucoisomerase (PGI), which has been purified from *P. furiosus* as a dimer of 23 kDa

subunits, exhibiting no sequence homology to the PGIs from Bacteria and Eukarya (34). Fructose-6-phosphate is converted to fructose-1,6-phosphate by phosphofructokinase (PFK). This is a tetramer of 52 kDa subunits and its activity is also ADP-dependent (35). Fructose-1,6-phosphate is then converted to glyceraldehyde-3-phosphate and dihydroxyacetone phosphate catalyzed by fructose bisphosphate aldolase (FBA), where triose phosphate isomerase (TPI) balances between these two C-3 forms (33). *P. furiosus* FBA has been heterolgously-expressed in *E. coli* and showed a preferred substrate specificity for fructose-1,6-phosphate in the catabolic direction (36), while TPI was characterized as having an additional novel endoglucanase/cellulose activity (37).

The tungsten-containing enzyme glyceraldehyde-3-phosphate oxidoreductase (GAPOR) converts glyceraldehyde-3-phosphate to 3-phosphoglycerate (38). This step is one of the major differences between the conventional EM and modified EM pathway found in *P. furiosus*. In the conventional EM pathway, the conversion of glyceraldehyde-3-phosphate to 3-phosphoglycerate is catalyzed by glyceraldehyde phosphate dehydrogenase (GAPDH) and phosphoglycerate kinase (PGK) in two steps. In these two steps, NADH is generated by GAPDH and an ATP is generated from the PGK reaction. In *P. furiosus*, glyceraldehyde-3-phosphate is directly converted to 3-phosphoglycerate by GAPOR, so no ATP is synthesized. In addition, instead of NAD, GAPOR uses Fd as an electron acceptor, which is the primary electron carrier in *P. furiosus* (39).

Phosphoglycerate mutase (PGM) catalyzes the conversion of 3-phosphoglycerate to 2-phosphoglycerate, which is then converted to phosphoenolpyruvate by enolase (31, 33, 40). Phosphoenolpyruvate is further turned to pyruvate by pyruvate kinase (PK). This step generates ATP by substrate-level phosphorylation and is the only step of ATP formation in the modified EM pathway in *P. furiosus* (33). Pyruvate generated by glycolysis is converted to acetyl-CoA and CO_2 by pyruvate ferredoxin oxidoreductase (POR), which also utilizes Fd as the electron carrier instead

of NAD(P) (41). Acetyl-CoA is then transformed to acetate by acetyl-CoA synthetase I and II, coupling a substrate-level phosphorylation-driven ATP generation (42). The reduced Fd generated by GAPOR and POR is used for energy conservation via MBH as described above. Acetate, CO_2, and H_2 are therefore the end-products of sugar metabolism in the absence of S^0.

Hydrogenases

Hydrogenases are a diverse group of metalloenzymes that catalyze one of the simplest reactions in nature—the reversible conversion of hydrogen gas to protons and electrons (43). These enzymes are found in bacteria, archaea, and some eukarya and can be located in the periplasm, cytoplasm or in the membrane (43, 44). In eukaryotic cells, hydrogenases are usually located in specialized compartments (45, 46). Their primary functions are to remove excess reducing equivalents through H_2 production or to provide reductant by splitting H_2. They can also provide reducing power and balance the redox potential of the cells by oxidizing H_2. Depending on the physiology of the cell, hydrogenases may have a bias toward H_2 production or H_2 oxidation *in vivo*, but they catalyze reversible reactions *in vitro*. The membrane-bound hydrogenases can also involve in the generation of transmembrane ion gradients. Based on the metal ion composition in their active sites, all hydrogenases can be classified into [Fe]-only, [FeFe] or [NiFe] enzymes (43, 44).

[Fe]-only or iron-sulfur cluster-free hydrogenases are the least studied of the three classes of hydrogenase. These enzymes are found only in methanogenic archaea and catalyze an intermediary step of H_2 oxidation in the energy conversion pathway of CO_2 to methane (47). They can only reversibly oxidize H_2 in the presence of a second substrate,

methenyltetrahydromethanopterin (methylene-H_4MPT^+), to methylene-H_4MPT and H^+; thus they are also referred to as H_2-forming methylene-H_4MPT dehydrogenase (Hmd) (48). [Fe]-only hydrogenases are upregulated when nickel is limited. Under such conditions, the F_{420}-reducing [NiFe] hydrogenase required for methanogenesis is not present and Hmd is used to remove excess reductant. Hmd has a unique iron cofactor, Fe-guanylylpyrodinol (Fe-GP, Figure 1.5), in the catalytic site and catalyzes a different reaction mechanism, which is methylene-H_4MPT-dependent, from the one of [NiFe] and [FeFe] hydrogenases, but it also catalyzes the standard H^+/H_2 exchange reaction of hydrogenases (49).

The first structure of Hmd was obtained of the apoenzyme from *Methanothermobacter jannaschii* expressed in *E. coli* and reconstituted with the Fe-GP cofactor purified from *Methanothermobacter marburgensis* (50). In this structure, the mononuclear Fe active site displays a square pyramidal geometry that is coordinated to a pyridinol nitrogen, a cysteine thiolate, two CO, an acyl-carbon, and an unknown ligand (Figure 1.5). The pyridinol ring may have ligand bonding properties to the Fe atom similar to that of cyanide binding to Fe in the catalytic site in [NiFe] and [FeFe] hydrogenases (50). Two CO molecules bind to the Fe at a 90° angle relative to each other, and the cysteine thiolate ligand, derived from Cys176, provides a covalent connection between the Fe-GP cofactor and the protein. An acyl-carbon from the pyridinol ring was also identified to be binding to the Fe in a study of the C176A Hmd mutant (51). The other coordination site of the Fe is believed to be occupied by hydrogen or the inhibitor CO.

[FeFe] hydrogenases are found in anaerobic bacteria and anaerobic or phototrophic eukaryotes but not in archaea (52). This class of hydrogenase is usually much more active in H_2 production than in H_2 uptake. Many [FeFe] hydrogenases are monomeric, but some are dimers, trimers and even heterotetramers (53). The catalytically-active metal center, the H-cluster, of [FeFe]

hydrogenases has a di-iron center connected to a [4Fe-4S] cluster via a thiolate group of a cysteine residue (44). The H-cluster is buried deep inside the molecule, which is also the case with the catalytic [NiFe] site in [NiFe] hydrogenases.

The H-cluster consists of the di-iron site bound to a disulfur bridge-head (Figure 1.5). The two Fe atoms are designated proximal or distal based on their positions. The proximal Fe binds to a cubane [4Fe-4S] cluster via a cysteine thiolate and to one CN and one CO ligand. The distance of the iron-sulfur cluster to the proximal cluster is 4 Å. The distal Fe is also coordinated with one CN and one CO ligand. A third bridging CO binds to both the proximal and distal Fe atoms. Some [FeFe] hydrogenases harbor additional iron-sulfur clusters, named F-clusters, such as CpI from *Clostridium pasteurianum* (54). The best studied [FeFe] hydrogenases are the monomeric ferredoxin-dependent enzymes, such as those from *Chlamydomonas reinhardtii* and *C. pasteurianum* (55). These monomeric [FeFe] hydrogenases contain only the H-cluster without additional iron-sulfur clusters, such as HydA from *C. reinhardtii*. Because of its structural simplicity, the [FeFe] hydrogenase from *C. reinhardtii* has been used as a model for active site maturation studies (56, 57).

A unique type of [FeFe] hydrogenase was identified in the hyperthermophilic bacterium *Thermotoga maritima.* It is a trimeric hydrogenase and contains two additional subunits that interact with ferredoxin and NADH (58). No H_2 production was detected when either reduced ferredoxin or NADH was used as the sole electron donor. However, the presence of both substrates led to efficient H_2 production. This type of reaction is called electron bifurcation, which represents the third form of energy conservation, in addition to substrate-level phosphorylation and electron transport phosphorylation (59). In the bifurcating reaction catalyzed by *T. maritima* [FeFe]

hydrogenase, the exergonic reduction of protons by electrons from reduced ferredoxin energizes the endergonic reduction of protons by electrons from NADH (55).

Three maturases are required for the assembly and insertion of the di-iron center in the H-cluster. These are HydE, HydF, and HydG, which are conserved in all [FeFe] hydrogenase-containing organisms (44, 55). In the mutant ΔHydEFG of *C. reinhardtii* (CpI), the crystal structure of the monomeric [FeFe] hydrogenase I shows only the cubane [4Fe-4S] cluster of the H-cluster without the di-iron center (56, 60). HydF is a monomeric enzyme that binds to a [4Fe-4S] cluster and hydrolyzes GTP to GDP. Both the iron-sulfur and GTP-binding motifs, at the C- and N-terminus, respectively, are essential for the maturation of the di-iron center in *Clostridium acetobutylicum*, although the results from the studies of *Shewanella oneidensis* maturases suggest that HydF is not essential (55).

In the *in vitro* studies of CpI, HydG was reported to be the only absolutely required maturase, and HydF is not required for the di-iron center assembly when using di-iron biomimetic analogs (61-63). HydG belongs to the radical SAM superfamily that uses an N-terminal [4Fe-4S] to reductively cleave S-adenosyl-L-methionine (SAM) to generate a radical as an intermediate. HydG utilizes tyrosine as a substrate to generate *p*-cresol, and the additional C-terminal [4Fe-4S] cluster in HydG is essential for the di-iron center maturation as well as for the formation of CO and CN ligands that bind to the diatomic center (64-67). HydE also belongs to the radical SAM superfamily and contains an additional C-terminal [2Fe-2S] cluster. The role of HydE in the maturation process is unknown, although it was suggested that HydE synthesizes the bridging dithiomethylamine ligand from a common metabolite (44, 55).

The maturation of the di-iron center begins with SAM cleavage at the N-terminal [4Fe-4S] cluster of HydG to produce a 5'-deoxyadenosyl radical species that interacts with tyrosine to

produce *p*-cresol and dehydroglycine at the C-terminal [4Fe-4S] cluster. Dehydroglycine is further used by HydG at the C-terminal [4Fe-4S] cluster by an unknown mechanism to generate CO and CN ligands that coordinate with the di-iron center. HydE is responsible for the dithiomethylamine ligand formation, and HypF serves as a scaffold to bring the assembled di-iron subcluster to the apoenzyme that contains a cubane [4Fe4S] to form an active [FeFe] hydrogenase (44, 55).

The third class of hydrogenase is the [NiFe]-type (45, 46). [NiFe] hydrogenases are taxonomically widespread in bacteria and archaea and have a distinct evolutionary history from [FeFe] hydrogenases (55). These two types of hydrogenase show no sequence similarity. [NiFe] hydrogenases contain at least two subunits, referred to as the large and small subunits (Figure 1.6) (68-70). The large subunit contains the catalytic [NiFe] site that is buried in the molecule, which is similar to the H-cluster in [FeFe] hydrogenases. Four conserved cysteine residues are found in the active site as two CXXC motifs at the N- and C-terminus (70, 71). The thiolate groups of two of these residues coordinate the Ni atom, while the other two bind to both the Ni and Fe atoms as bridging ligands. The Fe atom is also coordinated by two CN and one CO ligand that maintain the Fe atom in a low spin state (Fe^{2+}) where the reaction with H_2 is thermodynamically favored (55, 72). In some hydrogenases, one of the cysteine residues coordinating the Ni atom is replaced by selenocysteine, and this type of hydrogenase is named [NiFeSe] hydrogenase (55). Because of the deep buried catalytic site, hydrophobic tunnels have been identified in the large subunit for H_2 gas access to the active site (44, 70). The small subunit contains three iron-sulfur clusters to shuttle electrons between the [NiFe] active site and the electron carrier for the enzyme. Based on their positions relative to the active site, these iron-sulfur clusters are referred to as proximal, medial and distal clusters (44).

[NiFe] active site maturation

Due to the unique nature of the $NiFe(CN)_2CO$ complex at the active site of [NiFe] hydrogenases, the maturation process of these enzymes is complicated. It has been extensively studied in *E. coli* and eight accessory proteins has been identified for the assembly of the [NiFe] active site, including six hydrogen pleiotropy proteins (HypABCDEF), SlyD (sensitive to the lysis D) and a protease (Figure 1.7) (44, 73, 74). HypC, D, E, and F are involved in the assembly of the Fe atom with CN and CO ligands. The source of the CN ligand is carbamoyl phosphate used by HypE and F (75). HypF converts carbamoyl phosphate to two unstable intermediates, carbamate and carbamoyladenylate, in an ATP-dependent process before transferring the carbamoyl group to the thiol group of the C-terminal cysteine residue of HypE that forms thiocarboxamide with the release of AMP (76). The thiocarboxamide is then converted to thiocyanate in an ATP hydrolysis-dependent manner. This CN ligand binding to HypE is then transferred to the Fe atom in the HypCD complex.

How the diatomic ligands are coordinated to the Fe atom before the insertion of the $Fe(CN)_2CO$ moiety into the active site is still not fully resolved. In one of the proposed models (Figure 1.7), the $Fe(CN)_2CO$ group is assembled on the HypE, C, and D complex. HypD is thought to serve as the main scaffold as it was isolated harboring the spectroscopic signature of the assembled iron center (77-79). The CN ligands on HypE were transferred to the Fe atom prior to the binding of the CO ligand. An incomplete iron cofactor was identified in the purified HypCD complex, suggesting that the CN ligands are loaded to the Fe atom before the addition of the CO ligand (79). The HypCD-Fe-CN complex also maintains the Fe in a low-spin state, which is important for the binding of the CO ligand (80). However, the results from spectroscopic studies suggested the opposite order; thus, the sequence of this event is not clear (74, 81). HypC forms a

complex with the large subunit, where it may facilitate iron insertion (82-84). Therefore, the $Fe(CN)_2CO$ moiety is transferred to the large subunit precursor prior to the insertion of the Ni atom. Although the origin of CO is still debatable, the observation of the CO_2 signal from spectroscopic studies suggests that HypC delivers Fe-CO_2 to HypD and the CO_2 is reduced to CO (55, 80). Metabolic CO_2 can also be the source of CO in the maturation process, although no experimental evidence has yet been reported (55, 80, 85).

The insertion of the Ni atom is accomplished by three proteins: HypA, HypB, and SlyD (44, 73, 74). HypA and HypB are believed to be crucial for Ni insertion into the [NiFe] hydrogenase active site only under nickel-limited growth conditions because the addition of nickel could restore hydrogenase activity in the HypA and HypB knockout strains (86-89). The insertion of Ni occurs only when the $Fe(CN)_2CO$ moiety is present (73, 90). HypA has a high affinity for Ni and can interact with the large subunit precursor without other Hyp proteins, indicating that it serves as a scaffold and directs Ni insertion (91, 92). HypB has a high-affinity Ni-binding domain at the N-terminus and a GTPase domain at the C-terminus that can bind either Ni or Zn (93, 94). The GTP hydrolysis activity of HypB is crucial for the maturation process that may regulate HypB conformation and facilitate Ni delivery (95-97). The SlyD deletion mutant only resulted in a decrease in hydrogenase activity compared with no detectable activity in other Hyp protein mutants, suggesting that SlyD may optimize nickel delivery (98-100). The plausible process by which Ni is inserted is that the Ni atom at the C-terminus of HypB is transferred to HypA, where the release is stimulated by GTP hydrolysis, and further transferred to the large subunit in the presence of the $Fe(CN)_2CO$ moiety. SlyD can accelerate the release of Ni from HypB to HypA (99, 100).

After metal insertion, Ni-dependent proteolysis occurs at the C-terminus of the large subunit, which is believed to be a checkpoint for complete active site assembly before the large subunit binds to the small subunit (101). The C-terminal peptide extension is essential for the interaction with HypC and helps maintain the large subunit in an open conformation for the metal insertion (83, 84). The length of the peptide extension varies from 4 to 40 residues, and the cleavage is executed by proteases specific to their corresponding hydrogenases (74). For instance, three proteases have been identified for the cleavage of three different hydrogenases in *E. coli* (102, 103). These endopeptidases recognize the DPCxxCxxH/R conserved motif, where the two cysteine residues are coordinated with the NiFe site (104-107). Nickel promotes the recognition of proteases to the motif, explaining why the cleavage occurs after the insertion of Ni (108). After the C-terminus cleavage, a large conformation change is induced, resulting in the [NiFe] active site buried deeply in the large subunit (73). The processed large subunit then binds to the small subunit that already contains its iron-sulfur clusters to become an active hydrogenase. In some cases, the hydrogenase is further translocated to its appropriate locations (74).

Classification of [NiFe] hydrogenases

[NiFe] hydrogenases can be classified into four distinct groups based on sequence analysis of the large catalytic subunits (Figure 1.8). These four groups also generally represent their putative physiological functions (45, 109, 110). Group 1 hydrogenases are typically membrane-bound H_2 uptake enzymes that are found in both Archaea and Bacteria. These organisms usually use H_2 as the primary electron source to reduce oxygen, nitrate, sulfate, fumarate, CO_2 or oxidized sulfur compounds. Further, such hydrogenases typically consist of a heterodimer of the large [NiFe] containing catalytic subunit and the small subunit harboring three iron-sulfur clusters. A

cytochrome b is often found anchoring the hydrogenase to the cell membrane, allowing electron transfer between hydrogenases and the quinone pool (43). In *E. coli*, one of the two group 1 hydrogenases (Hya) has been shown to provide energy by oxidizing H_2 and transferring electrons to the quinone pool (111). The group 1 hydrogenase from the sulfate-reducing bacterium *Desulfovibrio gigas* (HynAB) was reported to oxidize H_2 to provide electrons to the quinone pool via a periplasmic cytochrome c (112). The first crystal structure of [NiFe] hydrogenase was also obtained from *D. gigas* HynAB (68). A subgroup of oxygen-tolerant hydrogenases was additionally identified in this class, including hydrogenase 1 from *E. coli* and H_2-oxidizing membrane-bound hydrogenases from *Ralstonia eutropha*, *Aquifex aeolicus* and *Hydrogenovibrio marinus* (113-119).

[NiFe] hydrogenases are reversibly inactivated by oxygen, but the group 1 oxygen-tolerant hydrogenases maintain their catalytic activities after initial exposure to oxygen (120). The Ni atom of [NiFe] hydrogenases exhibits different electron paramagnetic resonance (EPR) signals that are classified as Ni-R, Ni-C, Ni-SI, Ni-A, and Ni-B (Figure 1.9). Ni-R, Ni-C, and Ni-SI are the states detected in the catalytic cycle, while Ni-A and Ni-B are those seen when the enzymes are oxidized by oxygen or other oxidants. Ni-A or the unready state reactivates back to the NiSI state slowly (> 1 h), while the ready state Ni-B readily converts to the NiSI state (within 1 min) (44, 121). For oxygen-tolerant hydrogenases under oxidizing conditions, no Ni-A state is observed and they reactivate back to the catalytic cycle more rapidly than standard [NiFe] hydrogenases. Instead of the standard [4Fe-4S] cluster coordinated by four cysteine residues in conventional hydrogenases, the proximal cluster of oxygen-tolerant hydrogenases is a unique [4Fe-3S] cluster coordinated by six cysteine residues that provide an unusual ligand environment (118). One of the thiol groups of the additional cysteine residues replaces one of the sulfur atoms in the [4Fe-4S] cluster, fostering

a more open and flexible [4Fe-3S] structure (116, 122, 123). Conventional [4Fe-4S] clusters only undergo a one-electron transition as the second transition is out of the physiologically-accessible redox potential range. However, because of the unique structure, the two redox transitions of the unique [4Fe-3S] cluster are within the physiological window (44). These electrons are important for reducing oxygen to water to protect the active site. In the oxygen-tolerant *R. eutropha* MBH, when the two additional cysteine residues, Cys19 and Cys120, were mutated to glycine, the [4Fe-3S] cluster was replaced by a [4Fe-4S] and the enzyme became oxygen sensitive (118, 124). The high redox potential [3Fe-4S] medial cluster was also discovered to be important for oxygen tolerance, and a proline residue in the cluster plays a key role. When this proline was mutated to a cysteine in oxygen-tolerant *E. coli* hydrogenase I, it changed the medial cluster from a [3Fe-4S] to a [4Fe-4S] cluster and the enzyme became oxygen sensitive (120). It was hypothesized that the [3Fe-4S] medial cluster is important for the first stage of oxygen reduction (113). The distal cluster of the small subunit is close to the heme of cytochrome b that anchors the hydrogenase to the membrane. The proximity of heme to the distal cluster was thought to aid in transferring electrons to the active site in order to reduce oxygen before it inhibits the catalytic site (113).

Group 2 [NiFe] hydrogenases can be further categorized into two subgroups - 2a and 2b. Group 2a includes hydrogenases of cyanobacteria that are typically linked to N_2 fixation by nitrogenase (125, 126). This subgroup of heterodimeric H_2-uptake hydrogenases recapture H_2 lost in N_2 fixation and are collectively encoded by HupSL (127). The electrons from H_2 oxidation can be channeled to the quinone pool to reduce oxygen or to the reductive TCA cycle for carbon dioxide fixation in *Aquifex aeolicus* (128-130). The deletion of HupSL in *Anabaena siamensis* abolished the H_2-uptake activity and increased H_2 production, probably owing to the lack of recapture of the H_2 produced by nitrogenases (131). Group 2b contains H_2-sensing regulatory

hydrogenases (HupUV or HoxBC) that mostly regulate the expression of group 1 H_2-uptake hydrogenases by sensing the presence of H_2 (43). From a study of *Ralstonia eutropha*, it was determined that the small subunit of HoxBC harbors two [2Fe-2S] clusters and one [4Fe-4S] cluster compared to three [4Fe-4S] clusters in a conventional hydrogenase (132). *R. eutropha* HoxBC was also reported to regulate the expression of the membrane-bound (HoxKGZ) and cytoplasmic (HoxFUYH) hydrogenases (133).

Group 3 hydrogenases are generally composed of the typical large and small subunits and additional subunits that allow the enzymes to bind to other cofactors, such as F_{420} and NAD(P)H (43). Four subgroups are classified in group 3 [NiFe] hydrogenases, group 3a-3d. Group 3a contains the F_{420}-reducing hydrogenases (Frh) that are found in methanogenic archaea and reduce F_{420} by oxidizing H_2, supplying reductants for methane production from CO_2 (43). This subgroup of hydrogenases is composed of a large subunit (FrhA), a small subunit (FrhG), and a FAD-containing subunit (FrhB) that binds to F_{420} (134, 135). The structure of the F_{420}-reducing hydrogenase from *Methanothermobacter marburgensis* represents the first [NiFe] hydrogenase structure not obtained from group 1 (135).

Group 3b hydrogenases, mostly found in thermophilic archaea, also contain the typical large and small subunits plus two other subunits containing iron-sulfur clusters and the nicotinamide cofactor-binding site. These enzymes oxidize H_2 and reduce $NAD(P)^+$ (55). Soluble hydrogenase I and II (SHI and SHII) from *P. furiosus* are examples of this group. They are each encoded by four-gene operons and both enzymes have been purified and characterized (136, 137). The physiological functions of SHI and SHII were proposed to oxidize H_2 to regenerate NAD(P)H for biosynthesis purposes (138, 139). SHI was reported to be "oxygen-resilient" utilizing a different mechanism for oxygen tolerance compared to that of group 1 oxygen-tolerant

hydrogenases because it does not feature the crucial proximal [4Fe-3S] cluster (140). In the research reported in this thesis, SHI from *P. furiosus* has been engineered and used in many applications that will be discussed in Chapter 2 and the Appendix.

Group 3c consists of trimeric methyl viologen-reducing hydrogenases (MvhAGD) that are found in certain archaea, mostly methanogens. MvhAGD forms a complex with heterodisulfide dehydrogenase (HdrABC), which provides the electron acceptor heterodisulfide CoM-S-S-CoB (55, 141). This complex couples the exergonic reduction of heterodisulfide (E'_0= - 140 mV) with the endergonic reduction of ferredoxin (E'_0= - 500 mV) employing H_2 (E'_0= - 414 mV) as the electron donor, providing a mechanism of energy conservation in methanogens (47, 142, 143). This is also another example of enzymes using the bifurcating mechanism, in addition to the [FeFe] hydrogenase described above.

Group 3d contains so-called bidirectional heteromultimeric hydrogenases (HoxHY), where an additional NADH oxidoreductase module is associated with the large and small subunits (43, 55). This type of hydrogenase is found in aerobic H_2-utilizing organisms, such as *R. eutropha*, and in many cyanobacteria, like *Synechocystis* spp. PCC 6803 (144, 145). In *R. eutropha*, this type of hydrogenase oxidizes H_2 to produce NADH that is further used for biosynthesis purposes or by Complex I for energy generation (144). In *Synechocystis*, the bidirectional hydrogenase is able to produce H_2 directly employing Fd or flavodoxin, disposing of the excess electrons generated from photosynthesis and fermentation (129).

Group 4 [NiFe] hydrogenases are H_2-evolving, energy-conserving, membrane-bound and mostly Fd-dependent enzymes (23, 43, 109, 146, 147). This group has low sequence homology to the other groups of hydrogenase, except for the residues coordinating the [NiFe] active site and proximal cluster. These membrane-bound enzymes can be categorized into three major subgroups

(55). The first are energy-converting hydrogenases (Ech) that contain six subunits and catalyze H_2 production and generate an ion gradient. These are found in various bacteria and a few archaea. This subgroup was first characterized in *Methanosarcina barkeri* and it was demonstrated that the enzyme is essential for growth with acetate (146, 148). The second type of group 4 hydrogenases contains thirteen or more subunits including a H_2-evolving (Mbh) and a Na^+/H^+ antiporter (Mrp) module. This subgroup is mostly found in thermophilic archaea and was first described as the membrane-bound hydrogenase (MBH) from *P. furiosus* (149-151). The third type are variants of Mbh-Mrp hydrogenases (Eha/Ehb) observed in hydrogenotrophic methanogens. These enzymes possess extra subunits and reduce Fd at expense of the ionic gradient by oxidizing H_2 to balance the Fd-dependent reduction of CO_2, forming formylmethanofuran during the first step of methanogenesis (152, 153). The difference between Ech-type and Mrp-Mbh-type group 4 hydrogenases is that Ech lacks the Mrp-like antiporter module, hence Ech generates a proton gradient while Mrp-Mbh generates a sodium gradient. Group 4 hydrogenases also contain distinct H_2-evolving multisubunit enzymes that have additional subunits other than the Mrp-Mbh modules for electron input from different donors other than Fd. Examples of these enzymes include the formate hydrogen lyase from *E. coli* and *Thermococcus onnurienus*, which oxidize formate for H_2 production, and energy-conserving CO dehydrogenase complex from *T. onnurienus* and *Carboxydothermus hydrogenoformans*, which oxidize CO for H_2 generation (154-159).

A fifth class or group 5 hydrogenases was proposed recently based on a phylogenetic re-investigation, gene sequencing, and the biochemical properties of a hydrogenase from *Streptomyces spp*. that can oxidize low concentrations of H_2 (<1 ppm) (160-162). This group of hydrogenases can be found in many soil bacteria (163, 164). Group 5 is similar to group 1 enzymes in terms of sequence and structure, where they both consist of heterodimeric large and small

subunits and are associated with the cell membrane. However, group 5 enzymes do not contain a cytochrome-type anchor, and no redox partner has been identified. In addition, group 5 enzymes are oxygen-resistant, and the [NiFe]-binding cysteine residues are arranged differently in the sequence compared to the other enzymes in group 1 (160).

Homology and evolutionary relationship between MBH, MBX and Complex I

Complex I (NADH quinone oxidoreductase, NUO) is widespread taxonomically and found in the aerobic respiratory chain of a great number of microbial and eukaryote life forms. The composition of Complex I ranges from 11 subunits in some bacteria to more than 40 subunits in mitochondria (165). Complex I oxidizes NADH and transfers the electrons to quinone derivatives, generating a proton gradient that is used for energy conservation by ATP synthase (166, 167). The evolution of Complex I can be traced back to anaerobic respiratory systems, where they share a common ancestor (168). Group 4 [NiFe] hydrogenases, especially the Mbh-Mrp subgroup, have a close evolutionary relationship with Complex I (169-173). Based on the sequence analysis of the catalytic subunit, as depicted in Figure 1.8, NuoD, the catalytic subunit of Complex I involved in quinone-binding and reduction, was shown to be evolutionarily close to MbhL, the catalytic subunit of the group 4 hydrogenase. MbxL, the catalytic subunit of MBX that is thought to replace the function of MBH in the presence of S^0, is also classified within the same phylogenetic branch as NuoD and MbhL. MBX is ubiquitous within the order of Thermococcales and highly similar to MBH. MBX is thought to have originated by gene duplication of a proton-reducing Mbh-like ancestral respiratory complex (ARC) that arose during evolution, allowing the switch from the reduction of protons to S^0 (23, 149, 165). The homology between Complex I, MBH, MBX, and Mrp are portrayed in Figure 1.10. Mrp is a multiple resistance and pH-adaptation H^+/Na^+ antiporter

that has been studied extensively in *Bacillus subtilis* (174, 175). The major difference between MBH and MBX is that MbxL lacks two of the key cysteine residues coordinating the [NiFe] active site in MbhL, harboring a distinct catalytic activity. The properties of MBX will be further discussed in Chapter 3. MBH and MBX have a Mrp-type H^+/Na^+ antiporter module to balance the proton gradient with a Na^+ gradient for ATP generation, but Complex I lacks a subunit with homology to the Na^+ pumping antiporter. Thus, NUO can only translocate protons, which are utilized for ATP generation in these organisms. In addition, NUO has three additional subunits for electron input from NADH as portrayed in Figure 1.11. The net ion pumping for these complexes is 1 $H^+/2e^-$ for MBH and MBX, and 4 $H^+/2e^-$ for Complex I (165).

ARC was proposed to be the ancestor of MBH, MBX, and Complex I, with their diversification being driven by the redox state of the Earth's atmosphere and oceans. The energy yields increased when electron acceptors with higher electrochemical potential were reduced, which became available when the atmosphere and oceans became more oxidized primarily through oxygenic photosynthesis (165). The hypothetical ARC is believed to function similar to MBH, oxidizing Fd-like donors to reduce protons and generate a proton gradient. A trajectory of these extant complexes begins with MBH, reducing protons, then MBX, reducing S^0, and eventually Complex I, which reduces quinone (Figure 1.11) (165). The evolution of MBH involved the recruitment of the Mrp module to ARC to enable MBH to pump Na^+. The transition from proton-reducing MBH to S^0-reducing MBX represents a significant increase in energy yield from the electrochemical potential difference and proton pumping capacity (23, 165). The higher energy produced from S^0 reduction by Fd compared to proton reduction (1 ATP/H_2S compared to 0.3 ATP/H_2) is thought to be the evolutionary driving force (165). The early evolution of MBX is also supported by the geochemical data showing the presence of S^0 in the Archean (176, 177). For the

evolution of NUO, there was a switch in the electron donor from oxygen-sensitive Fd to oxygen-stable NADH in the high-oxygen environments, as well as a higher energy yield due to the large electrochemical potential difference between NADH and quinone derivatives (165).

S^0 metabolism

S^0 and other sulfur compounds are the most abundant sources that are used by microorganisms as either electron donors or acceptors to support growth in the volcanic environments and S^0 is also thought to be the ultimate source for metabolic sulfur-cycling in early Archaean (177-180). The solubility of S^0 in water is very low (5 µg/L at 25 °C) and it predominates in the form of a S_8-ring. S^0 dissolves in aqueous solution by the addition of sulfide and polysulfide is formed: $nS^0 + HS^- \rightarrow S^{2-}_{n+1} + H^+$. In this reaction, the S_8-ring is cleaved by nucleophilic attack of HS^- and the maximum amount of S^0 dissolved is nearly equivalent to the sulfide concentration at neutral pH (181). Polysulfide is also thought to be a possible intermediate during S^0 respiration because of the low solubility of S^0 and the reactive interaction between S^0 and sulfide, which are typically supplied in the growth media of sulfur-reducers (181).

The ability to reduce S^0 is widespread in anaerobic archaea and at least four types are known (182, 183). The first type of uses H_2 as the electron donor, as carried out by some species in the genera *Acidianus*, *Pyrodictium*, *Pyrobaculum* and *Thermoplasma*, while the second type uses organic compounds as the electron donors, as carried out by some species in the genera *Desulfurococcus*, *Caldivirga* and *Thermocladium*. The third type of S^0 respiration involves the fermentation of organic compounds and S^0 is used as an electron acceptor to remove reducing equivalents, as carried out by some species in the genera *Hyperthermus*, *Thermococcus* and

Pyrococcus. The fourth type of S^0 reduction can be found in methanogens that assimilate sulfur by reducing S^0 to H_2S without conserving energy during the process (183). Extensive studies have been performed into the mechanism by which H_2 is used as the electron donor for the S^0 respiration in *Acidianus ambivalens* and *Pyrodictium* spp. (178, 181, 184-186). This type of S^0 reduction is similar to that found in some bacteria, such as the mesophile *Wolinella succinogenes*, and is generally accepted as a model system for anaerobic S^0 respiration for H_2S production coupled with energy conservation (181, 183). This process involves two membrane-associated multisubunit complexes, a molybdopterin-containing sulfur reductase (SR) and a [NiFe] hydrogenase (Hyn). The electrons from H_2 oxidation by Hyn are transferred to SR for S^0 reduction and this is mediated by quinones or cytochromes, depending on the organism. In addition, the genes of SR and Hyn from *A. ambivalens* are very similar in sequence to their bacterial homologs, suggesting that they arose by a lateral gene transfer event (182, 184). Compared to the first type of S^0 reduction, the other three mechanisms are not well studied. In *P. furiosus*, no homolog of the molybdopterin-containing SR is present. *P. furiosus* employs the third type of fermentation-based S^0 reduction via Fd and MBX as described above. However, the exact role of MBX in S^0 respiration was not known and understanding how S^0 is reduced by this organism was one of the primary goals of this research.

Arsenic metabolism

While many hyperthermophiles use protons and S^0 as terminal electron acceptors, some are able to use some other compounds. For example, *Pyrobaculum aerophilum*, which grows optimally at 100 °C, is able to reduce arsenate (V) to support its growth (187, 188). Arsenic is a ubiquitous element and is released through various natural events, such as volcanic emissions, and through human activities, such as the use of arsenical pesticides and herbicides. Arsenic is very

toxic as well as carcinogenic and it is mostly found in inorganic forms at neutral pH as trivalent arsenite or pentavalent arsenate (189). Generally speaking, prokaryotes are an order of magnitude more sensitive to arsenite (III) than to arsenate (V) (190). The toxicity of arsenate (V) stems from its capacity to replace phosphate in many biochemical pathways because of the similarity in their structures and properties while arsenite (III) readily interacts with thiol-containing molecules, such as cysteine (191). Arsenate (V) disrupts the phosphorylation process that results in inhibition of ATP synthesis, wherein arsenate (V) interacts with ADP to form an arsenate-phosphate bond that is unstable and spontaneously hydrolyzes back to ADP and arsenate (V). Therefore, all ATP-dependent biochemical pathways will be impaired, such as ATP-dependent transport and signal transduction pathways (192). Arsenite (III) has a strong affinity for sulfhydryl groups, affecting the structures and activities of numerous proteins. Otherwise, it can also react with metabolites that contain dithiol groups, such as glutathione and thioredoxin, which are important for various intracellular redox homeostasis, protein folding, and sulfur metabolism. Arsenite (III) is also carcinogenic owing to the interaction with reduced glutathione, which is a major cellular antioxidant. The interaction between arsenite (III) and glutathione causes cells to be highly sensitive to reactive oxygen species that damage proteins and DNA (193, 194).

Microorganisms have not only developed arsenic-resistance mechanisms, but some of them can even use arsenic as a source of energy (195-197). Arsenic-resistance mechanisms usually include precipitation, chelation, compartmentalization, extrusion, or biochemical transformation (192, 196, 197). Figure 1.12 shows the reactions microorganisms have evolved for arsenic transformation, including arsenite (III) methylation, arsenate (V) reduction for detoxification or respiration, and arsenite (III) oxidation. The toxicity of arsenic depends on the chemistry of the compounds and their oxidation states (198).

Bacteria reduce arsenate (V) to arsenite (III) by two distinct reductases, cytoplasmic arsenate reductase (*arsC*) and respiratory arsenate reductase (*arr*) (195). ArsC is encoded by an arsenic-resistance (*ars*) operon that features the relevant genes in the order *arsR*, *arsB*, and *arsC* (199). In particular Gram-negative bacteria, two additional genes, *arsA* and *arsD*, are found on the same operon (in the order of RDABC) (200). The arsC-system is the most widely distributed and characterized arsenic detoxification system (196, 201, 202). ArsR functions as a repressor of the operon and is generally located at the beginning of the *ars* operon (203, 204), although a rare example has been reported in *Shewanella* where *arsR* is not on the same operon, but is located elsewhere on the chromosome (195). ArsD is a weak regulator of the operon that functions similar to ArsR (199, 205). ArsC is a cytoplasmic arsenate reductase that reduces arsenate (V) to arsenite (III) using glutathione as the electron donor, and arsenite (III) is transported out of the cell by ArsB, an arsenite (III) pump. The transportation of arsenite (III) is energized by either a proton gradient or ArsA ATPase (199). The detoxification mechanism of converting arsenate (V) to arsenite (III) and extruding out of cells using this ArsC system is conserved from bacteria to plants (206). Homologs of bacterial ArsC are also annotated in several archaeal genomes, including *P. furiosus*, although *arsC* is missing in certain archaeal genomes containing the *ars* operon or in the species resistant to arsenate (V) (207).

Arsenate respiratory reductase (Arr) is fundamentally different from ArsC in that it is involved in energy metabolism rather than detoxification. Compared to the extensively studied ArsC system, Arr has been much less investigated. Three Arr enzymes have been purified and characterized from *Chrysiogenes arsenatis*, *Bacillus selenitireducens* and *Shewanella trabarsenatis* strain ANA-3 (208-210). All of them are heterodimers composed of a large and small subunit, ArrA (~100 kDa) and ArrB (~30 kDa). ArrA belongs to the DMSO reductase family of

molybdoenzymes, containing the arsenate (V)-binding catalytic site with a molybdopterin cofactor and a [4Fe-4S] cluster, while ArrB is an iron-sulfur protein containing three [4Fe-4S] clusters. A twin-arginine translocation (TAT) signal was identified in ArrA that translocates ArrAB to the periplasm. A membrane-associated periplasmic tetraheme c-type cytochrome, CymA, has been reported to be crucial for the arsenate (V) reduction in *S. trabarsenatis* (211). Therefore, it was proposed that CymA receives the electrons from the quinol pool and transfers them to the catalytic site in ArrA for arsenate (V) reduction through the iron-sulfur clusters in ArrB and ArrA (212). A third gene has been found in the operon that encodes ArrAB in several microbes, including *Pyrobaculum aerophilum*, and this encodes the integral membrane protein ArrC. ArrC was proposed to be a membrane anchor and to mediate electron transfer between ArrAB and the quinol pool (213). The properties of Arr from *P. aerophilum* will be discussed in Chapter 4.

Goals of this work

The primary goal of this work is to gain a deeper understanding of structure and function of the hydrogenases and of closely related enzymes involved in respiration by *Pyrococcus furiosus*. Chapter 2 describes scaling up the purification process for soluble hydrogenase I (SHI) in which we employed an engineered strain to over-produce the enzyme. Sulfur respiration in *P. furiosus* has been investigated for more than a decade and a key enzyme closely related to MBH, membrane-bound oxidoreductase (MBX), was reported to be crucial for growth in the presence of S^0. However, no direct evidence has been reported regarding its substrate, leaving the function of MBX a mystery. Chapter 3 describes the purification and characterization of MBX and sheds light on S^0 metabolism in *P. furiosus*. The scope of the study of the respiratory systems of *P. furiosus* was also expanded to include another electron acceptor, arsenic, in addition to protons (MBH) and

S^0 (MBX). Chapter 4 describes the heterologous expression and characterization of an arsenate respiratory reductase from the hyperthermophilic archaeon *Pyrbaculum aerophilum* in *P. furiosus*. The effect of this enzyme on the growth of *P. furiosus* was also investigated.

Figure 1.1

Phylogenetic tree of three domains based on the rRNA sequence analysis. Red lines indicate hyperthermophiles. *Pyrococcus* and *Pyrobaculum* used in this study were classified in different branches of Archaea. Modified from (4).

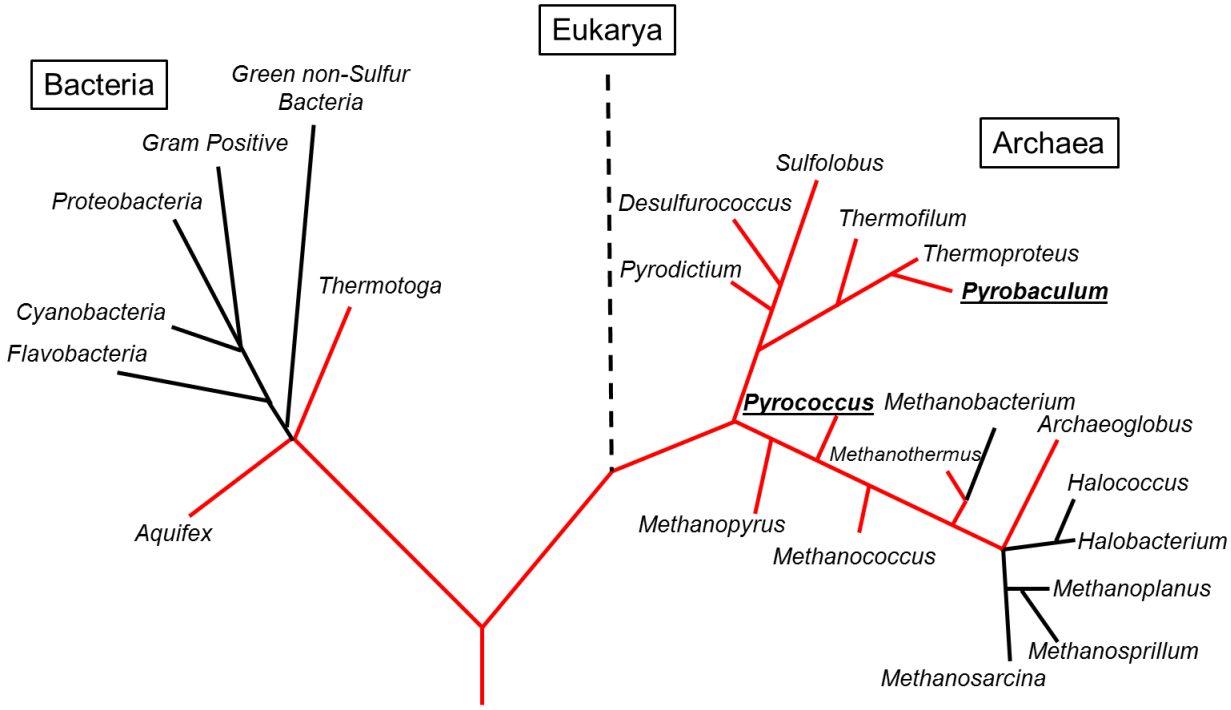
Eukarya
Bacteria
Green non-Sulfur Bacteria
Gram Positive
Proteobacteria
Thermotoga
Cyanobacteria
Flavobacteria
Aquifex
Archaea
Sulfolobus
Desulfurococcus
Thermofilum
Thermoproteus
Pyrodictium
Pyrobaculum
Pyrococcus
Methanobacterium
Archaeoglobus
Methanothermus
Halococcus
Methanopyrus
Methanococcus
Halobacterium
Methanoplanus
Methanosprillum
Methanosarcina

Figure 1.2

Electron micrograph of *Pyrococcus furiosus* showing the monopolar polytrichous flagellation.

Taken from (14).

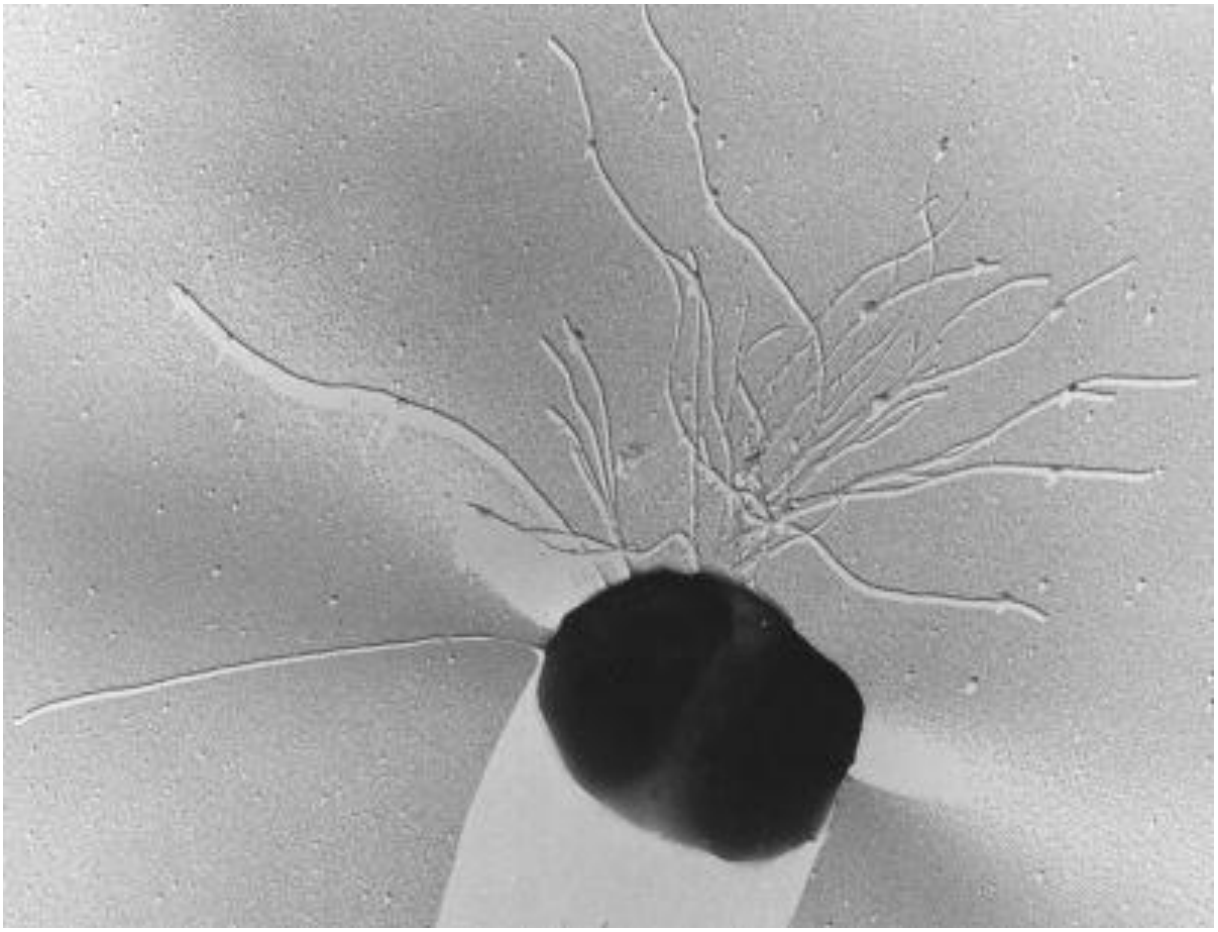

Figure 1.3

Proposed physiological roles of MBH, SHI/II, and MBX in hydrogen and sulfur metabolisms. MBH: membrane-bound hydrogenase; MBX: membrane-bound oxidoreductase; SHI: soluble hydrogenase I; SHII: soluble hydrogenase II; Fd_{red}: reduced form ferredoxin; Fd_{ox}: oxidized form ferredoxin. Modified from (23).

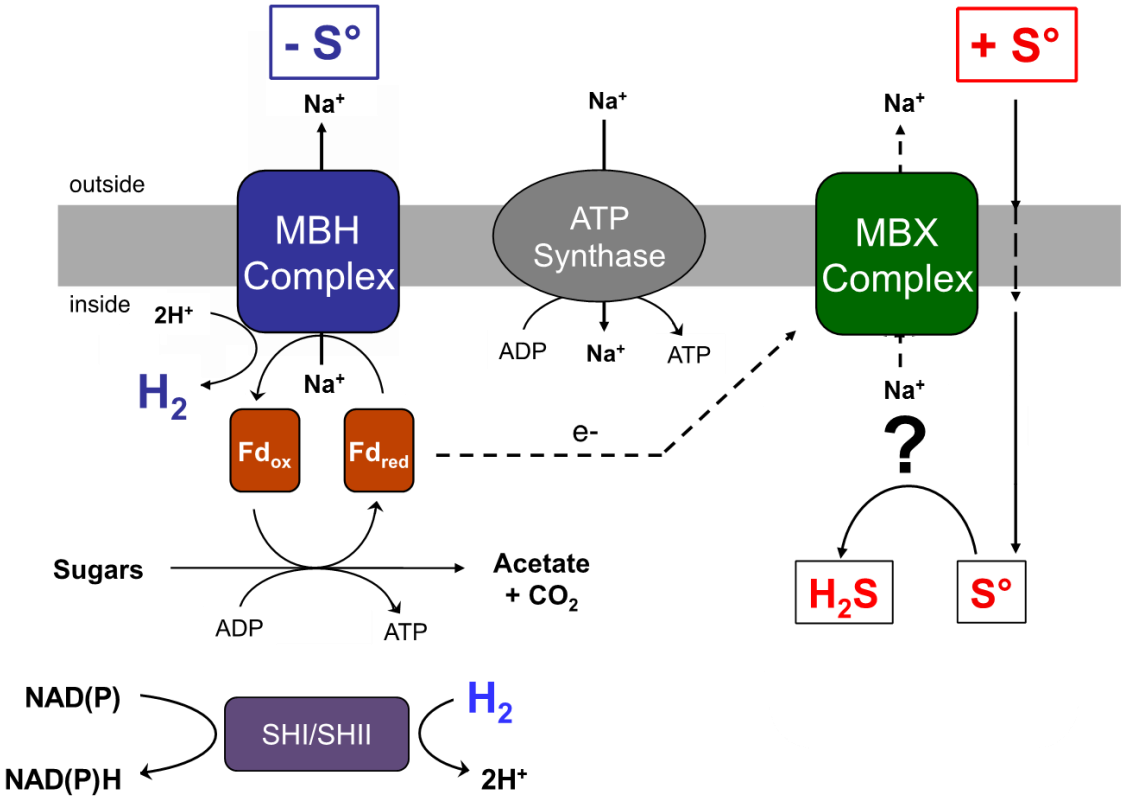
- S°
+ S°
Na+
Na+
Na+
outside
MBH Complex
ATP Synthase
MBX Complex
inside
2H+
ADP
Na+
ATP
H2
Na+
Na+
?
Fdox
Fdred
e-
Sugars
Acetate + CO2
ADP
ATP
H2S
S°
NAD(P)
SHI/SHII
H2
NAD(P)H
2H+

Figure 1.4

Modified Embden-Meyerhof pathway in *P. furiosus*. One molecule of glucose is converted to two molecules of acetate and CO_2. The primary electron carrier is ferredoxin (Fd), which is reduced by GAPOR and POR and transfers electrons to membrane-bound hydrogenase (MBH) for H_2 production. GK: glucokinase; PGI: phosphoglucoisomerase; PFK: phosphofructokinase; FBA: fructose bisphosphate aldolase; TPI: triose phosphate isomerase; GAPOR: glyceraldehyde-3-phosphate oxidoreductase; PGM: phosphoglycerate mutase; ENO: enolase; PK: pyruvate kinase; POR: pyruvate ferredoxin oxidoreductase; ACS: acetyl-CoA synthetase I and II. Modified from (149).

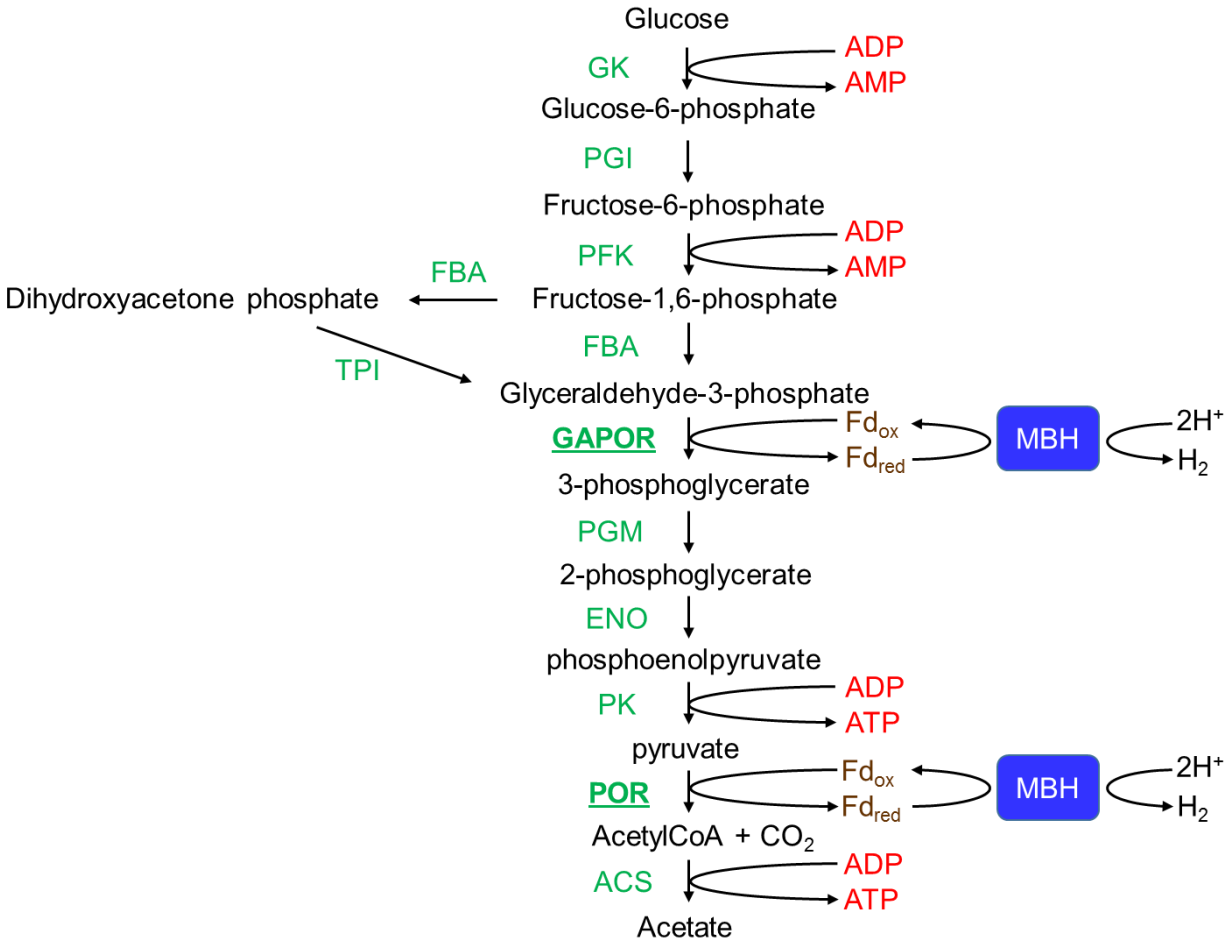
Glucose
GK
ADP
AMP
Glucose-6-phosphate
PGI
Fructose-6-phosphate
PFK
ADP
AMP
FBA
Dihydroxyacetone phosphate
Fructose-1,6-phosphate
FBA
TPI
Glyceraldehyde-3-phosphate
GAPOR
Fdox
Fdred
MBH
2H+
H2
3-phosphoglycerate
PGM
2-phosphoglycerate
ENO
phosphoenolpyruvate
PK
ADP
ATP
pyruvate
POR
Fdox
Fdred
MBH
2H+
H2
AcetylCoA + CO2
ACS
ADP
ATP
Acetate

Figure 1.5

Structure of Fe-guanylylpyrodinol (Fe-GP) cofactor (top) and the H cluster (bottom). Fe_p: proximal Fe; Fe_d: distal Fe. Taken from (44) (214).

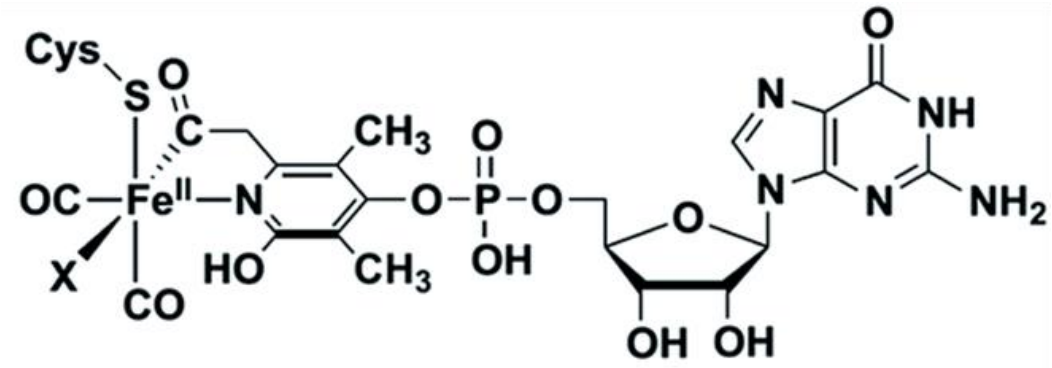
Cys
S
O
C
CH3
O
P
O
OC
Fe II
N
O
N
NH
N
N
NH2
X
HO
CH3
OH
CO
O
OH OH

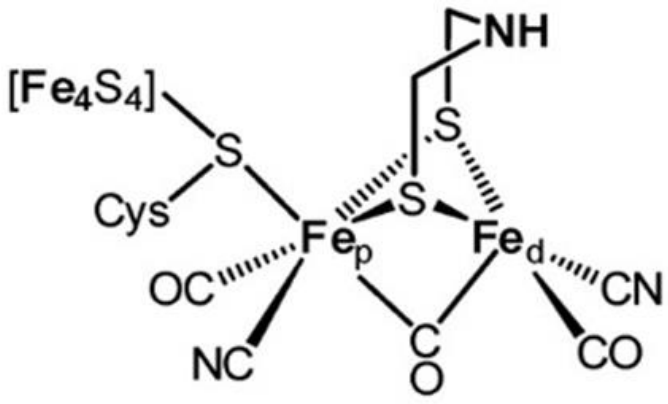
NH
[Fe4S4]
S
S
Cys
S
Fe p
Fe d
OC
CN
NC
C
O
CO

Figure 1.6

Structure of the [NiFe] hydrogenase from *Desulfovibrio gigas*. The large subunit is shown in blue and the small subunit is shown in red. An enlarged box of the NiFe site shows the CO and CN ligands binding the Fe atom and the four cysteine residues for the active site coordination. Modified from (68).

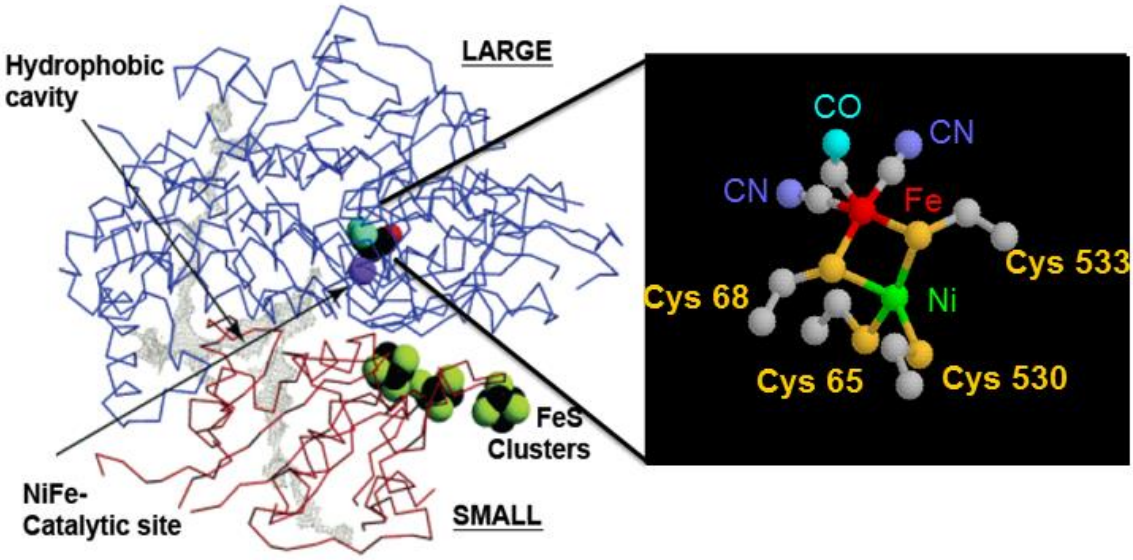
Hydrophobic cavity
LARGE
CO
CN
CN
Fe
Cys 533
Cys 68
Ni
Cys 65
Cys 530
FeS Clusters
NiFe-Catalytic site
SMALL

Figure 1.7

Proposed maturation pathway of [NiFe] hydrogenases. HypE and HypF generate the CN ligands and add them to the Fe atom and the ligands-bound Fe atom is transferred to the large subunit by HypC and HypD. HypA and HypB are responsible for the assembly of the Ni atom. A peptidase catalyzes a C-terminal cleavage before the large subunit binds to the small subunit to form a mature enzyme. Modified from (44).

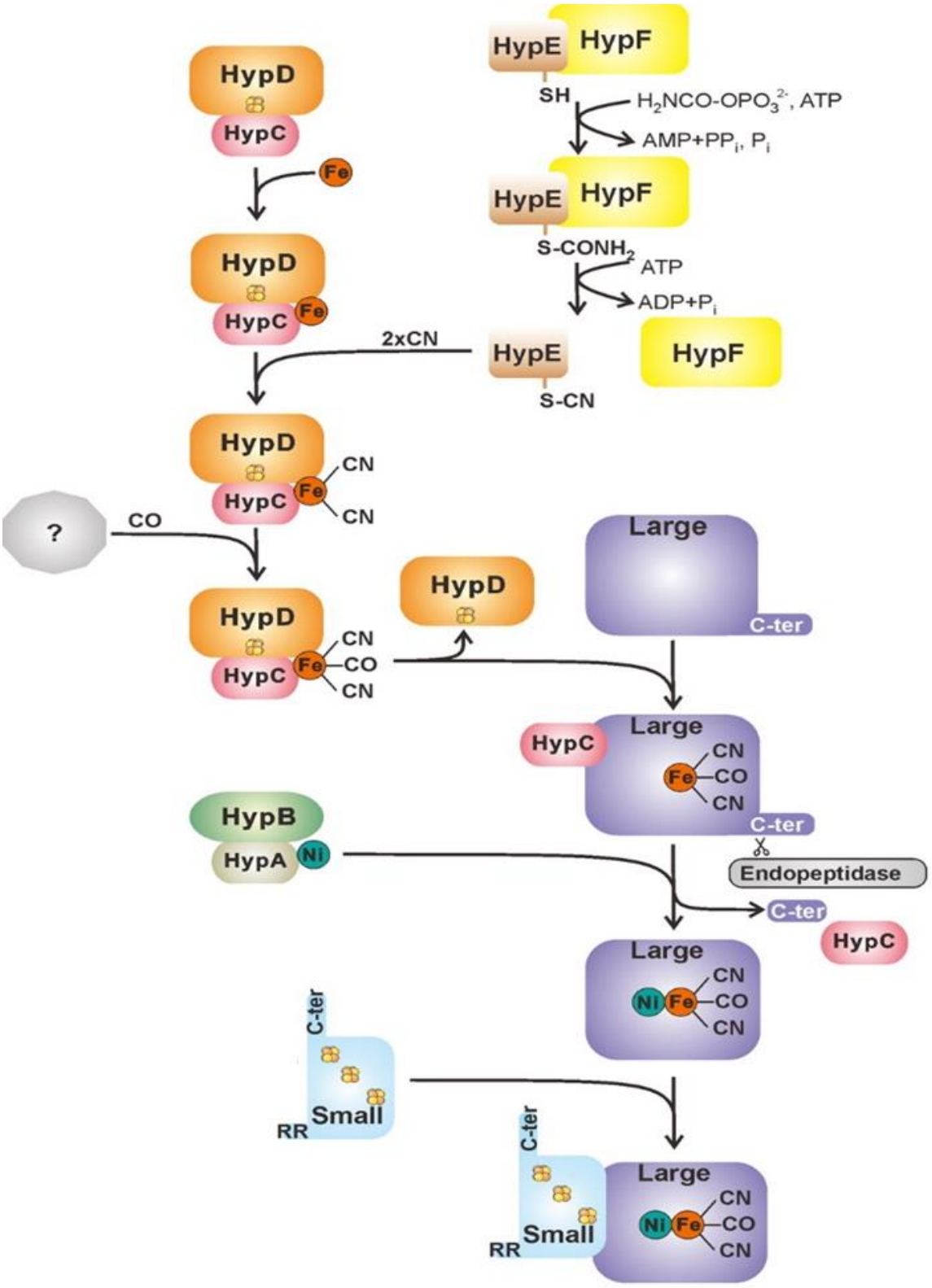
HypD
HypC
Fe
HypE
HypF
SH
$H_2NCO\text{-}OPO_3^{2-}$, ATP
AMP+PP_i, P_i
S-$CONH_2$
ATP
ADP+P_i
2xCN
S-CN
CN
CO
?
Large
C-ter
HypB
HypA
Ni
Endopeptidase
Small
RR

Figure 1.8

Phylogenetic tree of [NiFe] hydrogenases based on the sequence analysis of the catalytic subunits. Nuo: NADH quinone oxidoreductase; Mbx: membrane-bound oxidoreductase. NUO and MBX are not hydrogenases but their catalytic subunits are homologous to group 4 hydrogenases. Modified from (165).

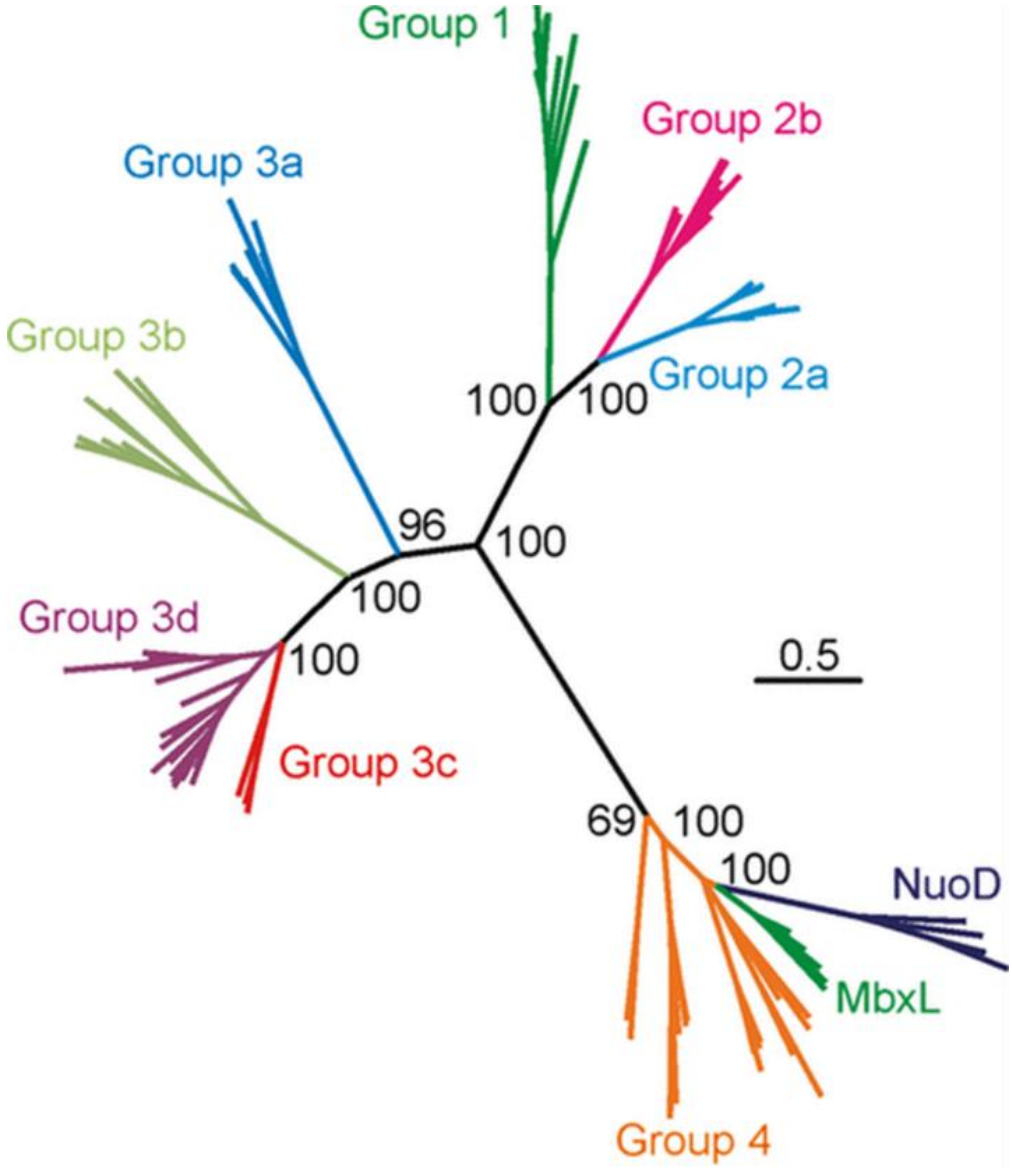
Group 1
Group 2b
Group 3a
Group 3b
Group 2a
100
100
96
100
100
Group 3d
100
0.5
Group 3c
69
100
100
NuoD
MbxL
Group 4

Figure 1.9

Redox states of the Ni atom of [NiFe] hydrogenases. NiR, NiC, and NiSI represent the states in the catalytic cycle, while NiA and NiB are the states after oxidation. Taken from (215).

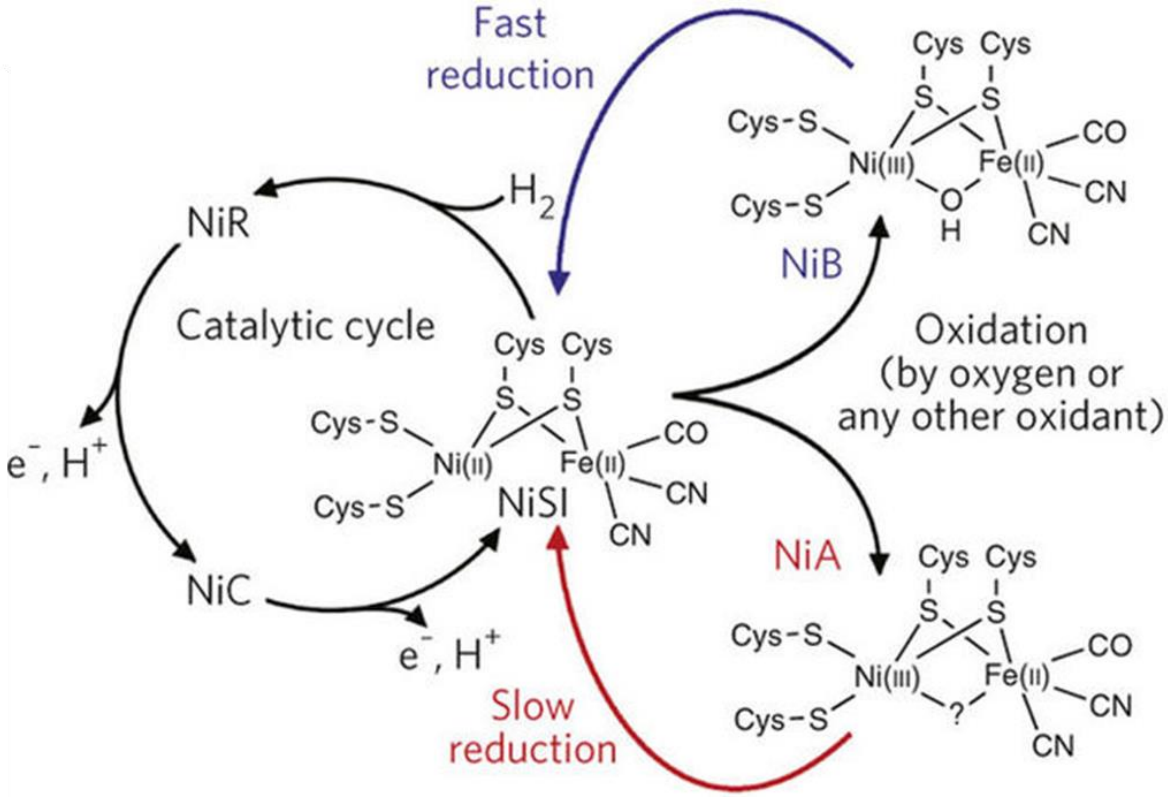
Fast
reduction
H_2
NiR
Catalytic cycle
e^-, H^+
NiC
e^-, H^+
Slow
reduction
NiSI
NiB
NiA
Oxidation
(by oxygen or
any other oxidant)
Cys Cys
S S
Cys-S
Cys-S
Ni(II)
Fe(II)
CO
CN
CN
Ni(III)
O
H
?

Figure 1.10

Models of Mrp, Complex I, Mbh and Mbx. The homology between complexes are shown in the same colors. Mrp: multiple resistane and pH antiporter; Nuo: NADH quinone oxidoreductase; Mbh: membrane-bound hydrogenase; Mbx: membrane-bound oxidoreductase. Modified from (165).

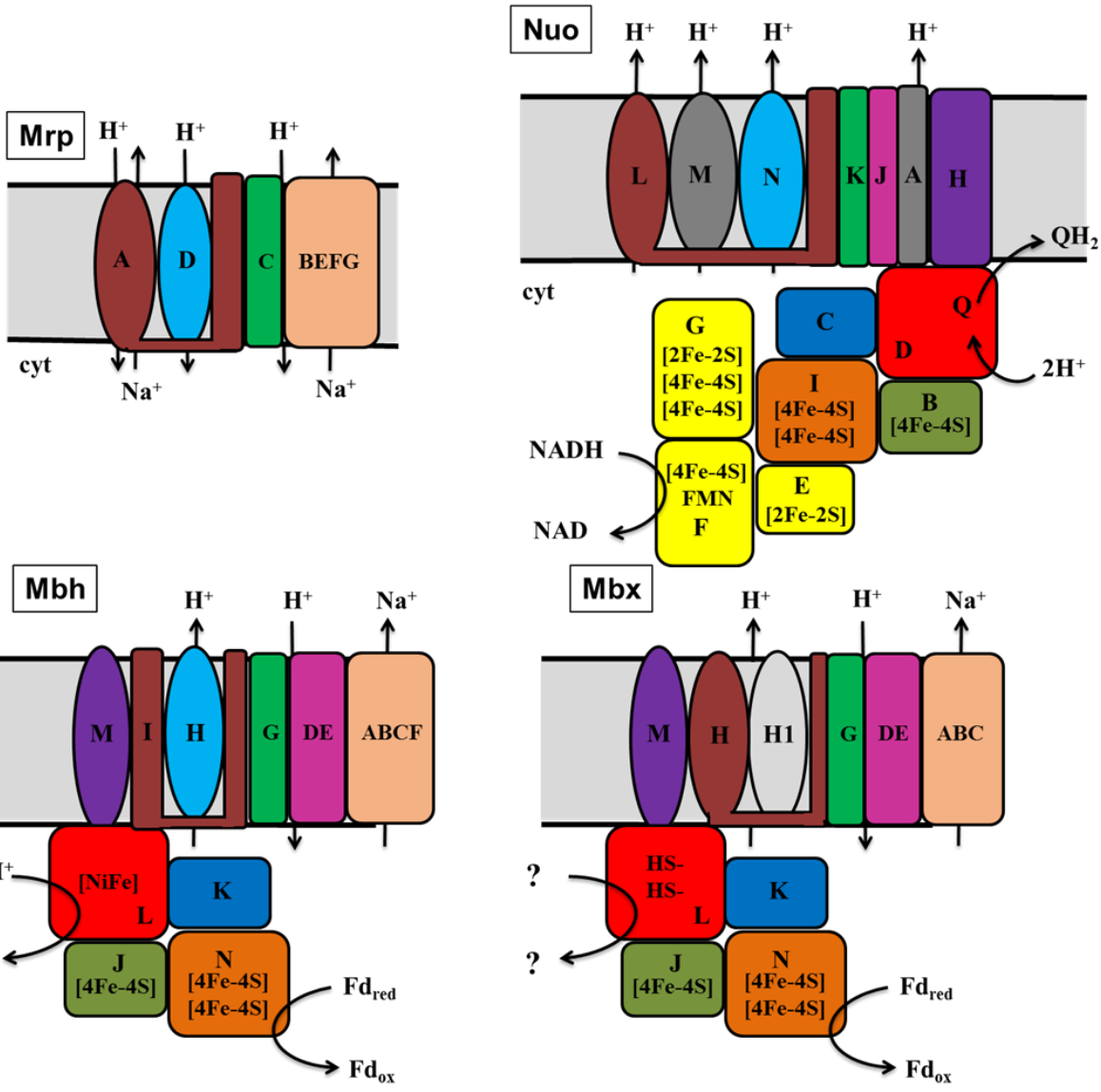
Mrp
H+
H+
H+
A
D
C
BEFG
cyt
Na+
Na+
Nuo
H+
H+
H+
H+
L
M
N
K
J
A
H
QH2
cyt
G
[2Fe-2S]
[4Fe-4S]
[4Fe-4S]
C
Q
D
2H+
I
[4Fe-4S]
[4Fe-4S]
B
[4Fe-4S]
NADH
[4Fe-4S]
FMN
F
E
[2Fe-2S]
NAD
Mbh
H+
H+
Na+
M
I
H
G
DE
ABCF
2H+
[NiFe]
L
K
H2
J
[4Fe-4S]
N
[4Fe-4S]
[4Fe-4S]
Fdred
Fdox
Mbx
H+
H+
Na+
M
H
H1
G
DE
ABC
?
HS-
HS-
L
K
?
J
[4Fe-4S]
N
[4Fe-4S]
[4Fe-4S]
Fdred
Fdox

Figure 1.11

The evolution of ARC-derived respiratory complexes based on geochemical potential. ARC: ancestral respiratory omplex; MRP: multiple resistane and pH antiporter; MBH: membrane-bound hydrogenase; MBX: membrane-bound oxidoreductase; NUO: NADH quinone oxidoreductase. Modified from (165).

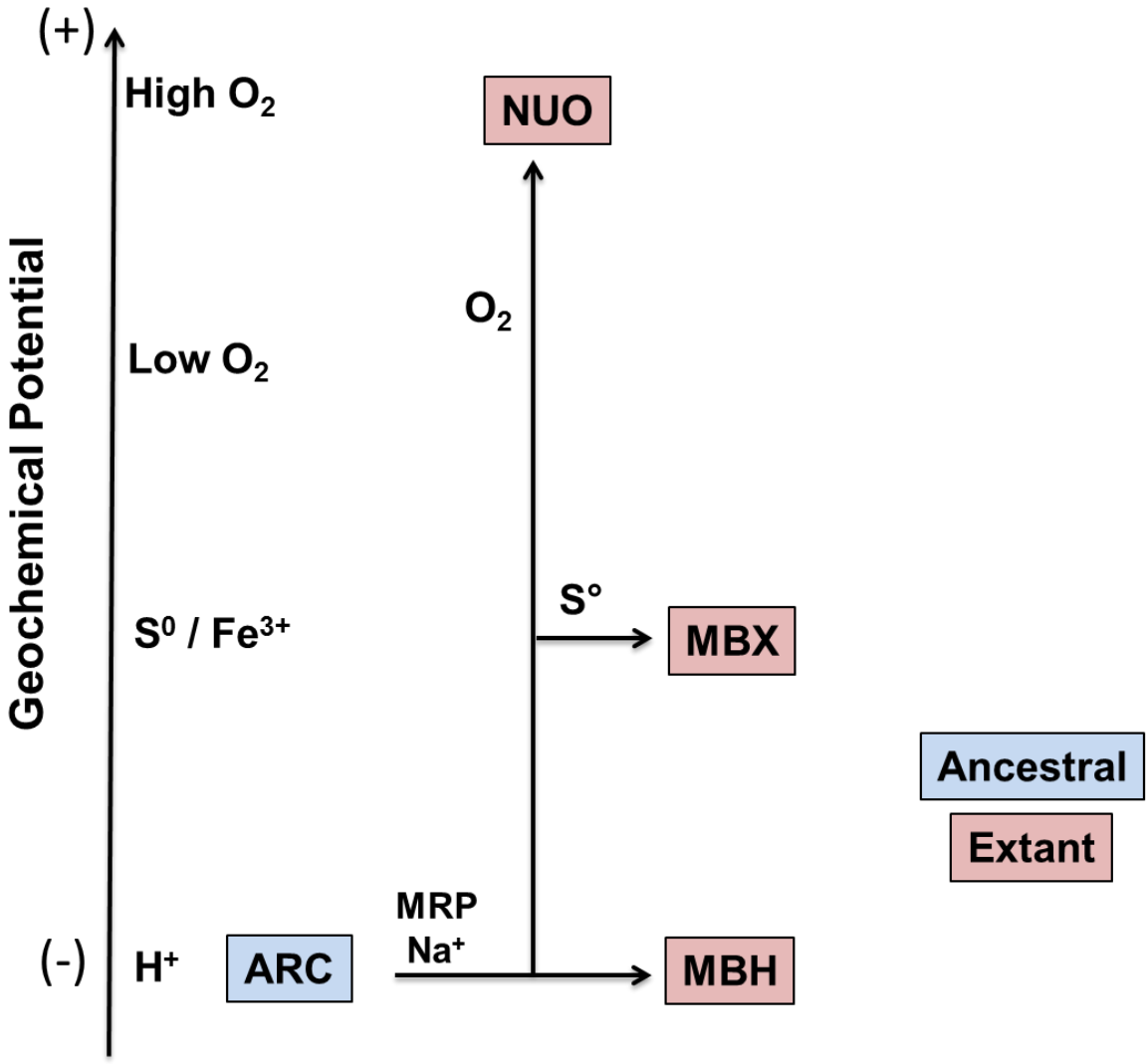
(+)
High O_2
Low O_2
S^0 / Fe^{3+}
(-)
H^+
Geochemical Potential
NUO
O_2
S°
MBX
MRP
Na^+
ARC
MBH
Ancestral
Extant

Figure 1.12

The processes evolved by prokaryotes for arsenic transformation. ArsC: detoxifying arsenate reductase; Ars(A)B: arsenite efflux pump; Arr: arsenate respiratory reductase; Aox/Arx: arsenite oxidase; Pit: phosphate inorganic transport system; Pst: phosphate specific transport system; GlpF: aquaglyceroporin; MMA: monomethylarsonic acid; DMAA: dimethylarsinic acid; DMA: dimethylarsine; TMAO: trimethylarsine oxide; TMA: trimethylarsine. Modified from (192).

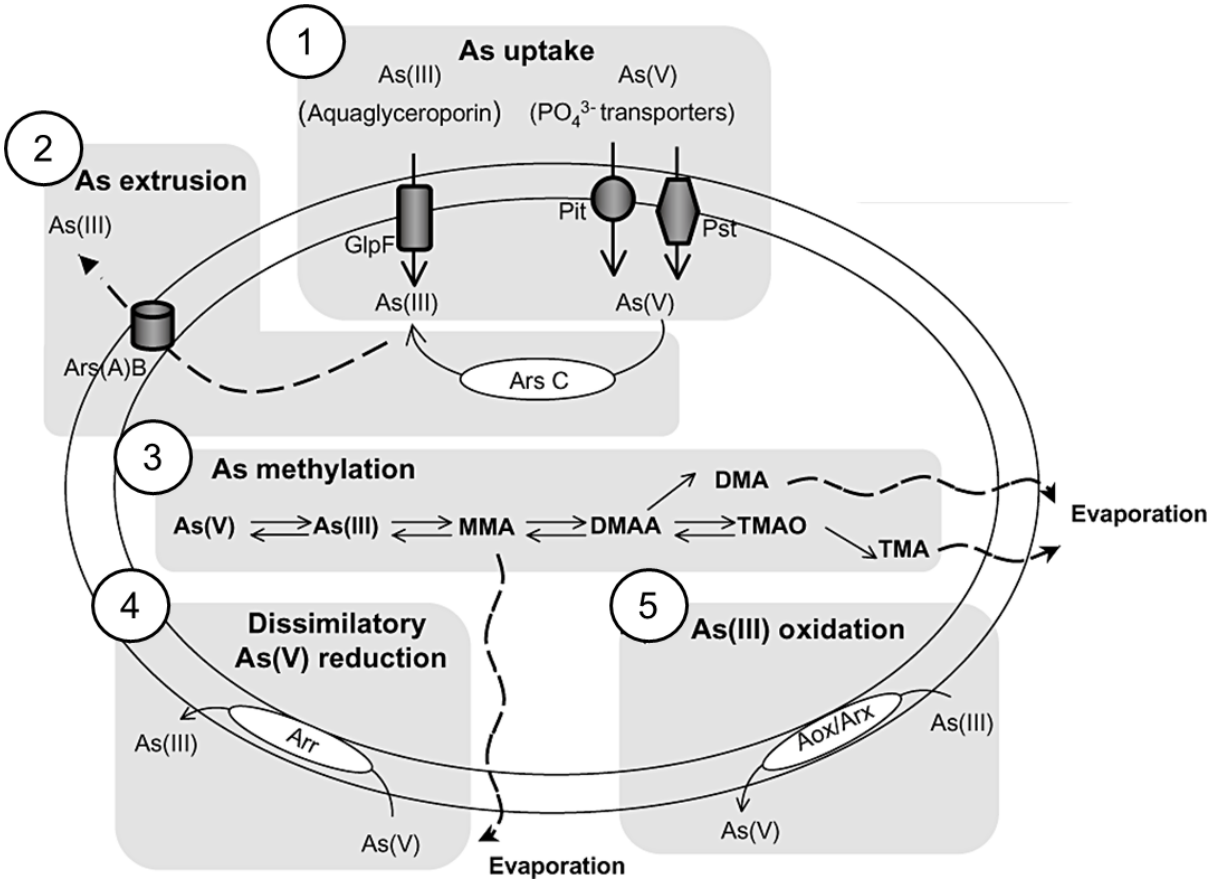
1
As uptake
As(III)
(Aquaglyceroporin)
As(V)
(PO_4^{3-} transporters)
2
As extrusion
As(III)
GlpF
Pit
Pst
As(III)
As(V)
Ars(A)B
Ars C
3
As methylation
DMA
As(V)
As(III)
MMA
DMAA
TMAO
TMA
Evaporation
4
Dissimilatory
As(V) reduction
As(III)
Arr
As(V)
5
As(III) oxidation
Aox/Arx
As(III)
As(V)
Evaporation

CHAPTER 2

IMPROVED PRODUCTION OF THE NIFE-HYDROGENASE FROM *PYROCOCCUS FURIOSUS* BY INCREASED EXPRESSION OF MATURATION GENES

Wu CH, Ponir CA, Haja DK, Adams MWW. Submitted to *Protein Eng Des Sel*.

Abstract

The NADPH-dependent cytoplasmic [NiFe]-hydrogenase (SHI) from the hyperthermophile *Pyrococcus furiosus*, which grows optimally near 100°C, is extremely thermostable and has many *in vitro* applications, including cofactor generation and hydrogen production. In particular, SHI is used in a cell-free synthetic pathway that contains more than a dozen other enzymes and produces three times more hydrogen (12 H_2/glucose) from sugars compared to cellular fermentations (4 H_2/glucose). We previously reported homologous over-expression and rapid purification of an affinity tagged (9x-His) version of SHI, which is a heterotetrameric enzyme. However, about 30% of the enzyme that was purified contained an inactive trimeric form of SHI lacking the catalytic [NiFe]-containing subunit. Herein, we constructed a strain of *P. furiosus* that contained a second set of the eight genes involved in the maturation of the catalytic subunit and insertion of the [NiFe]-site, along with a second set of the four genes encoding the SHI structural subunits. This resulted in a 40% higher yield of the purified affinity-tagged enzyme and the content of the inactive trimeric form decreased to 5% of the total protein. These results bode well for the future production of active SHI for both basic and applied purposes.

Key words (Max 5)

Affinity Purification/ Hydrogen/ Maturation/ [NiFe]-processing

Introduction

Transportation is a significant source of carbon emissions that contributes to climate damage as it still relies heavily on fossil fuels as the energy source (Rietveld, 2013). Hydrogen gas is a potential renewable energy carrier and the demand for it is expected to increase dramatically in the near future, especially with the recent availability of commercial hydrogen fuel-cell vehicles (HFCVs). HFCVs provide an alternative option for future transportation where water is the only waste product (Jacobson *et al.*, 2005). However, current methods of hydrogen production are also still heavily dependent on fossil fuels, typically involving steam reformation of natural gas. Although a clean method for hydrogen production has been developed involving water splitting by electrolysis, this requires the expensive metal platinum as the hydrogen-evolving catalyst (Lee *et al.*, 2010). The enzyme hydrogenase catalyzes hydrogen production by the reversible interconversion of protons, electrons and hydrogen gas, and most known hydrogenases use nickel and iron in their catalytic sites (Vignais and Billoud, 2007). Hydrogenases or biomimetic versions of their catalytic sites containing inexpensive nickel and iron could therefore be essential components of clean and renewable methods for industrial hydrogen production.

The hyperthermophilic archaeon *Pyrococcus furiosus*, which grows optimally near 100°C, contains three [NiFe]-hydrogenases. One is membrane-bound (MBH) while the other two are cytoplasmic (SHI and SHII). All three have been purified and characterized from native biomass and SHI has been studied extensively (Bryant and Adams, 1989, Chandrayan *et al.*, 2015, Ma *et al.*, 2000, McTernan *et al.*, 2015, McTernan *et al.*, 2014, Wu *et al.*, 2015). SHI is a heterotetrameric enzyme ($\alpha\beta\gamma\delta$) that catalyzes the reversible reduction of $NADP^+$ by hydrogen gas. The proposed metal cluster content of each of the subunits and the proposed pathway of electron flow between NADP(H) and hydrogen are shown in Figure 2.1. The enzyme has attracted a lot of attention

because $NADP^+$-dependent hydrogenases are quite rare in microbial metabolism (Spaans *et al.*, 2015). Based on kinetic studies, the predicted physiological function of SHI is to utilize hydrogen to generate NADPH, which can then be used for biosynthesis (van Haaster *et al.*, 2005, van Haaster *et al.*, 2008).

The reversible oxidation of NADPH coupled to hydrogen gas production catalyzed by SHI has several biotechnological implications (Wu, *et al.*, 2015). Among these, the most promising and extensively studied is a cell-free synthetic pathway for the conversion of various carbohydrate substrates to hydrogen. In this *in vitro* system, purified enzymes of the pentose phosphate pathway are used to oxidize glucose and generate NADPH, which is oxidized by SHI to produce hydrogen (Woodward *et al.*, 2000). This system was further modified to include a phosphorylation step to generate glucose-6-phosphate from starch, and SHI generates hydrogen from NADPH in the last step of the pathway (Zhang *et al.*, 2007). This cell-free system for carbohydrate to hydrogen conversion has a major advantage over cellular systems as it generates the theoretical yield of hydrogen from sugars (12 H_2/glucose equivalent), which is three times higher than the maximum yield obtained by microbial fermentation of sugar ($\leq$ 4 H_2/glucose equivalent).

The *in vitro* H_2 production system has been further modified to include additional enzymes that enable a variety of both simple and complex sugars to be used as energy sources for hydrogen production, including cellulosic materials (Ye *et al.*, 2009), xylose (Martin del Campo *et al.*, 2013), sucrose (Myung *et al.*, 2014), corn stover (Rollin *et al.*, 2015) and xylooligosaccharides (Moustafa *et al.*, 2016). A similar synthetic pathway converting glucose to hydrogen has also been reported wherein SHI was replaced by an [FeFe]-hydrogenase, wherein ferredoxin is the electron donor for hydrogen production instead of NADPH (Lu *et al.*, 2015). However, the stability and relative insensitivity to inactivation by oxygen of SHI is unmatched by any [FeFe]-hydrogenase.

The biosynthesis of the [NiFe]-containing catalytic site of [NiFe] hydrogenases is extremely complex (Bock *et al.*, 2006, Forzi and Sawers, 2007). Eight maturation enzymes are required for or enhance the synthesis of the [NiFe]-complex and its insertion into the apo-hydrogenase to generate the mature active enzyme (Blokesch *et al.*, 2002, Lacasse and Zamble, 2016). Based on elegant and extensive studies of the biosynthesis of *E. coli* hydrogenase 3, a model was proposed for the post-translational maturation of SHI in *P. furiosus* (Sun *et al.*, 2010, Lacasse and Zamble, 2016). The accessory proteins HypA, HypB and SlyD coordinate the nickel ion while HypF, HypE, HypC and HypD are responsible for the insertion of iron, along with its CO and CN ligands (see Figure 2.1), into the immature catalytic subunit (the SHI α-subunit). The final step involves proteolysis by FrxA, which removes the C-terminal tail of the α-subunit to produce the fully active form of the catalytic subunit of SHI within the heterotetrameric holoenzyme (Sun, *et al.*, 2010). *P. furiosus* and the related organism, *Thermococcus kodakarensis*, contain a second protease (HycI) that is responsible for the maturation of the membrane-bound [NiFe]-hydrogenase in these organisms (Kanai *et al.*, 2017, Sun, *et al.*, 2010).

When SHI was first purified from *P. furiosus*, the procedure required multi-column chromatography steps and was time-consuming (Bryant and Adams, 1989). A more efficient method of purification with higher yield is clearly required if SHI is to be used for any industrial application. Heterologous expression of SHI, or indeed any [NiFe]-hydrogenase, in *E. coli* is problematic because of the maturation of the [NiFe]-containing subunit. We previously co-expressed in *E. coli* the four-gene SHI operon as well as the eight required *P. furiosus* SHI maturation genes and successfully purified active SHI (Sun, *et al.*, 2010). We also showed that, except for the *P. furiosus* FrxA protease, the *E. coli* hydrogenase maturation enzymes were able to produce the mature SHI. However, independent of which maturation genes were used, the yield

of recombinant SHI in *E. coli* was poor and lower than that obtained from native purification in *P. furiosus* (Bryant and Adams, 1989, Wu, *et al.*, 2015). These results were consistent with a previous report demonstrating that heterologous expression of any [NiFe]-hydrogenases outside of a closely related host is extremely challenging (English *et al.*, 2009) with limited or no success (Grzeszik *et al.*, 1997, Sun, *et al.*, 2010, Voordouw *et al.*, 1987). A yield lower than that obtained from a native purification for a [NiFe] hydrogenase heterologously expressed in *E. coli* was also reported in the case of expressing *Cupriavidus necator* H16 hydrogenase (Schiffels *et al.*, 2013).

Consequently, with the development of a genetic system in *P. furiosus*, we previously put the expression of the SHI structural genes under the control of a highly-expressed *P. furiosus* promoter (P_{slp} for the S-layer protein), which increased the amount of SHI produced (as measured by an *in vitro* activity assay and by transcriptional analysis) by almost an order of magnitude (Chandrayan *et al.*, 2012, Chandrayan, *et al.*, 2015). Using an affinity purification tag (9x histidine) on the non-catalytic β-subunit (Figure 2.1), the purification was simplified to one step with a yield of 76 % by recovery of SHI activity. Interestingly, the expression of maturation genes did not change significantly in the SHI over-expression strain, suggesting that there is no feedback regulation in which increased amounts of the SHI apoprotein results in increased amounts of the maturation proteins (Chandrayan, *et al.*, 2012).

Herein, we performed a large-scale purification (using 500 g of recombinant cells) of the over-expressed (using P_{slp}), His-tagged form of SHI. Surprisingly, more than 30% of the purified enzyme was found to be in the inactive trimeric form (βγδ, see Figure 2.1), suggesting that the maturation process was the limiting factor in producing the active heterotetrameric enzyme. We therefore determined the effects of over-expressing the SHI maturation genes and also of expressing a second set of SHI structural genes (using another highly-expressed *P. furiosus*

promoter) on the amount of inactive SHI produced and the overall yield of the active SHI enzyme. A combination of both strategies resulted in a minimal amount of inactive enzyme and a significant increase in the overall yield of active SHI.

Materials and Methods

Strains construction

The parent strain of *P. furiosus* used for expressing a second set of genes was MW0430 where the selection marker, *pyrF*, that we constructed previously (Chandrayan, *et al.*, 2015), was popped-out by using a 5-fluoroorotic acid counter-selection method (Lipscomb *et al.*, 2011). Transformation cassettes for expressing a second set of SHI and maturation genes were constructed using overlapping PCR (Bryksin and Matsumura, 2010) and NEBuilder HiFi DNA Assembly (New England BioLabs). The cassettes were cloned into a plasmid and linearized for *P. furiosus* transformation, where the backbone was amplified from pGL054 (Lipscomb *et al.*, 2014). As shown in Figure S2.1 and S2.2, the UFR, DFR, *pyrF* marker, and *mbh* promoter were amplified from pGL054 along with the plasmid backbone. The genes of *shI* (PF0891-0894) and maturation genes, *frxA* (PF0975), *hypCD* (PF0548-0549), *hypF* (PF0559), *hypA/B* (PF0615-0616), *hypE* (PF0604) and *slyD* (PF1401), were amplified from *P. furiosus* genomic DNA. For MW0556 (H2M2), a 9x-histidine tag was added at the N-terminus of SHIβ, and ribosomal binding sites of S-layer protein (PF1399) or γ-subunit (PF0971) of pyruvate oxidoreductase (POR) were added at the 5' end of the maturation genes. No tag was used for strain MW0558 (H1M2) as this only expresses the second set of maturation genes. *hypCD* and *hypAB* are in the same operon so the native ribosomal binding sites were used for *hypD* and *hypB*. The sequence-confirmed plasmids

were linearized by the unique Pvu I restriction site and transformed into MW0450 (H1M1) as described previously (Lipscomb, *et al.*, 2011). For MW0477, the plasmid containing the SHIδ$^{G16C/G91C}$ variant of SHI operon was constructed by following the instruction of QuikChange II Site-Directed Mutagenesis Kit (Agilent Technologies). The site mutated SHI operon was amplified from the sequence confirmed plasmid and assembled with UFR, *pyrF* marker, *slp* promoter, a 9x-His tag at the N-terminus of SHIβ and DFR by overlapping PCR. The knock-in cassette was transformed into SHI native locus in MW0015 (Δ*pyrF* Δ*shIβγδα* Δ*shIIβγδα*) as shown in Figure S2.3. MW0015 lacks any cytoplasmic hydrogen evolution activity, so the activity of the SHI mutant could be screened by measuring MV-linked hydrogen production activity in the cytoplasmic extract. Strains used and constructed in this study are listed in Table 2.1.

Growth and cytoplasm preparation

P. furiosus strain MW0430 was grown in a 500-L fermenter at the Bioexpression and Fermentation Facility at the University of Georgia using the medium described previously (Chandrayan, *et al.*, 2015). For the growth of strains H1M1, H1M2 and H2M2, the medium was modified and contained per liter: 1x base salts, 2x trace minerals, 20 μM sodium tungstate, 0.25 μg resazurin, 1 μM nickel chloride, 100 μg riboflavin, 100 μg cobalamin, 10 g yeast extract, 10 g casein hydrolysate, 10 g maltose, 0.5 g cysteine hydrochloride, 0.5 g sodium sulfide, 1 g sodium bicarbonate, and 1 mM potassium phosphate buffer. Cytoplasmic extracts (S100) of *P. furiosus* cells were prepared anaerobically in an anaerobic chamber (Coy Laboratory Products). Cells were suspended in 25 mM Tris/HCl, pH 8.0, containing 1 mM dithiothreitol (DTT) and 50 μg/mL DNase I (5 ml of buffer per gram of cells) and lysed by osmotic shock with stirring for 1 hour. The

cell-free extracts were centrifuged at 100,000 x g for 1 hour (Beckman Coulter) and the supernatant was collected (S100), avoiding of taking the S-layer protein layer located at the bottom of the centrifuge tube.

RNA extraction and quantitative RT-PCR analysis

P. furiosus cells for qPCR analysis were harvested at mid log phase and RNA was isolated using Absolutely RNA Miniprep Kit (Agilent Technologies). Genomic DNA was digested using TURBO DNase (Ambion) and RNA was purified by a phenol: chloroform extraction method as previously described (Schut *et al.*, 2001). cDNA synthesis was carried out with 1 μg purified RNA using AffinityScript cDNA Synthesis Kit (Agilent Technologies) and qPCR analysis was performed using Brilliant III Ultra-Fast QPCR Master Mix (Agilent Technologies) with primers designed to amplify ~100 bp products within the target genes: PF0891 (*shIβ*), PF0894 (*shIα*), PF0975 (*frxA*), PF0548 (*hypC*), PF0559 (*hypF*), PF0616 (*hypB*), PF01401 (*slyD*) and PF0971 (*porγ*), where PF0971 was used as the reference gene.

Protein purification and SDS PAGE gel electrophoresis

For SHI purification using 500 g of cells, frozen cells were thawed and lysed anaerobically under Ar gas in 25 mM Tris/HCl, pH 8.0, containing 1 mM DTT and 50 μg/mL DNase I (10 mL per gram cells). Cell lysis was performed in two 4 L vacuum flasks connected to a vacuum manifold. A total of 250 g wet wt. of cells was added to each flask and lysis occurred over two hours at room temperature. Several cycles of vacuum and flushing with Ar were applied during

the lysis process in order to maintain anaerobic conditions. The lysate was then centrifuged at 18,000 x g for 1 hour and the supernatant (S80) was collected into a 5 L media bottle for batch purification. All the batch purification steps were performed in an anaerobic chamber. 40 mL of Ni-NTA resin (GE Healthcare Life Sciences) was directly added to S80 and the mixture was gently stirred for 10 minutes. The Ni-NTA resin was recovered by filtering the mixture and washed with 25 mM Tris/HCl, 300mM NaCl, pH 8.0 containing 1 mM DTT (buffer A). Buffer A containing 500mM imidazole (buffer B) was then used to block elute proteins bound to the resin. The eluted proteins were applied directly to a HiLoad 26/10 Q Sepharose High Performance column (GE Healthcare Life Sciences) using NGC Chromatography Systems (Bio-Rad), while diluting it 10-fold with 50mM HEPES, pH 7.5 containing 1 mM sodium dithionite (DT). The column was pre-equilibrated and washed with the same buffer, and a gradient from 0 to 500 mM NaCl in the same buffer was applied to elute SHI.

For purification of SHI using 10 g of frozen cells, they were lysed with 25 mM Tris/HCl, pH 8.0, containing 1 mM DTT and 50 μg/mL DNase I (5 mL per gram cells). After stirring for 1 hour in the anaerobic chamber, the cell-free extracts were centrifuged at 100,000 x g for 1 hour and the S100 supernatant was collected and directly applied on a HisTrap crude FF column (GE Healthcare Life Sciences). The column was equilibrated with 25 mM Tris/HCl, pH 8.0, containing 300 mM NaCl and 1 mM DTT (buffer A). A gradient from 0 to 100% buffer B (buffer A containing 500 mM imidazole) was used to elute the enzyme. The fractions containing SHI from the Ni-NTA step as measured by MV-linked hydrogen evolution activity were pooled and applied on a HiTrap Q HP column (GE Healthcare Life Sciences) equilibrated with 50 mM HEPES, pH 7.5, containing 1 mM DT. SHI was eluted with a gradient from 0 to 500 mM NaCl in the same buffer. The eluted

protein fractions were analyzed by MV-linked hydrogen evolution assay and by SDS-PAGE using Mini-PROTEAN TGX Gels (Bio-Rad).

Assays

Hydrogen evolution assay was carried out under an anaerobic conditions as reported previously with some modification (Bryant and Adams, 1989). In brief, an anaerobically-sealed 5 mL vial containing 2 mL of 10 mM DT and 1 mM MV in 100 mM EPPS, pH 8.4, was preheated at 80 °C for 1 min. The SHI sample was added to the vial and incubated for 4 min. 100 μL of the gaseous headspace was taken and the hydrogen concentration was measured by the 6850 Network GC system from Agilent Technologies. One unit of hydrogen evolution activity is equal to the production of 1 μmol of hydrogen per minute. Protein estimation was carried out using the Protein Assay Dye Reagent (Bio-Rad).

Results

We had previously shown that the yield of SHI from recombinant *P. furiosus* cells could be dramatically increased by using a highly expressed promoter (P_{slp}) to drive transcription of the 4-gene operon encoding SHI and by incorporating an affinity purification tag (9x-His) on the non-catalytic β-subunit (Chandrayan, *et al.*, 2015). From a 90 g-scale purification procedure, it was determined that a small amount of SHI (~2% of the total) existed as an inactive trimeric form lacking the catalytic α-subunit (see Figure 2.1). Herein we established a protocol for a 5-fold increase in scale for SHI purification using the over-expression strain.

500 g-scale preparation

The method for the one-step affinity purification of SHI that we reported previously (Chandrayan, *et al.*, 2015) involved direct application of the cytoplasmic fraction (S100) to the Ni-NTA affinity column and elution of SHI with an imidazole gradient. However, it was impractical to scale up for 500 g wet wt. of cells as the Ni-NTA columns became ineffective after prolonged exposure to the *P. furiosus* S100 fractions, presumably due to the presence of various organic reductants in the cytoplasmic extract. In addition, the procedure was extremely time-consuming as it was limited by the low flow rate of the affinity columns. In order to scale up the SHI purification, batch affinity purification was performed followed by an anion exchange chromatography step. Instead of using the S100 fraction obtained after an ultracentrifugation step, a lower speed centrifugation was used (S80), which is more feasible due for the increased volume of materials that are used in the larger scale procedure. It should be noted, however, that the S80 contains more S-layer protein than the S100 (the higher speed ultracentrifugation is required to completely separate this protein from the cytoplasmic extract). The S80 fraction was mixed directly with the Ni-NTA resin before pouring onto a drip column and SHI was then block eluted rapidly with 500 mM imidazole and then further purified using a Q HP step. Typical results using this purification protocol are shown in Table 2.2. From 500 g of cells, a total of 41% of SHI hydrogen evolution activity was recovered yielding approximately 320 mg of pure SHI with a specific activity $\geq$ 100 U/mg.

However, surprisingly, electrophoretic analysis revealed that more than 30% (90 mg) of the purified SHI protein was in an inactive trimeric ($\beta\gamma\delta$) form (see Figure 2.1). For example, as shown in Figure 2.2, the specific activities of the later fractions from the Q-HP column (Q3 and Q4) were much lower than that of the earlier fractions (Q1 and Q2), which lack detectable amounts

of the trimeric form. Specifically, electrophoretic analysis reveals that the catalytic α-subunit of SHI is missing in the later Q3 and Q4 fractions (Figure 2.2). Hence, the batch purification method coupled with a Q-HP step result in purification of a much greater fraction of the inactive trimeric form compared to the previous method (Chandrayan, *et al.*, 2015). The trimeric βγδ form was assumed to result from incomplete maturation of the catalytic α-subunit, and this appeared to be the limiting factor since we showed previously that over-expression of the structural genes for SHI did not affect the expression of maturation genes (Chandrayan, *et al.*, 2012). Therefore, increasing the expression levels of the maturation genes might also increase the yield of active SHI by decreasing the amount of the inactive trimeric βγδ enzyme.

Over-expression of the SHI maturation and structural genes

We attempted to overexpress all eight maturation genes individually in the same *P. furiosus* strain by placing each under control of the highly-expressed promoter, P_{slp}, but we were unable to obtain pure colonies after over expressing *FrxA* and *HypF* in the same strain (data not shown). The reason for this is unknown. An alternative strategy involved constructing a single operon containing all eight maturation genes (Figure S2.1) under the control of another highly expressed promoter, P_{mbh}, which controls express of the 14-gene operon encoding the membrane bond hydrogenase (*mbh*). The parent strain for this construction was MW0450, which is the strain (MW0430) that we reported previously for over-expressing 9x-His-tagged SHI (Chandrayan, *et al.*, 2015) except that the *pyrF* selection marker had been removed. We will now refer MW0450 to as the H1M1 strain, as it has one copy of the SHI hydrogenase (H) operon (under the control of P_{slp}) and one (native) set of maturation genes (M), most of which are unlinked, controlled by their

native promoters. The new recombinant strain (MW0558) will be referred to as strain H1M2 as it contains two copies of each maturation gene and a single copy of the SHI operon. As well as the native set of maturation genes, it contains a second set as an operon controlled by P_{mbh}, in addition to its over-expressed SHI operon (under the control of P_{slp}) encoding a 9-His-tag at the β-subunit.

We anticipated that the production of active SHI from the H1M2 strain might now be limited by the availability of SHI protein supplying the elevated levels of the maturation pathway gene products. Therefore, an additional strain (MW0556) was engineered from MW0450 that contained a second SHI operon as well as the eight maturation genes, all under control of P_{mbh} (Figure S2.2). The second SHI operon also encoded for a 9x-His-tag at the N-terminus of the β-subunit, the same as for the engineered SHI operon in MW0430. This second strain (MW0556) will be referred to as H2M2 as it contains two copies of the SHI operon (one driven by P_{slp} and a second driven by P_{mbh}, both 9-His-tagged) and two copies of the maturation genes (one set consisting of unlinked genes controlled by their native promoters and one set as an operon driven by P_{mbh}).

No significant differences in growth were observed for the H1MI, H1M2 and H2M2 strains grown under normal conditions. To determine the expression levels of the SHI operon (α- and β-subunits) and of five of the maturation genes (*frxA*, *hypD*, *hypF*, *hypB* and *slyD*), qPCR analysis was carried out and the results are shown in Figure 2.3. Compared to the H1M1 strain, the expression of *shI* did not change significantly in the H1M2 strain but it increased more than 1.5-fold in the H2M2 strain. For the maturation genes, compared to the levels in the H1M1 strain, their expression increased between approximately 2 and 30-fold (depending on the gene) in both the H1M2 and H2M2 strains and, for unknown reasons, were consistently slightly more highly

expressed in the H2M2 strain, suggesting perhaps some feedback relationship between the SHI and all (five) maturation genes.

Increased hydrogen evolution in cytoplasm and lower amount of trimeric SHI

In order to examine if the new strains produced a higher yield of active heterotetrameric SHI ($\alpha\beta\gamma\delta$), cytoplasmic extracts of the three new strains were prepared and the specific hydrogen production activity was determined using reduced methyl viologen as an artificial electron donor. The results for H1M1, H1M2 and H2M2 are summarized in Figure 2.4 and are compared with that of a control strain (CON). CON is the complemented parent strain of H1M1. The hydrogen production activities in the S100 fractions were approximately 2.7, 7.4, 8.5 and 12.2 U/mg for CON, H1M1, H1M2 and H2M2, respectively. Hence, compared to the parent strain H1M1, the specific activity of hydrogen production was 1.14-fold higher in H1M2 and 1.65 times higher in H2M2. A small-scale purification was also performed to examine the purification profiles of H1M1, H1M2 and H2M2 using 10 g wet wt. cells and the results are summarized in Table 2.3. After two steps of purification, 10.2, 11.8 and 14.6 mg active SHI was purified, respectively, where only the fractions with a specific activity higher than 60 U/mg were pooled. Hence, compared to H1M1, the yield of SHI was 15% and 43% higher in H1M2 and H2M2, respectively. As shown in Figure 2.5, SDS gel analysis of the later Q HP fractions from the H1M1 preparation contained significantly more trimeric SHI compared to the same fractions from the H1M2 and H2M2 purifications. The proportion of trimeric SHI in the H1M1 purification was approximately 20% of the SHI sample as Q3 and Q4 contained more than 20% of the total purified protein. This compares with approximately 5% trimeric form in the SHI sample purified from H1M2 and H2M2 strains.

Improving the oxygen tolerance of SHI

There are a limited number of [NiFe] hydrogenases that are referred to "oxygen-tolerant" as they are able to catalyze hydrogen production in the presence of oxygen (Fritsch *et al.*, 2011, Goris *et al.*, 2011). In such enzymes, the [4Fe-4S] cluster coordinated by four Cys residues that is adjacent to the [NiFe]-catalytic site of traditional oxygen-sensitive hydrogenases is replaced by an unusual [4Fe-3S] cluster coordinated by six Cys residues. This unusual iron-sulfur cluster is able to reduce molecular O_2 to water thereby conferring oxygen tolerance (Fritsch, *et al.*, 2011, Goris, *et al.*, 2011). Oxygen-sensitive hydrogenases like SHI have two conserved Gly residues in place of the two additional Cys residues in the oxygen-tolerant enzyme. Hence, in an attempt to confer oxygen-tolerance on SHI, using site-directed mutagenesis we replaced its two Gly residues (in the δ-subunit) in the hopes of converting its [4Fe-4S] cluster adjacent to the catalytic site into an O_2-reducing, [4Fe-3S] cluster. The mutated SHI was expressed in a strain of *P. furiosus* that lacked both of the cytoplasmic hydrogenases (SHI and SHII), and therefore had no cytoplasmic hydrogenase activity (Lipscomb, *et al.*, 2011), yielding strain MW0477. Unfortunately, we were unable to measure hydrogen evolution activity in the cytoplasmic extract of MW0477, indicating that the mutant SHI with the two additional Cys residues is either unstable or inactive.

Discussion

Herein, we developed a method for the purification of *P. furiosus* SHI on a 500 g-scale that avoids the destruction of Ni-NTA affinity columns, assumed to be due to the presence of reductants in the cytoplasmic fraction of *P. furiosus*. We also discovered the presence of trimeric SHI, lacking the catalytic subunit, in the samples of the purified enzyme, and this accounted for more than 30%

of the total protein. We show here that the presence of inactive trimeric enzyme is the result of inefficient maturation of SHI by the products of the maturation genes, as we suggested previously (Chandrayan, *et al.*, 2012, Sun, *et al.*, 2010). We were able to reduce the proportion of trimeric SHI in the purified protein to less than 5% of the total, by expressing a second set of maturation genes in the SHI over-expression strain (H1M1) yielding the new strain H1M2. We also improved the yield of SH1 by 40% by co-expressing a second set of the SHI operon into the new strain H2M2.

We also attempted to confer oxygen-tolerance onto SHI whereby it could catalyze hydrogen production in the presence of air (oxygen), a property that would be extremely useful for any industrial application. This was based on the presence of two additional Cys residues in oxygen-tolerant hydrogenases that generate an O_2-reducing [4Fe-3S] cluster, rather than a conventional [4Fe-4S] cluster, adjacent to the [NiFe]-catalytic site. Hence when these two Cys residues in the oxygen-tolerant [NiFe]-hydrogenase of *R. eutropha* were mutated to Gly residues, the enzyme became oxygen sensitive (Goris, *et al.*, 2011). Similar results were also reported for *E. coli* hydrogenase-1 (Lukey *et al.*, 2011). However, when the two Cys residues were added to SHI, replacing two Gly residues that are conserved in oxygen-sensitive hydrogenases, no activity was detected in the cytoplasmic extract, indicating that the mutated SHI enzyme was unstable or inactive. This is consistent with the reported attempt of mutating the same conserved Gly residues in the oxygen-sensitive hydrogenase Hyd-2 of *E. coli*. The mutant enzyme could not be purified, suggesting that the substitutions resulted in an unstable enzyme (Lukey, *et al.*, 2011). In spite of the lack of success with oxygen-tolerance, we recently demonstrated that site-specific mutants of SHI can be obtained, in the case for analyzing proton-coupled electron transfer during catalysis (Greene *et al.*, 2016). However, it is clear that engineering oxygen-tolerance into SHI is not

straightforward and cannot be obtained by simply mutating two residues. More sophisticated experiments based on structural information for SHI will be required for comparison with those of the oxygen-tolerant enzymes (Fritsch, *et al.*, 2011, Goris, *et al.*, 2011).

In addition to attempting to improve oxygen tolerance and increasing the yield of purified SHI for applied purposes in hydrogen production, there are several possibilities for engineering SHI in order to achieve a higher hydrogen production rate. For example, SHI has high affinities for hydrogen and for $NADP^+$ (van Haaster, *et al.*, 2008), which is consistent with it proposed physiological role of hydrogen recycling, but this bias for hydrogen oxidation is counter to efficient hydrogen production. The catalytic bias of the [NiFe]-hydrogenase of *E. coli* (Hyd-1) was changed by site-directed mutagenesis (E73Q) of the catalytic subunit and this increased the specific hydrogen production rate two-fold while its oxygen tolerance was unaffected (Flanagan *et al.*, 2016). Similarly, when changing the nature of an iron sulfur cluster (from [3Fe-4S] to a [4Fe-4S] cluster by site-directed mutagenesis) in the electron transfer chain to the catalytic site of the [NiFe]-hydrogenase of *Desulfovibrio fructosovorans* (HynA) increased its hydrogen evolution activity by two-fold while reducing its hydrogen uptake activity by 30% (Rousset *et al.*, 1998). It was also reported that hydrogen uptake activity was nearly abolished while the evolution activity was reduced only 50% when the ligation of a [4Fe4S] cluster was changed (Dementin *et al.*, 2006). *Changing the nature of one of the iron-sulfur clusters of the* hydrogenase of *Methanococcus voltae* also reduced its hydrogen oxidation activity (Bingemann and Klein, 2000). A combination of changing the nature of one of the iron-sulfur clusters and the nature of the ligation in one of the other clusters of the [NiFe]-hydrogenase of *Alteromonas macleodii resulted in an increase in its hydrogen evolution activity by approximately 4-fold, while* the *mutant enzyme still maintained similar hydrogen uptake activity, oxygen tolerance and thermal stability to that of the wild type*

enzyme (Yonemoto et al., 2013). Clearly, based on these studies, there are several potential mechanisms by which to increase the hydrogen evolution activity of *P. furiosus* SHI, and such studies are in progress.

Funding

All of the research described herein was supported by a grant (DE-EE0006968) from the Office of Energy Efficiency and Renewable Energy, Fuel Cell Technologies Office of the U.S. Department of Energy.

Acknowledgements

We thank Yi-Heng Percival Zhang for advice and helpful discussions and the Bioexpression and Fermentation Facility at the University of Georgia for assistance in carrying out the 500 L fermentation.

References

Bingemann R. and Klein A. (2000) Conversion of the central [4Fe-4S] cluster into a [3Fe-4S] cluster leads to reduced hydrogen-uptake activity of the F-420-reducing hydrogenase of *Methanococcus voltae*. *Eur J Biochem,* **267***,* 6612-6618.

Blokesch M., Paschos A., Theodoratou E., Bauer A., Hube M., Huth S. and Bock A. (2002) Metal insertion into NiFe-hydrogenases. *Biochem Soc T,* **30**, 674-680.

Bock A., King P.W., Blokesch M. and Posewitz M.C. (2006) Maturation of hydrogenases. *Adv Microb Physiol*, **51**, 1-71.

Bryant F.O. and Adams M.W. (1989) Characterization of hydrogenase from the hyperthermophilic archaebacterium, *Pyrococcus furiosus*. *J Biol Chem,* **264**, 5070-5079.

Bryksin A.V. and Matsumura I. (2010) Overlap extension PCR cloning: a simple and reliable way to create recombinant plasmids. *Biotechniques,* **48**, 463-465.

Chandrayan S.K., McTernan P.M., Hopkins R.C., Sun J., Jenney F.E., Jr. and Adams M.W. (2012) Engineering hyperthermophilic archaeon *Pyrococcus furiosus* to overproduce its cytoplasmic [NiFe]-hydrogenase. *J Biol Chem,* **287**, 3257-3264.

Chandrayan S.K., Wu C.H., McTernan P.M. and Adams M.W. (2015) High yield purification of a tagged cytoplasmic [NiFe]-hydrogenase and a catalytically-active nickel-free intermediate form. *Protein Expr Purif,* **107**, 90-94.

Dementin S., Belle V., Bertrand P., Guigliarelli B., Adryanczyk-Perrier G., De Lacey A.L., Fernandez V.M., Rousset M. and Leger C. (2006) Changing the ligation of the distal [4Fe4S] cluster in NiFe hydrogenase impairs inter- and intramolecular electron transfers. *J Am Chem Soc,* **128**, 5209-5218.

English C.M., Eckert C., Brown K., Seibert M. and King P.W. (2009) Recombinant and in vitro expression systems for hydrogenases: new frontiers in basic and applied studies for biological and synthetic H2 production. *Dalton Trans*, 9970-9978.

Flanagan L.A., Wright J.J., Roessler M.M., Moir J.W. and Parkin A. (2016) Re-engineering a NiFe hydrogenase to increase the H2 production bias while maintaining native levels of O2 tolerance. *Chem Commun (Camb),* **52**, 9133-9136.

Forzi L. and Sawers R.G. (2007) Maturation of [NiFe]-hydrogenases in *Escherichia coli*. *Biometals*, **20**, 565-578.

Fritsch J., Scheerer P., Frielingsdorf S., Kroschinsky S., Friedrich B., Lenz O. and Spahn C.M. (2011) The crystal structure of an oxygen-tolerant hydrogenase uncovers a novel iron-sulphur centre. *Nature*, **479**, 249-252.

Goris T., Wait A.F., Saggu M., Fritsch J., Heidary N., Stein M., Zebger I., Lendzian F., Armstrong F.A., Friedrich B. *et al.* (2011) A unique iron-sulfur cluster is crucial for oxygen tolerance of a [NiFe]-hydrogenase. *Nat Chem Biol*, **7**, 310-U387.

Greene B.L., Vansuch G.E., Wu C.H., Adams M.W. and Dyer R.B. (2016) Glutamate Gated Proton-Coupled Electron Transfer Activity of a [NiFe]-Hydrogenase. *J Am Chem Soc*, **138**, 13013-13021.

Grzeszik C., Lubbers M., Reh M. and Schlegel H.G. (1997) Genes encoding the NAD-reducing hydrogenase of *Rhodococcus opacus* MR11. *Microbiology,* **143**, 1271-1286.

Jacobson M.Z., Colella W.G. and Golden D.M. (2005) Cleaning the air and improving health with hydrogen fuel-cell vehicles. *Science,* **308**, 1901-1905.

Kanai T., Yasukochi A., Simons J.R., Scott J.W., Fukuda W., Imanaka T. and Atomi H. (2017) Genetic analyses of the functions of [NiFe]-hydrogenase maturation endopeptidases in the hyperthermophilic archaeon *Thermococcus kodakarensis*. *Extremophiles,* **21**, 27-39.

Lacasse M.J. and Zamble D.B. (2016) [NiFe]-Hydrogenase Maturation. *Biochemistry*, **55**, 1689-1701.

Lee H.S., Vermaas W.F. and Rittmann B.E. (2010) Biological hydrogen production: prospects and challenges. *Trends Biotechnol,* **28**, 262-271.

Lipscomb G.L., Schut G.J., Thorgersen M.P., Nixon W.J., Kelly R.M. and Adams M.W. (2014) Engineering hydrogen gas production from formate in a hyperthermophile by heterologous production of an 18-subunit membrane-bound complex. *J Biol Chem*, **289**, 2873-2879.

Lipscomb G.L., Stirrett K., Schut G.J., Yang F., Jenney F.E., Jr., Scott R.A., Adams M.W. and Westpheling J. (2011) Natural competence in the hyperthermophilic archaeon *Pyrococcus furiosus* facilitates genetic manipulation: construction of markerless deletions of genes encoding the two cytoplasmic hydrogenases. *Appl Environ Microbiol*, **77**, 2232-2238.

Lu F., Smith P.R., Mehta K. and Swartz J.R. (2015) Development of a synthetic pathway to convert glucose to hydrogen using cell free extracts. *Int J Hydrogen Energ*, **40**, 9113-9124.

Lukey M.J., Roessler M.M., Parkin A., Evans R.M., Davies R.A., Lenz O., Friedrich B., Sargent F. and Armstrong F.A. (2011) Oxygen-Tolerant [NiFe]-Hydrogenases: The Individual and Collective Importance of Supernumerary Cysteines at the Proximal Fe-S Cluster. *J Am Chem Soc*, **133**, 16881-16892.

Ma K., Weiss R. and Adams M.W. (2000) Characterization of hydrogenase II from the hyperthermophilic archaeon *Pyrococcus furiosus* and assessment of its role in sulfur reduction. *J Bacteriol*, **182**, 1864-1871.

Martin del Campo J.S., Rollin J., Myung S., Chun Y., Chandrayan S., Patino R., Adams M.W.W. and Zhang Y.H.P. (2013) High-Yield Production of Dihydrogen from Xylose by Using a Synthetic Enzyme Cascade in a Cell-Free System. *Angew Chem Int Edit,* **52**, 4587-4590.

McTernan P.M., Chandrayan S.K., Wu C.H., Vaccaro B.J., Lancaster W.A. and Adams M.W. (2015) Engineering the respiratory membrane-bound hydrogenase of the hyperthermophilic archaeon *Pyrococcus furiosus* and characterization of the catalytically active cytoplasmic subcomplex. *Protein Eng Des Sel,* **28**, 1-8.

McTernan P.M., Chandrayan S.K., Wu C.H., Vaccaro B.J., Lancaster W.A., Yang Q., Fu D., Hura G.L., Tainer J.A. and Adams M.W. (2014) Intact functional fourteen-subunit respiratory membrane-bound [NiFe]-hydrogenase complex of the hyperthermophilic archaeon *Pyrococcus furiosus*. *J Biol Chem,* **289**, 19364-19372.

Moustafa H.M.A., Kim E.J., Zhu Z.G., Wu C.H., Zaghloul T.I., Adams M.W.W. and Zhang Y.H.P. (2016) Water Splitting for High-Yield Hydrogen Production Energized by Biomass Xylooligosaccharides Catalyzed by an Enzyme Cocktail. *Chemcatchem,* **8**, 2898-2902.

Myung S., Rollin J., You C., Sun F.F., Chandrayan S., Adams M.W.W. and Zhang Y.H.P. (2014) In vitro metabolic engineering of hydrogen production at theoretical yield from sucrose. *Metab Eng,* **24**, 70-77.

Rietveld P. (2013) Climate change adaptation and transport: a review. *J Transp Geogr,* 29-48.

Rollin J.A., Martin del Campo J., Myung S., Sun F., You C., Bakovic A., Castro R., Chandrayan S.K., Wu C.H., Adams M.W. *et al.* (2015) High-yield hydrogen production from biomass by in vitro metabolic engineering: Mixed sugars coutilization and kinetic modeling. *Proc Natl Acad Sci U S A,* **112**, 4964-4969.

Rousset M., Montet Y., Guigliarelli B., Forget N., Asso M., Bertrand P., Fontecilla-Camps J.C. and Hatchikian E.C. (1998) [3Fe-4S] to [4Fe-4S] cluster conversion in *Desulfovibrio fructosovorans* [NiFe] hydrogenase by site-directed mutagenesis. *Proc Natl Acad Sci U S A,* **95**, 11625-11630.

Schiffels J., Pinkenburg O., Schelden M., Aboulnaga el H.A., Baumann M.E. and Selmer T. (2013) An innovative cloning platform enables large-scale production and maturation of an oxygen-tolerant [NiFe]-hydrogenase from *Cupriavidus necator* in *Escherichia coli*. *PLoS One,* **8**, e68812.

Schut G.J., Zhou J. and Adams M.W. (2001) DNA microarray analysis of the hyperthermophilic archaeon *Pyrococcus furiosus*: evidence for anNew type of sulfur-reducing enzyme complex. *J Bacteriol,* **183**, 7027-7036.

Spaans S.K., Weusthuis R.A., van der Oost J. and Kengen S.W. (2015) NADPH-generating systems in bacteria and archaea. *Front Microbiol,* **6**, 742.

Sun J., Hopkins R.C., Jenney F.E., McTernan P.M. and Adams M.W. (2010) Heterologous expression and maturation of an NADP-dependent [NiFe]-hydrogenase: a key enzyme in biofuel production. *PLoS One,* **5**, e10526.

Thorgersen M.P., Lipscomb G.L., Schut G.J., Kelly R.M. and Adams M.W. (2014) Deletion of acetyl-CoA synthetases I and II increases production of 3-hydroxypropionate by the metabolically-engineered hyperthermophile *Pyrococcus furiosus*. *Metab Eng,* **22**, 83-88.

van Haaster D.J., Hagedoorn P.L., Jongejan J.A. and Hagen W.R. (2005) On the relationship between affinity for molecular hydrogen and the physiological directionality of hydrogenases. *Biochem Soc T,* **33**, 12-14.

van Haaster D.J., Silva P.J., Hagedoorn P.L., Jongejan J.A. and Hagen W.R. (2008) Reinvestigation of the steady-state kinetics and physiological function of the soluble NiFe-hydrogenase I of *Pyrococcus furiosus*. *J Bacteriol,* **190**, 1584-1587.

Vignais P.M. and Billoud B. (2007) Occurrence, classification, and biological function of hydrogenases: an overview. *Chem Rev,* **107**, 4206-4272.

Voordouw G., Hagen W.R., Kruse-Wolters K.M., van Berkel-Arts A. and Veeger C. (1987) Purification and characterization of Desulfovibrio vulgaris (Hildenborough) hydrogenase expressed in *Escherichia coli*. *Eur J Biochem,* **162**, 31-36.

Woodward J., Orr M., Cordray K. and Greenbaum E. (2000) Enzymatic production of biohydrogen. *Nature,* **405**, 1014-1015.

Wu C.H., McTernan P.M., Walter M.E. and Adams M.W. (2015) Production and Application of a Soluble Hydrogenase from *Pyrococcus furiosus*. *Archaea,* **2015**, 912582.

Ye X., Wang Y., Hopkins R.C., Adams M.W., Evans B.R., Mielenz J.R. and Zhang Y.H. (2009) Spontaneous high-yield production of hydrogen from cellulosic materials and water catalyzed by enzyme cocktails. *ChemSusChem,* **2**, 149-152.

Yonemoto I.T., Matteri C.W., Nguyen T.A., Smith H.O. and Weyman P.D. (2013) Dual organism design cycle reveals small subunit substitutions that improve [NiFe] hydrogenase hydrogen evolution. *J Biol Eng,* **7**.

Zhang Y.H., Evans B.R., Mielenz J.R., Hopkins R.C. and Adams M.W. (2007) High-yield hydrogen production from starch and water by a synthetic enzymatic pathway. *PLoS One,* **2**, e456.

Table 2.1. Strains used and constructed in this study

Trivial Name	Strain Name	Description	Ref.
CON	COM1c	Δ*pyrF*::P_{gdh} *pyrF*	(Thorgersen *et al.*, 2014)
----	MW0430	Δ*pyrF*::P_{gdh} *pyrF-*P_{slp} *9X-His*	(Chandrayan, *et al.*, 2015)
H1M1	MW0450	Δ*pyrF*::P_{slp} *9X-His*	This study
H1M2	MW0558	Δ*pyrF*::P_{slp} *9X-His* P_{gdh} *pyrF* P_{mbh}*-(frxA-hypC/D-hypF-hypA/B-hypE-slyD)*	This study
H2M2	MW0556	Δ*pyrF*::P_{slp} *9X-His* P_{gdh} *pyrF* P_{mbh}*-(9X-His-shIβγδα-frxA-hypC/D-hypF-hypA/B-hypE-slyD)*	This study
----	MW0015	Δ*pyrF* Δ*shIβγδα* Δ*shIIβγδα*	(Lipscomb, *et al.*, 2011)
----	MW0477	Δ*pyrF* Δ*shIβγδα*:: P_{gdh} *pyrF-*P_{slp} (*9X-His-shIβγδ*$^{G16C/G91C}$*α*) Δ*shIIβγδα*	This study

Table 2.2. Purification of SHI using batch procedure

Step	Activity (U)	Protein (mg)	Specific Activity (U/mg)	% Yield	Fold Purification
S80	85,807	36,180	2.37	100	1
Ni-NTA	38,147	680	56.1	44.5	23.7
Q HP (Q1+Q2)	35,214	324	108.7	41	45.9

Table 2.3. Purification of SHI from H1M1, H1M2 and H2M2 strains

H1M1	Activity (U)	Protein (mg)	Specific Activity (U/mg)	% Yield	Fold Purification
S100	2666.8	807	3.3	100	1
Ni-NTA	1589.3	28.8	55.1	59.6	15.5
Q HP (Q1-Q2)	1233.3	10.2	120.9	46.2	36.6

H1M2	Activity (U)	Protein (mg)	Specific Activity (U/mg)	% Yield	Fold Purification
S100	3098.7	740.2	4.19	100	1
Ni-NTA	1864.3	24.5	76.1	60.2	18.2
Q HP (Q1-Q3)	1403.4	11.8	118.9	45.3	28.4

H2M2	Activity (U)	Total Protein (mg)	Specific Activity (U/mg)	% Yield	Fold Purification
S100	3664.5	790.5	4.64	100	1
Ni-NTA	2253.4	28.3	79.5	61.5	17.1
Q HP (Q1-Q3)	1936.3	14.6	132.6	52.8	28.6

Figure 2.1

Model of tetrameric SHI based on the sequence analysis (Chandrayan, *et al.*, 2015). The proposed electron flow from NADPH to proton is also shown.

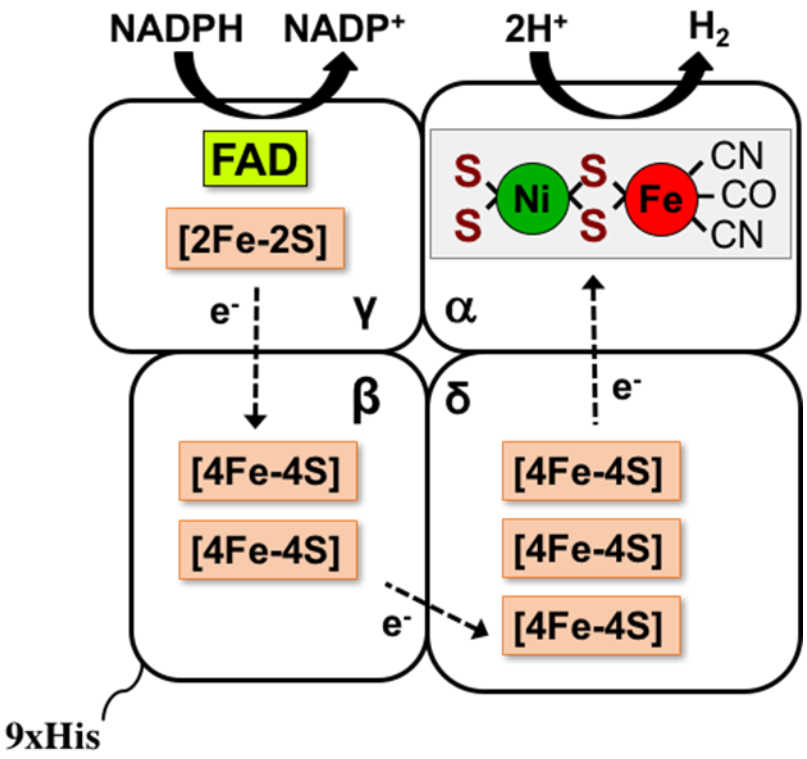
NADPH
NADP+
2H+
H2
FAD
[2Fe-2S]
e-
γ
α
S
Ni
S
Fe
CN
CO
CN
S
S
β
δ
e-
[4Fe-4S]
[4Fe-4S]
[4Fe-4S]
[4Fe-4S]
[4Fe-4S]
e-
9xHis

Figure 2.2

Left: SDS-PAGE gel shows the Q HP fractions from the purification in Table 2.2 that Q3 and Q4 are trimeric SHI. Right: the specific activity of hydrogen evolution for the four fractions of Q HP step in Table 2.2. The error bars represent standard deviations obtained using technical duplicate samples.

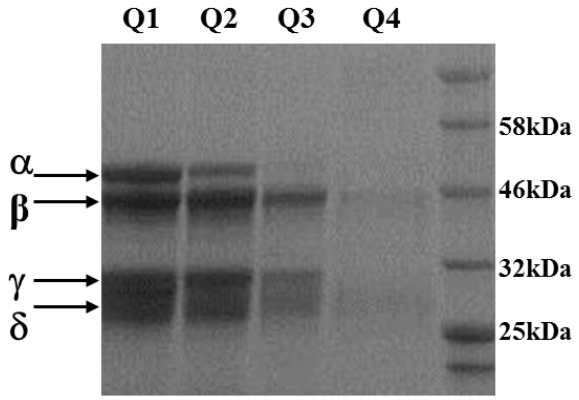
Q1
Q2
Q3
Q4
α
β
γ
δ
58kDa
46kDa
32kDa
25kDa

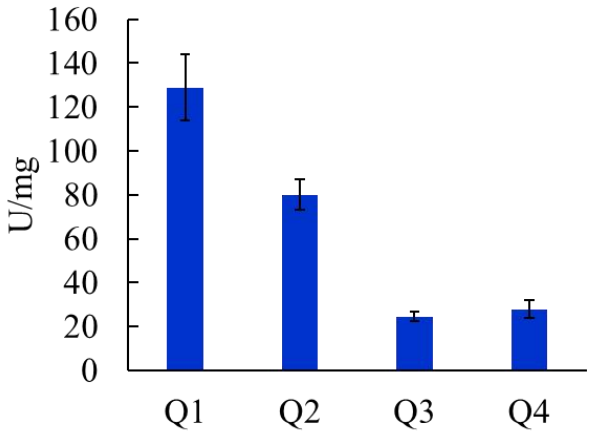
160
140
120
100
80
60
40
20
0
U/mg
Q1
Q2
Q3
Q4

Figure 2.3

qPCR analysis of the SHI and maturation genes in H1M2 and H2M2 compared to those in H1M1. The expression level of each gene was normalized by using *porγ* (PF0971) as a reference gene. The error bars represent standard deviations obtained using biological duplicate samples.

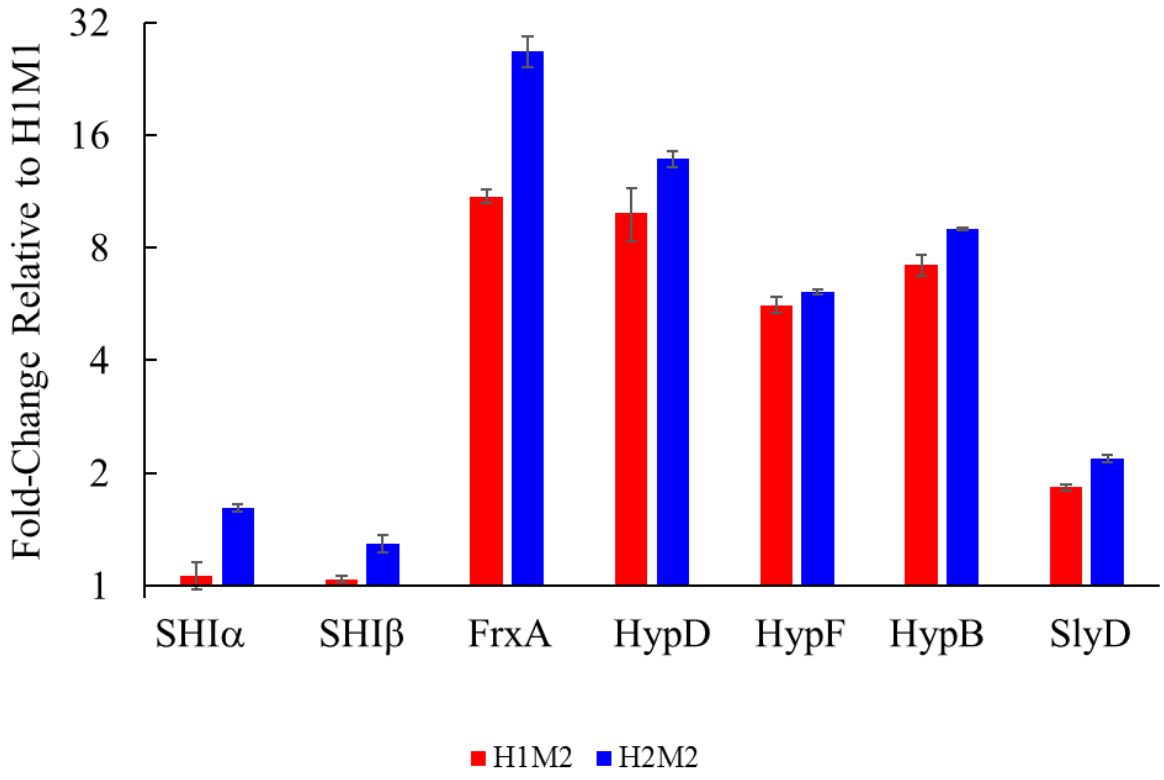
Fold-Change Relative to H1M1
32
16
8
4
2
1
SHIα
SHIβ
FrxA
HypD
HypF
HypB
SlyD
H1M2
H2M2

Figure 2.4

The specific activity of hydrogen evolution in the cytoplasmic extracts (S100) of four strains. The error bars represent standard deviations obtained using biological duplicate samples. CON is the complemented parent strain of H1M1.

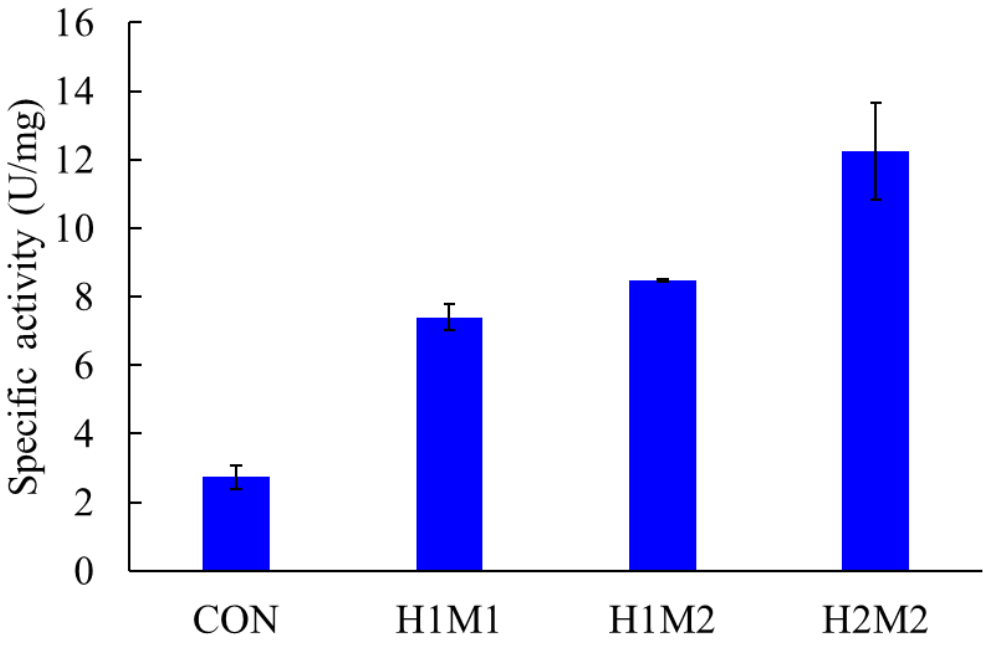
Specific activity (U/mg)
16
14
12
10
8
6
4
2
0
CON
H1M1
H1M2
H2M2

Figure 2.5

Top: SDS-PAGE gel shows the Q HP fractions from the purification profiles in Table 2.3 that Q3 and Q4 of H1M2 and H2M2 have less trimeric SHI compared to those of H1M1. Bottom: Specific activity of hydrogen evolution in Q3 and Q4 fractions. The error bars represent standard deviations obtained using technical duplicate samples.

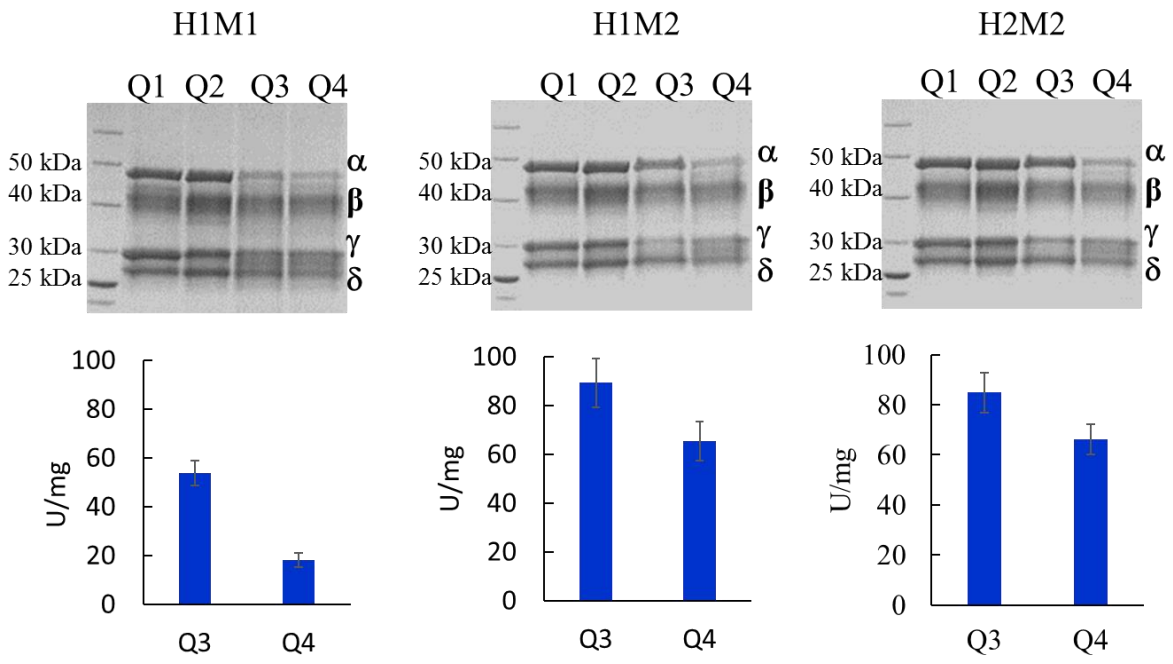
H1M1
H1M2
H2M2
Q1 Q2 Q3 Q4
50 kDa
40 kDa
30 kDa
25 kDa
α
β
γ
δ
U/mg
100
80
60
40
20
0
Q3
Q4

Figure S2.1

Scheme of the construction of H1M2 (MW0558). The knock in cassette has homologous regions shown as the upstream flanking region (UFR) and downstream flanking region (DFR). Marker cassette is indicated as P_{gdh}-*pyrF,* and the promoter is indicated as P_{mbh}. The ribosomal binding sites (RBS) of S-layer protein or pyruvate oxidoreductase γ-subunit were placed in the upstream of the genes as shown in black bars. The corresponding homologous loci of the UFR and DFR in the parent strain H1M1 (MW0450) are in the intergenic region between PF1232 and PF1233. Arrangement of the intergenic region after recombination is also shown.

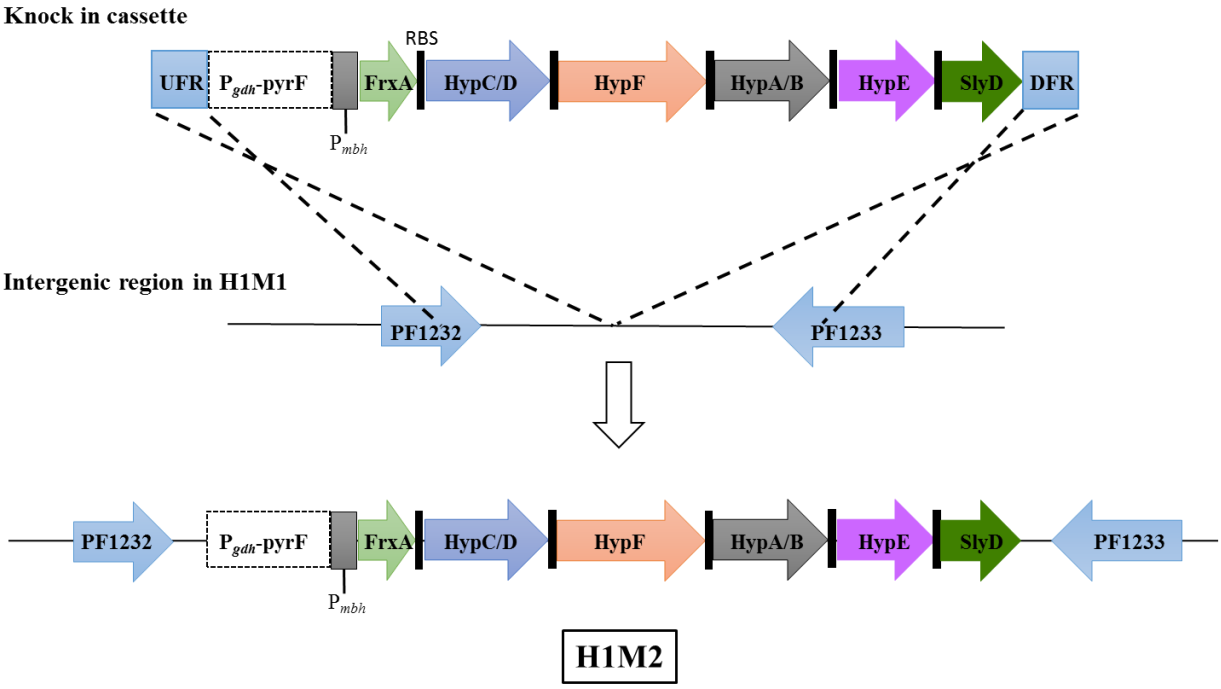
Knock in cassette
RBS
UFR
P_{gdh}-pyrF
FrxA
HypC/D
HypF
HypA/B
HypE
SlyD
DFR
P_{mbh}
Intergenic region in H1M1
PF1232
PF1233
PF1232
P_{gdh}-pyrF
FrxA
HypC/D
HypF
HypA/B
HypE
SlyD
PF1233
P_{mbh}
H1M2

Figure S2.2

Scheme of the construction of H2M2 (MW0556). The knock in cassette has homologous regions shown as the upstream flanking region (UFR) and downstream flanking region (DFR). Marker cassette is indicated as P_{gdh}-*pyrF,* and the promoter is indicated as P_{mbh}. The affinity tag is indicated as 9x-His tag. The ribosomal binding sites (RBS) of S-layer protein or pyruvate oxidoreductase γ-subunit were placed in the upstream of the genes as shown in black bars. The corresponding homologous loci of the UFR and DFR in the parent strain H1M1 (MW0450) are in the intergenic region between PF1232 and PF1233. Arrangement of the intergenic region after recombination is also shown.

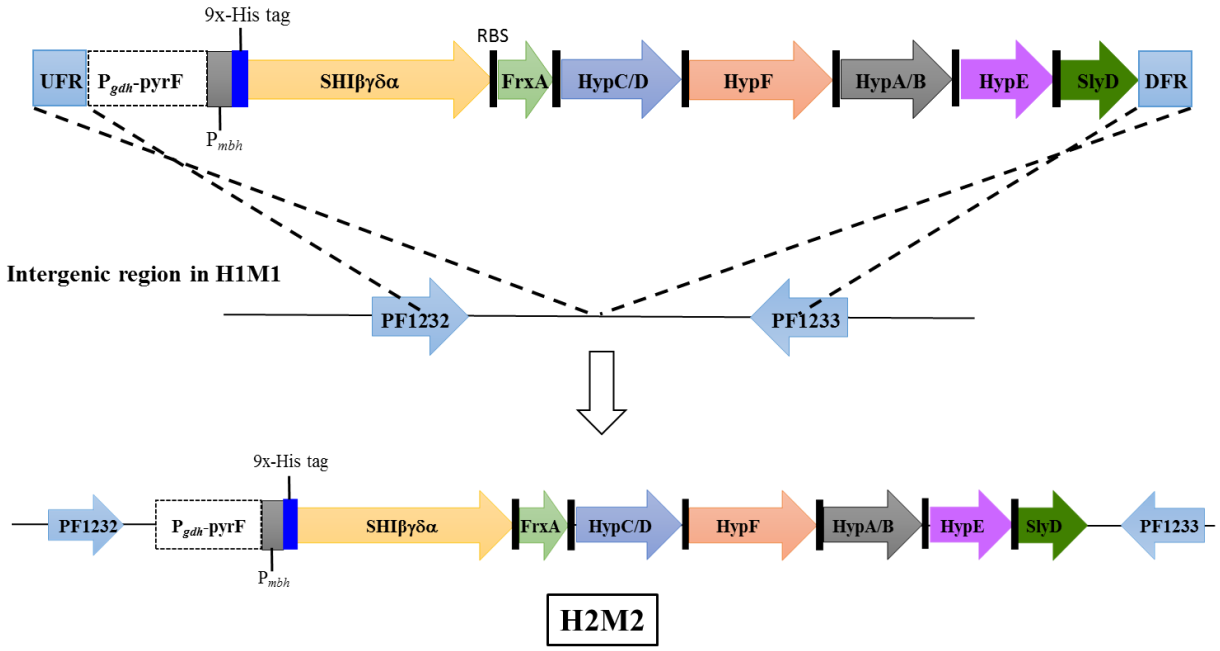
9x-His tag
RBS
UFR
P_{gdh}-pyrF
SHIβγδα
FrxA
HypC/D
HypF
HypA/B
HypE
SlyD
DFR
P_{mbh}
Intergenic region in H1M1
PF1232
PF1233
9x-His tag
PF1232
P_{gdh}-pyrF
SHIβγδα
FrxA
HypC/D
HypF
HypA/B
HypE
SlyD
PF1233
P_{mbh}
H2M2

Figure S2.3

Scheme of the construction of MW0477. The knock in cassette has homologous regions shown as the upstream flanking region (UFR) and downstream flanking region (DFR). Marker cassette is indicated as P_{gdh}-*pyrF,* and the promoter is indicated as P_{slp}. The affinity tag is indicated as 9x-His tag and the point mutations of G16C and G91C in SHIδ are also indicated. The corresponding homologous loci of the UFR and DFR in the parent strain MW0015 are in the SHI locus. Arrangement of the intergenic region after recombination is also shown.

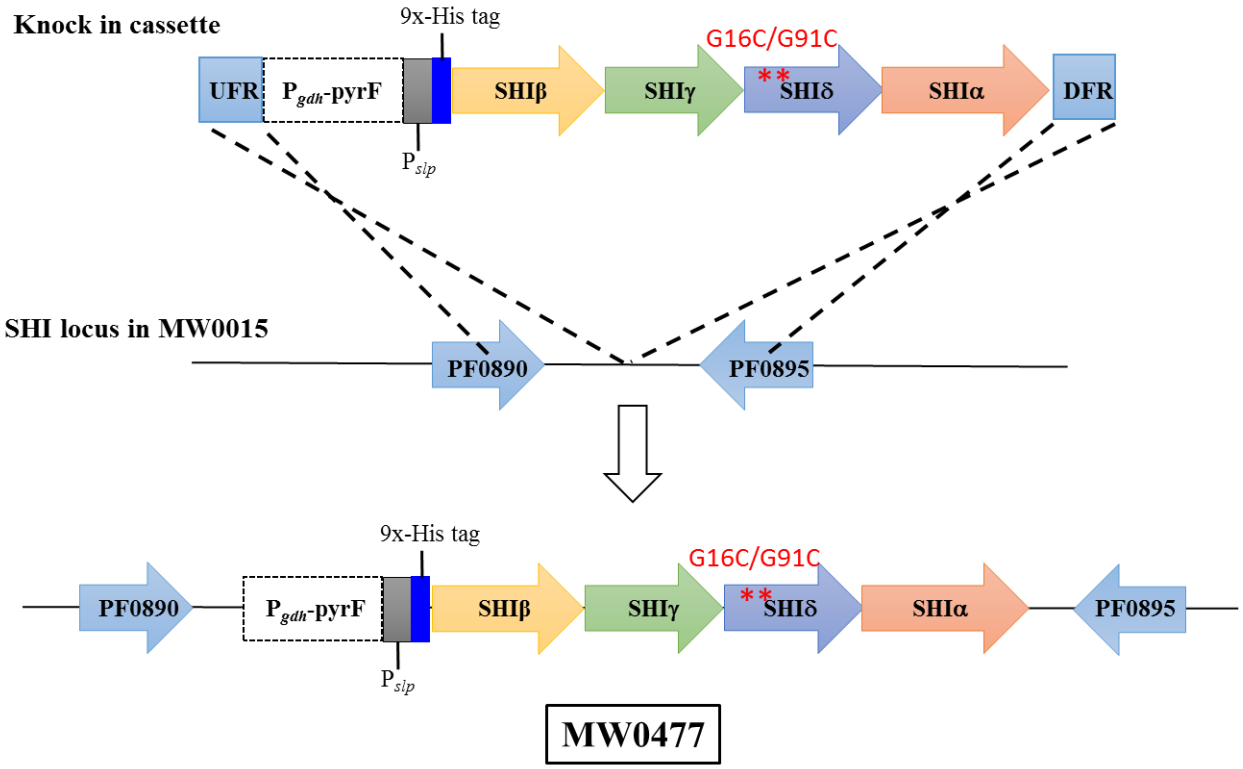
Knock in cassette
9x-His tag
G16C/G91C
UFR
P_{gdh}-pyrF
SHIβ
SHIγ
**SHIδ
SHIα
DFR
P_{slp}
SHI locus in MW0015
PF0890
PF0895
9x-His tag
G16C/G91C
PF0890
P_{gdh}-pyrF
SHIβ
SHIγ
**SHIδ
SHIα
PF0895
P_{slp}
MW0477

CHAPTER 3

MEMBRANE-BOUND SULFANE REDUCTASE IS A MISSING LINK IN THE EVOLUTION OF MODERN DAY RESPIRATORY COMPLEXES

Wu CH, Schut GJ, Poole FL, Haja DK, Adams MWW. Submitted to *Proc. Natl. Acad. Sci. U.S.A.*

Abstract

Hyperthermophilic archaea contain a hydrogen gas-evolving, respiratory membrane-bound NiFe-hydrogenase (MBH) that is very closely related to aerobic respiratory Complex I. These microorganisms also contain a homologous membrane-bound complex (MBX) whose expression is upregulated during growth on elemental sulfur (S°) which produces H_2S. MBX is an evolutionary link between MBH and Complex I but its catalytic function is unknown. Herein we show that MBX reduces dimethyl trisulfide (DMTS) using ferredoxin (Fd) as the electron donor and we rename it membrane-bound sulfane reductase (MBS). Two forms of affinity-tagged MBS were purified from genetically-engineered *Pyrococcus furiosus*: the 13-subunit holoenzyme (S-MBS) solubilized from membranes and a cytoplasmic 4-subunit catalytic sub-complex (C-MBS). S-MBS and C-MBS had comparable affinities for DMTS (K_m ~ 490 μM) and V_{max} values (12 μmoles/min/mg). The catalytic subunit of MBS (MbsL) but not that of Complex I (NuoD) retains two of four NiFe-coordinating cysteine residues of MBH (MbhL). However, these are not involved in catalysis as a mutant *P. furiosus* strain (MbsLC85A/C385A) grew normally in the presence of S°. From the products of DMTS reduction and properties of polysulfides, we conclude that MBS does not generate H_2S. Rather, it uses reduced Fd (E_o' ~ - 480 mV) to reduce sulfane sulfur (E_o' ~ - 260 mV) and cleave organic (RS_nR, $n \geq 3$) and anionic polysulfides (S_n^{2-}, $n \geq 4$) and, like MBH, creates an ion gradient for ATP synthesis. This work establishes an electrochemical reaction catalyzed by MBS that is intermediate in the evolution from proton- to quinone-reducing respiratory complexes.

Significance Statement

Membrane-bound sulfane reductase (MBS) of elemental sulfur (S°)-reducing hyperthermophiles shares a common ancestor with anaerobic respiratory [NiFe]-hydrogenases and aerobic respiratory Complex I and is proposed to be an intermediate step in the evolution from proton-reduction to quinone-reduction as a means of energy conservation. Herein we purified MBS and discovered an organic trisulfide that was reduced by MBS, the first substrate for this respiratory complex. In addition, cysteine residues that coordinate the NiFe site in hydrogenase that are conserved in MBS but lacking in Complex I were shown not to be involved in the MBS catalytic reaction. These findings expand our understanding of the evolutionary processes involved in going from anaerobic to aerobic respiration and of S° metabolism in general.

Introduction

The very close evolutionary relationship between respiratory membrane-bound NiFe-hydrogenases (MBH) found in anaerobic microbes and Complex I of the mitochondrial aerobic respiratory chain is well established (1-3). For example, *Pyrococcus furiosus* MBH oxidizes reduced ferredoxin (Fd) produced by fermentation, reduces protons to H_2 gas, and conserves energy by creating a sodium ion gradient that is used by ATP synthase to form ATP (4). MBH is encoded by a 14-gene operon and virtually all of its subunits have close homologs in Complex I (Figure 3.1). Indeed, the recent cryo-EM structure of MBH showed that its H_2-evolving, electron transfer cytoplasmic module and ion-pumping membrane module were virtually superimposable on components of Complex I in spite of different overall architectures (5). The cytoplasmic module common to MBH and Complex I contains three [4Fe-4S] clusters that channel electrons (from the

oxidation of Fd or NADH) to the catalytic subunit (MbhL or NuoD) that reduces protons or a quinone derivative (menaquinone or ubiquinone), respectively. Elucidating the evolutionary relationship between the quinone-reducing site of Complex I of the aerobic respiratory chain and the proton-reducing NiFe-site present in MBH is therefore a fundamental issue.

The catalytic subunits of NiFe-hydrogenases fall into four phylogenetic groups, three of which (groups 1-3) are clustered together along with a distantly related group 4 (2, 6). Only the group 4 hydrogenases include non-hydrogenase catalytic subunits. Besides that (NuoD) of Complex I, they are FpoD of a methanophenazine-reducing respiratory complex ($F_{420}H_2$:phenazine oxidoreductase, FPO) found in methanogens (7, 8), and MbxL of a membrane-bound respiratory complex (MBX) of unknown function that is up-regulated during growth with elemental sulfur (S°) by *P. furiosus* and related organisms (9). It has been proposed (2) that MBH, MBX, FPO and Complex I evolved from a common H_2-evolving ancestor and that this was driven by the reduction of oxidants with increasing electrochemical potential. For example, the free energy released in coupling the oxidation of ferredoxin (E°' ~ -480 mV) to the reduction of protons, S°, phenazine and ubiquinone is 12, 41, 61 and 112 kJ/mol, respectively (2). Such terminal electron acceptors likely became available as the Earth's atmosphere and oceans became more and more oxidized. The first step in the eventual evolution of a quinone-reducing complex may have been the appearance of S° in the Archean (10, 11) that drove the evolution of a S°-reducing respiratory system based on MBH. Characterization of MBX is therefore obviously required to understand this evolutionary transition at the molecular level. The goal of the present work was to purifiy the MBH-related MBX system from *P. furiosus* and to determine its role in S° reduction.

MBX is ubiquitous within the order of the S°-reducing *Thermococcales.* It is believed to be the product of an operon duplication of a proton-reducing MBH-like respiratory system that

allowed the switch from proton to S° reduction (2, 12, 13). *P. furiosus* MBX is encoded by a 13-gene operon and contains homologs of all of the 14 subunits of *P. furiosus* MBH, except that of MbhI, as shown in Figure 3.1. Hence MBX retains the same four subunit electron transfer module containing three [4Fe-4S] clusters. One major difference between MBH and MBX is that the catalytic subunit, MbxL, lacks two of four cysteine residues that coordinate the [NiFe] active site in MbhL. The same is true for the catalytic subunit (FpoD) of FPO while that of Complex I (NuoD) lacks all four of these cysteine residues (Figure 3.1). The great similarity between MBX to MBH is indicated by the fact that the *mbx* operon was originally proposed to encode a NiFe hydrogenase with unusual ligand coordination (14). However, the MBX deletion strain (Δ*mbxL*) of *P. furiosus* grows very poorly on S° showing that MBX is essential for efficient S° respiration (9).

P. furiosus grows optimally at 100°C using carbohydrates or peptides as carbon sources to produce acetate, CO_2 and H_2 in the absence of S° (15). Adding S° to a growing culture of *P. furiosus* stops H_2 production and H_2S is produced instead (16). Within 10 min of S° addition, 19 genes are up-regulated, including the 13-gene operon encoding MBX, while 34 genes are down-regulated, including the 14-gene operon encoding MBH (16). This S°-regulated, S°-reducing MBX-dependent system is unique to the hyperthermophilic Thermococcales and is very distinct from the S° respiration pathway of mesophilic bacteria wherein reductant from the oxidation of H_2 or formate is channeled via cytochromes and quinones to a membrane-bound, molybdopterin-containing sulfur reductase (17, 18). The primary S° response in *P. furiosus* is controlled by an unusual regulator, SurR (for sulfur response regulator; PF0095) which functions as a redox-dependent disulfide-based switch mechanism (19). In the absence of S° SurR activates transcription of MBH and represses that of MBX.

The production of H_2 from Fd oxidation by MBH lead to the formation of a Na^+ gradient that is used by ATP synthase (4, 12). In the presence of S°, MBX in essence replaces MBH and, given their high homology, it was assumed that MBX oxidizes Fd and also conserves energy by forming a Na^+ gradient. Indeed, when *P. furiosus* is grown with S°, the maximal yield coefficient is almost twice that obtained in the absence of S° (20), consistent with more energy conserved by coupling Fd oxidation to S° reduction (41 kJ/mol) than to proton reduction (12 kJ/mol). However, Fd-dependent reduction of S° by *P. furiosus* membranes could not be demonstrated *in vitro* and the only S°-reduction activity that could be measured in cell extracts was NADPH-dependent (16). The enzyme responsible, NADPH sulfur reductase (NSR), was characterized and its expression was also regulated by SurR. It was therefore proposed that MBX oxidized Fd and reduced NADP, which was then used by NSR to reduce S° (9, 21). This putative NSR-MBX type of S° reduction has only been found within the order of *Thermococcales* (9, 22). However, the NSR deletion mutant of *P. furiosus* grew similar to the wild-type in the presence of S° (9). In addition, no Fd-dependent $NADP^+$- or Fd-dependent S° reduction activities could be measured in the cell extracts or membranes from *P. furiosus*. The reaction catalyzed by MBX and its physiological function was therefore unresolved (9). Herein, we report the purification and characterization of MBX and the identification of a sulfane sulfur substrate. We also show that MBX is unlikely to produce H_2S directly and that the conserved cysteine residues in the MbxL catalytic subunit are not involved in catalysis. The results presented here provide new insights into this hitherto mysterious membrane-bound complex in terms of physiological function and its evolutionary relationship to MBH, FPO and Complex I.

Results

The MBX operon and construction of affinity-tagged MBX

The 13-gene operon encoding MBX is annotated based on homology with the genes encoding MBH (Figure 3.2). MBX lacks an MbhI homolog but contains a duplication of MbhH (MbxH') and a fusion of MbhE and MbhF (MbxE). Hence, MBX is encoded by MbxA-EGHH'MJKLN. The last four genes in the operon, MbxJKLN, encode the cytoplasmic module and contain the active site (MbxL) and iron-sulfur clusters, while the first nine genes all encode subunits with multiple transmembrane helices and form the membrane arm (Figure 3.1).

Our previous attempts to find a substrate for MBX using *P. furiosus* membranes had been plagued by non-specific reactions due to the high reactivity of potential sulfur-containing substrates, such as S° and polysulfides (vide infra), and the presence of S°-derived compounds in the membranes of S°-grown cells (even after extensive washing). The goal here was therefore to obtain the solubilized holoenzyme form of MBX to remove possible interferences from other membrane components and also to obtain the much simpler cytoplasmic subcomplex to minimize possible side reactions. The strategy to do this is shown in Figure 3.2. The 13-gene *mbx* operon was split into two transcripts by placing the transformation marker and a highly active constitutive promoter, P_{slp}, which controls expression of the gene encoding the S-layer protein, upstream of *mbxJ*. The construct also included a His_9-tag at the N-terminus of MbxJ. These two new operons should result in two transcripts controlled by two promoters: *mbxA-M* under control of the native *mbx* promoter and *mbxJ-N* driven by P_{slp}. Based on qPCR analysis (Figure S3.1), the expression of *mbxJ-N* was six times higher than that of *mbxA-M*. Assuming the transcripts are stable and translated into proteins with similar efficiencies, we anticipated that two versions of MBX would be produced, 9-subunit MbxA-M and 4-subunit MbxJ-N, both with an affinity tag at the N-

terminus of MbxJ. MbxA-M should combine with MbxJ-N to give the intact 13-subunit holoenzyme (MbxA-N) in the membrane, while excess 4-subunit MbxJ-N should accumulate in the cytoplasm.

Purification of S-MBX and C-MBX

For the purification of both forms of MBX, all steps and procedures were carried out under strict anaerobic conditions. The affinity-tagged holoenzyme form of MBX was solubilized from washed *P. furiosus* membranes by incubation with 10 % (v/v) Triton X-100 for 16 hr at 4 °C, the same procedure used to solubilize MBH (23), and purified by two steps of affinity chromatography. The solubilized and purified holoenzyme, now designated S-MBX (MbxA-N), was analyzed by SDS-PAGE. All 13 subunits could be assigned based on their predicted size (Figure 3.3) and all 13 were identified by liquid chromatography–tandem mass spectrometry (LC–MS/MS) analysis. To purify the affinity-tagged 4-subunit subcomplex from the cytoplasm, the supernatant fraction from the membrane preparation was concentrated by anion exchange chromatography and then subjected to affinity chromatrography. When the purified fraction was analyzed by SDS-PAGE (Figure 3.3), all four subunits (MbxJ-N) were evident based on their expected sizes and each was identified by LC-MS/MS and MALDI-TOF. This cytoplasmic subcomplex is termed C-MBX. The sizes of the two purified complexes estimated by gel filtration chromatography were 1.2 MDa for S-MBX (calculated to be 357 kDa for MbxA-N) and 125 kDa for C-MBX (calculated to be 113 kDa for MbxJKLN). These data indicate that the S-MBX holoenzyme was purified as a trimeric complex while C-MBX was a monomeric form of the heterotetramer. By ICP-MS analysis (for Fe, Mg, Co, Mo, V, Ni, Mn, Zn, W and Pb) iron was the only metal detected in the

two enzyme forms, thereby confirming the absence of nickel and molybdenum and supporting the model shown in Figure 3.1.

With the highly purified holoenzyme S-MBX and cytoplasmic subcomplex C-MBX in hand, we investigated their ability to use titanium (III)-reduced *P. furiosus* ferredoxin (Fd) to reduce S° directly. However, no activity was detected over the temperature range from 60 to 80°C above the high background from the direct reduction of S° by Fd. All artificial electron donors that were used (reduced by sodium dithionite), including methyl viologen (MV), benzyl viologen (BV), phenosafranine, safranin O and thionine, also reacted very rapidly with S° and addition of S-MBX or C-MBX did not have any effect. Although NADH and NADPH did no react directly with S°, the MBX complexes did not catalyze their oxidation. Attempts to replace S° with polysulfide and sodium tetrasulfide were also unsuccessful as no activity could be measured above the background. In contrast, dimethyl disulfide ($CH_3S_2CH_3$) and dibenzyl trisulfide ($PhCH_2S_3CH_2Ph$) did not react with Ti-reduced MV at an appreciable rate at 80°C, but no significant stimulation of activity was found with when either S-MBX or C-MBX were added. However, the reduction of dimethyl trisulfide ($CH_3S_3CH_3$, DMTS), which also gave only a low background activity with reduced MV, was dramatically greatly enhanced by the addition of both S-MBX or C-MBX. DMTS is stable at 80°C (6% decomposition after 20 hr (24)) and was therefore used as the model substrate.

Biochemical properties of S-MBX and C-MBX

A standard *in vitro* assay for MBX was developed using DMTS (2.0 mM) as the electron acceptor and Ti-reduced MV as the electron donor. With this assay we were unable to measure significant activity using washed *P. furiosus* membranes due to the high background activity

(compared to cells grown in the absence of S°) arising from the S° and S°-derived compounds within the membranes of S°-grown cells. Once these interferences were removed from the membranes by detergent treatment, DMTS reduction activity was measurable and this allowed S-MBH purification to be followed by activity. The results are summarized in Table 1. S-MBX was purified 110-fold with 23% recovery of activity and a yield of 3.6 mg from 100 g (wet wt. of cells). The purified enzyme had a specific activity of 9.9 units/mg. As shown in Table 2, C-MBX, was purified 33-fold with a yield of 4.2 mg from 100 g (wet wt. of cells). The purified enzyme had a specific activity of 9.5 units/mg. However, the recovery of activity was only 2% suggesting that some other cytoplasmic enzymes were able to reduce DMTS. This was not too surprising since S° is reduced to sulfide non-specifically at 80°C by several *P. furiosus* oxidoreductases, including hydrogenase (SHI), NADH-dependent ferredoxin NAD oxidoreductase (Nfn) and pyruvate ferredoxin oxidoreductase (25, 26). Analysis by MS showed that MBX reduced DMTS using methyl viologen as the electron donor to produce both methanethiol (CH_3SH) and methyl hydrogen disulfide (CH_3S-SH, see Figure S3.2) but H_2S could not be detected by the standard colorimetric assay.

As shown in Figure 3.1, MBX is proposed to use reduced Fd as an electron donor *in vivo* and this was confirmed by the *in vitro* assay. Ti-reduced Fd was able to replace Ti-reduced MV with both S-MBX and C-MBX with specific activities 3.8 and 3.2 U/mg, respectively. This showed that the iron-sulfur clusters responsible for the electron transport from MbxN to MbxL were intact in the purified enzymes, as shown Figure 3.1. The kinetic properties of S-MBX and C-MBX are summarized in Table 3. According to the K_m values, S-MBX has a slightly higher affinity for DMTS than C-MBX, and the low value (~ 0.4 mM) is consistent with the use of DMTS as a model sulfur-containing substrate. The V_{max} values were comparable for the two enzymes (~ 12 units/mg).

Since the molecular weight of C-MBX is about one-third of that of S-MBX, this suggests that C-MBX is not as active as it is when part of the holoenzyme complex. The lower than expected activity of C-MBX is not due to the stability of the enzyme as, surprisingly, C-MBX was more thermostable than S-MBX. The loss of activity at 90°C was a first order reaction with half-lives of 28 and 7 hrs, respectively. Accordingly, S-MBX and C-MBX exhibited similar sensitivities to inactivation by oxygen with half-lives in air (at 25°C) of 19 and 17 hrs, respectively. The optimal temperature for DMTS reduction by both S-MBX and C-MBX was above 90°C with almost an order of magnitude increase in activity upon increasing the assay temperature from 60° to 90°C (Figure S3.3).

The role of the cysteine residues in MbxL

As shown in Figure 3.1, the catalytic subunit of MBH contains four cysteine residues that coordinate the catalytic NiFe site, and two of these are conserved in MbxL (alignments are given in Figure S3.4). Hence, a key question is whether these two residues are essential for the catalytic reaction of MBX. We constructed a strain of *P. furiosus* wherein the MbxL subunit of MBX contained a double mutation, C85A and C385A. We had previously shown that a mutant strain of *P. furiosus* (ΔMbxL) lacking the gene encoding MbxL grew very poorly in the presence of S°, although growth in the absence of S° (when MBX is not produced) was the same as the wild type strain (9). We therefore constructed two strains based on the ΔMbxL strain. One (MbxL-WT) contained the wild type *mbxL* gene while the other (MbxL-C85A/C385A) contained *mbxL* with the double mutation, C85A and C385A. Both genes were inserted as part of a *mbxJKLN* construct into the intergenic space between PF0265 and PF0266 (an intergenic space with no detectable transcriptional activity, data not shown). As shown in Figure 3.4a, the ΔMbxL strain has minimal

growth on S° and, as anticipated, the wild type *mbxL* complemented the growth defect. However, and somewhat surprisingly, the MbxL-C85A/C385A strain showed no growth defect on S° and grew the same as the MbxL-WT strain. Moreover, as shown in Figure 3.4b, the MbxL-WT and MbxL-C85A/C385A strains produced comparable amounts of H_2S and the rates of production matched the growth rates of both strains. Hence, the defect in S° metabolism caused by the deletion of MbxL was restored by the MbxL subunit even when the two cysteine residues conserved in MBX were replaced by alanine residues. In addition, these results show that these two cysteine residues do not coordinate a unique type of iron center in MbxL that could be important for catalytic activity, although we cannot rule out the presence a novel iron site coordinated by non-cysteinyl residues.

Discussion

Herein we describe the purification and characterization of the solubilized holoenzyme S-MBX and the cytoplasmic subcomplex C-MBX of *P. furiosus*. The two subcomplexes of the holoenzyme, MbxA-M and MbxJ-N are encoded by separate transcripts and translated independently (Figure 3.2), yet they combine to generate a functional MBX, which is essential for cells to grow in the presence of S°. In the recombinant strain the SurR-regulated promoter of *mbx* (27) controls production of the MbxA-M subcomplex such that is only produced in S°-grown cells, but the generation of the MbxJ-N subcomplex is driven by the constitutive promoter, P_{slp}. Thus, the cytoplasmic subcomplex C-MBX should be produced at comparable levels in cells grown without S°. However, we were unable to purify C-MBX by affinity chromatography of the cytoplasmic extract of such cells. This suggests that accessory proteins whose genes are expressed only in the presence of S° might be required for production of a stable MbxJ-N subcomplex,

although what those might be is not known at present. On the other hand, the C-MBH (MbxJ-N) produced in S°-grown cells could be purified and was extremely stable, in fact, it was more thermostable at 90°C than the purified holoenzyme (S-MBX). This might due to the presence of Triton X-100 used to solubilize MBX as the cloud point is approximately 70 °C, above which micelles would aggregate to form a detergent-rich phase that could destabilize the holoenzyme (28).

Past attempts to assign a catalytic activity to the MBX complex *in vitro* using *P. furiosus* membranes suffered from high background activities as potential substrates are highly reactive sulfur species (S° and polysulfide, see below) that directly oxidize potential electron donors and do so at extremely high rates, particularly at high temperature (80°C). This situation was compounded by the apparent presence of S° and S°-derivatives in the membranes of S°-grown cells even after extensive washing that also react directly with potential electron donors (this was not evident with membranes from cells grown without S°). These problems were overcome by affinity-tagging and purifying MBX and by the use of several sulfur-containing substrates that have minimal reactivity with potential donors. One of these, dimethyl trisulfide (DMTS, $CH_3S_3CH_3$), was a very effective substrate for MBX. DMTS is well studied as it is produced by methionine degradation in various bacteria and gives flavor to a variety of foods and beverages (29, 30). It is not thought to be a physiological substrate for MBX, rather, it contains a three-sulfur polysulfide-like structure that mimics the natural substrate.

Elemental sulfur (S°) is also not thought to be a physiological substrate for *P. furiosus* or any other S°-reducing microbe due to its extremely low solubility. Its S_8-ring readily reacts with H_2S (HS^-, pK 7.0) to generate soluble polysulfides (S_n^{2-}) and in hydrothermal vent environments of the type inhabited by *P. furiosus*, polysulfides generated by the reaction of geothermally-

produced H_2S and S° are likely to be the true substrates for S°-reducing hyperthermophiles (the solubility of polysulfides increases ten-fold from 37 to 90°C) (31, 32). Above pH 6.0 the reaction of H_2S with S° generates predominantly linear tetra- and pentapolysulfides mainly in the dianionic S_n^{2-} form (their respective pK values are 6.3 and 5.7; (32)). Hepta-, octa- and nonasulfides are also produced but di- and trisulfides are unstable and readily disproportionate to S° and HS^- (33, 34). In addition, a variety of organic polysulfides were identified in the cytoplasm of several S°-grown hyperthermophilic species and these are thought to be generated by the reaction of anionic polysulfides with aldehydes produced during amino acid metabolism (35).

The ability of MBX to catalyze DMTS reduction provides insight into its physiological reaction. Methanethiol and methyl hydrogen disulfide are produced when DMTS is reduced by two electrons (Eqn. 1) but reduction by four electrons produces methanethiol and H_2S (Eqn. 2).

$$CH_3\text{-}S\text{-}S\text{-}S\text{-}CH_3 + 2\ H^+ + 2\ e^- \rightarrow CH_3SH + CH_3\text{-}S\text{-}SH \quad (1)$$

$$CH_3\text{-}S\text{-}S\text{-}S\text{-}CH_3 + 4\ H^+ + 4\ e^- \rightarrow 2\ CH_3SH + H_2S \quad (2)$$

In the MBX assay, H_2S was not detected as a product of DMTS reduction but both CH_3SH and CH_3S-SH were detected by MS analysis. These data indicate that MBX catalyzes only the two-electron reduction of DMTS. In addition, MBX did not use dimethyl disulfide or dibenzyl trisulfide as substrates. We therefore conclude that MBX reduces the sulfur-sulfur bond within a trisulfide (-S-S-S-) and catalyzes the reduction of organic polysulfides according to the general reaction shown in Eqn. 3, where $n \geq 3$ and R and R' are alkyl but not aryl. The corresponding reaction (R=R'=H) with anionic polysulfides is shown in Eqn. 4 (where $n \geq 4$ due to the stability of anionic polysulfides).

$$R\text{-}S_n\text{-}R' + 2\ e^- \rightarrow RS_{n-x}^- + R'S_x^- \quad (3)$$

$$S_n^{2-} + 2\ e^- \rightarrow S_{n-x}^{2-} + S_x^{2-} \quad (4)$$

$$S_n^{2-} + 2\ e^- + 2\ H^+ \rightarrow S_{n-1}^{2-} + H_2S \quad (5)$$

$$RS_n^- + 2\ e^- + 2\ H^+ \rightarrow RS_{n-1}^- + H_2S \quad (6)$$

Any di- and trisulfides that are produced by MBX according to Eqn. 4 will spontaneously convert to S° and H_2S. It seems unlikely that MBX generates H_2S directly from the reduction of anionic polysulfides (Eqn. 5) or of monoalkyl polysulfides (Eqn. 6) generated from Eqn. 3. Indeed, Eqns. 5 and 6 represent fundamentally different reactions from those of Eqns. 3 and 4, which involve simple 2 e^- transfer without a need for protons, consistent with the lack in MBH of the proton path to the catalytic site found in MBH (see below). We therefore propose that MBX reduces both organic ($n \geq 3$) and anionic polysulfides ($n \geq 4$) but that it does not generate H_2S per se, rather, it produces smaller polysulfides (S_n^{2-}) and when $n \leq 3$ they spontaneously disproportionate to H_2S and S°. Hence, we propose renaming MBX to MBS for membrane-bound sulfane reductase.

As shown in Figure 3.1, the catalytic subunit (MbxL, now MbsL) of MBS contains two cysteinyl residues and these correspond to two of the four that coordinate the NiFe catalytic site in MbhL of MBH. However, the growth study of the *P. furiosus* C85A/C385A mutant strain described herein unequivocally demonstrates that these two cysteine residues are not required for the physiological function of MBS. This is consistent with the proposed physiological reaction involving a 2 e^- transfer (Eqns. 3 and 4) where there is no obvious requirement for an active site thiol. Indeed, the residues of the proposed proton transfer pathway from the cytoplasm to the catalytic site in MBH (5) are not conserved in MBS (see Figure S3.4), which also supports MBX catalyzing the proton-independent reactions shown in Eqns. 3 and 4. The two conserved cysteinyl residues in MBX are also present in the catalytic subunit (FpoD) of FPO, which catalyzes the reduction of the hydrophobic aromatic phenazine, a reaction that also does not require thiol/disulfide chemistry (2). The same is true for the reaction (quinone reduction) catalyzed by

Complex I, but in this case the catalytic subunit (NuoD) lacks all four of the NiFe-coordinating cysteine residues of MBH. It therefore appears that these two cysteinyl residues in MbsL and FpoD, subunits that are thought to be intermediates in the evolution of NuoD (Figure 3.1, (2)), are not conserved because of catalytic constraints. The reason for their presence is still not clear as they are also not involved in the assembly of MBS since a functional complex was produced by the *P. furiosus* C85A/C385A mutant strain.

Based on the results presented here, we propose that MBS is the primary enzyme responsible for the reduction of polysulfides derived from S° during the growth of *P. furiosus.* This is consistent with previous mutational analysis (9) showing that MBS (MBX) is essential for growth on S° but NSR and two so-called sulfide dehydrogenases (PF1327-1328 and PF1910-1911, now known as NfnI and NfnII (36)) are not. Similarly, the two sulfhydrogenases of *P. furiosus,* (now known as soluble hydrogenases I and II or SHI and SHII (37, 38)), which can use H_2 or NAD(P)H to reduce S° *in vitro,* are also not involved in S° reduction *in vivo* (39). We show here that MBS uses reduced *P. furiosus* Fd to reduce the model substrate DMTS. MBS is proposed to use the reduced Fd (E_o' ~ - 480 mV) produced by glycolysis to reduce organic and anionic polysulfides (Eqns. 3 and 4; E_o' ~ - 260 mV (32)) to generate small anionic polysulfides ($n \leq 3$) that spontaneously generate H_2S and S° (Figure 3.5). It has been shown that *P. furiosus* uses polysulfides as growth substrates (40) although exactly how these enter the cell is not clear. By analogy with MBH (Figure 3.1), MBS is also proposed to couple its catalytic reaction to the formation of a sodium ion gradient, which is used for ATP synthesis (Figure 3.5).

There are, however, several fundamental differences between MBS and MBH besides the lack of a proton path to the proposed catalytic site in MBS (Figure S3.4). These include the lack of a MbhI homolog in MBX, a duplication of MbhH (MbsH') and a fusion of MbhE and MbhF

(MbsE) in MBX, and the absence in MbsM of the string of Glu residues found in MbhM (Figure S3.5). In addition, MBX appears to conserve much more energy than MBH (41 versus 12 kJ/mol; (2)) leading to a cellular yield coefficient almost twice that obtained in the absence of S° (20). With the advent of a catalytic activity for MBS (Eqns. 3 and 4) and of a substrate for in vitro assays (DMTS), it will now be possible to design and characterize MBS mutants based on the MBH structure (5) to investigate how these structural differences affect the functions of these two ancestral respiratory complexes from *P. furiosus* and how they differ in converting an electrochemical potential into an ion gradient.

Experimental procedures

Strain construction

The strains that were used in this study are summarized in Table S1. The genetically-tractable *P. furiosus* strain, COM1, was used for the genetic manipulation of MBX (41). A knock-in cassette was constructed using overlapping PCR (42). The upstream flanking region (UFR), which also contained the promoter of the gene encoding the S-layer protein (P_{slp}), and the downstream flanking region (DFR) were amplified from *P. furiosus* genomic DNA, and the selection marker (P_{gdh}-*pyrF*), was amplified from pGLW021 (41). A 9x-His-tag was also placed at the N-terminus of *mbxJ* (Figure S3.6). The split operon after transformation is shown in Figure 3.2. Strain MW0572 (MbxL-C85A/C385A) was constructed as shown in Figure S3.7. Mutagenesis was carried out using QuikChange II Site-Directed Mutagenesis Kit (Agilent Technologies) and the fragments were assembled using over-lapping PCR. The knock in cassette was transformed into the intergenic space between PF0265 and PF0266. The transformants were grown as

previously described (41) and the PCR-confirmed colonies were sequence verified using the Genewiz service.

Growth conditions

The growth medium (41) contained 1x base salt, 1x trace minerals, 10 μM tungstate, 5 g/L yeast extract, 5g/L casein hydrolysate, 5 g/L maltose, 0.5 g/L cysteine, 0.5 g/L sodium sulfide, 1 g/L sodium bicarbonate, 1 mM potassium phosphate (pH 6.8) and 5 g/L S°. All cultures were routinely grown at 90°C in 100 ml sealed bottles with shaking at 150 rpm. The same medium was used for the 20 L fermentations that were performed as previously described (43) and the harvested cells were frozen in liquid nitrogen and stored at -80 °C. To monitor growth, 1 mL samples were taken and centrifuged at 14,000 xg for 5 min. The cell pellet was lysed osmotically using 1 mL distilled H_2O and cell debris was removed by centrifugation at 14,000 xg for 1 min. The supernatant was collected for protein estimation using Protein Assay Reagent (Bio-Rad). H_2S production in the headspace was analyzed by the methylene blue method (44) and abiotic H_2S production was subtracted from the experimental samples using the control without the addition of cells.

RNA extraction and quantitative RT-PCR analysis

MW0491 (MbxJ-His) cells were harvested at mid log phase and RNA was isolated using Absolutely RNA Miniprep Kit (Agilent Technologies). Genomic DNA was digested before cDNA synthesis using TURBO DNase (Ambion) and RNA was purified by a phenol chloroform extraction method as previously described (45). cDNA synthesis was carried out with 1 μg purified RNA using AffinityScript cDNA Synthesis Kit (Agilent Technologies) and qPCR analysis was

performed using Brilliant III Ultra-Fast QPCR Master Mix (Agilent Technologies) with primers designed to amplify ~100 bp products within the target genes: *mbxA* (PF1453), *mbxE* (PF1449), *mbxM* (PF1445), *mbxJ* (PF1444), *mbxL* (PF1442), *mbxN* (PF1441), and *por*γ (PF0971), where PF0971 was used as the reference gene.

Purification of S-MBX and C-MBX

All purification procedures were performed under anaerobic conditions. Frozen cells were lysed osmotically in 25 mM Tris-HCl, pH 8.0, containing 1 mM DTT and 50 μg/mL DNase I (5 mL per gram of frozen cells) for 1 hr at room temperature in an anaerobic chamber (Coy Laboratory Products). The cell-free extract was centrifuged at 5,000 xg for 20 sec to remove the majority of the S° and then centrifuged at 100,000 xg for 1 hr using a Beckman-Coulter Optima L-90K ultracentrifuge. The supernatant representing the cytoplasmic extract was used to purify C-MBX. It was applied to a UNOsphere Q column (Bio-Rad) equilibrated with 25 mM Tris-HCl, pH 8.0, containing 1 mM DTT (Buffer A) while diluting it 10-fold with buffer A using a NGC Chromatography System (Bio-Rad). The bound protein was block eluted with Buffer B (Buffer A containing 0.5 M NaCl). The eluted protein was applied to a 5 mL His-Trap FF Ni-NTA column (GE Healthcare) for C-MBX purification, while diluting it 5-fold with 25 mM sodium phosphate, pH 7.5 containing 300 mM NaCl and 1 mM DTT (Buffer C). The column was equilibrated with Buffer C before loading the sample. The column was washed with five column volumes of Buffer C and the bound protein was eluted with a 20-column volume gradient from 0 to 100 % Buffer D (Buffer C containing 500 mM imidazole). The active enzyme as measured by the MV-linked DMTS reduction assay was pooled and applied to a 5 mL Q HP column (GE Healthcare) while

diluting it 10-fold with Buffer A. A 20-column volume gradient from 0 to 100 % Buffer B was used to elute the bound C-MBX.

For the purification of S-MBX, the pellet after 100,000 xg centrifugation step representing the membrane fraction was washed with 50 mM EPPS, pH 8.0, containing 5 mM $MgCl_2$, 50 mM NaCl, 10 % (v/v) glycerol, 2 mM DTT and 0.1 mM phenylmethylsulfonyl fluoride (PMSF). The washed membranes were collected by centrifugation at 100,000 xg for 1 hr. This washing step was repeated twice and the membrane-containing pellet was resuspended in 50 mM Tris-HCl, pH 8.0, containing 0.5 mM $MgCl_2$, 50 mM NaCl, 5 % (v/v) glycerol, 2 mM DTT and 0.1 mM PMSF using a Pyrex tissue grinder (Pyrex). The resuspended membranes were solubilized by stirring with 10% (v/v) Triton X-100 at 4 °C for 16 hr. The solubilized membranes were centrifuged at 100,000 xg for 1 hr and the supernatant was collected and applied to a 5 mL His-Trap FF column while diluting it 10-fold with 25 mM sodium phosphate, pH 7.5, containing 300 mM NaCl, 1 mM DTT, and 0.02% (v/v) Triton X-100 (Buffer A). The column was equilibrated with Buffer A before loading the sample. The bound protein was eluted with a 20-column volume gradient from 0 to 100% Buffer B (Buffer A containing 500 mM imidazole). The active enzyme as measured by the MV-linked DMTS reduction assay was collected and applied to a 1 mL His-Trap HP column equilibrated with Buffer A while diluting it 5-fold with Buffer A. A 10-column volume gradient from 0 to 100 % Buffer B was carried out to elute the bound S-MBX.

The size of S-MBX was estimated using a Superose 6 column (GE Healthcare) that was equilibrated with 50 mM Tris/HCl, pH 8.2, containing 300 mM NaCl, 1 mM sodium dithionite and 0.02% (v/v) Triton X-100. The size of C-MBX was determined using an ENrich SEC 650 column (Bio-Rad), which was equilibrated with 50 mM Tris, pH 8.2, containing 300 mM NaCl,

and 1 mM sodium dithionite. The eluted protein was analyzed by SDS-PAGE using precast Criterion TGX (4-15 %) gels (Bio-Rad) and 4-12 % Bis-Tris Novex NuPAGE gels (Invitrogen).

Enzyme assays

All assays were carried out at 80°C using anaerobic sealed cuvettes. The standard dimethyl trisulfide (DMTS) reduction assay used a 2 mL reaction mixture containing 100 mM 3-(N-morpholino) propanesulfonic acid (MOPS), pH 7.5, and 150 mM NaCl. After pre-heating to 80°C, 1 mM methyl viologen reduced by titanium citrate and 2 mM DMTS were added and the reaction was initiated by addition of the enzyme. The activity was measured by monitoring the oxidation of methyl viologen at 600 nm (ϵ = 8.25 mM^{-1} cm^{-1}) using a 100 Cary UV-Vis spectrophotometer with a peltier-based temperature controller from Agilent technologies (Santa Clara). One unit of activity is defined as 1 µmol of substrate reduced per minute. Where indicated, DMTS was replaced with dimethyl disulfide, dibenzyl trisulfide, polysulfide or sodium tetrasulfide. Polysulfide was prepared as previously described (26). Ferredoxin (Fd)-dependent DMTS reduction activity was measured in the same manner except that Fd replaced methyl viologen and was reduced using titanium citrate. The oxidation of Fd was measured at 425 nm (ϵ = 13 mM^{-1} cm^{-1}). *P. furiosus* Fd was purified as described previously (46). The oxygen sensitivity and thermostability experiments were carried out using the methyl viologen-linked DMTS reduction assay. H_2S production was measured using the double-vial system with the methylene blue assay as previously described (21).

Other methods

The identification of MBX subunits by MALDI-TOF and LC-MS/MS were performed by the PAMS Facility at the University of Georgia. The production of methanethiol (CH_3SH) and methyl hydrogen disulfide (CH_3S-SH) from DMTS reduction assay were identified as their 5,5'-dithiobis-(2-nitrobenzoic acid) (DTNB) derivatives. The standard DMTS reduction assay was carried out as described above but the reaction was extended for 30 min at 80°C before taking the samples from the headspace to interact with 1 mM DTNB. The reaction mixture was incubated for 1 hr at room temperature. The resulting solution was ran on a Bruker Daltonics Esquire 3000 Plus ion trap mass spectrometer using an electrospray source. Metal analysis was carried out using an octopole-based ICP-MS (7500ce; Agilent Technologies) as described previously (47).

Acknowledgments

This work was supported by a grant (DE-FG05-95ER20175 to MWA) from the Division of Chemical Sciences, Geosciences and Biosciences, Office of Basic Energy Sciences of the Department of Energy. We thank the Proteomics and Mass Spectrometry Core Facility at the University of Georgia for MS, MALDI-TOF and LC-MS/MS analyses.

References

1. Albracht SP. 1993. Intimate relationships of the large and the small subunits of all nickel hydrogenases with two nuclear-encoded subunits of mitochondrial NADH: ubiquinone oxidoreductase. Biochim Biophys Acta 1144:221-4.
2. Schut GJ, Zadvornyy O, Wu CH, Peters JW, Boyd ES, Adams MW. 2016. The role of geochemistry and energetics in the evolution of modern respiratory complexes from a proton-reducing ancestor. Biochim Biophys Acta 1857:958-70.
3. Sazanov LA. 2015. A giant molecular proton pump: structure and mechanism of respiratory complex I. Nat Rev Mol Cell Biol 16:375-88.
4. Pisa KY, Huber H, Thomm M, Muller V. 2007. A sodium ion-dependent A1AO ATP synthase from the hyperthermophilic archaeon *Pyrococcus furiosus*. FEBS J 274:3928-38.
5. Yu H, Wu CH, Schut GJ, Haja DK, Zhao G, Peters JW, Adams MWW, Li H. 2018. Structure of an ancient respiratory system. Cell doi:10.1016/j.cell.2018.03.071.
6. Boyd ES, Schut GJ, Adams MWW, Peters JW. 2014. Hydrogen metabolism and the evolution of biological respiration. Microbe 9:361-367.
7. Baumer S, Murakami E, Brodersen J, Gottschalk G, Ragsdale SW, Deppenmeier U. 1998. The F420H2:heterodisulfide oxidoreductase system from *Methanosarcina* species. 2-Hydroxyphenazine mediates electron transfer from F420H2 dehydrogenase to heterodisulfide reductase. FEBS Lett 428:295-8.
8. Baumer S, Ide T, Jacobi C, Johann A, Gottschalk G, Deppenmeier U. 2000. The $F_{420}H_2$ dehydrogenase from *Methanosarcina mazei* is a redox-driven proton pump closely related to NADH dehydrogenases. J Biol Chem 275:17968-73.

9. Bridger SL, Clarkson SM, Stirrett K, DeBarry MB, Lipscomb GL, Schut GJ, Westpheling J, Scott RA, Adams MW. 2011. Deletion strains reveal metabolic roles for key elemental sulfur-responsive proteins in *Pyrococcus furiosus*. J Bacteriol 193:6498-504.

10. Van Kranendonk MJ. 2006. Volcanic degassing, hydrothermal circulation and the flourishing of early life on Earth: A review of the evidence from c. 3490-3240 Ma rocks of the Pilbara Supergroup, Pilbara Craton, Western Australia. Earth-Sci Rev 74:197-240.

11. Philippot P, Van Zuilen M, Lepot K, Thomazo C, Farquhar J, Van Kranendonk MJ. 2007. Early Archaean microorganisms preferred elemental sulfur, not sulfate. Science 317:1534-1537.

12. Schut GJ, Boyd ES, Peters JW, Adams MWW. 2013. The modular respiratory complexes involved in hydrogen and sulfur metabolism by heterotrophic hyperthermophilic archaea and their evolutionary implications. FEMS Microbiol Rev 37:182-203.

13. Sapra R, Bagramyan K, Adams MW. 2003. A simple energy-conserving system: proton reduction coupled to proton translocation. *Proc Natl Acad Sci U S A* **100**:7545-50.

14. Silva PJ, van den Ban EC, Wassink H, Haaker H, de Castro B, Robb FT, Hagen WR. 2000. Enzymes of hydrogen metabolism in *Pyrococcus furiosus*. Eur J Biochem 267:6541-51.

15. Fiala G, Stetter KO. 1986. *Pyrococcus furiosus* sp nov represents a novel genus of marine heterotrophic archaebacteria growing optimally at 100°C. Arch Microbiol 145:56-61.

16. Schut GJ, Bridger SL, Adams MW. 2007. Insights into the metabolism of elemental sulfur by the hyperthermophilic archaeon *Pyrococcus furiosus*: characterization of a

coenzyme A- dependent NAD(P)H sulfur oxidoreductase. Journal of Bacteriology 189:4431-41.

17. Enemark JH, Cosper MM. 2002. Molybdenum enzymes and sulfur metabolism. Met Ions Biol Syst 39:621-54.

18. Prisner T, Lyubenova S, Atabay Y, MacMillan F, Kroger A, Klimmek O. 2003. Multifrequency cw-EPR investigation of the catalytic molybdenum cofactor of polysulfide reductase from *Wolinella succinogenes*. J Biol Inorg Chem 8:419-26.

19. Yang H, Lipscomb GL, Keese AM, Schut GJ, Thomm M, Adams MW, Wang BC, Scott RA. 2010. SurR regulates hydrogen production in *Pyrococcus furiosus* by a sulfur-dependent redox switch. Mol Microbiol 77:1111-22.

20. Schicho RN, Ma K, Adams MW, Kelly RM. 1993. Bioenergetics of sulfur reduction in the hyperthermophilic archaeon *Pyrococcus furiosus*. *J Bacteriol* **175**:1823-30.

21. Schut GJ, Bridger SL, Adams MWW. 2007. Insights into the metabolism of elemental sulfur by the hyperthermophilic archaeon *Pyrococcus furiosus*: Characterization of a coenzyme A-dependent NAD(P)H sulfur oxidoreductase. J Bacteriol 189:4431-4441.

22. Liu Y, Beer LL, Whitman WB. 2012. Sulfur metabolism in archaea reveals novel processes. Environ Microbiol 14:2632-44.

23. McTernan PM, Chandrayan SK, Wu CH, Vaccaro BJ, Lancaster WA, Yang Q, Fu D, Hura GL, Tainer JA, Adams MW. 2014. Intact functional fourteen-subunit respiratory membrane-bound [NiFe]-hydrogenase complex of the hyperthermophilic archaeon *Pyrococcus furiosus*. J Biol Chem 289:19364-72.

24. Pickering TL, Saunders KJ, Tobolsky AV. 1967. Disproportionation of organic polysulfides. J Am Chem Soc 89:2364.

25. Ma K, Schicho RN, Kelly RM, Adams MW. 1993. Hydrogenase of the hyperthermophile Pyrococcus furiosus is an elemental sulfur reductase or sulfhydrogenase: evidence for a sulfur-reducing hydrogenase ancestor. Proc Natl Acad Sci U S A 90:5341-4.

26. Ma K, Adams MW. 1994. Sulfide dehydrogenase from the hyperthermophilic archaeon *Pyrococcus furiosus*: a new multifunctional enzyme involved in the reduction of elemental sulfur. J Bacteriol 176:6509-17.

27. Lipscomb GL, Keese AM, Cowart DM, Schut GJ, Thomm M, Adams MW, Scott RA. 2009. SurR: a transcriptional activator and repressor controlling hydrogen and elemental sulphur metabolism in *Pyrococcus furiosus*. Mol Microbiol 71:332-49.

28. Arnold T, Linke D. 2007. Phase separation in the isolation and purification of membrane proteins. Biotechniques 43:427-30, 432, 434.

29. Isogai A, Kanda R, Hiraga Y, Nishimura T, Iwata H, Goto-Yamamoto N. 2009. Screening and identification of precursor compounds of dimethyl trisulfide (DMTS) in Japanese sake. J Agric Food Chem 57:189-95.

30. Dias B, Weimer B. 1998. Conversion of methionine to thiols by lactococci, lactobacilli, and brevibacteria. Appl Environ Microbiol 64:3320-6.

31. Schauder R, Muller E. 1993. Polysulfide as a possible substrate for sulfur-reducing bacteria. Arch Microbiol 160:377-382.

32. Hedderich R, Klimmek O, Kroger A, Dirmeier R, Keller M, Stetter KO. 1999. Anaerobic respiration with elemental sulfur and with disulfides. FEMS Microbiol Rev 22:353-381.

33. Giggenbach W. 1972. Optical-spectra and equilibrium distribution of polysulfide ions in aqueous-solution at 20 degrees. Inorg Chem 11:1201.

34. Kang J, Hick LA, Price WE. 2007. Using calibration approaches to compensate for remaining matrix effects in quantitative liquid chromatography/electrospray ionization multistage mass spectrometric analysis of phytoestrogens in aqueous environmental samples. Rapid Commun Mass Spectrom 21:4065-72.

35. Ritzau M, Keller M, Wessels P, Stetter KO, Zeeck A. 1993. Secondary metabolites by chemical-screening .25. New cyclic polysulfides from hyperthermophilic archaea of the genus *Thermococcus*. Liebigs Ann Chem:871-876.

36. Nguyen DMN, Schut GJ, Zadvornyy OA, Tokmina-Lukaszewska M, Poudel S, Lipscomb GL, Adams LA, Dinsmore JT, Nixon WJ, Boyd ES, Bothner B, Peters JW, Adams MWW. 2017. Two functionally distinct NADP(+)-dependent ferredoxin oxidoreductases maintain the primary redox balance of *Pyrococcus furiosus*. J Biol Chem 292:14603-14616.

37. Bryant FO, Adams MW. 1989. Characterization of hydrogenase from the hyperthermophilic archaebacterium, *Pyrococcus furiosus*. *J Biol Chem* 264:5070-9.

38. Ma K, Weiss R, Adams MW. 2000. Characterization of hydrogenase II from the hyperthermophilic archaeon *Pyrococcus furiosus* and assessment of its role in sulfur reduction. J Bacteriol 182:1864-71.

39. Schut GJ, Nixon WJ, Lipscomb GL, Scott RA, Adams MW. 2012. Mutational analyses of the enzymes involved in the metabolism of hydrogen by the hyperthermophilic archaeon *Pyrococcus furiosus*. Front Microbiol 3:163.

40. Blumentals, II, Itoh M, Olson GJ, Kelly RM. 1990. Role of polysulfides in reduction of elemental sulfur by the hyperthermophilic archaebacterium *Pyrococcus furiosus*. Appl Environ Microbiol 56:1255-62.

41. Lipscomb GL, Stirrett K, Schut GJ, Yang F, Jenney FE, Jr., Scott RA, Adams MW, Westpheling J. 2011. Natural competence in the hyperthermophilic archaeon *Pyrococcus furiosus* facilitates genetic manipulation: construction of markerless deletions of genes encoding the two cytoplasmic hydrogenases. Appl Environ Microbiol 77:2232-8.

42. Bryksin AV, Matsumura I. 2010. Overlap extension PCR cloning: a simple and reliable way to create recombinant plasmids. Biotechniques 48:463-5.

43. Chandrayan SK, McTernan PM, Hopkins RC, Sun J, Jenney FE, Jr., Adams MW. 2012. Engineering hyperthermophilic archaeon *Pyrococcus furiosus* to overproduce its cytoplasmic [NiFe]-hydrogenase. J Biol Chem 287:3257-64.

44. Chen JS, Mortenson LE. 1977. Inhibition of methylene blue formation during determination of the acid-labile sulfide of iron-sulfur protein samples containing dithionite. Anal Biochem 79:157-65.

45. Schut GJ, Zhou J, Adams MW. 2001. DNA microarray analysis of the hyperthermophilic archaeon *Pyrococcus furiosus*: evidence for an new type of sulfur-reducing enzyme complex. *J Bacteriol* 183:7027-36.

46. Aono S, Bryant FO, Adams MW. 1989. A novel and remarkably thermostable ferredoxin from the hyperthermophilic archaebacterium *Pyrococcus furiosus*. J Bacteriol 171:3433-9.

47. Cvetkovic A, Menon AL, Thorgersen MP, Scott JW, Poole FL, 2nd, Jenney FE, Jr., Lancaster WA, Praissman JL, Shanmukh S, Vaccaro BJ, Trauger SA, Kalisiak E, Apon JV, Siuzdak G, Yannone SM, Tainer JA, Adams MW. 2010. Microbial metalloproteomes are largely uncharacterized. Nature 466:779-82.

Table 3.1. Purification of S-MBX

S-MBX	Total Units (μmol min^{-1})	Total Protein (mg)	Specific Activity (U/mg)	% Yield	Fold Purification
Solubilized membranes	155	1,803	0.09	100	1
Ni-NTA FF	58.3	42.6	1.37	38	15
Ni-NTA HP	35.4	3.6	9.9	23	110

Table 3.2. Purification of C-MBX

C-MBX	Total Units (μmol min^{-1})	Total Protein (mg)	Specific Activity (U/mg)	% Yield	Fold Purification
Cytoplasmic extract	1,727	5,901	0.29	100	1
UNOsphere Q	1,454	2,640	0.55	84	1.9
Ni-NTA FF	75	306	0.25	4.3	0.9
Q HP	40	4.2	9.5	2.3	32.7

Table 3.3. Properties of S-MBX and C-MBX

Property	**S-MBX**	**C-MBX**
K_m (DMTS, µM)	369 ± 95	609 ± 90
V_{max} (U/mg)	12.4 ± 2.3	11.8 ± 0.4
Ferredoxin-linked DMTS reduction activity (U/mg)	3.8	3.2
Half-life ($t_{1/2}$) at 90°C under argon (h)	7	28
Half-life ($t_{1/2}$) at 25°C under air (h)	19	17

Figure 3.1

Diagrammatic representations of the membrane-bound hydrogenase (MBH) and the membrane-bound oxidoreductase of unknown function (MBX) of *P. furiosus*, and of Complex I. Homologous subunits are in the same color. The number of cysteinyl residues in the red catalytic subunits are indicated by –SH groups. Modified from (2).

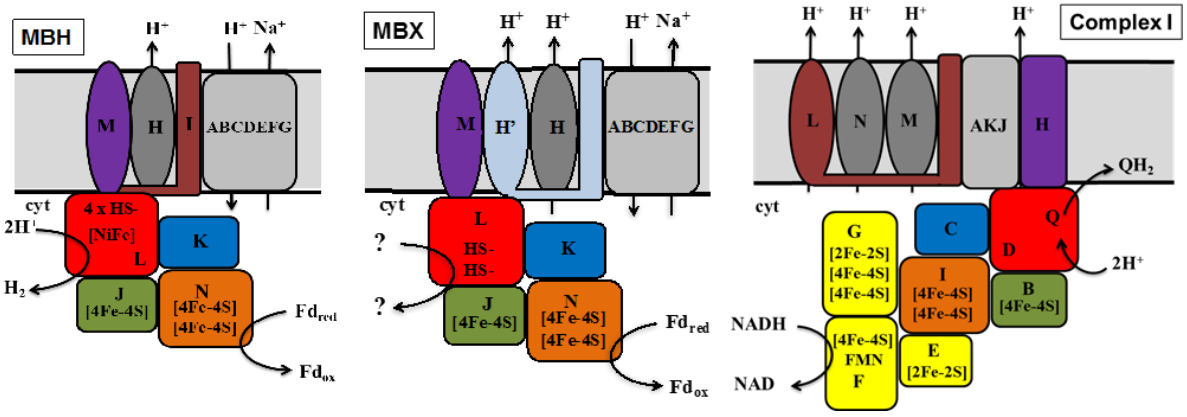
MBH
H+
H+ Na+
M
H
I
ABCDEFG
cyt
4 x HS-
[NiFe]
L
2H+
K
H2
J
[4Fe-4S]
N
[4Fe-4S]
[4Fe-4S]
Fdred
Fdox
MBX
H+
H+
H+ Na+
M
H'
H
ABCDEFG
cyt
L
HS-
HS-
?
K
?
J
[4Fe-4S]
N
[4Fe-4S]
[4Fe-4S]
Fdred
Fdox
H+
H+
H+
H+
Complex I
L
N
M
AKJ
H
QH2
cyt
G
[2Fe-2S]
[4Fe-4S]
[4Fe-4S]
C
Q
D
2H+
I
[4Fe-4S]
[4Fe-4S]
B
[4Fe-4S]
NADH
[4Fe-4S]
FMN
F
E
[2Fe-2S]
NAD

Figure 3.2

The operon-splitting strategy for the purification of MBX. The expression of *mbxA-M* was driven by the native promoter P_{mbx}, while the expression of *mbxJ-N* was under control of the constitutive promoter for the gene encoding the S-layer protein, P_{slp}.

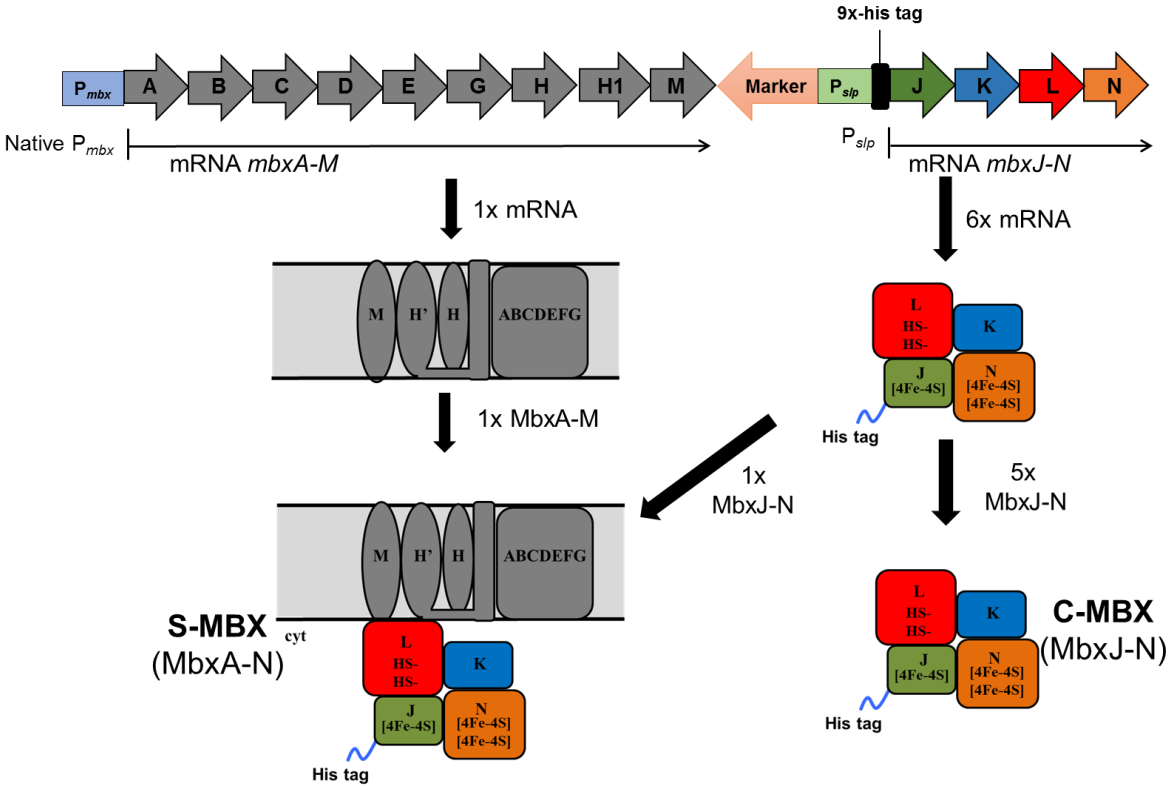
9x-his tag
P mbx
A
B
C
D
E
G
H
H1
M
Marker
P slp
J
K
L
N
Native P mbx
mRNA mbxA-M
P slp
mRNA mbxJ-N
1x mRNA
6x mRNA
M
H'
H
ABCDEFG
L
HS-
HS-
K
J
[4Fe-4S]
N
[4Fe-4S]
[4Fe-4S]
His tag
1x MbxA-M
1x
MbxJ-N
5x
MbxJ-N
S-MBX
cyt
(MbxA-N)
C-MBX
(MbxJ-N)

Figure 3.3

SDS-PAGE of purified S-MBX and C-MBX and the MBX model. The assigned subunits were also confirmed by either MALDI-TOF or LC-MS/MS.

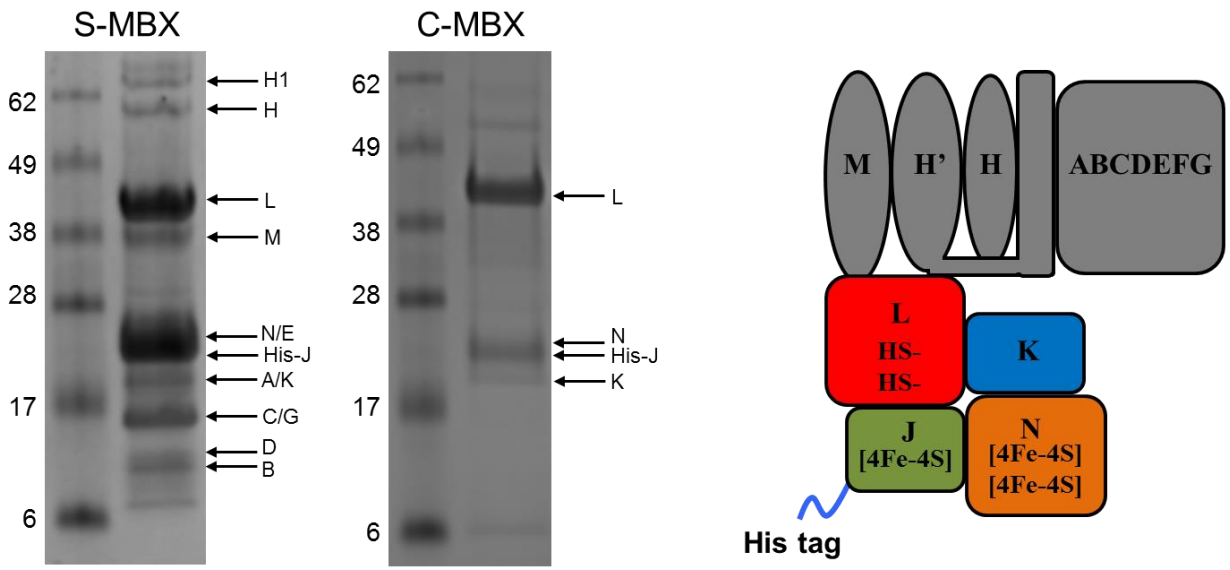
S-MBX
C-MBX
62
49
38
28
17
6
H1
H
L
M
N/E
His-J
A/K
C/G
D
B
L
N
His-J
K
M
H'
H
ABCDEFG
L
HS-
HS-
K
J
[4Fe-4S]
N
[4Fe-4S]
[4Fe-4S]
His tag

Figure 3.4

Growth on S° of the *P. furiosus* ΔMbxL strain lacking the catalytic subunit of MBX and of strains complemented with the wild-type version of MbxL (MbxL-WT) or a mutant in which two conserved cysteinyl residues are mutated (MbxL-C85A/C385A). The panels show growth measured by cell protein (A) and H_2S production (B). The error bars represent the standard deviation from biological triplicate samples.

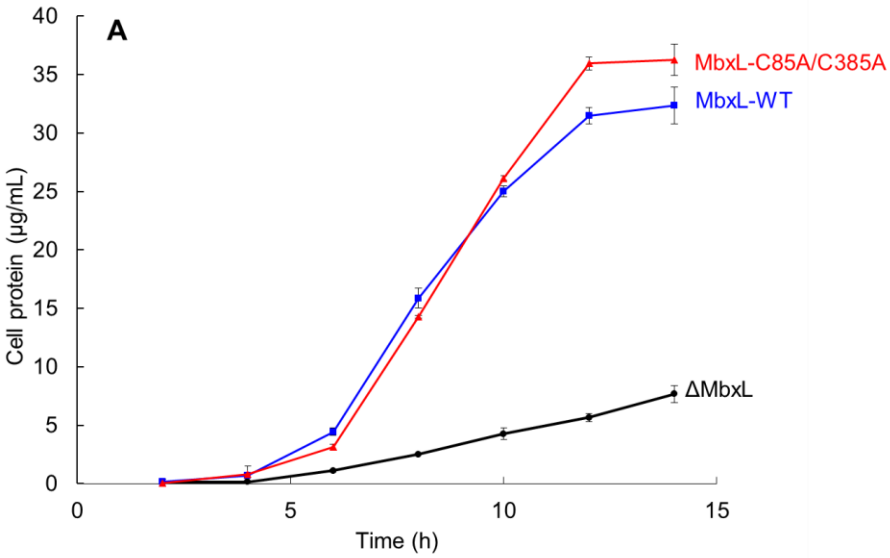
A
Cell protein (µg/mL)
Time (h)
MbxL-C85A/C385A
MbxL-WT
ΔMbxL
0
5
10
15
20
25
30
35
40

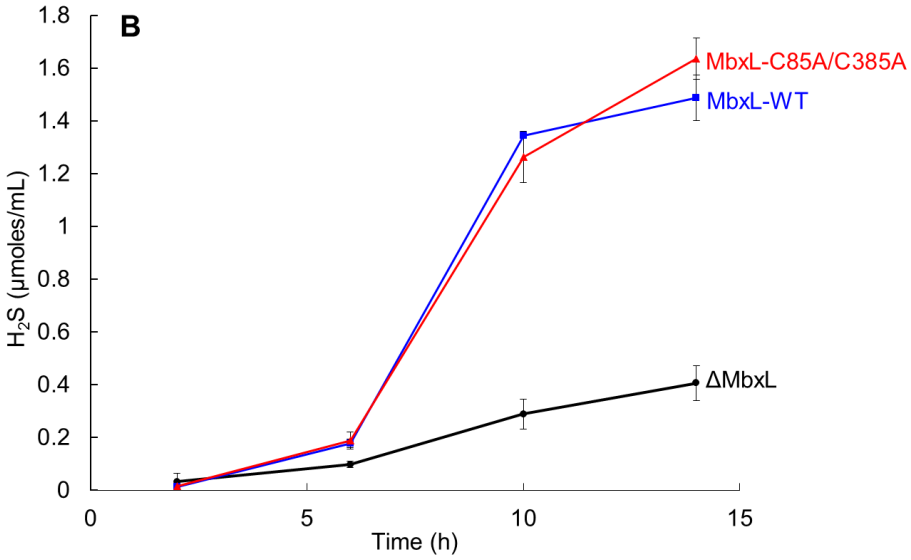
B
H2S (µmoles/mL)
Time (h)
MbxL-C85A/C385A
MbxL-WT
ΔMbxL
0
0.2
0.4
0.6
0.8
1
1.2
1.4
1.6
1.8
5
10
15

Figure 3.5

The proposed model for the respiration of *P. furiosus* in the presence and absence of S° and the role of MBS (MBX). Reduced ferredoxin, Fd_{red}

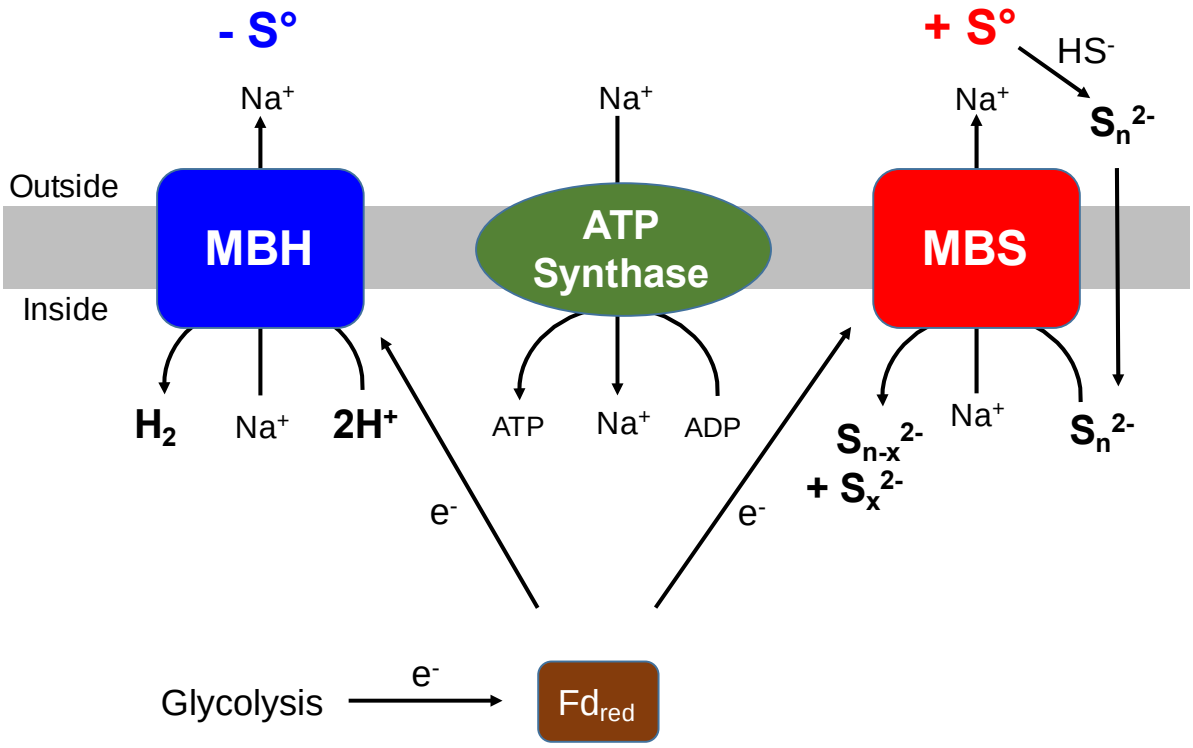
- S°
+ S°
HS-
Na+
Na+
Na+
Sn2-
Outside
MBH
ATP Synthase
MBS
Inside
H2
Na+
2H+
ATP
Na+
ADP
Sn-x2-
+ Sx2-
Na+
Sn2-
e-
e-
Glycolysis
e-
Fdred

Table S3.1. Strains used and constructed in this study

Trivial Name	**Strain Name**	**Description**	**Ref.**
COM1	MW0002	Δ*pyrF*	(41)
MbxJ-His	MW0491	Δ*pyrF*::P_{gdh} *pyrF* P_{slp} 9x His *mbxJ*	This study
ΔMbxL	MW0011	Δ*pyrF* Δ*mbxL*	(9)
MbxL-WT	MW0567	Δ*pyrF* Δ*mbxL*::P_{gdh} *pyrF* P_{slp} 9x His *mbxJ-N*	This study
MbxL-C85A/C385A	MW0572	Δ*pyrF* Δ*mbxL*::P_{gdh} *pyrF* P_{slp} 9x His *mbxJ-N* (MbxL$^{C85A/C385A}$)	This study

Figure S3.1

qPCR analysis of the expression of the *mbx* genes in the MbxJ-His strain. The expression level of each gene was normalized by using *por*γ (PF0971) as a reference gene. The error bars represent standard deviations obtained using biological duplicate samples.

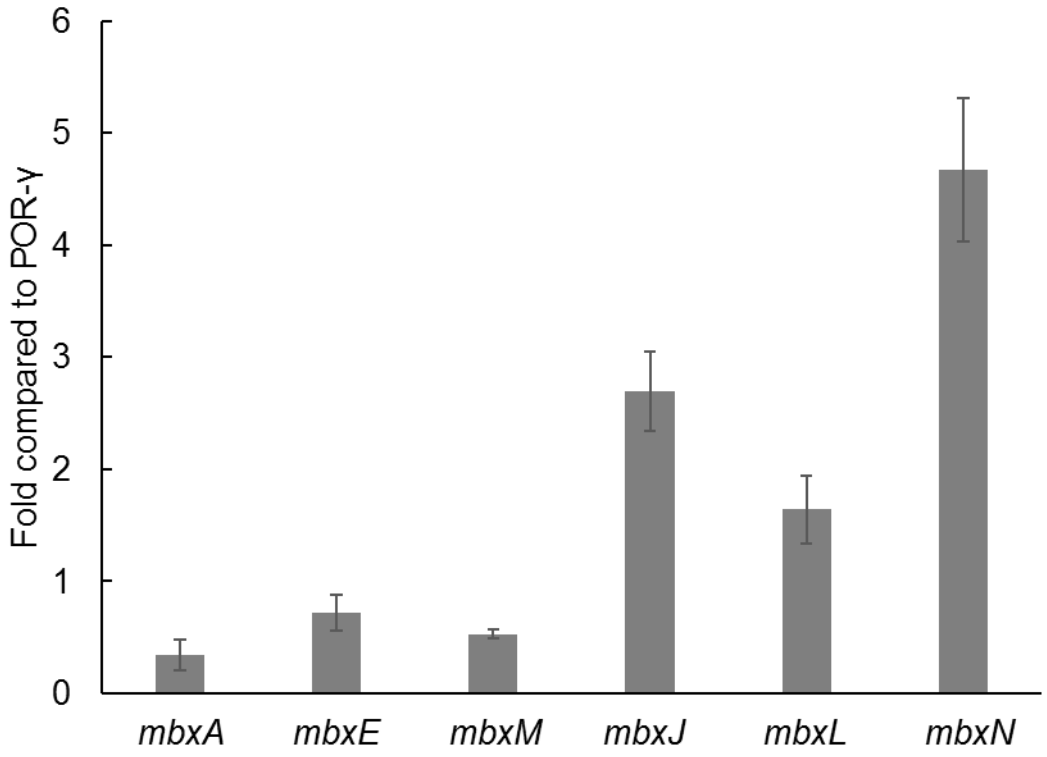
Fold compared to POR-γ
6
5
4
3
2
1
0
mbxA
mbxE
mbxM
mbxJ
mbxL
mbxN

Figure S3.2

Identification of methanethiol (CH_3SH) and methyl hydrogen disulfide (MHD) by MS. The schemes at the top show the expected products after their reaction with DTNB.

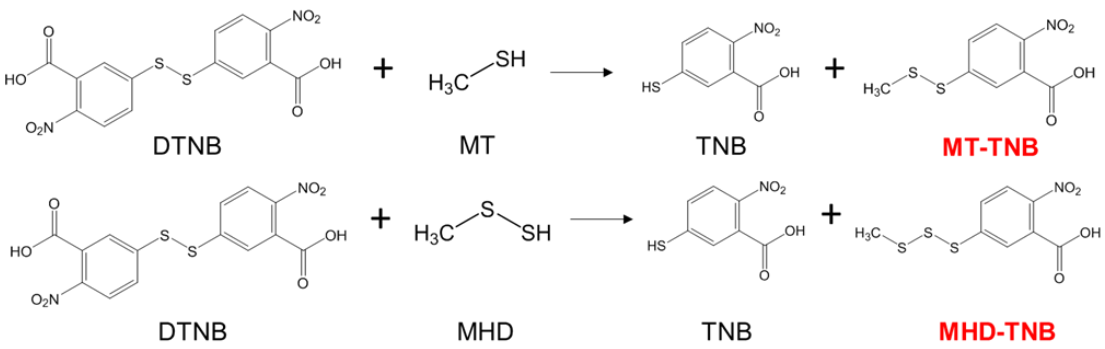
DTNB
MT
TNB
MT-TNB
DTNB
MHD
TNB
MHD-TNB

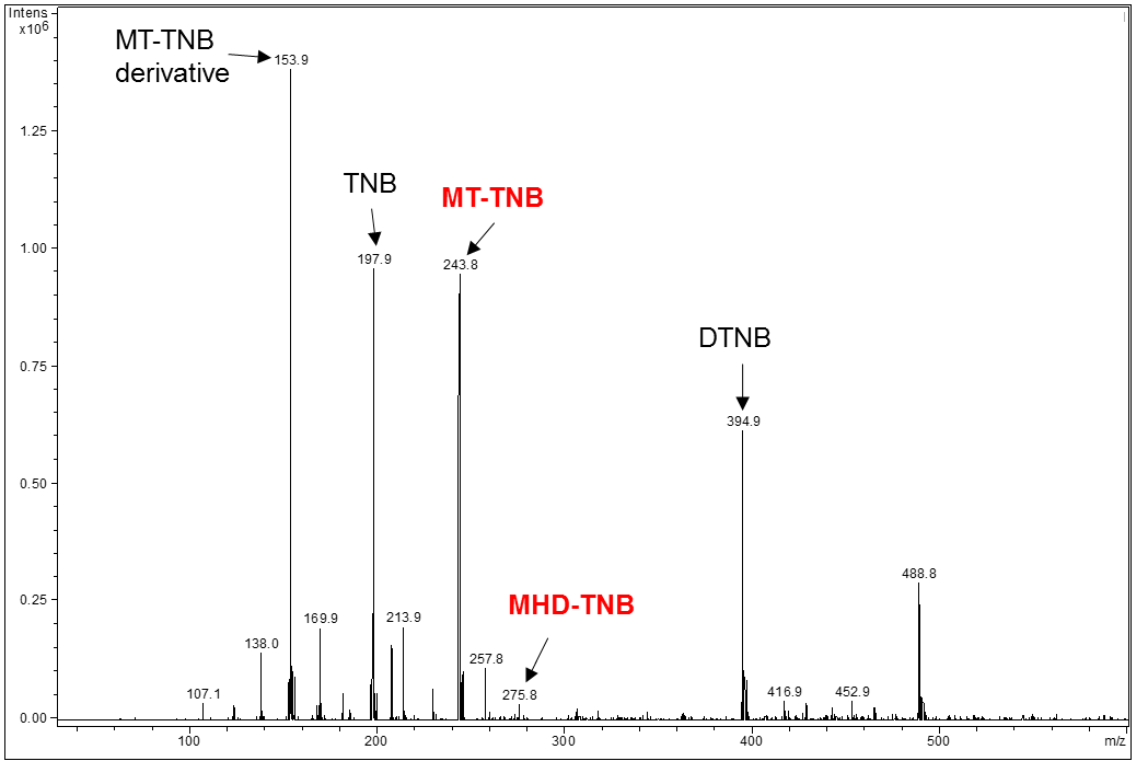
Intens
x10^6
MT-TNB
derivative
153.9
TNB
197.9
MT-TNB
243.8
DTNB
394.9
MHD-TNB
275.8
488.8
169.9
213.9
138.0
257.8
107.1
416.9
452.9
1.25
1.00
0.75
0.50
0.25
0.00
100
200
300
400
500
m/z

Figure S3.3

Temperature-dependent activities of S-MBX and C-MBX in the MV-linked DMTS reduction assay. S-MBX is shown by the closed circles and C-MBX is shown by the closed squares. The error bars represent the standard deviation from biological triplicate samples.

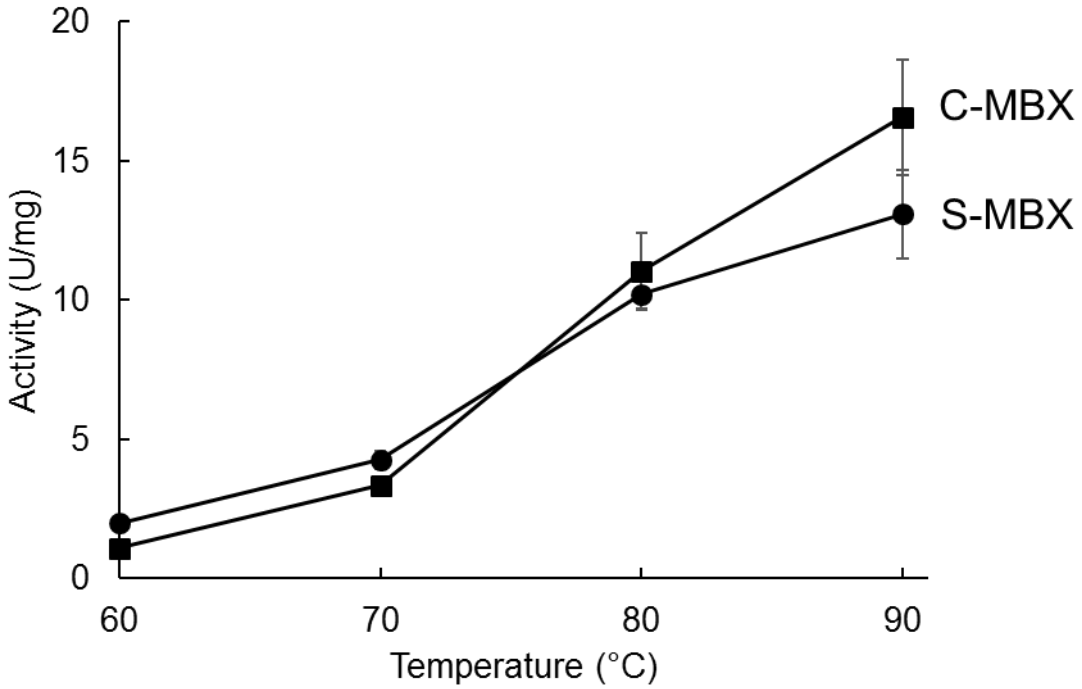
20
15
10
5
0
Activity (U/mg)
60
70
80
90
Temperature (°C)
C-MBX
S-MBX

Figure S3.4

Sequence alignment of MbhL and MbxL using Clustal Omega. Residues highlighted in red are involved in the proposed path of proton transfer from the bulk solvent to the catalytic NiFe site in MBH and are not present in MbxL (MbsL). Those highlighted in green are the four Cys residues that coordinate the NiFe cluster in MBH and two are conserved in MbxL (MbsL).

```
MbhL      --------------------MKKVEYWVKIPFGPIHPGLEEPEKFIITLDGERIVNVDVK      40
MbxL      MVSQEELIREARQNGMELYPIDKD--TYELFFGPQHMATE-NFSIILKMDGNRVVKAIAN      57
                           :.*     :: *** * . *   .:*:.:**:*:*:. .:

MbhL      LGYNLRGVQWIGMRRNYVQIMYLAERMCGICSFSHNHTYVRAVEEMAGIEVPERAEYIRV      100
MbxL      PGFLHRGFEKLAEYRPWYTNIALLLRICVPEPDVPEAIYSMAVDEIIGWEVPERAQWIRT      117
           *:  **.: :.  * :   : *  *:*       :  *  **:*: * ******::**.

MbhL      IVGELERIHSHLLNLGVVGHDIGYDTVLHLTWLARERVMDVLEAVSGNRVNYSMVTIGGV      160
MbxL      LVLEMARVTAYLFWIMGLSFKLGVYTAGQWAAAYRERFMALFEQLTGARVYHIYTIPGGV      177
          :* *: *: ::*: :  :...:*  *. : :   ***.* ::* ::* ** :  .  ***

MbhL      RRDIG-EKQKRLILDMIKYYREVLPQIEDVFLHDSTIEARLRDVAVVPKKLAIEMGAVGP      219
MbxL      RRDIPGDKWLRQVRDTVEYLKDKLKDFDNVLFENYITYKRLEGIGVMDKKFALEEGVTGP      237
          ****  :*  * : * ::* :: * ::::*::.:     **..:.*: **:*:* *..**

MbhL      TARGSGIKEDSRWSEQLGVYPDLGIKPVTPEDVTGEKARGDVYDRMAVRIGELWMSLDLL      279
MbxL      NLRATGVAYDVRKSDPYLLYPELDFEIPVL-------KEGDALARVLVRRYELEQDLYII      290
          . *.:*:  * * *:   :**:*.::  .         .**.  *: **  **  .* ::

MbhL      EHALDQMPEGKIKTFPKDNILVAKLKLLGDGEGIGRYEAPRGELVHYVRGQKGRDGPVRW      339
MbxL      EQLLDMGPPSGPYKVQDPKLKNLPRFKVPPGEAFAHVEATKGDFGAYVVSDGG-HKPYRV      349
          *: **  * .   .. . ::       :  **.:.: ** :*::  ** .: * . * *

MbhL      KPREPTFPN-LFTIAKALEGNELADLVVAIASIDPCLSCTDRVAIVKEGKKVVLTEKDLL      398
MbxL      HIRGPSIAHGVRVLEQLLVGARLADVPAILMSLDNCPPDIDR------------------      391
          : * *:: : : .: : * * .***: . : *:* *    **

MbhL      KLSIEKTKEINPNVKGDPTPTGIGCSRGV       427
MbxL      ----------------------------       391
```

Figure S3.5

Sequence alignment of MbhM and MbxM using Clustal Omega. The highlighted residues represent a string of glutamates proposed to be involved in energy transduction in MBH. Only two of these eight residues are conserved in MbxM (MbsM).

```
MbhM      MKIVYGVIGLILIYIYVSVVSLLFSGIDRKLVARMQRRIGPPILQPFYDFLKLMSKETII      60
MbxM      --MIGVFLRALLIIIYATFVGFIFMGIIRKVTARIHRRIGPPIYQPIIDTLKFFGKKENI      58
            ::  .:  :** **.:.*.::* ** **:.**::******* **: * **::.*:  *

MbhM      PKTANFMFKAAPILMLATVIALLAYTPLGFPPIFGTKGDIIVFIYLLTLADFFLVVGVMS      120
MbxM      THGLIY--DFGIIYAVGATILALMFIPLGPISVLRAYGDLILVTFLLEIPMLGIMFAAMS      116
           :   :  . . *  :.:.*  * : ***   :: : **:*:. :** :  : ::...**

MbhM      SGSPYGRIGAARGIALLVSREPAMMLGVFAVMWAISKLGVEKPFSLSSLYEHTIWDFGPV      180
MbxM      SGNPYAGIGAQRALLTLLAIQVPLGLAIIAVAE---YYGTFSTYEIVMAQQKMGWSIFHL      173
          **.**. *** *.:  *:: :  : *.::**       *. . :.:    ::  *.:  :

MbhM      AWVAGVVLIYVFMAWLASEIEVGFFNIPEAEQEIAEGTLVEYSGRYLGIIKLAESIKEFI      240
MbxM      PLLLAA---IAYDIVLQAMFGKEPFDIMIAPGEISLGPMVEFGGKHMGMLQIQHAMALFA      230
            : ..    .:   * : :    *:*  *  **: * :**:.*:::*:::: .::  *

MbhM      AASLVVAVLFPWQLNIPGVQGYLINLLLHTLKVFIVLL-------VSKTIFRTITGRLKI      293
MbxM      ETLFFSNIFLG-----GGVVTAFGSPLLNTLASLAVLLVKQIAVLLIAIFVGAIFPRFTI      285
           : :.  :::       **   : . **:**  : ***       :   :. :*  *:.*

MbhM      SQAVNLLWTRVFTASVIGALLLALGVML321
MbxM      DQAAKFYWKWPTIIAAIGAIMASL----309
          .**.:: *.     :.***:: :*
```

Figure S3.6

Scheme depicting the construction of strain MbxJ-His (MW0491). The knock-in cassette has homologous regions shown as the upstream flanking region (UFR) and downstream flanking region (DFR). The marker cassette is indicated as P_{gdh}-*pyrF* and the promoter is shown as P_{slp}. A 9x-histidine-tag was placed at the N-terminus of *mbxJ*. The corresponding homologous loci of the UFR and DFR in the parent strain COM1 are *mbxJ* and *mbxM*. The arrangement of the region after recombination is also shown.

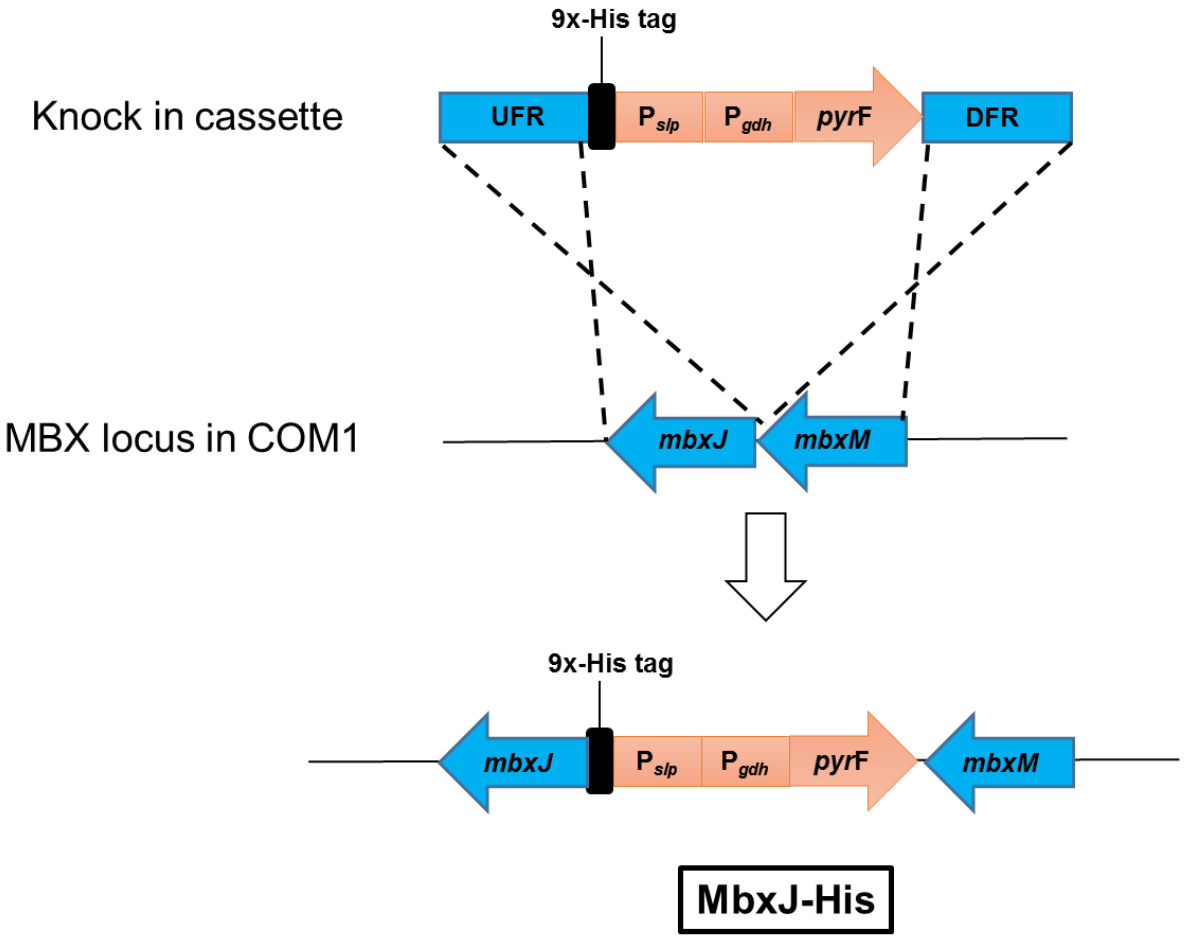
Knock in cassette
9x-His tag
UFR
P_{slp}
P_{gdh}
pyrF
DFR
MBX locus in COM1
mbxJ
mbxM
9x-His tag
mbxJ
P_{slp}
P_{gdh}
pyrF
mbxM
MbxJ-His

Figure S3.7

Scheme depicting the construction of strain MbxL-C85A/C385A (MW0572). The knock-in cassette has homologous regions shown as the upstream flanking region (UFR) and downstream flanking region (DFR). The marker cassette is indicated as P_{gdh}-*pyrF*, and the promoter is shown as P_{slp}. A 9x-histidine-tag was placed at the N-terminus of *mbxJ*. C85A and C385A mutations were constructed in *mbxL*. The corresponding homologous loci of the UFR and DFR in the parent strain ΔMbxL (MW0011) are in the intergenic region between PF0265 and PF0266. The arrangement of the intergenic region after recombination is also shown.

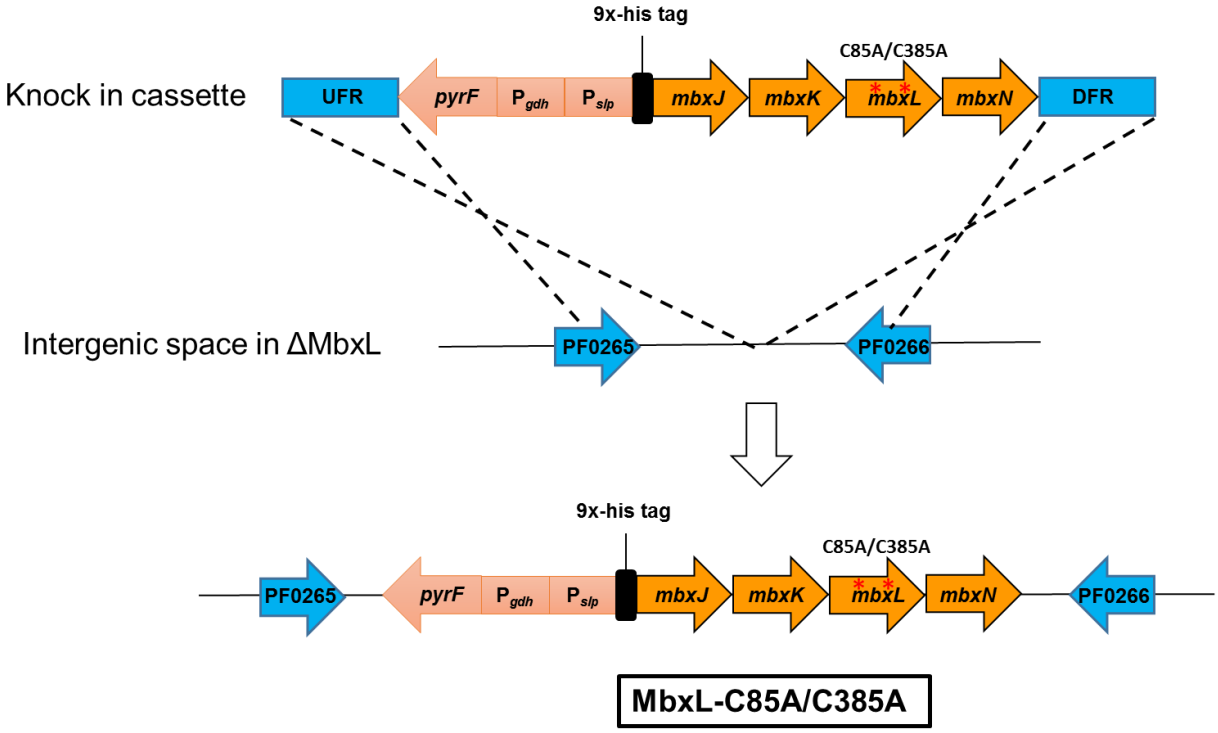
9x-his tag
C85A/C385A
Knock in cassette
UFR
pyrF
P gdh
P slp
mbxJ
mbxK
mbxL
mbxN
DFR
Intergenic space in ΔMbxL
PF0265
PF0266
9x-his tag
C85A/C385A
PF0265
pyrF
P gdh
P slp
mbxJ
mbxK
mbxL
mbxN
PF0266
MbxL-C85A/C385A

CHAPTER 4

A NEW MECHANISM OF ARSENIC RESISTANCE EVIDENT FROM THE HETEROLOGOUS EXPRESSION OF A RESPIRATORY ARSENATE REDUCTASE IN *PYROCOCCUS FURIOSUS*

Wu CH, Poole FL, Haja DK, Adams MWW. Submitted to *Appl. Environ. Microbiol.*

Abstract

Arsenate is a notorious toxicant that is known to disrupt multiple biochemical pathways. Many microorganisms have developed mechanisms to detoxify arsenate using the ArsC-type arsenate reductase and some even use arsenate as a terminal electron acceptor for respiration involving the arsenate respiratory reductase (Arr). ArsC-type reductases have been studied extensively but the phylogenetically-unrelated Arr system is less investigated and has not been characterized from Archaea. Herein, we heterologously-expressed the genes encoding Arr from the crenarchaeon *Pyrobaculum aerophilum* in the euryarchaeon *Pyrococcus furiosus*, both of which grow optimally near 100°C. Recombinant *P. furiosus* was grown on molybdenum (Mo)- or tungsten (W)-containing media and two types of recombinant Arr enzymes were purified, one containing Mo (Arr-Mo) and one containing W (Arr-W). Purified Arr-Mo had a 140-fold higher specific activity in arsenate (AsV) reduction than Arr-W and Arr-Mo also reduced arsenite (AsIII). The *P. furiosus* strain expressing Arr-Mo (the Arr strain) was able to use arsenate as a terminal electron acceptor during growth on peptides. In addition, the Arr strain had increased tolerance compared to the parent strain to arsenate and also, surprisingly, to arsenite. Compared to the parent, the Arr strain accumulated intracellularly almost an order of magnitude more arsenic when cells were grown in the presence of arsenite. The results suggest that the Arr strain of *P. furiosus* has a new Arr-dependent mechanism of detoxifying arsenite in which it is converted to a less toxic, low molecular weight compound that has yet to be characterized.

Importance

Arsenate respiratory reductases (Arr) are much less characterized than the detoxifying arsenate reductase system. The heterologous expression and characterization of an Arr from *Pyrobaculum aerophilum* in *Pyrococcus furiosus* provides a new insight into the function of this enzyme. From *in vivo* studies, production of Arr not only enabled *P. furiosus* to use arsenate (AsV) as a terminal electron acceptor, it also provided the organism with a higher resistance to arsenate and also, surprisingly, to arsenite (AsIII), by a novel and as yet uncharacterized mechanism that led to the accumulation of high intracellular concentrations of arsenic. In contrast to the tungsten-containing oxidoreductase enzymes natively produced by *P. furiosus*, recombinant *Pb. aerophilum* Arr was much more active with molybdenum than it was with tungsten.

Introduction

Arsenic is a well-known toxicant. The biologically-relevant oxidized pentavalent form, arsenate (AsV), replaces phosphate in many biochemical pathways due to the similarity in their structures and properties, while the reduced form, trivalent arsenite (AsIII), readily interacts with thiol-containing molecules such as cysteine (1). Microorganisms have developed systems to protect them against arsenic toxicity and to survive in natural environments where arsenic compounds are prevalent (2). Two distinct types of arsenate reductases are known, the cytoplasmic ArsC-type and the membrane-bound Arr-type, both of which reduce arsenate to arsenite (3).

The ArsC-type has been studied extensively in bacteria in which it functions in detoxification. The enzyme is encoded by an arsenic resistance (*ars*) operon that contains *arsR*, *arsD*, *arsA* and *arsB,* as well as *arsC* (4). ArsR functions as a repressor of the operon (5, 6) while ArsD is an inducer (7). ArsC is a pyranopterin-containing enzyme with a bound molybdenum that reduces arsenate to arsenite using glutathione as the electron donor. Arsenite is then transported out of the cell by the arsenite transporter ArsB, which is energized by either a proton motive force or by the ArsA ATPase (4). In contrast to ArsC, the Arr system enables arsenate to be used as a terminal electron acceptor of a respiratory chain. The enzyme consists of ArrA, the catalytic subunit that a contains pyranopterin cofactor and an iron sulfur cluster, and ArrB, which also contains iron-sulfur clusters. Compared to ArsC, the Arr-type of arsenate reductase is much less studied. Three ArrAB have been purified from bacteria but none have been characterized from archaea (8-10), which, as descrirbed below, appear to contain a different type of Arr.

The crenarchaeon *Pyrobaculum aerophilum* grows optimally at 100 °C using arsenate, as well as several other compounds, such as oxygen, nitrate and thiosulfate, as a terminal electron acceptor (11, 12). Based on transcriptional analyses in response to these respiratory substrates, the

genes PAE1263-1265 were predicted to encode an arsenate respiratory reductase (Arr). Their expression increased up to eight-fold when arsenate was supplied in the growth medium (12, 13). Although the *Pb. aerophilum* Arr operon was not detected using degenerate PCR primers to bacterial Arr genes, the catalytic domain of bacterial Arr is conserved in *arrA* (PAE1265) (14). A model of *Pb. aerophilum* Arr based on the sequence analysis is shown in Figure 4.1. ArrA is the catalytic subunit containing a pyranopterin-binding site and a [4Fe-4S] cluster, while ArrB harbors three [4Fe-4S] clusters. In further contrast to characterized bacterial Arr, which are heterodimers, the enzyme from *Pb. aerophilum* contains a third subunit, ArrC, which is predicted to be a membrane bound anchor for ArrAB. ArrC is thought to oxidize quinol and transport the electrons to ArrA through the iron-sulfur clusters in ArrB (15). In contrast to this archaeal system, bacteria that respire arsenate, such as *Shewanella* species, do not have a gene encoding ArrC but contain the membrane-bound MKH_2-oxidizing protein CymA, which does not show any sequence similarity to ArrC. CymA has been shown by mutational studies to be crucial for arsenate reduction by *Shewanella* although it has not been biochemically characterized (16).

Since a genetic system is not available for *Pb. aerophilum,* we used the euyarchaeon *Pyrococcus furiosus* to heterologously produce its Arr with an affinity tag to facilitate purification. *P. furiosus* is a strict anaerobe that also grows optimally near 100 °C (17) but unlike *Pb. aerophilum,* it grows only by fermenting carbohydrates or peptides. S° is essential as a terminal electron acceptor when cells are grown solely on peptides while H_2 rather than H_2S is produced during growth on sugars in the absence of S° (18). The production of both H_2 and H_2S involve homologous respiratory complexes that use reduced ferredoxin (Fd) as the electron donor (19). *P. furiosus* has a well-developed genetic system and genes from other euryarcheota have been

heterologously-expressed that enable the organism to oxidize formate and carbon monoxide and produce H_2 (20, 21).

The use of *P. furiosus* as an expression system also raises the issue of which metal it would insert into the recombinant Arr. The three bacterial ArsC enzymes contain molybdenum (8-10), indeed, almost all life forms have one or more pyranopterin enzymes that all contain molybdenum (22). However, *P. furiosus* is very unusual in that expresses five pyranopterin-containing oxidoreductases that instead contain tungsten (23), a chemically-analogous metal (22). *P. furiosus* does not produce active molybdoenzymes (24) and it has been proposed that in general hyperthermophilic microbes growing near the boiling point are predisposed to use tungsten rather than molybdenum as the metal in their pyranopterin enzymes (22). Hence, a key question was, does *P. furiosus* insert tungsten or molybdenum into *Pb. aerophilum* Arr and, if both can be purified, which is the most active form?

To gain a deeper understanding of the biochemical properties of an archaeal Arr, we therefore heterologously-expressed the *arr* operon (PAE1263-1265) from *Pb. aerophilum* in *P. furiosus*. The recombinant Arr enzyme was purified from *P. furiosus* cells grown on media with added molybdenum or tungsten and the recombinant enzymes were affinity purified and characterized. The response of *P. furiosus* with and without expressing the *Pb. aerophilum* Arr genes to growth in the presence of arsenate (AsV) and arsenite (AsIII) was also investigated.

Results

Recombinant Pb. aerophilum Arr produced in P. furiosus

The *P. furiosus* strain expressing the *Pb. aerophilum* Arr genes will be referred to as the Arr strain. It was constructed using the parent strain COM1 by homologous recombination of the

knock-in cassette containing PAE1263-1265 into the intergenic space between PF0265 and PF0266, as shown in Figure S4.1. Initially a strain was constructed containing a sequence encoding a 9x-His-affinity tag at the N-terminus of ArrA, but we were unable to purify the Arr enzyme using a Ni-NTA column. A second strain was therefore constructed (MW0548) with the His-tag at the C-terminus of ArrA, and this enabled affinity purification of the recombinant Arr protein as described below. The expression of *arrA* (PAE1265), driven by the consecutive promoter P_{slp}, in the Arr strain was confirmed by qPCR analysis, where the level of expression was similar to that of pyruvate oxidoreductase (γ subunit, data not shown), an abundant enzyme involved in fermentation.

The *P. furiosus* Arr strain was initially grown in a medium containing both 10 μM W and 10 μM Mo, and the arsenate (AsV) reduction activity using reduced methyl viologen as the artificial electron donor was measured in the cell-free extract. As shown in Figure S4.2, no significant activity was observed in the parent strain (Par). To investigate if all three subunits were present as an intact complex in the Arr strain, the arsenate reduction assay was carried out using the cytoplasmic and membrane fractions, as shown in Figure S4.3. Unexpectedly, 80% of the activity was found in the cytoplasmic extract and ArrC not could be identified by LC-MS/MS in the active Arr-containing fractions purified from either the cytoplasmic or membrane fraction (see Figure 4.1). qPCR analysis indicated that its gene was transcribed at the expected level, suggesting that a stable ArrC subunit is not produced in the Arr strain.

Characterization of recombinant Arr containing Mo or W

The catalytic subunit ArrA is predicted to contain a pyranopterin cofactor. To investigate whether the active enzyme contained molybdenum or tungsten bound to the pyranopterin site, the

Arr strain was grown under two different conditions: 1) a so-called Mo condition in which 10 μM Mo but no W were added to the growth medium, and 2) a W condition, in which 10 μM W but no Mo were added. Cells (25 g wet wt.) grown under the Mo or W condition were used for the affinity purification of Arr and the results are summarized in Tables 1 and 2, respectively. With both cell types, after two chromatography steps (Ni-NTA and hydrophobic interaction), each enzyme was purified more than 1,400-fold with at least a 60% yield of activity. Surprisingly, we were able to purify active forms of the enzyme from both cell types but the Mo-containing enzyme (Arr-Mo) had more than a 140-fold higher arsenate reduction activity than the W-containing enzyme (Arr-W). Metal analysis revealed that the Mo to W ratio in these enzymes was 9.4:1 and 1:86, respectively, and kinetic analysis showed that Arr-W had a 20-fold higher affinity for arsenate compared to Arr-Mo (Table 3). The arsenite (AsIII) reduction activity and ferredoxin-linked arsenate (AsV) reduction activities (using the ferredoxin from *P. furiosus* in place of methyl viologen) were also measured for Arr-Mo and the activities were more than 100-fold lower than the arsenate (AsV) reduction activity using the artificial mediator (Table 3). Arr from *Alkalilimnicola ehrlichii* and *Shewanella* sp. strain ANA-3 were reported to exhibit arsenite (AsIII) oxidation activity (25). However, we were unable to measure arsenite oxidation activity with Arr-Mo using the high potential dye dichlorophenolindophenol as the electron acceptor. Because of the much higher arsenate reduction activity of Arr-Mo compared to Arr-W, the Mo growth condition was used to carry out the following *in vivo* experiments.

Arsenate (AsV) serves as a terminal electron acceptor for the Arr strain

P. furiosus shows significant growth on peptides only in the presence of S°, which is reduced to hydrogen sulfide. S° serves as a terminal electron acceptor with a reduction potential

(E_0' ~ -280 mV) higher than the hydrogen (E_0' = -420 mV) (18). The *P. furiosus* Arr strain (grown with Mo) was examined for the ability to use arsenate (E_0' = 60 mV) as a terminal acceptor to support peptide metabolism. The experiment was performed using a growth medium containing only peptides as the carbon source, and the Arr strain grew as well as the parent in the presence of S° (Figure 4.2a). However, the Arr strain showed increased growth on peptides (by more than 50%, measured by cell protein) compared to the parent strain when 10 mM arsenate was present, although a long lag phase (30 hr) was observed before there was an effect. Stimulation of growth by arsenate was highly reproducible with the Arr strain, although under such conditions the strain did not reach the growth attained in the presence of S° (Figure 4.2a). These data suggested that the Arr strain was able to reduce arsenate (AsV) to arsenite (AsIII) to support growth. However, the parent strain also reduced arsenate to arsenite, as shown by the increase in the concentration of arsenite in growth medium, although the Arr strain produced slightly more arsenite than the parent (Figure 4.2b). Accordingly, as shown in Figure 4.2c, in the presence of arsenate, both the Par and Arr strains produced much less hydrogen gas during growth if arsenate was present. These results therefore suggest that *P. furiosus* can non-specifically reduce arsenate, and that the presence of Arr allows arsenate to stimulate growth, an effect not seen with the parent strain.

Arsenic toxicity

As shown in Figure 4.3a, the growth of *P. furiosus* by sugar (maltose) fermentation was strongly inhibited by the presence of 10 mM arsenate but the Arr strain was more resistant than the parent strain. Note that such inhibition of the parent strain was not observed during growth on peptides, presumably because there was minimal growth and the effect was not significant enough to be observed. As shown in Figure 4.3a, the maximum growth of the parent was about half that

of the Arr strain, although both strains exhibited a long lag phase compared to the control in the absence of arsenate (AsV). In addition, arsenite (AsIII) was detected in the growth medium of arsenate-inhibited cells. However, although the Arr strain generated slightly more (approximately 0.6 mM) than the parent strain (approximately 0.5 mM), arsenite production was largely abiotic since a similar concentration was measured using the *P. furiosus* growth medium in the absence of cells (Figure 4.3b).

These data raised the issue of which species, arsenate or arsenite, was responsible for the growth inhibition. As shown in Figure 4.4, arsenite is a much more powerful inhibitor of growth than arsenate, and surprisingly, the Arr enzyme system once more confered high resistance. For example, in the presence of 1.0 mM arsenite, the growth of the parent was completely inhibited while that of the Arr strain decreased by about 30% (in terms of total cellular protein) although there was a significant lag phase. With 0.5 mM arsenite, the parent strain had a growth phenotype similar to that observed in the presence of 10 mM arsenate, and maximum growth was approximately half that of the Arr strain (Figure 4.4). These data therefore suggest that *P. furiosus* is inhibited not by arsenate (using 10 mM, Figure 4.3a) but by the arsenite (using 0.5 – 1.0 mM, Figure 4.4) that is generated abiotically (~ 0.5 mM, Figure 4.3b) and Arr confers resistance to arsenite rather than to arsenate.

Higher intracellular arsenic concentrations in the Arr strain

The intracellular arsenic concentration was determined in the parent and Arr strains when grown in the presence of 0.5 mM arsenite. As shown in Figure 4.5, the arsenic concentration in the cell-free extract of the Arr strain was almost an order of magnitude higher than that of the parent strain. A similar result was observed in the presence of 0.1 mM arsenite, where no lag phase

was found before reaching stationary phase in the parent (data not shown). This suggests that the higher concentration of intracellular arsenic in the Arr strain might be due to the presence of the Arr enzyme. To investigate this, the cytoplasmic extract of the Arr strain grown with 0.5 mM arsenite was applied to a desalting column and the distribution of arsenic was determined. As shown in Figure S4.5, most of arsenic was recovered in the low molecular weight fractions (< 5 kDa) suggesting that the majority of the arsenic in the cell is not asscoiated with proteins.

Discussion

Herein we heterologously-expressed in *P. furiosus* an archaeal arsenate respiratory reductase (Arr) from *Pb. aerophilum.* The enzyme was affinity purified and is a heterodimer (ArrAB) although it is predicted to contain a third and membrane-bound subunit (ArrC). Even though the *arrC* gene was transcribed as expected, most of the Arr activity was in the cytoplasmic extract rather than in the membranes (Figure S4.3) and ArrC was not detected by mass spectrometry in the purified enzyme. This is probably because *Pb. aerophilum* uses a Twin-Arginine Translocation (TAT) system for membrane transport and *arrC* has a TAT signal motif for translocation to the periplasmic side of the membrane (12). However, *P. furiosus* does not contain the TAT export system (31) and in its absence ArrC appears to be unstable and disassociates from ArrAB.

Although both Arr-Mo and Arr-W are active in reducing arsenate (AsV), the Mo form is about 100-fold more active, suggesting that the native enzyme contains molybdenum rather than tungsten. Nitrate reductase is the only other pyranopterin-containing enzyme that has been characterized previously from *Pb. aerophilum* and in that case the Mo-from was twice as active as the W-form (32). In contrast, five pyranopterin-containing enzymes have been purified and

characterized from *P. furiosus* and all contain tungsten. They all oxidize aldehydes of various types and are known as formaldehyde ferredoxin oxidoreductase (FOR) (33), aldehyde ferredoxin oxidoreductase (AOR) (34), glyceraldehyde-3-phosphate:ferredoxin oxidoreductase (GAPOR) (35), tungsten-containing oxidoreductase 4 (WOR4) (36) and tungsten-containing oxidoreductase 5 (WOR5) (23). It appears that the only W-containing forms of these enzymes are active since Mo-containing FOR and WOR5 have been characterized and their activities correlated with the residual W content (24). *P. furiosus* is therefore remarkably specific in terms of discriminating against molybdenum and inserts only tungsten into its five oxidoreductases. It was therefore somewhat surprising that the organism efficiently incorporated molybdenum into *Pb. aerophilum* Arr. In fact, this is the first active Mo-containing enzyme to be purified from *P. furiosus.* The low catalytic activity of the W-containing form could be due to the residual Mo that is present, although this seems unlikely since Arr-W had a 20-fold higher affinity for arsenate compared to Arr-Mo, which would be consistent with different metals in the catalytic site.

The Mo-form of Arr was extremely active *in vitro* in reducing arsenate with reduced methyl viologen and exhibited significant activity with reduced ferredoxin as the electron donor (Table 3). We assume that ferredoxin was also an electron donor *in vivo* and enabled *P. furiosus* to exhibit significant growth on peptides using arsenate as the electron donor compared to the parent strain (Figure 4.2a). The production of less H_2 also supported the diversion of reducuing equilvalents for arsenate reduction (Figure 4.2c). Interestingly, we also observed a similar result for the parent strain in H_2 production but, in contrast to the Arr strain, there was no stimulation of growth in the presence of arsenate. This lack of growth may be due to the toxicity of parent strain, but not the Arr strain, to the arsenite (AsIII) that is generated abiotically after 30 hours. As discussed below,

the physiological effects of heterologously-expressed Arr appear to be related to removing arsenite rather than arsenate.

Purified Arr-Mo had significant arsenite reduction activity (methyl viologen-linked, Table 3) and we hypothesize that this is responsible for the Arr strain of *P. furiosus* being much more resistant to both arsenate (10 mM AsV, Figure 4.3a), which generates ~ 0.5 mM arsenite abiotically (Figure 4.3b), and arsenite (1.0 mM AsIII, Figure 4.4) compared to the parent strain. If so, then this is a novel mechanism of arsenite resistance. For example, in arsenate-resistant bacteria, arsenate (AsV) enters cells via phosphate transporters and is reduced by ArsC to arsenite (AsIII). The arsenite is then extruded to the outside of the cell by an energy-dependent ArsAB transporter (37). In arsenite resistance, arsenite enters cells through aquaglyceroporins (38) and an arsenite methyltransferase (ArsM) is involved in the process of detoxification, where arsenite is methylated to volatile compounds, monomethylarsonic acid (MMA), dimethylarsine (DMA) and trimethylarsine (TMA), that leave cells (39). A homolog of ArsC was annotated in *P. furiosus* genome but the parent cells did not contain detectable arsenate reductase activity indicating that it is not involved in the resistance to arsenate in the parent strain (37) and there is no ArsM homolog in the *P. furiosus* genome. Hence, the arsenite-reduction activity of Arr likely explains the resistance of the *P. furiosus* Arr strain to both arsenate and to arsenite. Arsenite is reduced by Arr to a less toxic compound that accumulates intracellularly (Figure 4.5) as a low molecular weight species that is not associated with proteins. The recombinant *P. furiosus* strain therefore has a new mechanism of arsenite (and arsenate) resistance whereby the reduced arsenic species generated by Arr-Mo is a non-volatile compound that is retained inside the cell. Studies are underway to identify this compound and to determine if arsenic also accumulates in *Pb. aerophilum* when exposed to arsenate and arsenite.

Materials and Methods

Strain construction

A genetically tractable *Pyrococcus furiosus* strain, COM1, was used for the heterologous expression of the arsenate respiratory reductase (Arr) from *Pyrobaculum aerophilum* (40). A knock-in cassette, containing the fragments shown in Figure S4.1, was assembled using overlapping PCR (41). The upstream flanking region (UFR), the promoter of the gene encoding the S-layer protein (P_{slp} of PF1399), and the downstream flanking region (DFR), were amplified from *P. furiosus* genomic DNA, and the selection marker (P_{gdh}-*pyrF*), was amplified from pGLW021 (40). PAE1263-PAE1265 were amplified using *Pb. aerophilum* genomic DNA as the template. A 9x-His-tag was placed at the C-terminus of PAE1265 and the ribosomal binding sites (RBS) of *P. furiosus* pyruvate oxidoreductase γ subunit (PORγ, PF0971) and S-layer protein were placed at upstream of *arrC* (PAE1264) and *arrA* (PAE1265), respectively. The genomic DNA of *P. furiosus* and *Pb. aerophilum* was isolated by ZymoBead Genomic DNA Kit (Zymo Research). The *Pb. aerophilum* strain was purchased from DSMZ (DSMZ-7523) and medium 611 was used for cultivation. The transformants were grown as previously described (40). Genomic DNA was also used for PCR screening using GXL polymerase (Takara, ClonTech). The PCR screening was performed using a pair of primers outside the UFR and DFR. The PCR confirmed colony was sequence verified using the Genewiz service.

Growth condition

The *P. furiosus* strains constructed and used in this study are listed in Table 4. The growth medium was used as previously described with some modifications (40). The inoculum was first transferred in the medium containing no exogenous Mo or W for ten generations before being used

in the experiments. All media contained 1x base salt, 1x trace minerals without molybdenum, 2 g/L yeast extract, 5 g/L maltose, 0.17 g/L cysteine, 1 g/L sodium bicarbonate, 1 mM potassium phosphate (pH 6.8) and 1 mM MOPS buffer (pH 6.8). Molybdenum or tungstate (to a final concentration of 10 μM) and sodium arsenate (10 mM) or sodium arsenite (0.5 and 1.0 mM) were added as indicated. For the growth study with peptides, the medium contained 1x base salt, 1x trace minerals without molybdenum, 0.1 g/L yeast extract, 5 g/L casein, 0.17 g/L cysteine, 1 g/L sodium bicarbonate, 1 mM potassium phosphate (pH 6.8), 1 mM MOPS buffer (pH 6.8), 10 μM molybdenum and 10 mM sodium arsenate. The medium for the 20 L fermentations contained 1x base salt, 1 x trace minerals without molybdenum, 5 g/L yeast extract, 5 g/L maltose, 5 g/L casein, 1 g/L cysteine and 1 mM potassium phosphate (pH 6.8) with 10 μM molybdenum or tungstate supplied where indicated. The 20 L fermentations were carried out as previously described (42) and the harvested cells were frozen in liquid nitrogen and store at -80 °C. For growth studies, 1 mL cultures were harvested by centrifugation at 14,000 xg for 5 min. The cells were lysed osmotically using 1 mL distilled H_2O and cell debris was removed by centrifugation at 14,000 xg for 1 min. The supernatant was taken for protein estimation using Protein Assay Reagent (Bio-Rad).

Purification of Arr

All purification steps were performed under anaerobic conditions. Frozen cells were lysed osmotically in 25 mM sodium phosphate, pH 7.5, containing 1 mM DTT and 50 μg/mL DNase I (5 mL per gram of frozen cells) for 1 hour at room temperature in an anaerobic chamber (Coy, Grass Lake, MI). The cell-free extract was centrifuged at 100,000 xg for 1 hour using a Beckman-Coulter Optima L-90K ultracentrifuge. The supernatant was collected and applied to a 5 mL His-

Trap FF Ni-NTA column (GE Healthcare) using a NGC Chromatography System (Bio-Rad). The column was equilibrated with 25 mM sodium phosphate, pH 7.5, containing 300 mM NaCl and 1 mM DTT (Buffer A) before loading the sample and 2% Buffer B (Buffer A containing 500 mM imidazole) was loaded with the cytoplasmic extract. The column was washed with Buffer A, and the bound protein was eluted with a 20-column volume gradient from 0 to 100% Buffer B. Active fractions containing MV-linked arsenate reduction were pooled and applied to an equilibrated 1 mL phenyl HP column (GE Healthcare) while diluting 5-fold with 50 mM sodium phosphate, pH 7.0, containing 1.5 M ammonium sulfate. A 30-column volume gradient from 20 to 100% 50 mM sodium phosphate, pH 7.0, was used to elute the bound protein.

Enzyme assays

All assays were carried out anaerobically at 80°C. The routine arsenate (AsV) reduction assay was carried out anaerobically using sealed cuvettes that contained 2 mL 100 mM 3-(N-morpholino) propanesulfonic acid (MOPS), pH 7.5, 150 mM NaCl, 5 mM sodium arsenate and 1 mM methyl viologen (MV). The assay cuvettes were pre-heated to 80°C. 0.1 mM Titanium citrate was added to reduce MV, and the activity was measured by monitoring the decrease in absorbance at 600 nm using a 100 Cary UV-Vis spectrophotometer with a peltier-based temperature controller from Agilent technologies (Santa Clara). The reaction was started with the addition of the enyzme. An extinction coefficient of 8.25 mM^{-1} cm^{-1} was used for reduced MV. One unit of activity is defined as 1 µmol of substrate reduced per minute. The arsenite (AsIII) reduction assay was performed similarly with 5 mM sodium arsenite, which was purified using HPLC as described below, as the substrate. For arsenite oxidation activity, 1 mM dichlorophenolindophenol (DCPIP) was used to measure the activity in the presence of 5 mM sodium arsenite. For *Pf* ferredoxin (Fd)-

dependent arsenate reduction activity, Fd was reduced using titanium citrate and the oxidation of Fd was monitored at 425 nm (ϵ = 13 mM^{-1} cm^{-1}).

Metal concentration determination

The concentrations of arsenic in spent media and the concentrations of Mo and W in purified proteins were measured using an octopole-based ICP-MS (7500ce; Agilent Technologies). Arsenite (AsIII) concentration was measured using HPLC for speciation followed by ICP-MS for concentration determination. A Zorbax SAX column (Agilent Technologies) was used in the speciation with a mobile phase of 60 mM KH_2PO_4 and a flow rate of 1 mL/min.

Intracellular arsenic concentration determination

Cultures grown with 5g/L maltose, 2g/L yeast extract and 0.5 mM sodium arsenite were centrifuged at 5,000 xg for 1 min to remove insoluble materials. The cells were washed three times with 1x *P. furiosus* base salt medium. Washed cells were lysed osmotically with 50 mM Tris-HCl, pH 8.0, containing 50 μg/mL DNase I (5 mL per gram of wet cells) for 1 hour at room temperature in an anaerobic chamber. Cell debris was removed by centrifugation at 14,000 xg for 10 min. The supernatant was collected and the arsenic concentration was determined by ICP-MS. To estimate the size of the arsenic species in the cytoplasmic extract, the Arr strain was grown with 0.5 mM sodium arsenite ande prepared as described above. After a 1-hour lysis, the cell-free extract was centrifuged at 100,000 xg for 1 hour, and the supernatant was applied to a 5 mL HiTrap Desalting Column (GE Healthcare) that was equilibrated with 50 mM Tris-HCl, pH 8.0. ICP-MS was used to measure the arsenic concentration.

Other methods

Hydrogen was measured in the headspace for growth studies with the 6850 Network GC system from Agilent Technologies. Purified ArrAB was analyzed by SDS-PAGE using precast Criterion TGX (4-15%) gels (Bio-Rad). MALDI-TOF and LC-MS/MS were performed by the PAMS Facility at the University of Georgia.

Acknowledgments

This work was supported by a grant (DE-FG05-95ER20175 to MWA) from the Division of Chemical Sciences, Geosciences and Biosciences, Office of Basic Energy Sciences of the Department of Energy. We thank the Proteomics and Mass Spectrometry Core Facility at the University of Georgia for MALDI-TOF and LC-MS/MS analyses.

References

1. Hughes MF. 2002. Arsenic toxicity and potential mechanisms of action. Toxicol Lett 133:1-16.
2. Lebrun E, Brugna M, Baymann F, Muller D, Lievremont D, Lett MC, Nitschke W. 2003. Arsenite oxidase, an ancient bioenergetic enzyme. Mol Biol Evol 20:686-93.
3. Silver S, Phung LT. 2005. Genes and enzymes involved in bacterial oxidation and reduction of inorganic arsenic. Appl Environ Microbiol 71:599-608.
4. Rosen BP. 2002. Biochemistry of arsenic detoxification. FEBS Lett 529:86-92.
5. Silver S, Phung LT. 1996. Bacterial heavy metal resistance: new surprises. Annu Rev Microbiol 50:753-89.
6. Cai J, DuBow MS. 1996. Expression of the *Escherichia coli* chromosomal ars operon. Can J Microbiol 42:662-71.
7. Wu J, Rosen BP. 1993. The arsD gene encodes a second trans-acting regulatory protein of the plasmid-encoded arsenical resistance operon. Mol Microbiol 8:615-23.
8. Afkar E, Lisak J, Saltikov C, Basu P, Oremland RS, Stolz JF. 2003. The respiratory arsenate reductase from *Bacillus selenitireducens* strain MLS10. FEMS Microbiol Lett 226:107-12.
9. Malasarn D, Keeffe JR, Newman DK. 2008. Characterization of the arsenate respiratory reductase from *Shewanella sp*. strain ANA-3. J Bacteriol 190:135-42.
10. Krafft T, Macy JM. 1998. Purification and characterization of the respiratory arsenate reductase of *Chrysiogenes arsenatis*. Eur J Biochem 255:647-53.

11. Volkl P, Huber R, Drobner E, Rachel R, Burggraf S, Trincone A, Stetter KO. 1993. *Pyrobaculum aerophilum* sp. nov., a novel nitrate-reducing hyperthermophilic archaeum. Appl Environ Microbiol 59:2918-26.

12. Cozen AE, Weirauch MT, Pollard KS, Bernick DL, Stuart JM, Lowe TM. 2009. Transcriptional map of respiratory versatility in the hyperthermophilic crenarchaeon *Pyrobaculum aerophilum*. J Bacteriol 191:782-94.

13. Fitz-Gibbon ST, Ladner H, Kim UJ, Stetter KO, Simon MI, Miller JH. 2002. Genome sequence of the hyperthermophilic crenarchaeon *Pyrobaculum aerophilum*. Proc Natl Acad Sci U S A 99:984-9.

14. Duval S, Ducluzeau AL, Nitschke W, Schoepp-Cothenet B. 2008. Enzyme phylogenies as markers for the oxidation state of the environment: the case of respiratory arsenate reductase and related enzymes. BMC Evol Biol 8:206.

15. van Lis R, Nitschke W, Duval S, Schoepp-Cothenet B. 2013. Arsenics as bioenergetic substrates. Biochim Biophys Acta, Bioenerg 1827:176-188.

16. Murphy JN, Saltikov CW. 2007. The cymA gene, encoding a tetraheme c-type cytochrome, is required for arsenate respiration in *Shewanella* species. J Bacteriol 189:2283-2290.

17. Fiala G, Stetter KO. 1986. *Pyrococcus furiosus* sp nov represents a novel genus of marine heterotrophic archaebacteria growing optimally at 100°C. Arch Microbiol 145:56-61.

18. Adams MW, Holden JF, Menon AL, Schut GJ, Grunden AM, Hou C, Hutchins AM, Jenney FE, Jr., Kim C, Ma K, Pan G, Roy R, Sapra R, Story SV, Verhagen MF. 2001. Key role for sulfur in peptide metabolism and in regulation of three hydrogenases in the hyperthermophilic archaeon *Pyrococcus furiosus*. J Bacteriol 183:716-24.

19. Schut GJ, Boyd ES, Peters JW, Adams MWW. 2013. The modular respiratory complexes involved in hydrogen and sulfur metabolism by heterotrophic hyperthermophilic archaea and their evolutionary implications. FEMS Microbiol Rev 37:182-203.

20. Lipscomb GL, Schut GJ, Thorgersen MP, Nixon WJ, Kelly RM, Adams MW. 2014. Engineering hydrogen gas production from formate in a hyperthermophile by heterologous production of an 18-subunit membrane-bound complex. J Biol Chem 289:2873-9.

21. Schut GJ, Lipscomb GL, Nguyen DM, Kelly RM, Adams MW. 2016. Heterologous production of an energy-conserving carbon monoxide dehydrogenase complex in the hyperthermophile *Pyrococcus furiosus*. Front Microbiol 7:29.

22. Johnson MK, Rees DC, Adams MW. 1996. Tungstoenzymes. Chem Rev 96:2817-2840.

23. Bevers LE, Bol E, Hagedoorn PL, Hagen WR. 2005. WOR5, a novel tungsten-containing aldehyde oxidoreductase from *Pyrococcus furiosus* with a broad substrate Specificity. J Bacteriol 187:7056-61.

24. Sevcenco AM, Bevers LE, Pinkse MW, Krijger GC, Wolterbeek HT, Verhaert PD, Hagen WR, Hagedoorn PL. 2010. Molybdenum incorporation in tungsten aldehyde oxidoreductase enzymes from *Pyrococcus furiosus*. J Bacteriol 192:4143-52.

25. Richey C, Chovanec P, Hoeft SE, Oremland RS, Basu P, Stolz JF. 2009. Respiratory arsenate reductase as a bidirectional enzyme. Biochem Biophys Res Commun 382:298-302.

26. Hering JG, Chen PY, Wilkie JA, Elimelech M, Liang S. 1996. Arsenic removal by ferric chloride. J Am Water Works Assoc 88:155-167.

27. Chen HW, Frey MM, Clifford D, McNeill LS, Edwards M. 1999. Arsenic treatment considerations. J Am Water Works Assoc 91:74-85.

28. Baskan MB, Pala A. 2009. Determination of arsenic removal efficiency by ferric ions using response surface methodology. J Hazard Mater 166:796-801.

29. Dixit S, Hering JG. 2003. Comparison of arsenic(V) and arsenic(III) sorption onto iron oxide minerals: implications for arsenic mobility. Environ Sci Technol 37:4182-9.

30. Sekar N, Wu CH, Adams MWW, Ramanathan R. 2016. Exploring extracellular electron transfer in hyperthermophiles for electrochemical energy conversion. ECS Trans 72:1-7.

31. Dilks K, Rose RW, Hartmann E, Pohlschroder M. 2003. Prokaryotic utilization of the twin-arginine translocation pathway: a genomic survey. J Bacteriol 185:1478-83.

32. de Vries S, Momcilovic M, Strampraad MJ, Whitelegge JP, Baghai A, Schroder I. 2010. Adaptation to a high-tungsten environment: *Pyrobaculum aerophilum* contains an active tungsten nitrate reductase. Biochemistry 49:9911-21.

33. Roy R, Mukund S, Schut GJ, Dunn DM, Weiss R, Adams MW. 1999. Purification and molecular characterization of the tungsten-containing formaldehyde ferredoxin oxidoreductase from the hyperthermophilic archaeon *Pyrococcus furiosus*: the third of a putative five-member tungstoenzyme family. J Bacteriol 181:1171-80.

34. Mukund S, Adams MW. 1991. The novel tungsten-iron-sulfur protein of the hyperthermophilic archaebacterium, *Pyrococcus furiosus*, is an aldehyde ferredoxin oxidoreductase. Evidence for its participation in a unique glycolytic pathway. J Biol Chem 266:14208-16.

35. Mukund S, Adams MW. 1995. Glyceraldehyde-3-phosphate ferredoxin oxidoreductase, a novel tungsten-containing enzyme with a potential glycolytic role in the hyperthermophilic archaeon *Pyrococcus furiosus*. J Biol Chem 270:8389-92.

36. Roy R, Adams MW. 2002. Characterization of a fourth tungsten-containing enzyme from the hyperthermophilic archaeon *Pyrococcus furiosus*. J Bacteriol 184:6952-6.

37. Bini E. 2010. Archaeal transformation of metals in the environment. FEMS Microbiol Ecol 73:1-16.

38. Rosen BP, Tamas MJ. 2010. Arsenic transport in prokaryotes and eukaryotic microbes. Adv Exp Med Biol 679:47-55.

39. Qin J, Rosen BP, Zhang Y, Wang G, Franke S, Rensing C. 2006. Arsenic detoxification and evolution of trimethylarsine gas by a microbial arsenite S-adenosylmethionine methyltransferase. Proc Natl Acad Sci U S A 103:2075-80.

40. Lipscomb GL, Stirrett K, Schut GJ, Yang F, Jenney FE, Jr., Scott RA, Adams MW, Westpheling J. 2011. Natural competence in the hyperthermophilic archaeon *Pyrococcus furiosus* facilitates genetic manipulation: construction of markerless deletions of genes encoding the two cytoplasmic hydrogenases. Appl Environ Microbiol 77:2232-8.

41. Bryksin AV, Matsumura I. 2010. Overlap extension PCR cloning: a simple and reliable way to create recombinant plasmids. Biotechniques 48:463-5.

42. Chandrayan SK, McTernan PM, Hopkins RC, Sun J, Jenney FE, Jr., Adams MW. 2012. Engineering hyperthermophilic archaeon *Pyrococcus furiosus* to overproduce its cytoplasmic [NiFe]-hydrogenase. J Biol Chem 287:3257-64.

43. Thorgersen MP, Lipscomb GL, Schut GJ, Kelly RM, Adams MW. 2014. Deletion of acetyl-CoA synthetases I and II increases production of 3-hydroxypropionate by the metabolically-engineered hyperthermophile *Pyrococcus furiosus*. Metab Eng 22:83-8.

Table 4.1. Purification of Arr-Mo

Step	Total Units (μmol min^{-1})	Total Protein (mg)	Specific Activity (U/mg)	Yield (%)	Fold Purification
Cell-free extract	1,571	3,402	0.46	100	1
Cytoplasmic extract	1,236	2,319	0.53	79	1.1
Ni-NTA	1,221	4.45	274	78	596
Phenyl HP	1,027	1.07	960	65	2,087

Table 4.2. Purification of Arr-W

Step	Total Units (μmol min^{-1})	Total Protein (mg)	Specific Activity (U/mg)	Yield (%)	Fold Purification
Cell-free extract	20.9	3,465	0.006	100	1
Cytoplasmic extract	14.9	2,498	0.006	71	1
Ni-NTA	14.7	3.7	3.97	70	661
Phenyl HP	12.9	1.5	8.6	62	1,430

Table 4.3. Properties of Arr

Property	**Arr-Mo**	**Arr-W**
K_m (arsenate, μM)	340 ± 50	17.9 ± 2
V_{max} (U/mg)	1,833 ± 166	13.0 ± 2.0
Metal content (Mo:W)	9.4 : 1	1 : 86.1
Ferredoxin-linked arsenate (AsV) reduction (U/mg)	20.9 ± 1.7	N.D.
Arsenite (5 mM AsIII) reduction (U/mg)	6.79 ± 0.36	N.D.

N.D. Not determined

Table 4.4. Strains used and constructed in this study

Trivial Name	**Strain Name**	**Description**	**Ref.**
Par	COM1c	Δ*pyrF*::P_{gdh} *pyrF*	(43)
Arr	MW0548	Δ*pyrF*::P_{gdh} *pyrF* P_{slp} (PAE1263-PAE1265-9x His)	This study

Figure 4.1

SDS-PAGE of purified Arr and the proposed cofactor content of ArrABC based on sequence analysis. ArrA and ArrB were identified by MALDI-TOF from bands cut from the gel. ArrC was not identified in the purified protein and is shown with a dashed outline in the model.

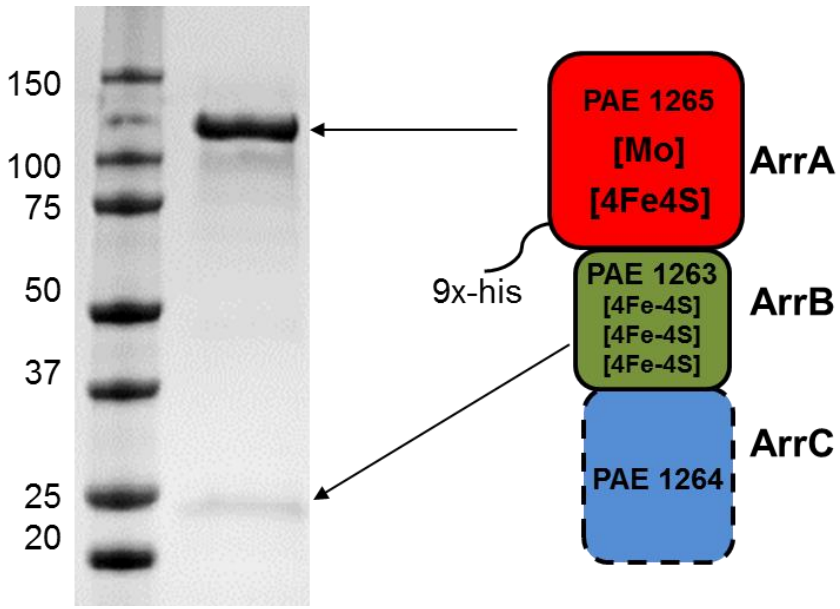
150
100
75
50
37
25
20
PAE 1265
[Mo]
[4Fe4S]
ArrA
9x-his
PAE 1263
[4Fe-4S]
[4Fe-4S]
[4Fe-4S]
ArrB
PAE 1264
ArrC

Figure 4.2

Growth of *P. furiosus* on peptides with and without arsenate (10 mM). a) The colors refer to: orange, the Arr strain with the addition of S° without arsenate; purple, Par with the addition of S° without arsenate; red, the Arr strain with the addition of arsenate; black, Par with the addition of arsenate; blue, Par without arsenate; green, the Arr strain without arsenate. b) Arsenite (AsIII) concentration in the spent media after the addition of 10 mM arsenate. Black line: Par; red line: the Arr strain. c) Hydrogen production normalized by protein concentration during the growth. The colors refer to: blue, Par; green, the Arr strain; black line, Par with the addition of arsenate; red, the Arr strain with the addition of arsenate. The error bars represent standard deviations obtained using biological triplicate samples.

a

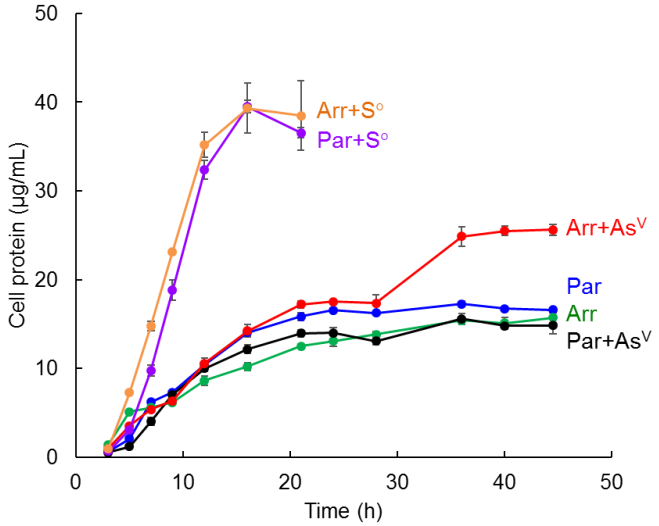
Cell protein (µg/mL)
Time (h)
Arr+S°
Par+S°
Arr+As^{V}
Par
Arr
Par+As^{V}

b

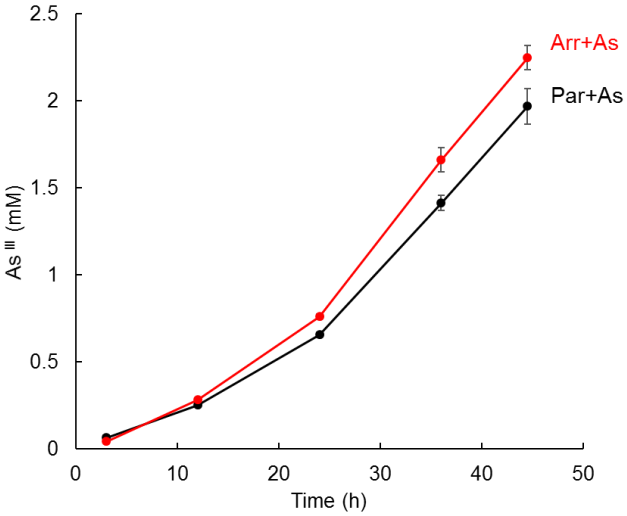
As^{III} (mM)
Time (h)
Arr+As
Par+As

c

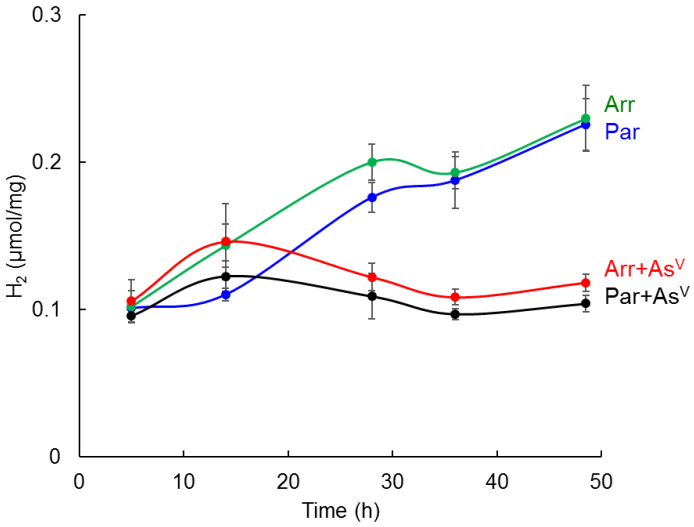
H_2 (µmol/mg)
Time (h)
Arr
Par
Arr+As^{V}
Par+As^{V}

Figure 4.3

Inhibition of *P. furiosus* growing on maltose by arsenate. a) The colors refer to: blue, Par; green, the Arr strain; black, Par with the addition of 10 mM arsenate; red, the Arr strain with the addition of 10 mM arsenate. b) Arsenite (AsIII) concentration in the spent media with the addition of 10 mM arsenate. Black line: Par; red line: the Arr strain; purple line: abiotic control without addition of innoculumn. The error bars represent standard deviations obtained using biological triplicate samples.

a

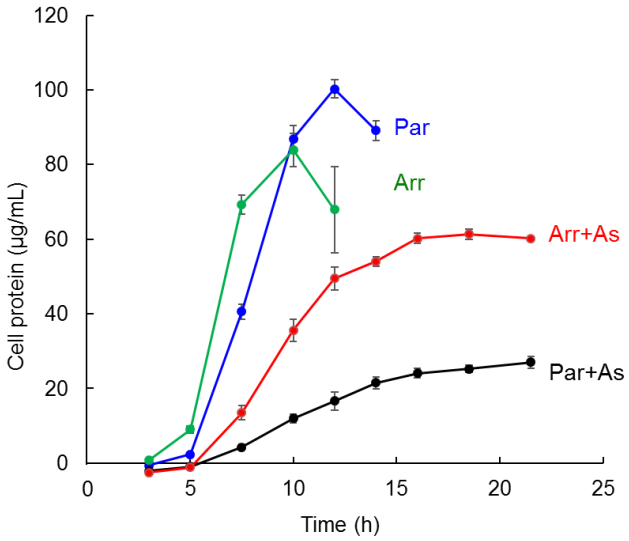
120
100
80
60
40
20
0
Cell protein (µg/mL)
0
5
10
15
20
25
Time (h)
Par
Arr
Arr+As
Par+As

b

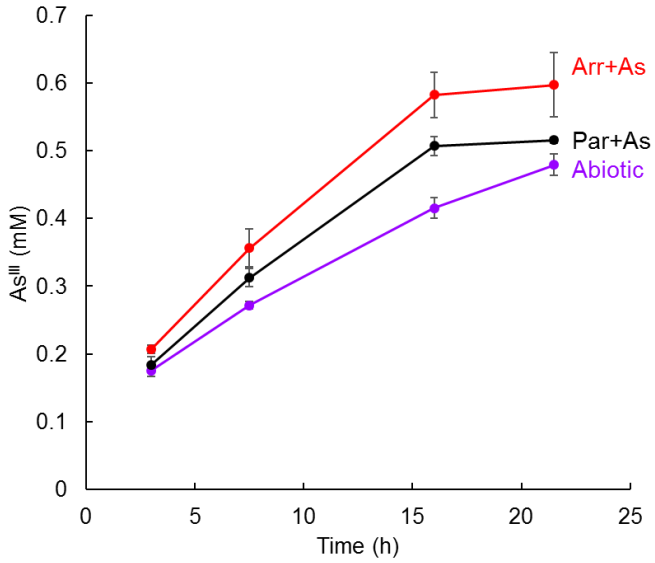
0.7
0.6
0.5
0.4
0.3
0.2
0.1
0
AsIII (mM)
0
5
10
15
20
25
Time (h)
Arr+As
Par+As
Abiotic

Figure 4.4

Inhibition of *P. furiosus* growing on maltose by arsenite (AsIII). Par and the Arr strain were grown on 5 g/L maltose in the presence of 0.5 mM or 1 mM arsenite. The error bars represent standard deviations obtained using biological triplicate samples.

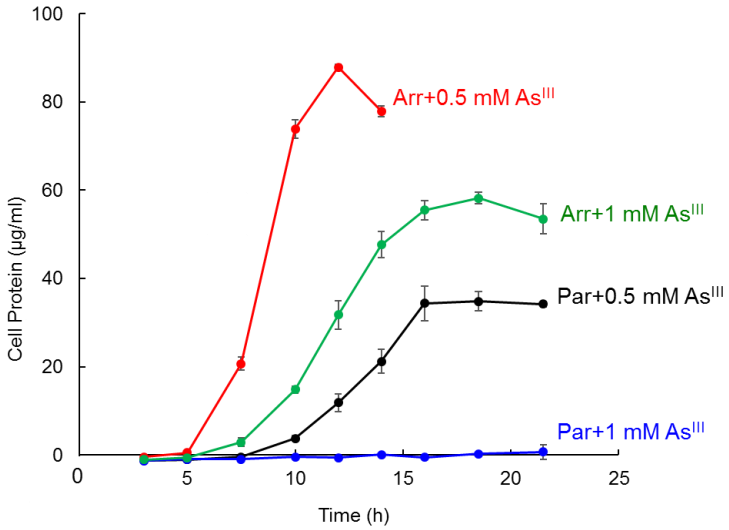
100
80
60
40
20
0
Cell Protein (µg/ml)
0
5
10
15
20
25
Time (h)
Arr+0.5 mM As^III
Arr+1 mM As^III
Par+0.5 mM As^III
Par+1 mM As^III

Figure 4.5

The intracellular arsenic concentrations in the parent and Arr strains grown on maltose with 0.5 mM arsenite (AsIII). The error bars represent standard deviations obtained using biological triplicate samples.

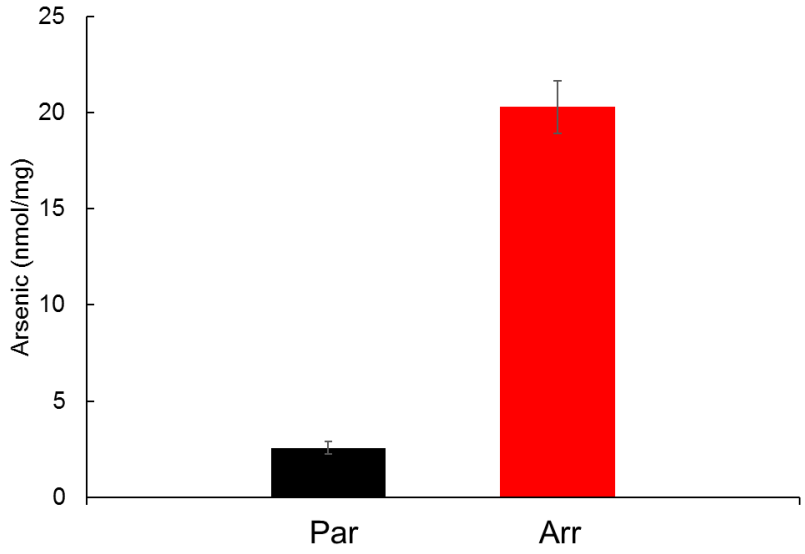
25
20
15
10
5
0
Arsenic (nmol/mg)
Par
Arr

Figure S4.1

Scheme for the construction of the Arr strain (MW0548). The knock-in cassette has homologous regions shown as the upstream flanking region (UFR) and downstream flanking region (DFR). The marker cassette is indicated as P_{gdh}-*pyrF*, and the promoter is indicated as P_{slp}. A 9x-his-tag was placed at the C-terminus of *arrA* (PAE1265). The ribosomal binding sites (RBS) of pyruvate oxidoreductase γ-subunit and the S-layer protein were placed upstream of *arrC* (PAE1264) and *arrA*, respectively. The corresponding homologous loci of the UFR and DFR in the parent strain COM1 are in the intergenic region between PF0265 and PF0266, which have minimal transcriptional activity (data not shown). The arrangement of the intergenic region after recombination is also shown.

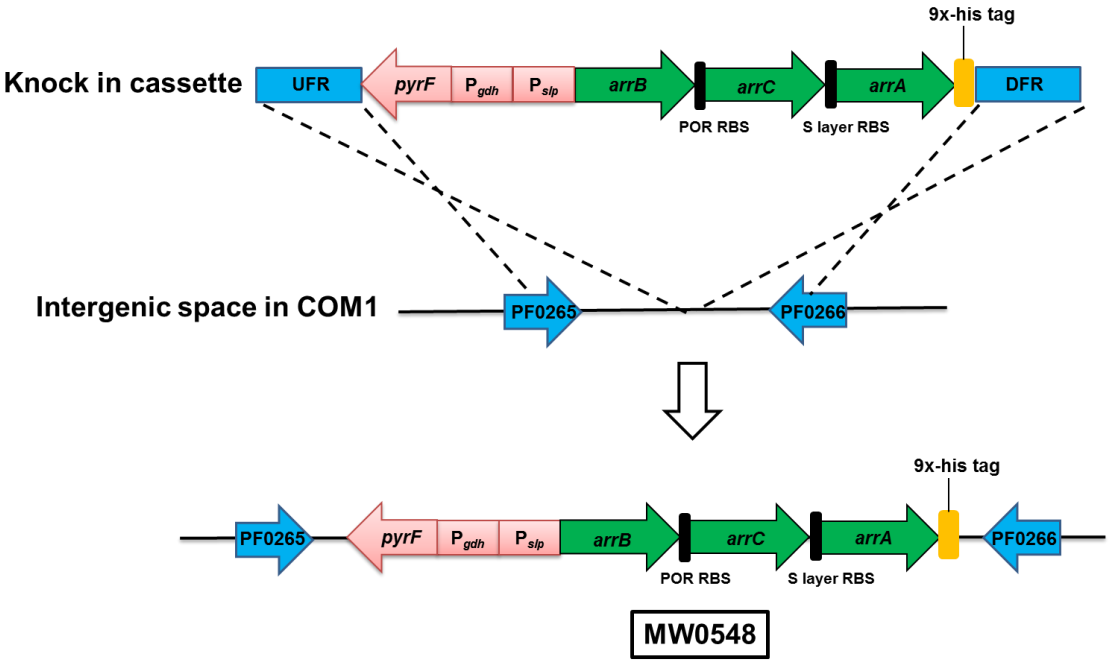
Knock in cassette
UFR
pyrF
P gdh
P slp
arrB
arrC
arrA
9x-his tag
DFR
POR RBS
S layer RBS
Intergenic space in COM1
PF0265
PF0266
PF0265
pyrF
P gdh
P slp
arrB
arrC
arrA
9x-his tag
PF0266
POR RBS
S layer RBS
MW0548

Figure S4.2

Arsenate reductase activity in the cell-free extracts of the Par and Arr strains grown in a medium containing 10 µM Mo and 10 µM W. The activity was measured by MV-linked arsenate (AsV) reduction. The activity measured for Par was below the detection limit (<0.001 U/mg).

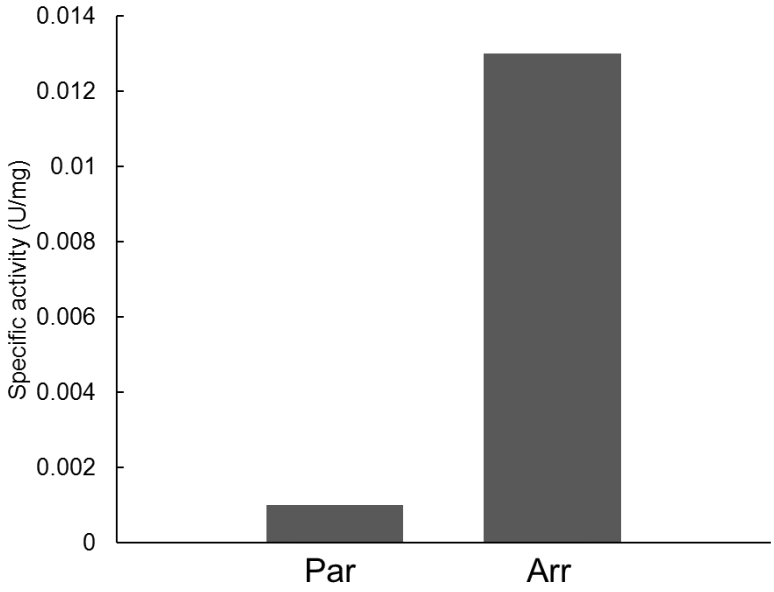
0.014
0.012
0.01
0.008
0.006
0.004
0.002
0
Specific activity (U/mg)
Par
Arr

Figure S4.3

Localization of arsenate reductase activity in the Arr strain. The activity was measured by MV-linked arsenate (AsV) reduction.

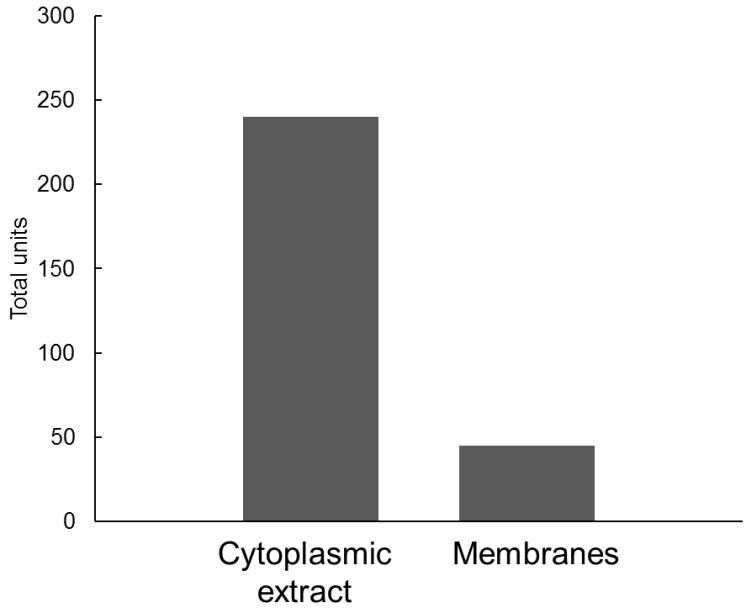
300
250
200
150
100
50
0
Total units
Cytoplasmic extract
Membranes

Figure S4.4

Molecular weight distribution of arsenic in the cytoplasmic extract of the Arr strain grown with 0.5 mM arsenite (AsIII). The elution from the desalting column was collected in fractions and the arsenic concentration was determined by ICP-MS (red line). The blue line represents the 280 nm absorbance.

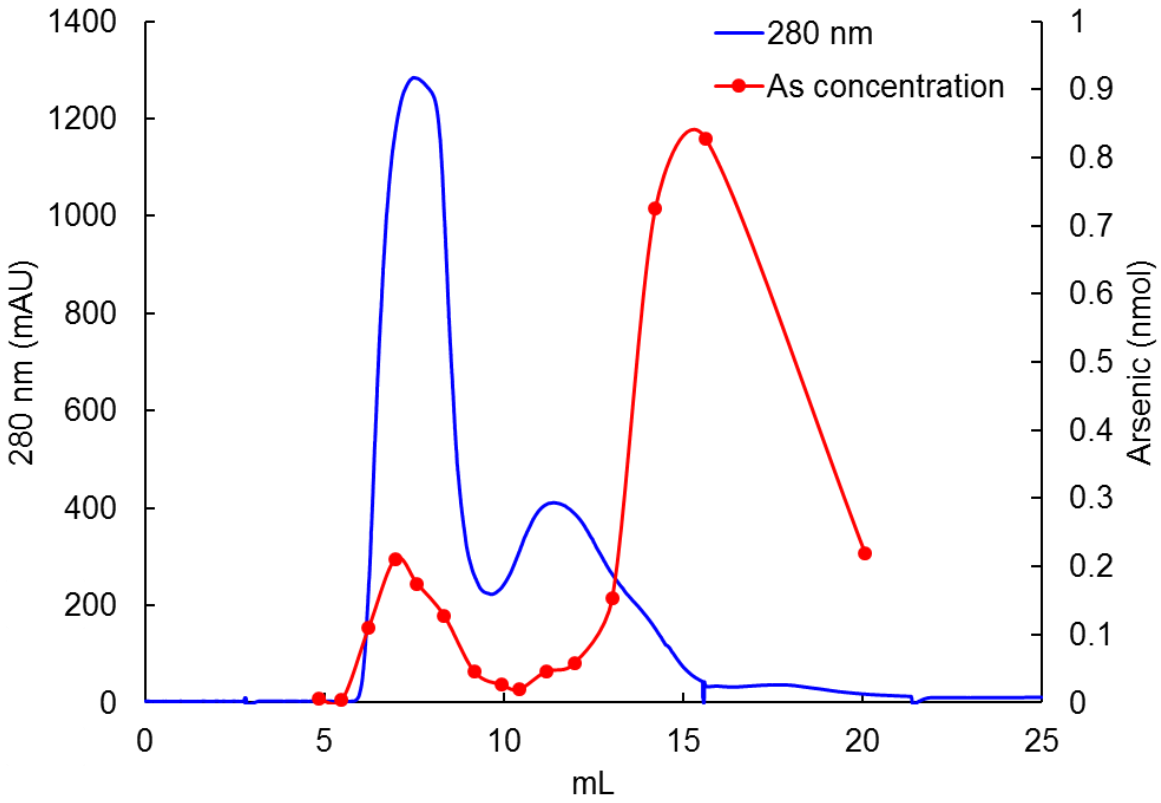
280 nm
As concentration
280 nm (mAU)
Arsenic (nmol)
mL
1400
1200
1000
800
600
400
200
0
1
0.9
0.8
0.7
0.6
0.5
0.4
0.3
0.2
0.1
0
0
5
10
15
20
25

CHAPTER 5

DISCUSSION AND CONCLUSIONS

Pyrococcus furiosus has been used as a platform for heterologous gene expression and metabolic engineering for the production of useful chemicals, such as ethanol (216), butanol (217) and 3-hydroxypropionate (218). In addition, the genes encoding the energy-conserving membrane-bound complexes, CO dehydrogenase and formate hydrogen lyase, from the related hyperthermophile *Thermococcus onnurineus*, have been expressed in *P. furiosus*, and the resulting strains had the ability to use CO or formate to generate H_2 (159, 219). Herein, we demonstrate that *P. furiosus* can also be used as a platform for the large-scale production of hyperthermophilic enzymes, such as SHI. SHI has been utilized in several applications, including NADPH and H_2 production. Among these, an *in vitro* synthetic H_2-production pathway is one of the most promising methods for clean H_2 production. In the laboratory scale of this pathway, 2 mg of purified SHI was used in a 1 mL reaction mixture (220). In order to scale up the pathway to 1 L reaction, a large amount of SHI is required. In Chapter 2, I expressed a second copy of the eight accessory genes required for SHI maturation into the SHI-overexpression strain to further increase the yield of the purified enzyme by 40 %. In addition, this maturase-overexpressed strain also overcame the earlier problem encountered when using a large-scale purification procedure (with 500 g wet-wt. of cells), where more than 30 % of the purified SHI was in the inactive trimeric form. However, a further evaluation of the cultivation conditions is required before using this maturase-overexpressed strain for large-scale purification of SHI for industrial scale purposes.

This is because an enriched medium was used to grow the strain to ensure that all vitamins and possible factors for high enzyme expression were provided. Therefore, a fundamental question is whether a less expensive minimal growth medium can be established that gives a comparable yield of SHI in order to lower the cost of the overall purification process.

In a modified version of the synthetic *in vitro* H_2-production pathway using SHI, an artificial electron mediator, benzyl viologen (BV), was used (221, 222). SHI oxidized reduced BV that was generated by NADPH rubredoxin oxidoreductase from *P. furiosus* as the electron donor instead of NADPH for H_2 production. In combination with enzymes purified from other thermophiles, the H_2 productivity from starch at 50 ºC was increased more than 200-fold from 0.4 mmol L^{-1} h^{-1} to 90.2 mmol L^{-1} h^{-1} compared to the original report (222, 223). This synthetic pathway has the potential for another 10-fold increase in H_2 productivity by raising the operating temperature from 50 ºC to 80 ºC, at which the H_2 evolution activity of SHI is 10-fold higher (136). However, whether or not the corresponding enzymes responsible for starch conversion are also active at 80 ºC needs to be addressed. If not, analogous enzymes from other hyperthermophiles will be required in order to maximize starch to H_2 conversion at the higher temperature.

We were unable to construct an active oxygen-tolerant SHI (Chapter 2) by mutagenesis of the relevant cysteine residues binding to the iron-sulfur clusters that are crucial for group 1 oxygen-tolerant hydrogenases. This suggests that these residues in SHI are important for enzyme activity or for its stability. In fact, the lack of a structure for SHI is a major obstacle to future engineering of SHI for various properties and this should be a primary goal of future studies. That we are able to purify a large amount (>0.5 gram) of intact and active tetrameric SHI will be very advantageous for crystallographic screens. In addition, a structure of SHI would be extremely useful for the design and construction of the catalytic site studies in collaboration with Dr. Brian Dyer at Emory

University, as described below. For the future engineering of SHI, a change in the catalytic bias of SHI towards H_2 production might eventually be a desired property for the *in vitro* synthetic pathway for H_2 production. In addition, in collaboration with Dr. Anne Jones at Arizona State University, SHI was found to have an unusual mechanism of oxygen-resilience (140) but it is still O_2 sensitive with a half-life in air of 21 hours (224). Obtaining an oxygen-tolerant enzyme might be very useful for broader applications, such as enzyme-based fuel cells for electricity generation.

Besides applications in H_2 production and NADPH generation, we have taken advantage of the stability of SHI to study its catalytic mechanism. As mentioned in Chapter 1, the change in the redox state of the Ni atom in the catalytic site can be measured by EPR (see Figure 1.9). In collaboration with Dr. Brian Dyer at Emory University, SHI was further examined by nanosecond transient infrared and visible absorbance spectroscopy and three intermediate states were identified in the catalytic cycle (225). Site-directed mutational studies enabled a deeper examination of the proton-coupled electron transfer pathway in SHI, and a glutamate residue near the catalytic site was found to be essential (226). In addition, an arginine residue near the active NiFe site was shown by others to be important for the activity of hydrogenase-1 from *E.coli* and was proposed to serve as a general base in H_2 catalysis (227). Therefore, I have recently constructed the R355K mutant of SHI and this has been provided to Dr. Dyer to investigate the roles of intermediate states using nanosecond transient infrared spectroscopy.

In Chapter 3, two forms of the sulfane-sulfur reducing enzyme MBS were purified and characterized through an operon-splitting strategy that had been used previously for MBH studies (228, 229). It was previously thought that the function of MBS (or MBX as it was called) was to generate NADPH, which was used by NSR for S^0 reduction (26). In this work, we demonstrated that MBS is able to directly reduce a polysulfide-like substrate (DMTS). Hence, the reduced

ferredoxin generated from the glycolysis pathway is oxidized by MBH for proton reduction in the absence of S^0. Alternatively, ferredoxin is oxidized by MBS for polysulfide reduction in the presence of S^0. Both MBH and MBS are predicted to pump protons that are exchanged for Na^+, which is used by ATP synthase for energy conservation (Figure 4.5). However, we could not utilize polysulfide-like compounds, such as sodium tetrasulfide, as the substrates for the *in vitro* assays owing to the extremely high background activity from these reactive compounds. In order to potentially identify a physiological substrate, we have supplied *P. furiosus* grown with and without S^0 to Dr. Gary Siuzdak at the Scripps Research Institute for metabolomics studies. To date, 38 unique unknown sulfur-containing metabolites were identified in the presence of S^0 compared to that without S^0. Further studies using ^{34}S are in progress to identify these compounds and provide insight into the native substrates for MBS.

Interestingly, S-MBS, which has a calculated size of 357 kDa, purified with Triton X-100 was larger than 1 MDa in size based on gel filtration analysis, suggesting that the purified enzyme forms a trimer or tetramer. However, when n-Dodecyl β-D-maltoside (DDM) was used to solubilize the enzyme, it eluted with a size of 700 kDa, suggesting a dimeric structure. The presence of a dimeric form was also evident in preliminary results from the cryo-EM structure determination in our collaboration with Dr. Huilin Li at the Van Andel Institute. At present, a 5 Å resolution structure of MBS has been obtained but further screening is required to obtain the structure at a resolution similar to that of MBH (3 Å). Hence, we should soon be able to compare the structures of MBH and MBS and use the information to determine the evolutionary steps that took place within the catalytic subunit that account for the switch from proton to sulfane-sulfur metabolism.

We recently determined structure of *P. furiosus* MBH and have provided remarkable atomic level detail on this ancient membrane-bound complex as well as the first structure of a group 4 [NiFe] hydrogenase (Figure 5.1) (230). As discussed in Chapter 1, group 4 [NiFe] hydrogenases had been thought to share a common ancestor with Complex I (NADH quinone oxidoreductase), where MBH, MBS and Complex I were clustered in the same phylogenetical group after sequence analysis of the catalytic subunits (Figure 1.8). Complex I is present in all aerobic forms of microbial and eukaryotic life and ranges in size from 11 subunits in some bacteria to more than 40 subunits in mitochondria (165). The atomic structures of Complex I are available from *Thermus thermophilus*, in which it contains 16 subunits (231), and from the mitochondria of *Yarrowia lipolytica*, in which it contains 37 subunits (232). The structure of mammalian Complex I, composed of 44 subunits, from *Bos taurus* heart mitochondria was subsequently determined (233).

MBH and Complex I are believed to have evolved from a proton-reducing ancestor termed ARC (165, 234). It was proposed that MBH incorporated the Na^+-pumping subunits from the multiple resistance and pH antiporter (Mrp) to enable it to generate a Na^+ gradient that can be utilized for energy generation (165). The overall structure of MBH is similar to that of Complex I. Both are L-shaped with a peripheral arm and a membrane arm that includes a common core comprised of MbhH, MbhG, MbhD, and MbhE in MBH. This common core is well-aligned between Complex I and MBH as shown in Figure 5.2. Interestingly, there is a distinct difference in terms of the arrangement of the subunits, where the peripheral module is rotated 180° in the membrane in MBH relative to that in Complex I. Other than the orientation of the modules attached to the membrane arm, these two complexes share important structural features. These features include a lateral helix formed by MbhI and two putative hydrophilic channels across the membrane

arm as depicted in Figure 5.3. The channels formed by the polar and charged residues in this common core are thought to be the site of the proton translocation pathway that is common to Complex I. However, Complex I does not contain a Na^+-pumping module and in MBH this is proposed to be located in MbhA-C and MbhF. Two negatively charged cavities were identified in these subunits (Figure 5.4) where one faces the cytoplasm while the other faces the outside of the membrane. The subunits containing these cavities are homologous to the sodium-pumping subunits in Mrp, MrpE-G, and MrpB, respectively, but a structure for Mrp has not been reported. The ability of MbhA-C to pump Na^+ was also supported by the analysis of the MbhA-C knockout of *P. furiosus* MBH which had diminished Na^+-dependent H_2 evolution activity (230).

The four cytoplasmic subunits of MBH, MbhJ, K, L, and N, are anchored to the membrane arm by docking to MbhM. These five subunits form the hydrogenase module and are more similar in structure and sequence to the hydrophilic quinone-binding module in Complex I than to the other three groups of [NiFe] hydrogenases. In fact, the similarity between MBH and the other three groups is limited to the residues that coordinate the proximal FeS cluster and the NiFe active site. In the hydrogenase module, MbhN contains two [4Fe-4S] clusters while MbhJ contains a [4Fe-4S] cluster, and MbhL is the catalytic subunit containing the NiFe site. The edge-to-edge distances between these clusters and NiFe site are less than 12 Å, consistent with efficient electron tunneling (Figure 5.1) (235). MbhI bridges the hydrogenase module with the proton-translocating membrane module, as shown in Figure 5.3.

Complex I has three conserved loops from three different subunits that link the catalytic subunit to two subunits involved in proton pumping. These are thought to couple quinone reduction with induced structure and electrostatic interactions that are transferred through a series of charged residues across the membrane arm, resulting in proton translocation via the four proton

translocation channels (Figure 5.3). The lateral helix might be involved in this transfer although its exact role is still debatable. MBH could also use a similar mechanism for redox-linked proton pumping, as MBH also contains a homologous lateral helix (MbhI) and a three-loop cluster formed by MbhL, I, and M (Figure 5.3). Therefore, it is predicted that the redox energy from the oxidation of ferredoxin in the hydrogenase module could be coupled to translocation of protons via the lateral helix and the three-loop cluster. In MBH, the pumped protons then flow back inward through the second proton channel, MbhDEG, that is tightly coupled to and drives the translocation of Na^+ through the predicted sodium channel formed by MbhA-C and F. Based on the proposed ion translocation model in MBH, a predicted model of Mrp was also generated (Figure 5.3) (230).

The MBH structure confirms that an evolutionary relationship between MBH, Complex I and the Mrp antiporter exist, as well as supporting the hypothesis of a common ancestor (146, 165, 167). To validate the proposed energy transduction mechanism and the ion translocation pathways based on MBH structure, site-directed mutational studies of the key residues involved in the pathways are required. For instance, deletion of one or more residues in the three loop clusters would provide insight into the roles of these conserved loops. In addition, mutational studies of the conserved residues in the H^+- and Na^+-pumping channels should affect the predicted ion-pumping pathways. H_2 evolution activity, pH and Na^+ gradient formation, and ATP generation can be measured with inverted membrane vesicles to establish the roles of these residues in MBH, as using the methods that were established with the homologous formate hydrogen lyase (FHL) complex in *T. onnurineus* (156).

In Chapter 4, we heterologously expressed Arr from *Pb. aerophilum* into *P. furiosus* and showed that the Arr strain was able to use arsenate (V) as the terminal electron acceptor to support growth. The heterologously-expressed respiratory enzyme also provided *P. furiosus* with the

capacity to use a non-native substrate as the terminal electron acceptor. These findings represent a unique and yet uncharacterized arsenite (III) detoxification mechanism in *P. furiosus*. In order to identify the putative intracellular arsenic-containing compound, an MS-based metabolomics study will be carried out. The metabolites isolated from the parent and Arr strains grown with arsenite (III) will be analyzed and will lead to identification of the arsenic-containing compound. This would provide a much deeper understanding of this unique detoxification mechanism in *P. furiosus*.

A gene annotated as encoding polysulfide reductase from *Pb. aerophilum* was also heterologously expressed in *P. furiosus* using the same strategy as we used for the expression of Arr in *P. furiosus* (236). However, this enzyme was characterized as a thiosulfate reductase (Tsr) because it lacked polysulfide reduction activity in *in vitro* assays. Instead, the enzyme had a high activity with thiosulfate as the substrate. Tsr contains three subunits that are similar to Arr, where TsrA is a pyranopterin-containing catalytic subunit and TsrB is an iron-sulfur cluster-containing subunit. TrsC is a membrane-bound subunit that is predicted in *Pb. aerophilum* to interact with quinol to transfer electrons from the quinol pool to Tsr to reduce thiosulfate to H_2S. In contrast to the Arr strain, the Tsr strain was unable to use thiosulfate as the terminal electron acceptor to support growth. We were unable to purify the intact heterotrimeric form of Tsr using an affinity chromatography as the purified enzyme lacked the membrane-bound subunit TsrC. This was probably because of the TAT translocation system in *Pb. aerophilum* does not exist in *P. furiosus*. In addition, we purified two forms of Tsr containing either Mo (Tsr-Mo) or W (Tsr-W). Tsr-Mo is 10-fold more active than Tsr-W in reducing thiosulfate, which is similar to that of Arr. Interestingly, the affinity of Tsr-Mo for thiosulfate was two-fold higher than that of Tsr-W, while Arr-W had a 20-fold higher affinity for arsenate (V) than that of Arr-Mo. From the results with the Tsr and Arr strains, we demonstrated the potential use of *P. furiosus* as a platform for the

characterization of Mo-containing enzymes from other hyperthermophiles that lack genetic systems, such as *Pb. aerophilum*.

In conclusion, the works outlines in this thesis has provided a greater understanding of hydrogen and S^0 metabolism, as well as arsenic detoxification. In addition, this work shows that *P. furiosus* has great potential as a platform for the expression and purification of hyperthermophilic enzymes in general. This also include large-scale purification of cytoplasmic enzymes such as SHI. *P. furiosus* has a higher Codon Adaptation Index than *E. coli*, thus it could be used for expressing hyperthermophilic enzymes that cannot be efficiently expressed in *E. coli*. For instance, SHI from *P. furiosus* was expressed in *E. coli*, but only at extremely low concentrations, suggesting that an alternative expression system is required (237). In addition, limited genetic systems for hyperthermophiles are available and this greatly restricts the characterization of enzymes from these organisms. The successful expression, purification, and characterization of both native and non-native enzymes in *P. furiosus* during this project demonstrated the potential utility of this genetic platform in general.

Figure 5.1

Cryo-EM structure of *P. furiosus* MBH. The inset shows the distance, including center-to-center and edge-to-edge (in brackets) between metal sites in an orientation as in the right panel. Taken from (230).

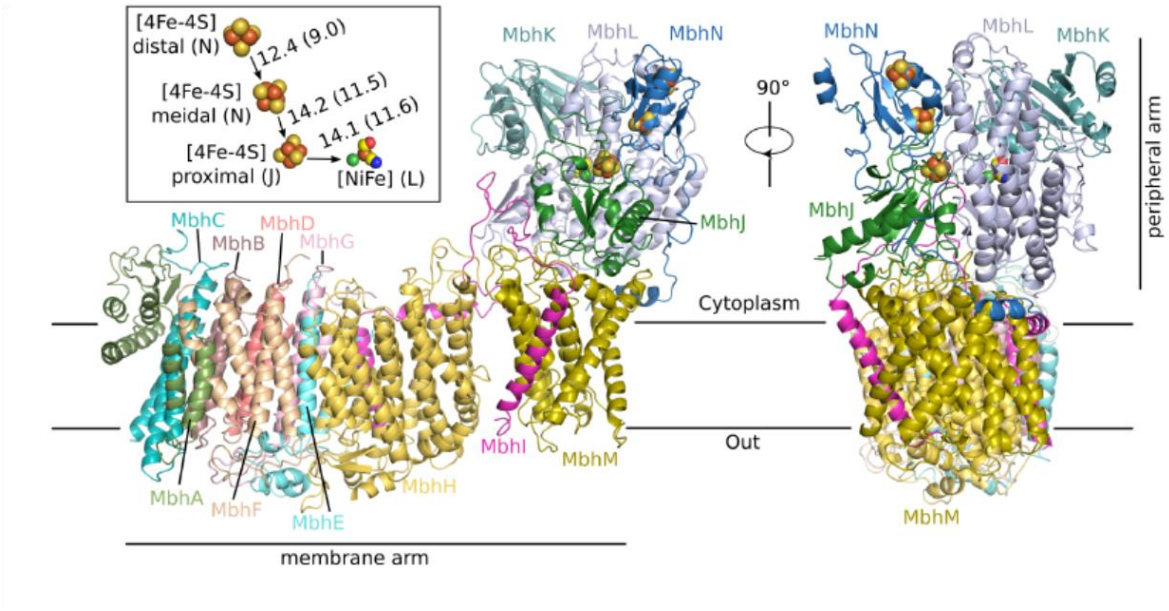
[4Fe-4S]
distal (N)
12.4 (9.0)
[4Fe-4S]
meidal (N)
14.2 (11.5)
14.1 (11.6)
[4Fe-4S]
proximal (J)
[NiFe] (L)
MbhK
MbhL
MbhN
90°
MbhN
MbhL
MbhK
peripheral arm
MbhJ
MbhJ
MbhC
MbhB
MbhD
MbhG
Cytoplasm
Out
MbhI
MbhM
MbhA
MbhF
MbhE
MbhH
MbhM
membrane arm

Figure 5.2

A structural comparison of Complex I and MBH. Both complexes contain a peripheral arm and a membrane arm that includes a common core showing in transparent surfaces. Taken from (230).

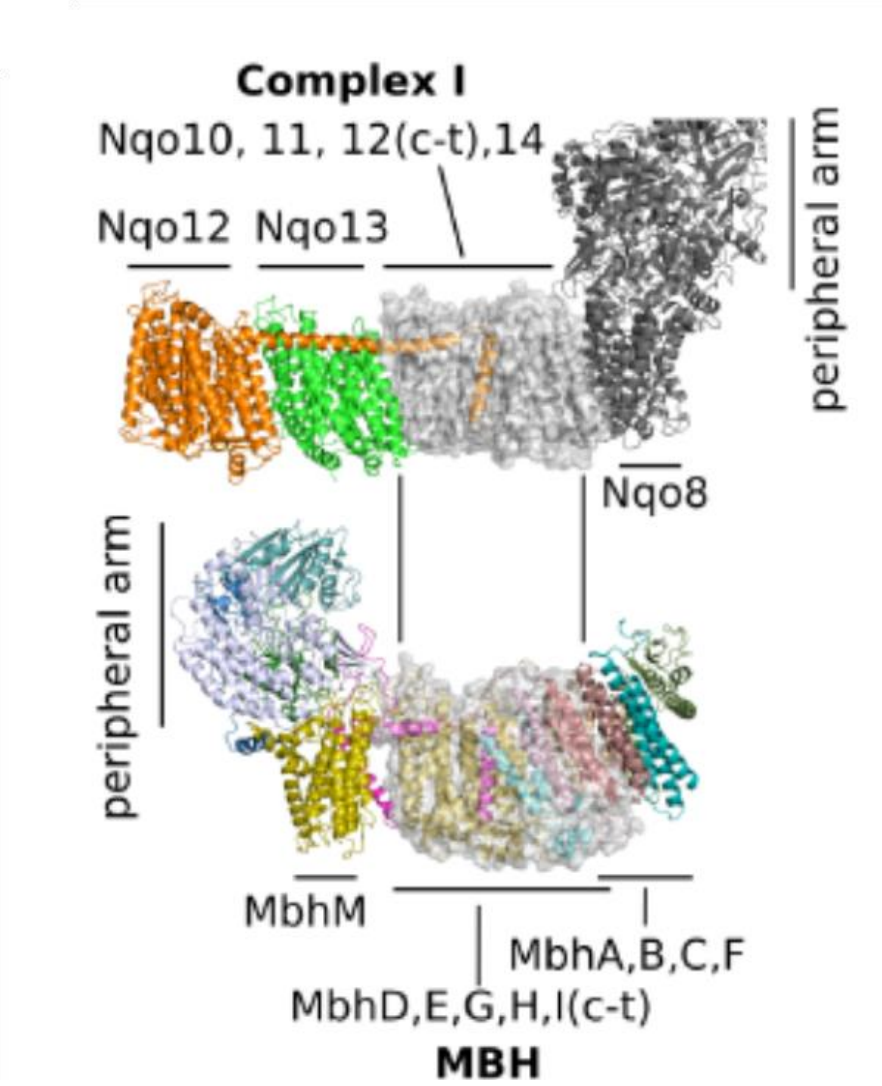
Complex I
Nqo10, 11, 12(c-t),14
Nqo12
Nqo13
peripheral arm
Nqo8
peripheral arm
MbhM
MbhA,B,C,F
MbhD,E,G,H,I(c-t)
MBH

Figure 5.3

Proposed redox-driven proton pumping mechanism of Complex I (a), MBH (b) and Mrp (c). a) the conformational propagation in the Complex I membrane module is shown in red arrows, and the four outward-pumping proton pathways are shown in gray arrows. b) the conformational coupling in MBH is in opposite directions (red arrows). Proton and Na^+ translocation pathways are shown in gray arrows. The lateral helix of MbhI is shown in magenta. (c) the predicted ion translocation in Mrp based on the studies of MBH. Proton and Na^+ translocation pathways are shown in gray arrows. Taken from (230).

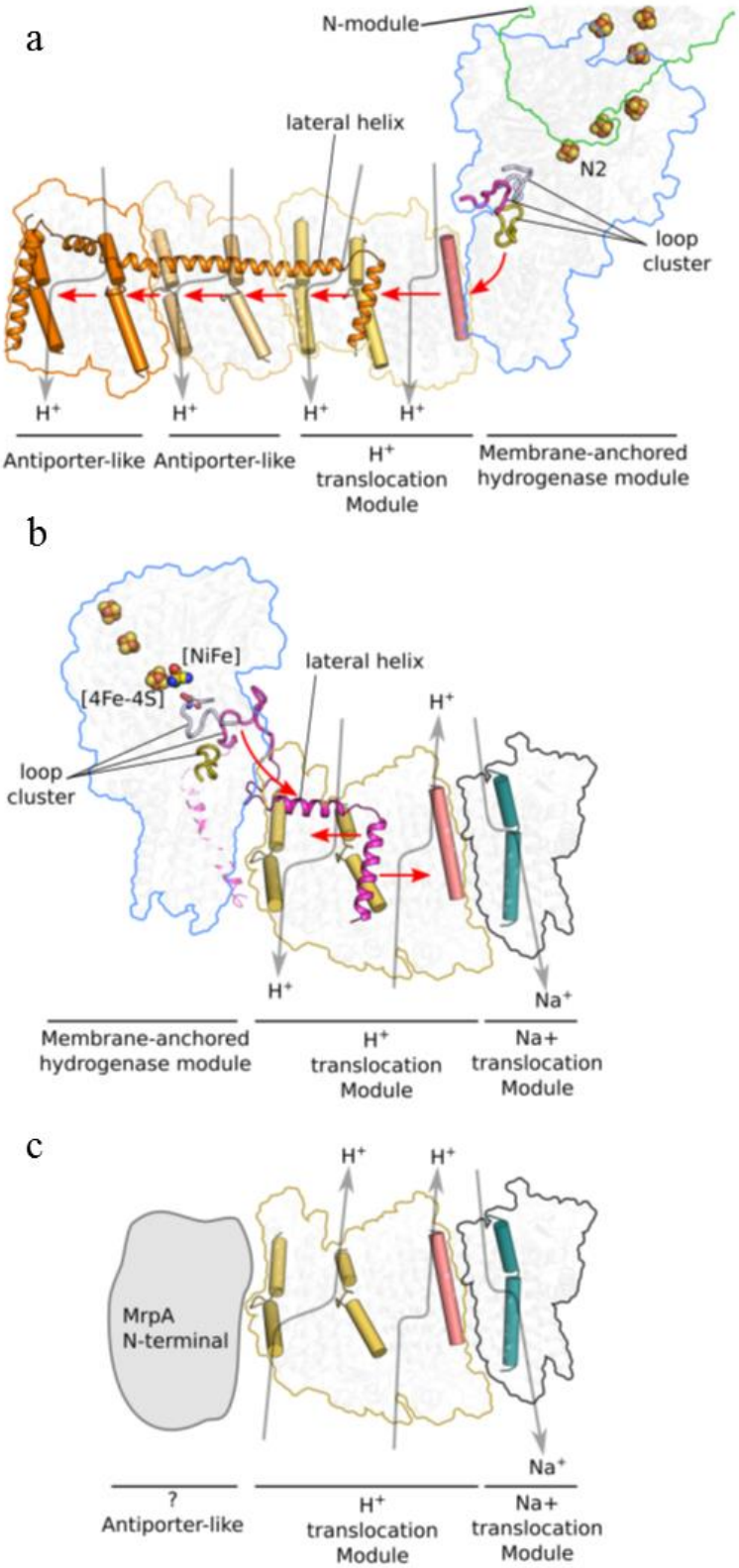
a
N-module
lateral helix
N2
loop
cluster
H+
H+
H+
H+
Antiporter-like
Antiporter-like
H+
translocation
Module
Membrane-anchored
hydrogenase module
b
[NiFe]
[4Fe-4S]
lateral helix
H+
loop
cluster
H+
Na+
Membrane-anchored
hydrogenase module
H+
translocation
Module
Na+
translocation
Module
c
H+
H+
MrpA
N-terminal
Na+
?
Antiporter-like
H+
translocation
Module
Na+
translocation
Module

Figure 5.4

Two negatively charged cavities (red surface) identified in MbhA-C and MbhF. Taken from (230).

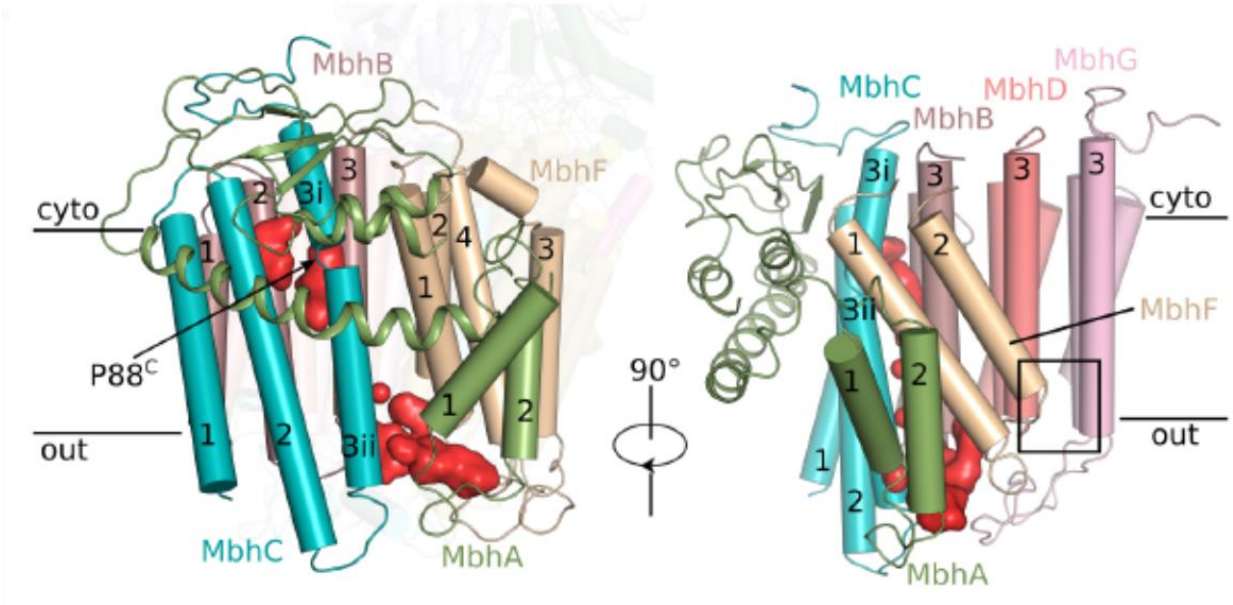
MbhB
MbhF
cyto
P88C
out
MbhC
MbhA
90°
MbhG
MbhC
MbhD
MbhB
cyto
MbhF
out
MbhA

REFERENCES

1. Leigh JA, Albers SV, Atomi H, Allers T. 2011. Model organisms for genetics in the domain Archaea: methanogens, halophiles, Thermococcales and Sulfolobales. FEMS Microbiol Rev 35:577-608.
2. Winker S, Woese CR. 1991. A definition of the domains Archaea, Bacteria and Eucarya in terms of small subunit ribosomal RNA characteristics. Syst Appl Microbiol 14:305-10.
3. Blochl E, Burggraf S, Fiala G, Lauerer G, Huber G, Huber R, Rachel R, Segerer A, Stetter KO, Volkl P. 1995. Isolation, taxonomy and phylogeny of hyperthermophilic microorganisms. World J Microbiol Biotechnol 11:9-16.
4. Woese CR, Kandler O, Wheelis ML. 1990. Towards a natural system of organisms: proposal for the domains Archaea, Bacteria, and Eucarya. Proc Natl Acad Sci U S A 87:4576-9.
5. Forterre P, Brochier C, Philippe H. 2002. Evolution of the Archaea. Theor Popul Biol 61:409-22.
6. Geiduschek EP, Ouhammouch M. 2005. Archaeal transcription and its regulators. Mol Microbiol 56:1397-407.
7. Koonin EV, Mushegian AR, Galperin MY, Walker DR. 1997. Comparison of archaeal and bacterial genomes: computer analysis of protein sequences predicts novel functions and suggests a chimeric origin for the archaea. Mol Microbiol 25:619-37.
8. Benelli D, Londei P. 2011. Translation initiation in Archaea: conserved and domain-specific features. Biochem Soc Trans 39:89-93.

9. Beattie TR, Bell SD. 2011. Molecular machines in archaeal DNA replication. Curr Opin Chem Biol 15:614-9.

10. Matsumi R, Atomi H, Driessen AJ, van der Oost J. 2011. Isoprenoid biosynthesis in Archaea--biochemical and evolutionary implications. Res Microbiol 162:39-52.

11. Robertson CE, Harris JK, Spear JR, Pace NR. 2005. Phylogenetic diversity and ecology of environmental Archaea. Curr Opin Microbiol 8:638-42.

12. Huber R, Stetter KO. 2001. Discovery of hyperthermophilic microorganisms. Methods Enzymol 330:11-24.

13. Takai K, Nakamura K, Toki T, Tsunogai U, Miyazaki M, Miyazaki J, Hirayama H, Nakagawa S, Nunoura T, Horikoshi K. 2008. Cell proliferation at 122 degrees C and isotopically heavy CH4 production by a hyperthermophilic methanogen under high-pressure cultivation. Proc Natl Acad Sci U S A 105:10949-54.

14. Fiala G, Stetter KO. 1986. *Pyrococcus furiosus* sp. nov represents a novel genus of marine heterotrophic archaebacteria growing optimally at 100 degrees C. Arch Microbiol 145:56-61.

15. Koning SM, Elferink MGL, Konings WN, Driessen AJM. 2001. Cellobiose uptake in the hyperthermophilic archaeon *Pyrococcus furiosus* is mediated by an inducible, high-affinity ABC transporter. J Bacteriol 183:4979-4984.

16. Lee HS, Shockley KR, Schut GJ, Conners SB, Montero CI, Johnson MR, Chou CJ, Bridger SL, Wigner N, Brehm SD, Jenney FE, Jr., Comfort DA, Kelly RM, Adams MW. 2006. Transcriptional and biochemical analysis of starch metabolism in the hyperthermophilic archaeon *Pyrococcus furiosus*. J Bacteriol 188:2115-25.

17. Gao J, Bauer MW, Shockley KR, Pysz MA, Kelly RM. 2003. Growth of hyperthermophilic archaeon *Pyrococcus furiosus* on chitin involves two family 18 chitinases. Appl Environ Microbiol 69:3119-28.

18. Stetter KO. 1999. Extremophiles and their adaptation to hot environments. FEBS Lett 452:22-25.

19. Brown SH, Kelly RM. 1993. Characterization of Amylolytic Enzymes, Having Both alpha-1,4 and alpha-1,6 Hydrolytic Activity, from the Thermophilic Archaea *Pyrococcus furiosus* and *Thermococcus litoralis*. Appl Environ Microbiol 59:2614-21.

20. Bauer MW, Bylina EJ, Swanson RV, Kelly RM. 1996. Comparison of a beta-glucosidase and a beta-mannosidase from the hyperthermophilic archaeon *Pyrococcus furiosus*. Purification, characterization, gene cloning, and sequence analysis. J Biol Chem 271:23749-55.

21. Robb FT, Maeder DL, Brown JR, DiRuggiero J, Stump MD, Yeh RK, Weiss RB, Dunn DM. 2001. Genomic sequence of hyperthermophile, *Pyrococcus furiosus*: implications for physiology and enzymology. Methods Enzymol 330:134-57.

22. Bridger SL, Lancaster WA, Poole FL, 2nd, Schut GJ, Adams MW. 2012. Genome sequencing of a genetically tractable *Pyrococcus furiosus* strain reveals a highly dynamic genome. J Bacteriol 194:4097-106.

23. Schut GJ, Boyd ES, Peters JW, Adams MWW. 2013. The modular respiratory complexes involved in hydrogen and sulfur metabolism by heterotrophic hyperthermophilic archaea and their evolutionary implications. FEMS Microbiol Rev 37:182-203.

24. Pisa KY, Huber H, Thomm M, Muller V. 2007. A sodium ion-dependent A1AO ATP synthase from the hyperthermophilic archaeon *Pyrococcus furiosus*. FEBS J 274:3928-38.

25. Lipscomb GL, Stirrett K, Schut GJ, Yang F, Jenney FE, Jr., Scott RA, Adams MW, Westpheling J. 2011. Natural competence in the hyperthermophilic archaeon *Pyrococcus furiosus* facilitates genetic manipulation: construction of markerless deletions of genes encoding the two cytoplasmic hydrogenases. Appl Environ Microbiol 77:2232-8.

26. Schut GJ, Bridger SL, Adams MWW. 2007. Insights into the metabolism of elemental sulfur by the hyperthermophilic archaeon *Pyrococcus furiosus*: Characterization of a coenzyme A-dependent NAD(P)H sulfur oxidoreductase. J Bacteriol 189:4431-4441.

27. Lipscomb GL, Keese AM, Cowart DM, Schut GJ, Thomm M, Adams MW, Scott RA. 2009. SurR: a transcriptional activator and repressor controlling hydrogen and elemental sulphur metabolism in *Pyrococcus furiosus*. Mol Microbiol 71:332-49.

28. Yang H, Lipscomb GL, Keese AM, Schut GJ, Thomm M, Adams MW, Wang BC, Scott RA. 2010. SurR regulates hydrogen production in *Pyrococcus furiosus* by a sulfur-dependent redox switch. Mol Microbiol 77:1111-22.

29. Lipscomb GL, Schut GJ, Scott RA, Adams MWW. 2017. SurR is a master regulator of the primary electron flow pathways in the order Thermococcales. Mol Microbiol 104:869-881.

30. Kengen SWM, Stams AJM. 1994. Growth and energy-conservation in batch cultures of *Pyrococcus furiosus*. FEMS Microbiol Lett 117:305-309.

31. Kengen SWM, Stams AJM, deVos WM. 1996. Sugar metabolism of hyperthermophiles. FEMS Microbiol Rev 18:119-137.

32. Kengen SW, de Bok FA, van Loo ND, Dijkema C, Stams AJ, de Vos WM. 1994. Evidence for the operation of a novel Embden-Meyerhof pathway that involves ADP-dependent kinases during sugar fermentation by *Pyrococcus furiosus*. J Biol Chem 269:17537-41.

33. Verhees CH, Kengen SW, Tuininga JE, Schut GJ, Adams MW, De Vos WM, Van Der Oost J. 2003. The unique features of glycolytic pathways in Archaea. Biochem J 375:231-46.

34. Hansen T, Oehlmann M, Schonheit P. 2001. Novel type of glucose-6-phosphate isomerase in the hyperthermophilic archaeon *Pyrococcus furiosus*. J Bacteriol 183:3428-35.

35. Tuininga JE, Verhees CH, van der Oost J, Kengen SW, Stams AJ, de Vos WM. 1999. Molecular and biochemical characterization of the ADP-dependent phosphofructokinase from the hyperthermophilic archaeon *Pyrococcus furiosus*. J Biol Chem 274:21023-8.

36. Siebers B, Brinkmann H, Dorr C, Tjaden B, Lilie H, van der Oost J, Verhees CH. 2001. Archaeal fructose-1,6-bisphosphate aldolases constitute a new family of archaeal type class I aldolase. J Biol Chem 276:28710-8.

37. Sharma P, Guptasarma P. 2017. Endoglucanase activity at a second site in *Pyrococcus furiosus* triosephosphate isomerase-Promiscuity or compensation for a metabolic handicap? FEBS Open Bio 7:1126-1143.

38. Mukund S, Adams MWW. 1996. Molybdenum and vanadium do not replace tungsten in the catalytically active forms of the three tungstoenzymes in the hyperthermophilic archaeon *Pyrococcus furiosus*. J Bacteriol 178:163-167.

39. Aono S, Bryant FO, Adams MW. 1989. A novel and remarkably thermostable ferredoxin from the hyperthermophilic archaebacterium *Pyrococcus furiosus*. J Bacteriol 171:3433-9.

40. Siebers B, Schonheit P. 2005. Unusual pathways and enzymes of central carbohydrate metabolism in Archaea. Curr Opin Microbiol 8:695-705.

41. Blamey JM, Adams MW. 1994. Characterization of an ancestral type of pyruvate ferredoxin oxidoreductase from the hyperthermophilic bacterium, *Thermotoga maritima*. Biochemistry 33:1000-7.

42. Mai X, Adams MW. 1996. Purification and characterization of two reversible and ADP-dependent acetyl coenzyme A synthetases from the hyperthermophilic archaeon *Pyrococcus furiosus*. J Bacteriol 178:5897-903.

43. Vignais PM, Billoud B. 2007. Occurrence, classification, and biological function of hydrogenases: an overview. Chem Rev 107:4206-72.

44. Lubitz W, Ogata H, Rudiger O, Reijerse E. 2014. Hydrogenases. Chem Rev 114:4081-148.

45. Vignais PM, Billoud B, Meyer J. 2001. Classification and phylogeny of hydrogenases. FEMS Microbiol Rev 25:455-501.

46. Wu LF, Mandrand MA. 1993. Microbial hydrogenases: primary structure, classification, signatures and phylogeny. FEMS Microbiol Rev 10:243-69.

47. Thauer RK, Kaster AK, Goenrich M, Schick M, Hiromoto T, Shima S. 2010. Hydrogenases from methanogenic archaea, nickel, a novel cofactor, and H2 storage. Annu Rev Biochem 79:507-36.

48. Schworer B, Fernandez VM, Zirngibl C, Thauer RK. 1993. H2-forming N5,N10-methylenetetrahydromethanopterin dehydrogenase from *Methanobacterium thermoautotrophicum*. Studies of the catalytic mechanism of H2 formation using hydrogen isotopes. Eur J Biochem 212:255-61.

49. Vogt S, Lyon EJ, Shima S, Thauer RK. 2008. The exchange activities of [Fe] hydrogenase (iron-sulfur-cluster-free hydrogenase) from methanogenic archaea in comparison with the exchange activities of [FeFe] and [NiFe] hydrogenases. J Biol Inorg Chem 13:97-106.

50. Shima S, Pilak O, Vogt S, Schick M, Stagni MS, Meyer-Klaucke W, Warkentin E, Thauer RK, Ermler U. 2008. The crystal structure of [Fe]-hydrogenase reveals the geometry of the active site. Science 321:572-5.

51. Hiromoto T, Ataka K, Pilak O, Vogt S, Stagni MS, Meyer-Klaucke W, Warkentin E, Thauer RK, Shima S, Ermler U. 2009. The crystal structure of C176A mutated [Fe]-hydrogenase suggests an acyl-iron ligation in the active site iron complex. FEBS Lett 583:585-90.

52. Ikeda S, Satake H, Hisano T, Terazawa T. 1972. Potentiometric argentimetric method for the successive titration of sulphide and dissolved sulphur in polysulphide solutions. Talanta 19:1650-4.

53. Mulder DW, Shepard EM, Meuser JE, Joshi N, King PW, Posewitz MC, Broderick JB, Peters JW. 2011. Insights into [FeFe]-hydrogenase structure, mechanism, and maturation. Structure 19:1038-52.

54. Peters JW, Lanzilotta WN, Lemon BJ, Seefeldt LC. 1998. X-ray crystal structure of the Fe-only hydrogenase (CpI) from Clostridium pasteurianum to 1.8 angstrom resolution. Science 282:1853-8.

55. Peters JW, Schut GJ, Boyd ES, Mulder DW, Shepard EM, Broderick JB, King PW, Adams MW. 2015. [FeFe]- and [NiFe]-hydrogenase diversity, mechanism, and maturation. Biochim Biophys Acta 1853:1350-69.

56. Mulder DW, Boyd ES, Sarma R, Lange RK, Endrizzi JA, Broderick JB, Peters JW. 2010. Stepwise [FeFe]-hydrogenase H-cluster assembly revealed in the structure of HydA(DeltaEFG). Nature 465:248-51.

57. English CM, Eckert C, Brown K, Seibert M, King PW. 2009. Recombinant and in vitro expression systems for hydrogenases: new frontiers in basic and applied studies for biological and synthetic H2 production. Dalton Trans:9970-8.

58. Schut GJ, Adams MW. 2009. The iron-hydrogenase of *Thermotoga maritima* utilizes ferredoxin and NADH synergistically: a new perspective on anaerobic hydrogen production. J Bacteriol 191:4451-7.

59. Buckel W, Thauer RK. 2013. Energy conservation via electron bifurcating ferredoxin reduction and proton/Na(+) translocating ferredoxin oxidation. Biochim Biophys Acta 1827:94-113.

60. Mulder DW, Ortillo DO, Gardenghi DJ, Naumov AV, Ruebush SS, Szilagyi RK, Huynh B, Broderick JB, Peters JW. 2009. Activation of HydA(DeltaEFG) requires a preformed [4Fe-4S] cluster. Biochemistry 48:6240-8.

61. Kuchenreuther JM, Britt RD, Swartz JR. 2012. New insights into [FeFe] hydrogenase activation and maturase function. Plos One 7.

62. Berggren G, Adamska A, Lambertz C, Simmons TR, Esselborn J, Atta M, Gambarelli S, Mouesca JM, Reijerse E, Lubitz W, Happe T, Artero V, Fontecave M. 2013. Biomimetic assembly and activation of [FeFe]-hydrogenases. Nature 499:66-69.

63. Esselborn J, Lambertz C, Adamska-Venkates A, Simmons T, Berggren G, Noth J, Siebel J, Hemschemeier A, Artero V, Reijerse E, Fontecave M, Lubitz W, Happe T. 2013. Spontaneous activation of [FeFe]-hydrogenases by an inorganic [2Fe] active site mimic. Nat Chem Biol 9:607-609.

64. Driesener RC, Challand MR, McGlynn SE, Shepard EM, Boyd ES, Broderick JB, Peters JW, Roach PL. 2010. [FeFe]-hydrogenase cyanide ligands derived from S-adenosylmethionine-dependent cleavage of tyrosine. Angew Chem Int Ed Engl 49:1687-90.

65. Kuchenreuther JM, Myers WK, Suess DL, Stich TA, Pelmenschikov V, Shiigi SA, Cramer SP, Swartz JR, Britt RD, George SJ. 2014. The HydG enzyme generates an Fe(CO)2(CN) synthon in assembly of the FeFe hydrogenase H-cluster. Science 343:424-7.

66. King PW, Posewitz MC, Ghirardi ML, Seibert M. 2006. Functional studies of [FeFe] hydrogenase maturation in an Escherichia coli biosynthetic system. J Bacteriol 188:2163-72.

67. Rubach JK, Brazzolotto X, Gaillard J, Fontecave M. 2005. Biochemical characterization of the HydE and HydG iron-only hydrogenase maturation enzymes from *Thermatoga maritima*. FEBS Lett 579:5055-60.

68. Volbeda A, Charon MH, Piras C, Hatchikian EC, Frey M, Fontecilla-Camps JC. 1995. Crystal structure of the nickel-iron hydrogenase from *Desulfovibrio gigas*. Nature 373:580-7.

69. Nicolet Y, Cavazza C, Fontecilla-Camps JC. 2002. Fe-only hydrogenases: structure, function and evolution. J Inorg Biochem 91:1-8.

70. Ogata H, Lubitz W, Higuchi Y. 2016. Structure and function of [NiFe] hydrogenases. J Biochem 160:251-258.

71. Shafaat HS, Rudiger O, Ogata H, Lubitz W. 2013. [NiFe] hydrogenases: a common active site for hydrogen metabolism under diverse conditions. Biochim Biophys Acta 1827:986-1002.

72. Tard C, Pickett CJ. 2009. Structural and functional analogues of the active sites of the [Fe]-, [NiFe]-, and [FeFe]-hydrogenases. Chem Rev 109:2245-74.

73. Bock A, King PW, Blokesch M, Posewitz MC. 2006. Maturation of hydrogenases. Adv Microb Physiol 51:1-71.

74. Lacasse MJ, Zamble DB. 2016. [NiFe]-hydrogenase maturation. Biochemistry 55:1689-701.

75. Reissmann S, Hochleitner E, Wang H, Paschos A, Lottspeich F, Glass RS, Bock A. 2003. Taming of a poison: biosynthesis of the NiFe-hydrogenase cyanide ligands. Science 299:1067-70.

76. Shomura Y, Higuchi Y. 2012. Structural basis for the reaction mechanism of S-carbamoylation of HypE by HypF in the maturation of [NiFe]-hydrogenases. J Biol Chem 287:28409-19.

77. Soboh B, Stripp ST, Muhr E, Granich C, Braussemann M, Herzberg M, Heberle J, Gary Sawers R. 2012. [NiFe]-hydrogenase maturation: isolation of a HypC-HypD complex carrying diatomic CO and CN- ligands. FEBS Lett 586:3882-7.

78. Stripp ST, Soboh B, Lindenstrauss U, Braussemann M, Herzberg M, Nies DH, Sawers RG, Heberle J. 2013. HypD is the scaffold protein for Fe-(CN)2CO cofactor assembly in [NiFe]-hydrogenase maturation. Biochemistry 52:3289-96.

79. Burstel I, Siebert E, Winter G, Hummel P, Zebger I, Friedrich B, Lenz O. 2012. A universal scaffold for synthesis of the Fe(CN)2(CO) moiety of [NiFe] hydrogenase. J Biol Chem 287:38845-53.

80. Soboh B, Stripp ST, Bielak C, Lindenstrauss U, Braussemann M, Javaid M, Hallensleben M, Granich C, Herzberg M, Heberle J, Sawers RG. 2013. The [NiFe]-hydrogenase accessory chaperones HypC and HybG of *Escherichia coli* are iron- and carbon dioxide-binding proteins. FEBS Lett 587:2512-6.

81. Stripp ST, Lindenstrauss U, Granich C, Sawers RG, Soboh B. 2014. The influence of oxygen on [NiFe]-hydrogenase cofactor biosynthesis and how ligation of carbon monoxide precedes cyanation. PLoS One 9:e107488.

82. Blokesch M, Magalon A, Bock A. 2001. Interplay between the specific chaperone-like proteins HybG and HypC in maturation of hydrogenases 1, 2, and 3 from *Escherichia coli*. J Bacteriol 183:2817-22.

83. Blokesch M, Bock A. 2002. Maturation of [NiFe]-hydrogenases in *Escherichia coli*: the HypC cycle. J Mol Biol 324:287-96.

84. Drapal N, Bock A. 1998. Interaction of the hydrogenase accessory protein HypC with HycE, the large subunit of *Escherichia coli* hydrogenase 3 during enzyme maturation. Biochemistry 37:2941-8.

85. Roseboom W, Blokesch M, Bock A, Albracht SP. 2005. The biosynthetic routes for carbon monoxide and cyanide in the Ni-Fe active site of hydrogenases are different. FEBS Lett 579:469-72.

86. Jacobi A, Rossmann R, Bock A. 1992. The hyp operon gene products are required for the maturation of catalytically active hydrogenase isoenzymes in *Escherichia coli*. Arch Microbiol 158:444-51.

87. Lutz S, Jacobi A, Schlensog V, Bohm R, Sawers G, Bock A. 1991. Molecular characterization of an operon (hyp) necessary for the activity of the three hydrogenase isoenzymes in *Escherichia coli*. Mol Microbiol 5:123-35.

88. Waugh R, Boxer DH. 1986. Pleiotropic hydrogenase mutants of *Escherichia coli* K12: growth in the presence of nickel can restore hydrogenase activity. Biochimie 68:157-66.

89. Olson JW, Mehta NS, Maier RJ. 2001. Requirement of nickel metabolism proteins HypA and HypB for full activity of both hydrogenase and urease in *Helicobacter pylori*. Mol Microbiol 39:176-82.

90. Forzi L, Sawers RG. 2007. Maturation of [NiFe]-hydrogenases in *Escherichia coli*. *Biometals* 20:565-78.

91. Chan Chung KC, Zamble DB. 2011. Protein interactions and localization of the *Escherichia coli* accessory protein HypA during nickel insertion to [NiFe] hydrogenase. J Biol Chem 286:43081-90.

92. Herbst RW, Perovic I, Martin-Diaconescu V, O'Brien K, Chivers PT, Pochapsky SS, Pochapsky TC, Maroney MJ. 2010. Communication between the zinc and nickel sites in dimeric HypA: metal recognition and pH sensing. J Am Chem Soc 132:10338-51.

93. Leach MR, Sandal S, Sun H, Zamble DB. 2005. Metal binding activity of the *Escherichia coli* hydrogenase maturation factor HypB. Biochemistry 44:12229-38.

94. Gasper R, Scrima A, Wittinghofer A. 2006. Structural insights into HypB, a GTP-binding protein that regulates metal binding. J Biol Chem 281:27492-27502.

95. Watanabe S, Kawashima T, Nishitani Y, Kanai T, Wada T, Inaba K, Atomi H, Imanaka T, Miki K. 2015. Structural basis of a Ni acquisition cycle for [NiFe] hydrogenase by Ni-metallochaperone HypA and its enhancer. Proc Natl Acad Sci U S A 112:7701-6.

96. Douglas CD, Ngu TT, Kaluarachchi H, Zamble DB. 2013. Metal transfer within the *Escherichia coli* HypB-HypA complex of hydrogenase accessory proteins. Biochemistry 52:6030-6039.

97. Sydor AM, Lebrette H, Ariyakumaran R, Cavazza C, Zamble DB. 2014. Relationship between Ni(II) and Zn(II) coordination and nucleotide binding by the *Helicobacter pylori* [NiFe]-hydrogenase and urease maturation factor HypB. J Biol Chem 289:3828-41.

98. Zhang JW, Butland G, Greenblatt JF, Emili A, Zamble DB. 2005. A role for SlyD in the *Escherichia coli* hydrogenase biosynthetic pathway. J Biol Chem 280:4360-6.

99. Pinske C, Sargent F, Sawers RG. 2015. SlyD-dependent nickel delivery limits maturation of [NiFe]-hydrogenases in late-stationary phase *Escherichia coli* cells. Metallomics 7:683-90.

100. Leach MR, Zhang JW, Zamble DB. 2007. The role of complex formation between the *Escherichia coli* hydrogenase accessory factors HypB and SlyD. J Biol Chem 282:16177-16186.

101. Theodoratou E, Huber R, Bock A. 2005. [NiFe]-Hydrogenase maturation endopeptidase: structure and function. Biochem Soc Trans 33:108-11.

102. Fritsche E, Paschos A, Beisel HG, Bock A, Huber R. 1999. Crystal structure of the hydrogenase maturating endopeptidase HYBD from *Escherichia coli*. J Mol Biol 288:989-98.

103. Rossmann R, Maier T, Lottspeich F, Bock A. 1995. Characterisation of a protease from *Escherichia coli* involved in hydrogenase maturation. Eur J Biochem 227:545-50.

104. Gollin DJ, Mortenson LE, Robson RL. 1992. Carboxyl-terminal processing may be essential for production of active NiFe hydrogenase in *Azotobacter vinelandii*. FEBS Lett 309:371-375.

105. Sorgenfrei O, Linder D, Karas M, Klein A. 1993. A novel very small subunit of a selenium-containing [NiFe] hydrogenase of *Methanococcus voltae* ss posttranslationally processed by cleavage at a defined position. Eur J Biochem 213:1355-1358.

106. Menon NK, Robbins J, Vartanian MD, Patil D, Peck HD, Menon AL, Robson RL, Przybyla AE. 1993. Carboxy-terminal processing of the large subunit of [NiFe] hydrogenases. FEBS Lett 331:91-95.

107. Rossmann R, Sauter M, Lottspeich F, Bock A. 1994. Maturation of the large subunit (HycE) of *Escherichia coli* hydrogenase 3 requires nickel incorporation followed by C-terminal processing at Arg537. Eur J Biochem 220:377-384.

108. Theodoratou E, Paschos A, Magalon A, Fritsche E, Huber R, Bock A. 2000. Nickel serves as a substrate recognition motif for the endopeptidase involved in hydrogenase maturation. Eur J Biochem 267:1995-1999.

109. Vignais PM, Colbeau A. 2004. Molecular biology of microbial hydrogenases. Curr Issues Mol Biol 6:159-88.

110. Sondergaard D, Pedersen CN, Greening C. 2016. HydDB: A web tool for hydrogenase classification and analysis. Sci Rep 6:34212.

111. Trchounian K, Pinske C, Sawers RG, Trchounian A. 2012. Characterization of *Escherichia coli* [NiFe]-hydrogenase distribution during fermentative growth at different pHs. Cell Biochem Biophys 62:433-40.

112. Morais-Silva FO, Santos CI, Rodrigues R, Pereira IA, Rodrigues-Pousada C. 2013. Roles of HynAB and Ech, the only two hydrogenases found in the model sulfate reducer *Desulfovibrio gigas*. J Bacteriol 195:4753-60.

113. Volbeda A, Darnault C, Parkin A, Sargent F, Armstrong FA, Fontecilla-Camps JC. 2013. Crystal structure of the O(2)-tolerant membrane-bound hydrogenase 1 from *Escherichia coli* in complex with its cognate cytochrome b. Structure 21:184-190.

114. Pandelia ME, Fourmond V, Tron-Infossi P, Lojou E, Bertrand P, Leger C, Giudici-Orticoni MT, Lubitz W. 2010. Membrane-bound hydrogenase I from the hyperthermophilic bacterium *Aquifex aeolicus*: enzyme activation, redox intermediates and oxygen tolerance. J Am Chem Soc 132:6991-7004.

115. Shomura Y, Yoon KS, Nishihara H, Higuchi Y. 2011. Structural basis for a [4Fe-3S] cluster in the oxygen-tolerant membrane-bound [NiFe]-hydrogenase. Nature 479:253-6.

116. Fritsch J, Scheerer P, Frielingsdorf S, Kroschinsky S, Friedrich B, Lenz O, Spahn CM. 2011. The crystal structure of an oxygen-tolerant hydrogenase uncovers a novel iron-sulphur centre. Nature 479:249-52.

117. Shomura Y, Higuchi Y. 2013. Structural aspects of [NiFe]-hydrogenases. Rev Inorg Chem 33:173-192.

118. Goris T, Wait AF, Saggu M, Fritsch J, Heidary N, Stein M, Zebger I, Lendzian F, Armstrong FA, Friedrich B, Lenz O. 2011. A unique iron-sulfur cluster is crucial for oxygen tolerance of a [NiFe]-hydrogenase. Nat Chem Biol 7:310-U87.

119. Buhrke T, Lenz O, Krauss N, Friedrich B. 2005. Oxygen tolerance of the H2-sensing [NiFe] hydrogenase from *Ralstonia eutropha* H16 is based on limited access of oxygen to the active site. J Biol Chem 280:23791-6.

120. Evans RM, Parkin A, Roessler MM, Murphy BJ, Adamson H, Lukey MJ, Sargent F, Volbeda A, Fontecilla-Camps JC, Armstrong FA. 2013. Principles of sustained enzymatic hydrogen oxidation in the presence of oxygen--the crucial influence of high potential Fe-S clusters in the electron relay of [NiFe]-hydrogenases. J Am Chem Soc 135:2694-707.

121. Ogata H, Hirota S, Nakahara A, Komori H, Shibata N, Kato T, Kano K, Higuchi Y. 2005. Activation process of [NiFe] hydrogenase elucidated by high-resolution X-ray analyses: conversion of the ready to the unready state. Structure 13:1635-42.

122. Fritsch J, Lenz O, Friedrich B. 2013. Structure, function and biosynthesis of O(2)-tolerant hydrogenases. Nat Rev Microbiol 11:106-14.

123. Frielingsdorf S, Fritsch J, Schmidt A, Hammer M, Lowenstein J, Siebert E, Pelmenschikov V, Jaenicke T, Kalms J, Rippers Y, Lendzian F, Zebger I, Teutloff C,

Kaupp M, Bittl R, Hildebrandt P, Friedrich B, Lenz O, Scheerer P. 2014. Reversible [4Fe-3S] cluster morphing in an O(2)-tolerant [NiFe] hydrogenase. Nat Chem Biol 10:378-85.

124. Pandelia ME, Nitschke W, Infossi P, Giudici-Orticoni MT, Bill E, Lubitz W. 2011. Characterization of a unique [FeS] cluster in the electron transfer chain of the oxygen tolerant [NiFe] hydrogenase from *Aquifex aeolicus*. Proc Natl Acad Sci U S A 108:6097-102.

125. Appel J, Schulz R. 1998. Hydrogen metabolism in organisms with oxygenic photosynthesis: hydrogenases as important regulatory devices for a proper redox poising? J Photoch Photobio B 47:1-11.

126. Ludwig M, Schulz-Friedrich R, Appel J. 2006. Occurrence of hydrogenases in cyanobacteria and anoxygenic photosynthetic bacteria: implications for the phylogenetic origin of cyanobacterial and algal hydrogenases. J Mol Evol 63:758-68.

127. Berman-Frank I, Lundgren P, Falkowski P. 2003. Nitrogen fixation and photosynthetic oxygen evolution in cyanobacteria. Res Microbiol 154:157-64.

128. Brugna-Guiral M, Tron P, Nitschke W, Stetter KO, Burlat B, Guigliarelli B, Bruschi M, Giudici-Orticoni MT. 2003. [NiFe] hydrogenases from the hyperthermophilic bacterium *Aquifex aeolicus*: properties, function, and phylogenetics. Extremophiles 7:145-57.

129. Tamagnini P, Leitao E, Oliveira P, Ferreira D, Pinto F, Harris DJ, Heidorn T, Lindblad P. 2007. Cyanobacterial hydrogenases: diversity, regulation and applications. FEMS Microbiol Rev 31:692-720.

130. Zhang X, Sherman DM, Sherman LA. 2014. The uptake hydrogenase in the unicellular diazotrophic cyanobacterium *Cyanothece* sp. strain PCC 7822 protects nitrogenase from oxygen toxicity. J Bacteriol 196:840-9.

131. Khetkorn W, Lindblad P, Incharoensakdi A. 2012. Inactivation of uptake hydrogenase leads to enhanced and sustained hydrogen production with high nitrogenase activity under high light exposure in the cyanobacterium *Anabaena siamensis* TISTR 8012. J Biol Eng 6:19.

132. Buhrke T, Loscher S, Lenz O, Schlodder E, Zebger I, Andersen LK, Hildebrandt P, Meyer-Klaucke W, Dau H, Friedrich B, Haumann M. 2005. Reduction of unusual iron-sulfur clusters in the H2-sensing regulatory Ni-Fe hydrogenase from *Ralstonia eutropha* H16. J Biol Chem 280:19488-95.

133. Lenz O, Bernhard M, Buhrke T, Schwartz E, Friedrich B. 2002. The hydrogen-sensing apparatus in *Ralstonia eutropha*. J Mol Microbiol Biotechnol 4:255-62.

134. Alex LA, Reeve JN, Orme-Johnson WH, Walsh CT. 1990. Cloning, sequence determination, and expression of the genes encoding the subunits of the nickel-containing 8-hydroxy-5-deazaflavin reducing hydrogenase from *Methanobacterium thermoautotrophicum* delta H. Biochemistry 29:7237-44.

135. Vitt S, Ma K, Warkentin E, Moll J, Pierik AJ, Shima S, Ermler U. 2014. The F(4)(2)(0)-reducing [NiFe]-hydrogenase complex from *Methanothermobacter marburgensis*, the first X-ray structure of a group 3 family member. J Mol Biol 426:2813-26.

136. Bryant FO, Adams MW. 1989. Characterization of hydrogenase from the hyperthermophilic archaebacterium, *Pyrococcus furiosus*. J Biol Chem 264:5070-9.

137. Ma K, Weiss R, Adams MW. 2000. Characterization of hydrogenase II from the hyperthermophilic archaeon *Pyrococcus furiosus* and assessment of its role in sulfur reduction. J Bacteriol 182:1864-71.

138. van Haaster DJ, Hagedoorn PL, Jongejan JA, Hagen WR. 2005. On the relationship between affinity for molecular hydrogen and the physiological directionality of hydrogenases. Biochem Soc Trans 33:12-14.

139. van Haaster DJ, Silva PJ, Hagedoorn PL, Jongejan JA, Hagen WR. 2008. Reinvestigation of the steady-state kinetics and physiological function of the soluble NiFe-hydrogenase I of *Pyrococcus furiosus*. J Bacteriol 190:1584-7.

140. Kwan P, McIntosh CL, Jennings DP, Hopkins RC, Chandrayan SK, Wu CH, Adams MW, Jones AK. 2015. The [NiFe]-hydrogenase of *Pyrococcus furiosus* exhibits a new type of oxygen tolerance. J Am Chem Soc 137:13556-65.

141. Stojanowic A, Mander GJ, Duin EC, Hedderich R. 2003. Physiological role of the F420-non-reducing hydrogenase (Mvh) from *Methanothermobacter marburgensis*. Arch Microbiol 180:194-203.

142. Thauer RK, Kaster AK, Seedorf H, Buckel W, Hedderich R. 2008. Methanogenic archaea: ecologically relevant differences in energy conservation. Nat Rev Microbiol 6:579-91.

143. Kaster AK, Moll J, Parey K, Thauer RK. 2011. Coupling of ferredoxin and heterodisulfide reduction via electron bifurcation in hydrogenotrophic methanogenic archaea. Proc Natl Acad Sci U S A 108:2981-6.

144. Cramm R. 2009. Genomic view of energy metabolism in *Ralstonia eutropha* H16. J Mol Microbiol Biotechnol 16:38-52.

145. Gutekunst K, Chen X, Schreiber K, Kaspar U, Makam S, Appel J. 2014. The bidirectional NiFe-hydrogenase in *Synechocystis* sp. PCC 6803 is reduced by flavodoxin and ferredoxin and is essential under mixotrophic, nitrate-limiting conditions. J Biol Chem 289:1930-7.

146. Hedderich R. 2004. Energy-converting [NiFe] hydrogenases from archaea and extremophiles: ancestors of complex I. J Bioenerg Biomembr 36:65-75.

147. Hedderich R, Forzi L. 2005. Energy-converting [NiFe] hydrogenases: More than just H-2 activation. J Mol Microb Biotech 10:92-104.

148. Meuer J, Bartoschek S, Koch J, Kunkel A, Hedderich R. 1999. Purification and catalytic properties of Ech hydrogenase from *Methanosarcina barkeri*. Eur J Biochem 265:325-35.

149. Sapra R, Bagramyan K, Adams MW. 2003. A simple energy-conserving system: proton reduction coupled to proton translocation. Proc Natl Acad Sci U S A 100:7545-50.

150. Sapra R, Verhagen MF, Adams MW. 2000. Purification and characterization of a membrane-bound hydrogenase from the hyperthermophilic archaeon *Pyrococcus furiosus*. J Bacteriol 182:3423-8.

151. Silva PJ, van den Ban EC, Wassink H, Haaker H, de Castro B, Robb FT, Hagen WR. 2000. Enzymes of hydrogen metabolism in *Pyrococcus furiosus*. Eur J Biochem 267:6541-51.

152. Tersteegen A, Hedderich R. 1999. *Methanobacterium thermoautotrophicum* encodes two multisubunit membrane-bound [NiFe] hydrogenases. Transcription of the operons and sequence analysis of the deduced proteins. Eur J Biochem 264:930-43.

153. Major TA, Liu Y, Whitman WB. 2010. Characterization of energy-conserving hydrogenase B in *Methanococcus maripaludis*. J Bacteriol 192:4022-30.

154. Kim YJ, Lee HS, Kim ES, Bae SS, Lim JK, Matsumi R, Lebedinsky AV, Sokolova TG, Kozhevnikova DA, Cha SS, Kim SJ, Kwon KK, Imanaka T, Atomi H, Bonch-Osmolovskaya EA, Lee JH, Kang SG. 2010. Formate-driven growth coupled with H(2) production. Nature 467:352-5.

155. Sawers RG, Ballantine SP, Boxer DH. 1985. Differential expression of hydrogenase isoenzymes in *Escherichia coli* K-12: evidence for a third isoenzyme. J Bacteriol 164:1324-31.

156. Lim JK, Mayer F, Kang SG, Muller V. 2014. Energy conservation by oxidation of formate to carbon dioxide and hydrogen via a sodium ion current in a hyperthermophilic archaeon. Proc Natl Acad Sci U S A 111:11497-502.

157. Lee HS, Kang SG, Bae SS, Lim JK, Cho Y, Kim YJ, Jeon JH, Cha SS, Kwon KK, Kim HT, Park CJ, Lee HW, Kim SI, Chun J, Colwell RR, Kim SJ, Lee JH. 2008. The complete genome sequence of *Thermococcus onnurineus* NA1 reveals a mixed heterotrophic and carboxydotrophic metabolism. J Bacteriol 190:7491-9.

158. Soboh B, Linder D, Hedderich R. 2002. Purification and catalytic properties of a CO-oxidizing:H2-evolving enzyme complex from *Carboxydothermus hydrogenoformans*. Eur J Biochem 269:5712-21.

159. Schut GJ, Lipscomb GL, Nguyen DM, Kelly RM, Adams MW. 2016. Heterologous production of an energy-conserving carbon monoxide dehydrogenase complex in the hyperthermophile *Pyrococcus furiosus*. Front Microbiol 7:29.

160. Constant P, Chowdhury SP, Hesse L, Pratscher J, Conrad R. 2011. Genome data mining and soil survey for the novel group 5 [NiFe]-hydrogenase to explore the diversity and

ecological importance of presumptive high-affinity H(2)-oxidizing bacteria. Appl Environ Microbiol 77:6027-35.

161. Schafer C, Friedrich B, Lenz O. 2013. Novel, oxygen-insensitive group 5 [NiFe]-hydrogenase in *Ralstonia eutropha*. Appl Environ Microbiol 79:5137-45.

162. Constant P, Chowdhury SP, Pratscher J, Conrad R. 2010. Streptomycetes contributing to atmospheric molecular hydrogen soil uptake are widespread and encode a putative high-affinity [NiFe]-hydrogenase. Environ Microbiol 12:821-9.

163. Meredith LK, Rao D, Bosak T, Klepac-Ceraj V, Tada KR, Hansel CM, Ono S, Prinn RG. 2014. Consumption of atmospheric hydrogen during the life cycle of soil-dwelling actinobacteria. Environ Microbiol Rep 6:226-38.

164. Greening C, Berney M, Hards K, Cook GM, Conrad R. 2014. A soil actinobacterium scavenges atmospheric H2 using two membrane-associated, oxygen-dependent [NiFe] hydrogenases. Proc Natl Acad Sci U S A 111:4257-61.

165. Schut GJ, Zadvornyy O, Wu CH, Peters JW, Boyd ES, Adams MW. 2016. The role of geochemistry and energetics in the evolution of modern respiratory complexes from a proton-reducing ancestor. Biochim Biophys Acta 1857:958-70.

166. Letts JA, Sazanov LA. 2015. Gaining mass: the structure of respiratory complex I-from bacterial towards mitochondrial versions. Curr Opin Struct Biol 33:135-45.

167. Sazanov LA. 2015. A giant molecular proton pump: structure and mechanism of respiratory complex I. Nat Rev Mol Cell Biol 16:375-88.

168. Dibrova DV, Cherepanov DA, Galperin MY, Skulachev VP, Mulkidjanian AY. 2013. Evolution of cytochrome bc complexes: from membrane-anchored dehydrogenases of

ancient bacteria to triggers of apoptosis in vertebrates. Biochim Biophys Acta 1827:1407-27.

169. Albracht SP. 1993. Intimate relationships of the large and the small subunits of all nickel hydrogenases with two nuclear-encoded subunits of mitochondrial NADH: ubiquinone oxidoreductase. Biochim Biophys Acta 1144:221-4.

170. Friedrich T, Weiss H. 1997. Modular evolution of the respiratory NADH:ubiquinone oxidoreductase and the origin of its modules. J Theor Biol 187:529-40.

171. Bohm R, Sauter M, Bock A. 1990. Nucleotide sequence and expression of an operon in *Escherichia coli* coding for formate hydrogenlyase components. Mol Microbiol 4:231-43.

172. Sauter M, Bohm R, Bock A. 1992. Mutational analysis of the operon (hyc) determining hydrogenase 3 formation in *Escherichia coli*. Mol Microbiol 6:1523-32.

173. Albracht SP, Hedderich R. 2000. Learning from hydrogenases: location of a proton pump and of a second FMN in bovine NADH--ubiquinone oxidoreductase (Complex I). FEBS Lett 485:1-6.

174. Ito M, Guffanti AA, Oudega B, Krulwich TA. 1999. mrp, a multigene, multifunctional locus in *Bacillus subtilis* with roles in resistance to cholate and to Na+ and in pH homeostasis. J Bacteriol 181:2394-402.

175. Ito M, Guffanti AA, Krulwich TA. 2001. Mrp-dependent Na(+)/H(+) antiporters of *Bacillus* exhibit characteristics that are unanticipated for completely secondary active transporters. FEBS Lett 496:117-20.

176. Van Kranendonk MJ. 2006. Volcanic degassing, hydrothermal circulation and the flourishing of early life on Earth: A review of the evidence from c. 3490-3240 Ma rocks of the Pilbara Supergroup, Pilbara Craton, Western Australia. Earth-Sci Rev 74:197-240.

177. Philippot P, Van Zuilen M, Lepot K, Thomazo C, Farquhar J, Van Kranendonk MJ. 2007. Early Archaean microorganisms preferred elemental sulfur, not sulfate. Science 317:1534-1537.

178. Kletzin A, Urich T, Muller F, Bandeiras TM, Gomes CM. 2004. Dissimilatory oxidation and reduction of elemental sulfur in thermophilic archaea. J Bioenerg Biomembr 36:77-91.

179. Amend JP, Shock EL. 2001. Energetics of overall metabolic reactions of thermophilic and hyperthermophilic Archaea and bacteria. FEMS Microbiol Rev 25:175-243.

180. Schonheit P, Schafer T. 1995. Metabolism of hyperthermophiles. World J Microbiol Biotechnol 11:26-57.

181. Hedderich R, Klimmek O, Kroger A, Dirmeier R, Keller M, Stetter KO. 1998. Anaerobic respiration with elemental sulfur and with disulfides. FEMS Microbiol Rev 22:353-381.

182. Blank CE. 2009. Phylogenomic dating--the relative antiquity of archaeal metabolic and physiological traits. Astrobiology 9:193-219.

183. Liu Y, Beer LL, Whitman WB. 2012. Sulfur metabolism in archaea reveals novel processes. Environ Microbiol 14:2632-44.

184. Laska S, Lottspeich F, Kletzin A. 2003. Membrane-bound hydrogenase and sulfur reductase of the hyperthermophilic and acidophilic archaeon *Acidianus ambivalens*. Microbiology 149:2357-71.

185. Pihl TD, Black LK, Schulman BA, Maier RJ. 1992. Hydrogen-oxidizing electron transport components in the hyperthermophilic archaebacterium *Pyrodictium brockii*. J Bacteriol 174:137-43.

186. Dirmeier R, Keller M, Frey G, Huber H, Stetter KO. 1998. Purification and properties of an extremely thermostable membrane-bound sulfur-reducing complex from the hyperthermophilic *Pyrodictium abyssi*. Eur J Biochem 252:486-91.

187. Volkl P, Huber R, Drobner E, Rachel R, Burggraf S, Trincone A, Stetter KO. 1993. *Pyrobaculum aerophilum* sp. nov., a novel nitrate-reducing hyperthermophilic archaeum. Appl Environ Microbiol 59:2918-26.

188. Cozen AE, Weirauch MT, Pollard KS, Bernick DL, Stuart JM, Lowe TM. 2009. Transcriptional map of respiratory versatility in the hyperthermophilic crenarchaeon *Pyrobaculum aerophilum*. J Bacteriol 191:782-94.

189. Cullen WR, Reimer KJ. 1989. Arsenic Speciation in the Environment. Chem Rev 89:713-764.

190. Tamaki S, Frankenberger WT, Jr. 1992. Environmental biochemistry of arsenic. Rev Environ Contam Toxicol 124:79-110.

191. Hughes MF. 2002. Arsenic toxicity and potential mechanisms of action. Toxicol Lett 133:1-16.

192. Slyemi D, Bonnefoy V. 2012. How prokaryotes deal with arsenic. Env Microbiol Rep 4:571-586.

193. Liu SX, Athar M, Lippai I, Waldren C, Hei TK. 2001. Induction of oxyradicals by arsenic: implication for mechanism of genotoxicity. Proc Natl Acad Sci U S A 98:1643-8.

194. Dopp E, Kligerman AD, Diaz-Bone RA. 2010. Organoarsenicals. Uptake, metabolism, and toxicity. Met Ions Life Sci 7:231-65.

195. Silver S, Phung LT. 2005. Genes and enzymes involved in bacterial oxidation and reduction of inorganic arsenic. Appl Environ Microbiol 71:599-608.

196. Paez-Espino D, Tamames J, de Lorenzo V, Canovas D. 2009. Microbial responses to environmental arsenic. Biometals 22:117-30.

197. Tsai SL, Singh S, Chen W. 2009. Arsenic metabolism by microbes in nature and the impact on arsenic remediation. Curr Opin Biotechnol 20:659-67.

198. Mandal BK, Suzuki KT. 2002. Arsenic round the world: a review. Talanta 58:201-35.

199. Rosen BP. 2002. Biochemistry of arsenic detoxification. FEBS Lett 529:86-92.

200. Lin YF, Walmsley AR, Rosen BP. 2006. An arsenic metallochaperone for an arsenic detoxification pump. Proc Natl Acad Sci U S A 103:15617-22.

201. Rosen BP. 1999. Families of arsenic transporters. Trends Microbiol 7:207-12.

202. Silver S, Phung le T. 2005. A bacterial view of the periodic table: genes and proteins for toxic inorganic ions. J Ind Microbiol Biotechnol 32:587-605.

203. Silver S, Phung LT. 1996. Bacterial heavy metal resistance: new surprises. Annu Rev Microbiol 50:753-89.

204. Cai J, DuBow MS. 1996. Expression of the *Escherichia coli* chromosomal ars operon. Can J Microbiol 42:662-71.

205. Wu J, Rosen BP. 1993. The arsD gene encodes a second trans-acting regulatory protein of the plasmid-encoded arsenical resistance operon. Mol Microbiol 8:615-23.

206. Ellis DR, Gumaelius L, Indriolo E, Pickering IJ, Banks JA, Salt DE. 2006. A novel arsenate reductase from the arsenic hyperaccumulating fern *Pteris vittata*. Plant Physiol 141:1544-54.

207. Bini E. 2010. Archaeal transformation of metals in the environment. FEMS Microbiol Ecol 73:1-16.

208. Krafft T, Macy JM. 1998. Purification and characterization of the respiratory arsenate reductase of *Chrysiogenes arsenatis*. Eur J Biochem 255:647-53.

209. Afkar E, Lisak J, Saltikov C, Basu P, Oremland RS, Stolz JF. 2003. The respiratory arsenate reductase from *Bacillus selenitireducens* strain MLS10. FEMS Microbiol Lett 226:107-12.

210. Malasarn D, Keeffe JR, Newman DK. 2008. Characterization of the arsenate respiratory reductase from *Shewanella sp*. strain ANA-3. J Bacteriol 190:135-42.

211. Murphy JN, Saltikov CW. 2007. The cymA gene, encoding a tetraheme c-type cytochrome, is required for arsenate respiration in *Shewanella* species. J Bacteriol 189:2283-2290.

212. Zargar K, Saltikov CW. 2009. Lysine-91 of the tetraheme c-type cytochrome CymA is essential for quinone interaction and arsenate respiration in *Shewanella* sp strain ANA-3. Arch Microbiol 191:797-806.

213. van Lis R, Nitschke W, Duval S, Schoepp-Cothenet B. 2013. Arsenics as bioenergetic substrates. Biochim Biophys Acta, Bioenerg 1827:176-188.

214. Bai L, Fujishiro T, Huang G, Koch J, Takabayashi A, Yokono M, Tanaka A, Xu T, Hu X, Ermler U, Shima S. 2017. Towards artificial methanogenesis: biosynthesis of the [Fe]-hydrogenase cofactor and characterization of the semi-synthetic hydrogenase. Faraday Discuss 198:37-58.

215. Abou Hamdan A, Burlat B, Gutierrez-Sanz O, Liebgott PP, Baffert C, De Lacey AL, Rousset M, Guigliarelli B, Leger C, Dementin S. 2013. O2-independent formation of the inactive states of NiFe hydrogenase. Nat Chem Biol 9:15-7.

216. Keller MW, Lipscomb GL, Nguyen DM, Crowley AT, Schut GJ, Scott I, Kelly RM, Adams MWW. 2017. Ethanol production by the hyperthermophilic archaeon *Pyrococcus furiosus* by expression of bacterial bifunctional alcohol dehydrogenases. Microb Biotechnol 10:1535-1545.

217. Keller MW, Lipscomb GL, Loder AJ, Schut GJ, Kelly RM, Adams MW. 2015. A hybrid synthetic pathway for butanol production by a hyperthermophilic microbe. Metab Eng 27:101-6.

218. Keller MW, Schut GJ, Lipscomb GL, Menon AL, Iwuchukwu IJ, Leuko TT, Thorgersen MP, Nixon WJ, Hawkins AS, Kelly RM, Adams MWW. 2013. Exploiting microbial hyperthermophilicity to produce an industrial chemical, using hydrogen and carbon dioxide. Proc Natl Acad Sci U S A 110:5840-5845.

219. Lipscomb GL, Schut GJ, Thorgersen MP, Nixon WJ, Kelly RM, Adams MW. 2014. Engineering hydrogen gas production from formate in a hyperthermophile by heterologous production of an 18-subunit membrane-bound complex. J Biol Chem 289:2873-9.

220. Rollin JA, Martin del Campo J, Myung S, Sun F, You C, Bakovic A, Castro R, Chandrayan SK, Wu CH, Adams MW, Senger RS, Zhang YH. 2015. High-yield hydrogen production from biomass by in vitro metabolic engineering: Mixed sugars coutilization and kinetic modeling. Proc Natl Acad Sci U S A **112**:4964-9.

221. Kim EJ, Wu CH, Adams MW, Zhang YP. 2016. Exceptionally high rates of biological hydrogen production by biomimetic in vitro synthetic enzymatic pathways. Chemistry 22:16047-16051.

222. Kim JE, Kim EJ, Chen H, Wu CH, Adams MWW, Zhang YHP. 2017. Advanced water splitting for green hydrogen gas production through complete oxidation of starch by in vitro metabolic engineering. Metab Eng 44:246-252.

223. Zhang YH, Evans BR, Mielenz JR, Hopkins RC, Adams MW. 2007. High-yield hydrogen production from starch and water by a synthetic enzymatic pathway. PLoS One 2:e456.

224. Chandrayan SK, McTernan PM, Hopkins RC, Sun J, Jenney FE, Jr., Adams MW. 2012. Engineering hyperthermophilic archaeon *Pyrococcus furiosus* to overproduce its cytoplasmic [NiFe]-hydrogenase. J Biol Chem 287:3257-64.

225. Greene BL, Wu CH, McTernan PM, Adams MW, Dyer RB. 2015. Proton-coupled electron transfer dynamics in the catalytic mechanism of a [NiFe]-hydrogenase. J Am Chem Soc 137:4558-66.

226. Greene BL, Vansuch GE, Wu CH, Adams MW, Dyer RB. 2016. Glutamate Gated Proton-Coupled Electron Transfer Activity of a [NiFe]-Hydrogenase. J Am Chem Soc 138:13013-13021.

227. Evans RM, Brooke EJ, Wehlin SA, Nomerotskaia E, Sargent F, Carr SB, Phillips SE, Armstrong FA. 2016. Mechanism of hydrogen activation by [NiFe] hydrogenases. Nat Chem Biol 12:46-50.

228. McTernan PM, Chandrayan SK, Wu CH, Vaccaro BJ, Lancaster WA, Yang Q, Fu D, Hura GL, Tainer JA, Adams MW. 2014. Intact functional fourteen-subunit respiratory

membrane-bound [NiFe]-hydrogenase complex of the hyperthermophilic archaeon *Pyrococcus furiosus*. J Biol Chem 289:19364-72.

229. McTernan PM, Chandrayan SK, Wu CH, Vaccaro BJ, Lancaster WA, Adams MW. 2015. Engineering the respiratory membrane-bound hydrogenase of the hyperthermophilic archaeon *Pyrococcus furiosus* and characterization of the catalytically active cytoplasmic subcomplex. Protein Eng Des Sel 28:1-8.

230. Yu H, Wu CH, Schut GJ, Haja DK, Zhao G, Peters JW, Adams MWW, Li H. 2018. Structure of an ancient respiratory system. Cell doi:10.1016/j.cell.2018.03.071.

231. Baradaran R, Berrisford JM, Minhas GS, Sazanov LA. 2013. Crystal structure of the entire respiratory complex I. Nature 494:443-8.

232. Zickermann V, Wirth C, Nasiri H, Siegmund K, Schwalbe H, Hunte C, Brandt U. 2015. Structural biology. Mechanistic insight from the crystal structure of mitochondrial complex I. Science 347:44-9.

233. Vinothkumar KR, Zhu J, Hirst J. 2014. Architecture of mammalian respiratory complex I. Nature 515:80-84.

234. Efremov RG, Sazanov LA. 2012. The coupling mechanism of respiratory complex I - a structural and evolutionary perspective. Biochim Biophys Acta 1817:1785-95.

235. Page CC, Moser CC, Chen X, Dutton PL. 1999. Natural engineering principles of electron tunnelling in biological oxidation-reduction. Nature 402:47-52.

236. Haja DK, Wu CH, Poole II FL, Willams S, Sugar J, Jones AK, Adams MWW. 2018. *Pyrobaculum aerophilum* thiosulfate reductase heterologously-expressed in *Pyrococcus furiosus* is more active with molybdenum than with tungsten. Biochemistry Submitted.

237. Sun J, Hopkins RC, Jenney FE, McTernan PM, Adams MW. 2010. Heterologous expression and maturation of an NADP-dependent [NiFe]-hydrogenase: a key enzyme in biofuel production. PLoS One 5:e10526.

APPENDIX A

PRODUCTION AND APPLICATION OF A SOLUBLE HYDROGENASE FROM *PYROCOCCUS FURIOSUS*

Wu CH, McTernan PM, Walter ME, Adams MW. (2015) Production and Application of a Soluble Hydrogenase from *Pyrococcus furiosus*. Archaea. *2015*:912582.

Abstract

Hydrogen gas is a potential renewable alternative energy carrier that could be used in the future to help supplement humanity's growing energy needs. Unfortunately, current industrial methods for hydrogen production are expensive or environmentally unfriendly. In recent years research has focused on biological mechanisms for hydrogen production and specifically on hydrogenases, the enzyme responsible for catalyzing the reduction of protons to generate hydrogen. In particular, a better understanding of this enzyme might allow us to generate hydrogen that does not use expensive metals, such as platinum, as catalysts. The soluble hydrogenase I (SHI) from the hyperthermophile *Pyrococcus furiosus*, a member of the euryarchaeota, has been studied extensively and used in various biotechnological applications. This review summarizes the strategies used in engineering and characterizing three different forms of SHI and the properties of the recombinant enzymes. SHI has also been used in in vitro systems for hydrogen production and NADPH generation and these systems are also discussed.

Introduction

Hydrogen is a potential renewable and carbon neutral energy carrier. It has three times the energy content per unit mass of fossil fuels [1]. The concept of replacing current gasoline-based vehicles with hydrogen fuel cell vehicles (HFCVs) has gained a lot of attention recently [2]. A major advantage of HFCVs is that water is the only waste product, and hence they eliminate the harmful exhaust of current vehicles, thereby benefiting human health and the climate [2, 3]. With the introduction of commercially available HFCVs in many counties in 2015, the demand for hydrogen is anticipated to dramatically increase in the near future [3]. Unfortunately, current methods of producing hydrogen rely on fossil fuels and are expensive. They include steam reforming of natural gas, which produces greenhouse gases, and electrolysis to split water uses the expensive metal platinum as a catalyst [4]. New and renewable methods are obviously needed for the generation of hydrogen and biological-based systems have a great deal of potential.

The enzyme hydrogenase catalyzes the simplest chemical reaction in nature, the reversible interconversion of protons, electrons, and hydrogen gas: $2H^+ + 2e^- \leftrightarrow H_2$. Such enzymes are widespread in bacteria and Archaea and are even found in some Eukarya [5]. Hydrogenases enable organisms to remove excess reducing power generated during metabolism by evolving hydrogen, or they can oxidize hydrogen to generate reducing power for growth [6]. Hydrogenases can be classified into three types based on the metal content of their catalytic sites, and they are referred to as [NiFe] hydrogenases, [FeFe] hydrogenases, and mononuclear Fe hydrogenases [7]. The [NiFe] hydrogenases are the most ubiquitous and have been extensively studied [5]. They are further classified into four different types (groups 1–4) based on the peptide sequence used to bind the [NiFe]-containing active site [7]. Group 1 [NiFe] hydrogenases are the best studied among the four groups [5]. The assembly of the [NiFe] catalytic site of these hydrogenases requires eight

maturation proteins, based on the mechanism elucidated for Escherichia coli hydrogenase 3 [8]. The [NiFe] hydrogenases are also reversibly inactivated in the presence of oxygen [9].

Herein we focus on the [NiFe] hydrogenases of *Pyrococcus furiosus*, a strictly anaerobic archaeon that grows optimally at 100°C. This organism utilizes carbohydrates as a carbon source for growth and generates acetate, carbon dioxide, and hydrogen gas as end products. *P. furiosus* contains three different types of [NiFe] hydrogenase, a membrane-bound enzyme (MBH) and two soluble hydrogenases (SHI and SHII). MBH is the hydrogenase responsible for producing H_2 during its fermentative metabolism wherein it oxidizes the reduced ferredoxin generated during the oxidation of glucose to acetate [15, 16]. In contrast, SHI and SHII utilize NADP(H) and NAD(H) as electron carriers, respectively, and while their functions have not been established, it is assumed that they can recycle some of the H_2 produced by MBH under the appropriate growth conditions. All three hydrogenases have been purified and characterized [6, 17–19]. This review focuses on the engineering, properties, and applications of SHI.

Expression and purification

P. furiosus SHI is a heterotetramer encoded by a four-gene operon (PF0891–0894). A structural model of SHI has been proposed based on sequence analyses of the four subunits [10]. As shown in Figure A1, PF0894 is the subunit harboring the Fe- and Ni-containing catalytic site wherein the Fe atom has three diatomic ligands, one -CO and two -CN. PF0892 contains the flavin and a [2] cluster and is the site of interaction with NADP(H). PF0891 and PF0893 contain two and three [4] clusters, respectively, for electron transfer between the flavin and the active site. SHI was first purified and characterized using four chromatographic steps, which yielded the intact

heterotetramer [6]. The yield from this purification was very low and an improvement in yield was needed in order to generate the enzyme for detailed characterization studies.

In order to improve the yield of SHI, an attempt was made to heterologously express SHI in E. coli, with coexpression of the genes encoding the accessory proteins that are necessary for proper assembly of the [NiFe] active site [10]. This was also the first example of heterologously expressing a functional [NiFe] hydrogenase in E. coli, as well as demonstrating expression of a hydrogenase in a distantly related host. Unfortunately, the yield of this heterologous expressed SHI was lower than the natively purified SHI from *P. furiosus* [10]. Although the expression of SHI in a genetically tractable host, such as E. coli, was a significant achievement, this system was not suitable to produce large amounts of this enzyme.

Once a genetic system was established in *P. furiosus*, the host organism could be used to both overproduce and engineer SHI [20]. The genetic system was established by removing the *pyrF* gene in a genetically tractable strain of *P. furiosus* termed COM1. *pyrF* is essential for uracil biosynthesis and allows for selection and counter selection based on uracil biosynthesis in a minimal medium. Moreover, it was demonstrated that the genes encoding SHI could be deleted from *P. furiosus* without any apparent effect on cell growth [20]. This suggested that SHI was not an essential enzyme and could be engineered in various ways without affecting the metabolism of *P. furiosus*, and this proved to be the case.

In the first attempt to overexpress the four genes encoding SHI and to affinity-tag the enzyme [11], transcription of SHI was put under the control of a strong constitutive promoter, P_{slp}, which controls expression of the gene encoding the S-layer protein. In addition, PF0891 was engineered to include a Strep-II affinity tag (Figure A2). A Strep tag was chosen instead of a polyhistidine tag as the latter might interfere with the incorporation of nickel into the catalytic site

of SHI. Using this approach and a one-step affinity purification, approximately seven times more SHI (per gram of cells) was purified from the cytoplasmic fraction of *P. furiosus* compared to the original purification of SHI [11]. Interestingly, expression of the genes encoding the [NiFe]-maturation proteins was at the same level in the recombinant strain as in the parent strain even though the genes encoding SHI (under the control of P_{slp}) were increased by about 10-fold. The native levels of the maturation proteins were therefore able to synthesize almost an order of magnitude more SHI and produce the active enzyme.

Since a functional SHI is not required for growth of *P. furiosus* [20], this allowed the engineering of nonfunctional forms that did not utilize H_2 and/or NADP(H) as substrates. A dimeric version of SHI that contained only PF0893 and PF0894 was successfully produced (Figure A1). This enzyme evolved H_2 from artificial electron donors but did not oxidize NADPH, as it lacked the NADPH-oxidizing subunit [13]. Engineering dimeric SHI also involved the development of another selectable marker, arginine decarboxylase (pdaD), to be used for genetic manipulations in *P. furiosus*. In addition, the purified dimeric SHI had a polyhistidine (9-His) tag at the N-terminus of PF0893. The results demonstrated that this type of tag does not interfere with the assembly of nickel into the catalytic site of SHI as the enzyme retained its H_2-production activity (using an artificial dye as the electron donor) after purification using the immobilized nickel-affinity chromatography step.

Based on the success in engineering and purifying 9x-His tag dimeric SHI, the tetrameric SHI was engineered to contain a polyhistidine affinity tag to determine if this would improve the efficiency of purification compared to the Strep-tag II tetramer [12]. The same strategy to overexpress SHI (tagging at the N-terminus of PF0891) was used, except that the Strep-tag II was replaced by a 9x-His tag (Figure A2). This resulted in an 8-fold improvement in the yield compared

to the Strep-tag II and a 50-fold higher yield of SHI compared to the original native purification. A comparison of the yields for the different purification procedures is shown in Table A1 and the strains constructed for SHI expression are shown in Table A2.

During the affinity purification of the His-tagged tetrameric form of SHI, a trimeric form was observed eluting from the affinity column that lacked the large [NiFe]-containing subunit (PF0894, see Figure A1). This Ni-free trimeric SHI represented approximately 2% of total SHI [12]. This discovery supports the proposed maturation mechanism of [NiFe] hydrogenases in which the three subunits of the *P. furiosus* enzyme (PF0891–PF0893) form a trimeric complex before the catalytic subunit (PF0894) is assembled [8]. This complex then binds to the catalytic subunit to generate the active enzyme. Hence, in an overexpressed strain, the processing machinery may not be able to keep up with the production of the four protein subunits, such that there is a very slight excess of the Ni-free trimeric form. These results are also consistent with the notion that the catalytic subunit alone cannot be expressed and isolated in an active form and needs the other hydrogenase subunits to be processed. For example, when the catalytic subunit of a cytoplasmic hydrogenase of *Thermococcus kodakarensis* was expressed in *E. coli*, the purified subunit was inactive and contained Fe, Zn, and Ca atoms but not Ni, indicating that it was not properly assembled [21].

Properties

SHI is classified as a group 3 bidirectional [NiFe] hydrogenase based on the amino acid sequence that surround the four cysteinyl residues that coordinate the [NiFe] catalytic site [7]. In in vitro assays, SHI oxidizes H_2 and reduces NADP+ and can also reduce protons in vitro to evolve

H_2 using NADPH as the electron donor [22]. Kinetic studies on SHI showed that it has ten times higher hydrogen consumption activity than hydrogen production and has a high affinity for hydrogen (K_m 20 μM) and NADP+ (K_m 37 μM) [6, 23, 24]. This suggested that the physiological function of SHI is to regenerate NADPH from the hydrogen produced by MBH [24]. However, since the SHI deletion mutant strain did not have a phenotype under the growth conditions used in the laboratory, the true physiological function of SHI is still a mystery [20]. As shown in Figure A1, it is predicted that NADPH binds to the flavin-containing subunit PF0892 and the electrons are transferred through the iron-sulfur clusters of PF0892, PF0891, and PF0893 and finally to the catalytic site in PF0894 in order to evolve hydrogen. As expected, the dimeric form of SHI did not interact with NADP(H) but, interestingly, it accepted electrons directly from pyruvate ferredoxin oxidoreductase (POR) to produce hydrogen in the absence of an intermediate electron carrier. This two-enzyme system therefore directly oxidized pyruvate to hydrogen gas (and acetyl-CoA) [13]. Potentially, the POR subunit that would normally reduce ferredoxin is able to directly transfer electrons to iron-sulfur clusters in dimeric SHI that are exposed due to the lack of the other two subunits (Figure A1).

P. furiosus is a hyperthermophile that grows at 100°C so it would be expected that SHI is extremely stable at high temperature and this proved to be the case. The half-life of SHI at 90°C (as measured by its hydrogen evolution activity) is 14 hours for the native enzyme and 6 hours for the affinity tagged enzyme [12]. SHI is not a very oxygen-sensitive enzyme. The half-life in air at 25°C (as measured by loss of hydrogen evolution activity at 80°C) was 21 hours for native SHI and 25 hours for the affinity tagged version [11]. SHI is much less sensitive to inactivation by oxygen compared to the well-characterized group 1 [NiFe] hydrogenases, which are typically inactivated within an hour after exposure to oxygen [25]. Although it is regarded as a strictly

anaerobic microorganism, *P. furiosus* is also resistant to oxygen and contains a mechanism of oxygen detoxification. This allows it to grow even in the presence of 8% (v/v) oxygen. SHI does not contribute to the resistance mechanism as the SHI deletion strain behaved similarly to the parent strain [26]. The general resistance to oxygen of SHI is an attractive property for biofuel-related applications.

SHI has been characterized previously by electron paramagnetic resonance (EPR) and Fourier transform infrared (FTIR) spectroscopy [6, 27–29]. The EPR properties of the enzyme are consistent with the iron-sulfur clusters predicted in the model as shown in Figure A1 [6, 29]. EPR can also be used to follow the electronic state of the [NiFe] active site. In general, the Ni atom in [NiFe] hydrogenases typically exhibits three paramagnetic states referred to as Ni-A, Ni-B, and Ni-C. Ni-A is referred to as the inactive unready state and requires incubation under reducing conditions for hours to become active. Ni-B is referred to as the inactive ready state of the enzyme and this can be reactivated within minutes under reducing conditions [5]. These EPR-active states are further distinguished by the type of oxygen ligand bound in the active site. Ni-A is believed to harbor a peroxide ligand while Ni-B is thought to harbor a bound hydroxide ligand, which may explain the faster reactivation for Ni-B state as the hydroxide would be easier to remove upon reduction. Ni-C represents the active ready state of the enzyme, which is free of any oxygen species, and performs the catalytic reaction with hydrogen [5]. These EPR detectable states (Ni-A-like, Ni-B-like, Ni-C) have been observed within *P. furiosus* SHI although a heat treatment step was required to observe some of these signals [27].

The diamagnetic states of the Ni atom in [NiFe] hydrogenases can be observed by FTIR, which detects the vibration frequencies of the CO and CN ligands bound to the Fe atom in the active site. The FTIR signals on the CN ligand of SHI have been reported [28]. The frequencies at

1959, 1950, 1967, and 1954 cm−1 were assigned to the $Ni_{u/r}$-A/B, Ni_a-S, Ni_a-C, and Ni_a-SR states, respectively [5, 28]. These are in agreement with the data obtained from the extensively studied group 1 hydrogenases. The results from X-ray absorption spectroscopy also show that the nickel coordination geometry of SHI is identical to that of the active site of the group 1 hydrogenases [30]. Taken together, all of these data show that the [NiFe] site of SHI assumes the same redox states and similar architecture as the catalytic sites of the standard group 1 hydrogenases. Indeed, SHI was recently used as a model [NiFe] hydrogenase to investigate the catalytic mechanism using nanosecond transient infrared and visible absorbance spectroscopy [31]. This approach identified three new catalytic intermediates and established the first elementary mechanistic description of catalysis by a [NiFe] hydrogenase.

Biotechnological applications

Like all hydrogenases, SHI catalyzes the reversible oxidation of hydrogen but it is extremely unusual in that it is one of the few hydrogenases that use NAD(P)H as an electron carrier. Hence, SHI can oxidize NADPH to produce hydrogen or can use hydrogen to reduce NADP+, and applications exist that rely on both of these reactions. In general industrial applications, oxidoreductase-type enzymes have been used as biocatalysts in organic synthesis where they catalyze stereoselective reductions. The products from these syntheses include pharmaceuticals, artificial flavors, and agrochemicals [32]. However, such oxidoreductases require a cofactor, either NADH or NADPH, as a source of reductant, but these are too expensive to be used directly in industrial synthesis. SHI was the first hydrogenase reported to be used in an application to regenerate NADPH using hydrogen as the source of reducing power. It was used to regenerate NADPH in enantioselective reductive reactions in vitro catalyzed by Thermoanaerobium alcohol

dehydrogenase [32]. With SHI and hydrogen, the yield of product was greatly improved compared to using NADPH alone. It was also reported that SHI was able to produce approximately 200 μmol of NADPH in 100 hours of repetitive batch reactions. SHI was used at 40°C, at which temperature it had a half-life of 208 hours [32]. These results demonstrate that SHI functions efficiently at temperatures far below its optimum (>90°C). Instead of batch reactions, SHI has been attached on graphite and glass beads in a continuous NADPH production system, and it was also demonstrated that SHI was electrochemically active in the presence of hydrogen in cyclic voltammetric experiments [33]. Electrochemical and spectrophotometric studies also supported the potential applications on biofuel cell and bioelectrocatalytic applications, where SHI immobilized electrodes are used to replace electrocatalysts, such as platinum [34, 35].

SHI has also been used in several different hydrogen production systems. In an in vitro hydrogen photoproduction system, SHI accepted electrons from a light activated semiconductor, titanium dioxide (TiO_2) [36, 37]. In this system, a mediator, methyl viologen, was used initially as the electron carrier, but it was found that SHI accepted electrons directly from the photoactivated TiO_2. Improvements on this system have also been reported [38, 39]. Instead of using a mixture of SHI and TiO_2, a two-compartment system was developed that was separated by a membrane. Anodized tubular TiO_2 electrode (ATTE) was placed at the anode and SHI immobilized on the ATTE was used at the cathode. ATTE on the anode splits water into protons and oxygen, and the electrons were conducted into a solar cell and then transferred to cathodic SHI immobilized ATTE for hydrogen production. This system avoided using the rate-limiting step of electron transfer from the photocatalyst to the enzyme thereby improving system performance [38]. It was also shown that SHI and ATTE could be chemically cross-linked, which had a higher hydrogen production yield compared to either a slurry of SHI-ATTE or the direct adsorption of SHI onto ATTE [39].

SHI is also essential for a hydrogen-producing in vitro system that has been developed whereby a variety of sugars are completely oxidized to hydrogen and carbon dioxide. This stemmed from an initial report showing that purified SHI could successfully be used in an in vitro hydrogen production system when combined with purified glucose dehydrogenase (GDH) from Thermoplasma acidophilum [40]. In this system, glucose was oxidized by GDH to generate NADPH and the NADPH was utilized by SHI for hydrogen production. NADP+ produced by SHI was recycled by GDH for continual hydrogen production. In addition, this two-enzyme hydrogen production system also generated a high value by-product, gluconic acid, from glucose oxidation [40]. This system was further modified to use renewable resources for hydrogen production, including sucrose, lactose, cellulose, xylan, starch, and pretreated aspen wood, where corresponding enzymes were added to produce monosaccharides. These monosaccharides were further hydrolyzed by the appropriate enzymes for the hydrogen production [41, 42]. This has now been developed into a novel and highly efficient method for in vitro hydrogen production using a range of sugars and various mixtures of purified enzymes where, in all cases, SHI is the catalyst for hydrogen production [43]. Compared to biological fermentations (4 H_2/glucose), this cell-free synthetic pathway biotransformation (SyPaB) has a three-time higher theoretical yield (12 H_2/glucose). Different sugar sources can be used, including starch [43], cellulosic materials [44], xylose [45], and sucrose [46]. SyPaB has three basic modules for biohydrogen production as shown in Figure A3, for example, using starch as the sugar source, which is first phosphorylated using inorganic phosphate rather than ATP to produce glucose 6-phosphate (G6P). G6P is oxidized by the pentose phosphate pathway in the second module in order to generate NADPH and to regenerate G6P. In the third module, NADPH produced in the second module is used for hydrogen generation by SHI [43]. This coupled system of SHI and pentose phosphate pathway for

biohydrogen production was first described by Woodward et al. [47]. The net reaction is given by the following equation: $C_6H_{10}O_5$ (l) + 7 H_2O (l) → 12 H_2 (g) + 6 CO_2 (g). The rate of hydrogen production from glucose was reported to be two times higher than the other substrate sources [48]. Moreover, this pathway exhibited one of the highest biohydrogen generation rates, 157 mmol/L/h, while using glucose 6-phosphate as the electron source [48]. The cost of biohydrogen production by SyPaB using carbohydrates as the source of reductant could be 40–75% lower than commodity prices [14]. Interestingly, a very recent study showed that glucose and xylose from plant biomass could be completely converted to hydrogen by the in vitro enzymatic pathway containing *P. furiosus* SHI [49], which bodes well for the future development of this synthetic approach.

Conclusions

P. furiosus SHI has been successfully overexpressed in the native host in affinity-tagged forms and can be purified from the cytoplasmic extract in high yield by a single chromatography step. The most efficient purification used a polyhistidine tag, and the overall yield was 50 times higher than that obtained in the original purification of native SHI, which used multistep column chromatography. SHI has been characterized spectroscopically using EPR and FTIR. Although SHI is classified as a group 3 hydrogenase, the properties of its [NiFe] catalytic site appear to be very similar to those of the extensively characterized group 1 enzymes. SHI has a wide temperature spectrum of enzyme activity (30–95°C) and is less sensitive to oxygen inactivation than typical [NiFe] hydrogenases. It is one of the few hydrogenases that uses NADP(H) as an electron carrier and this has been taken advantage of in several biotechnological applications. These include using SHI to regenerate NADPH with hydrogen as the electron donor for NADPH-dependent

oxidoreductase reactions and using SHI to produce hydrogen from NADPH in cell-free synthetic pathways that oxidize a variety of sugars, as well as those in plant biomass, completely to hydrogen gas and carbon dioxide. The availability of significant quantities of recombinant and affinity-tagged SHI should facilitate the further development of these applications, as well as enabling more fundamental structure-function studies of this fascinating enzyme.

Acknowledgments

This work was supported by a Grant (DE-FG05-95ER20175 to Michael W. W. Adams) from the Division of Chemical Sciences, Geosciences and Biosciences, Office of Basic Energy Sciences of the Department of Energy.

References

1. T. N. Vezirolu and F. Barbir, “Hydrogen: the wonder fuel,” *International Journal of Hydrogen Energy*, vol. 17, no. 6, pp. 391–404, 1992.

2. M. Z. Jacobson, W. G. Colella, and D. M. Golden, “Cleaning the air and improving health with hydrogen fuel-cell vehicles,” *Science*, vol. 308, no. 5730, pp. 1901–1905, 2005.

3. J. E. Kang, T. Brown, W. W. Recker, and G. S. Samuelsen, “Refueling hydrogen fuel cell vehicles with 68 proposed refueling stations in California: measuring deviations from daily travel patterns,” *International Journal of Hydrogen Energy*, vol. 39, no. 7, pp. 3444–3449, 2014.

4. H.-S. Lee, W. F. J. Vermaas, and B. E. Rittmann, “Biological hydrogen production: prospects and challenges,” *Trends in Biotechnology*, vol. 28, no. 5, pp. 262–271, 2010.

5. W. Lubitz, H. Ogata, O. Rüdiger, and E. Reijerse, “Hydrogenases,” *Chemical Reviews*, vol. 114, no. 8, pp. 4081–4148, 2014.

6. F. O. Bryant and M. W. Adams, “Characterization of hydrogenase from the hyperthermophilic archaebacterium, *Pyrococcus furiosus*,” *The Journal of Biological Chemistry*, vol. 264, no. 9, pp. 5070–5079, 1989.

7. P. M. Vignais and B. Billoud, “Occurrence, classification, and biological function of hydrogenases: an overview,” *Chemical Reviews*, vol. 107, no. 10, pp. 4206–4272, 2007.

8. A. Böck, P. W. King, M. Blokesch, and M. C. Posewitz, “Maturation of hydrogenases,” *Advances in Microbial Physiology*, vol. 51, pp. 1–71, 2006.

9. J. O. Eberly and R. L. Ely, "Thermotolerant hydrogenases: biological diversity, properties, and biotechnological applications," *Critical Reviews in Microbiology*, vol. 34, no. 3-4, pp. 117–130, 2008.

10. J. Sun, R. C. Hopkins, F. E. Jenney Jr., P. M. McTernan, and M. W. W. Adams, "Heterologous expression and maturation of an NADP-Dependent [NiFe]-Hydrogenase: a key enzyme in biofuel production," *PLoS ONE*, vol. 5, no. 5, Article ID e10526, 2010.

11. S. K. Chandrayan, P. M. McTernan, R. C. Hopkins, J. Sun, F. E. Jenney Jr., and M. W. W. Adams, "Engineering hyperthermophilic archaeon *Pyrococcus furiosus* to overproduce its cytoplasmic [NiFe]-hydrogenase," *The Journal of Biological Chemistry*, vol. 287, no. 5, pp. 3257–3264, 2012.

12. S. K. Chandrayan, C.-H. Wu, P. M. McTernan, and M. W. W. Adams, "High yield purification of a tagged cytoplasmic [NiFe]-hydrogenase and a catalytically-active nickel-free intermediate form," *Protein Expression and Purification*, vol. 107, pp. 90–94, 2015.

13. R. C. Hopkins, J. Sun, F. E. Jenney, S. K. Chandrayan, P. M. McTernan, and M. W. W. Adams, "Homologous expression of a subcomplex of *Pyrococcus furiosus* hydrogenase that interacts with pyruvate ferredoxin oxidoreductase," *PLoS ONE*, vol. 6, no. 10, Article ID e26569, 2011.

14. Y.-H. P. Zhang, "A sweet out-of-the-box solution to the hydrogen economy: is the sugar-powered car science fiction?" *Energy and Environmental Science*, vol. 2, no. 3, pp. 272–282, 2009.

15. P. J. Silva, E. C. D. van den Ban, H. Wassink et al., "Enzymes of hydrogen metabolism in *Pyrococcus furiosus*," *European Journal of Biochemistry*, vol. 267, no. 22, pp. 6541–6551, 2000.

16. R. Sapra, K. Bagramyan, and M. W. W. Adams, “A simple energy-conserving system: proton reduction coupled to proton translocation,” *Proceedings of the National Academy of Sciences of the United States of America*, vol. 100, no. 13, pp. 7545–7550, 2003.

17. K. Ma, R. Weiss, and M. W. W. Adams, “Characterization of hydrogenase II from the hyperthermophilic archaeon *Pyrococcus furiosus* and assessment of its role in sulfur reduction,” *Journal of Bacteriology*, vol. 182, no. 7, pp. 1864–1871, 2000.

18. P. M. McTernan, S. K. Chandrayan, C.-H. Wu et al., “Intact functional fourteen-subunit respiratory membrane-bound [NiFe]-hydrogenase complex of the hyperthermophilic archaeon *Pyrococcus furiosus*,” *The Journal of Biological Chemistry*, vol. 289, no. 28, pp. 19364–19372, 2014.

19. P. M. McTernan, S. K. Chandrayan, C. H. Wu, B. J. Vaccaro, W. A. Lancaster, and M. W. Adams, “Engineering the respiratory membrane-bound hydrogenase of the hyperthermophilic archaeon *Pyrococcus furiosus* and characterization of the catalytically active cytoplasmic subcomplex,” *Protein Engineering, Design & Selection*, vol. 28, no. 1, pp. 1–8, 2015.

20. G. L. Lipscomb, K. Stirrett, G. J. Schut et al., “Natural competence in the hyperthermophilic archaeon *Pyrococcus furiosus* facilitates genetic manipulation: construction of markerless deletions of genes encoding the two cytoplasmic hydrogenases,” *Applied and Environmental Microbiology*, vol. 77, no. 7, pp. 2232–2238, 2011.

21. D. Sasaki, S. Watanabe, T. Kanai, H. Atomi, T. Imanaka, and K. Miki, “Characterization and in vitro interaction study of a [NiFe] hydrogenase large subunit from the hyperthermophilic archaeon *Thermococcus kodakarensis* KOD1,” *Biochemical and Biophysical Research Communications*, vol. 417, no. 1, pp. 192–196, 2012.

22. K. S. Ma, Z. H. Zhou, and M. W. W. Adams, “Hydrogen production from pyruvate by enzymes purified from the hyperthermophilic archaeon, *Pyrococcus furiosus*: a key role for NADPH,” *FEMS Microbiology Letters*, vol. 122, no. 3, pp. 245–250, 1994.

23. D. J. van Haaster, P.-L. Hagedoorn, J. A. Jongejan, and W. R. Hagen, “On the relationship between affinity for molecular hydrogen and the physiological directionality of hydrogenases,” *Biochemical Society Transactions*, vol. 33, no. 1, pp. 12–14, 2005.

24. D. J. van Haaster, P. J. Silva, P.-L. Hagedoorn, J. A. Jongejan, and W. R. Hagen, “Reinvestigation of the steady-state kinetics and physiological function of the soluble NiFe-hydrogenase I of *Pyrococcus furiosus*,” *Journal of Bacteriology*, vol. 190, no. 5, pp. 1584–1587, 2008.

25. H. M. Van Der Westen, S. G. Mayhew, and C. Veeger, “Effect of growth conditions on the content and O_2-stability of hydrogenase in the anaerobic bacterium *Desulfovibrio vulgaris* (Hildenborough),” *FEMS Microbiology Letters*, vol. 7, no. 1, pp. 35–39, 1980.

26. M. P. Thorgersen, K. Stirrett, R. A. Scott, and M. W. W. Adams, “Mechanism of oxygen detoxification by the surprisingly oxygen-tolerant hyperthermophilic archaeon, *Pyrococcus furiosus,” Proceedings of the National Academy of Sciences of the United States of America*, vol. 109, no. 45, pp. 18547–18552, 2012.

27. P. J. Silva, B. de Castro, and W. R. Hagen, “On the prosthetic groups of the NiFe sulfhydrogenase from *Pyrococcus furiosus*: topology, structure, and temperature-dependent redox chemistry,” *Journal of Biological Inorganic Chemistry*, vol. 4, no. 3, pp. 284–291, 1999.

28. H. X. Wang, C. Y. Ralston, D. S. Patil et al., "Nickel L-edge soft X-ray spectroscopy of nickel-iron hydrogenases and model compounds—evidence for high-spin nickel(II) in the active enzyme," *Journal of the American Chemical Society,* vol. 122, no. 43, pp. 10544–10552, 2000.

29. A. F. Arendsen, P. T. M. Veenhuizen, and W. R. Hagen, "Redox properties of the sulfhydrogenase from *Pyrococcus furiosus*," *FEBS Letters,* vol. 368, no. 1, pp. 117–121, 1995.

30. J. Van Elp, G. Peng, Z. H. Zhou et al., "Nickel L-edge X-ray absorption spectroscopy of *Pyrococcus furiosus* hydrogenase," *Inorganic Chemistry,* vol. 34, no. 10, pp. 2501–2504, 1995.

31. B. L. Greene, C. Wu, P. M. McTernan, M. W. Adams, and R. B. Dyer, "Proton-coupled electron transfer dynamics in the catalytic mechanism of a [NiFe]-hydrogenase," *Journal of the American Chemical Society,* vol. 137, no. 13, pp. 4558–4566, 2015.

32. R. Mertens, L. Greiner, E. C. D. van den Ban, H. B. C. M. Haaker, and A. Liese, "Practical applications of hydrogenase I from *Pyrococcus furiosus* for NADPH generation and regeneration," *Journal of Molecular Catalysis B: Enzymatic,* vol. 24-25, pp. 39–52, 2003.

33. L. Greiner, I. Schröder, D. H. Müller, and A. Liese, "Utilization of adsorption effects for the continuous reduction of NADP+ with molecular hydrogen by *Pyrococcus furiosus* hydrogenase," *Green Chemistry,* vol. 5, no. 6, pp. 697–700, 2003.

34. W. Johnston, M. J. Cooney, B. Y. Liaw, R. Sapra, and M. W. W. Adams, "Design and characterization of redox enzyme electrodes: new perspectives on established techniques with application to an extremeophilic hydrogenase," *Enzyme and Microbial Technology,* vol. 36, no. 4, pp. 540–549, 2005.

35. O. G. Voronin, D. J. Van Haaster, E. E. Karyakina, W. R. Hagen, and A. A. Karyakin, “Direct bioelectrocatalysis by NADP-reducing hydrogenase from *Pyrococcus furiosus*,” *Electroanalysis*, vol. 19, no. 21, pp. 2264–2266, 2007.

36. A. Selvaggi, C. Tosi, U. Barberini, E. Franchi, F. Rodriguez, and P. Pedroni, “In vitro hydrogen photoproduction using *Pyrococcus furiosus* sulfhydrogenase and TiO_2,” *Journal of Photochemistry and Photobiology A: Chemistry*, vol. 125, no. 1–3, pp. 107–112, 1999.

37. P. Pedroni, G. M. Mura, G. Galli, C. Pratesi, L. Serbolisca, and G. Grandi, “The hydrogenase from the hyperthermophilic archaeon *Pyrococcus furiosus*: from basic research to possible future applications,” *International Journal of Hydrogen Energy*, vol. 21, no. 10, pp. 853–858, 1996.

38. S. Bae, E. Shim, J. Yoon, and H. Joo, “Enzymatic hydrogen production by light-sensitized anodized tubular TiO_2 photoanode,” *Solar Energy Materials and Solar Cells*, vol. 92, no. 4, pp. 402–409, 2008.

39. J. Yoon, S. Bae, E. Shim, and H. Joo, “*Pyrococcus furiosus*-immobilized anodized tubular titania cathode in a hydrogen production system,” *Journal of Power Sources*, vol. 189, no. 2, pp. 1296–1301, 2009.

40. J. Woodward, S. M. Mattingly, M. Danson, D. Hough, N. Ward, and M. Adams, “In vitro hydrogen production by glucose dehydrogenase and hydrogenase,” *Nature Biotechnology*, vol. 14, no. 7, pp. 872–874, 1996.

41. J. Woodward and M. Orr, “Enzymatic conversion of sucrose to hydrogen,” *Biotechnology Progress*, vol. 14, no. 6, pp. 897–902, 1998.

42. J. Woodward, K. A. Cordray, R. J. Edmonston, M. Blanco-Rivera, S. M. Mattingly, and B. R. Evans, “Enzymatic hydrogen production: conversion of renewable resources for energy production,” *Energy and Fuels*, vol. 14, no. 1, pp. 197–201, 2000.

43. Y.-H. P. Zhang, B. R. Evans, J. R. Mielenz, R. C. Hopkins, and M. W. W. Adams, “High-yield hydrogen production from starch and water by a synthetic enzymatic pathway,” *PLoS ONE*, vol. 2, no. 5, article e456, 2007.

44. X. Ye, Y. Wang, R. C. Hopkins et al., “Spontaneous high-yield production of hydrogen from cellulosic materials and water catalyzed by enzyme cocktails,” *ChemSusChem*, vol. 2, no. 2, pp. 149–152, 2009.

45. J. S. Martín del Campo, J. Rollin, S. Myung et al., “High-yield production of dihydrogen from xylose by using a synthetic enzyme cascade in a cell-free system,” *Angewandte Chemie—International Edition*, vol. 52, no. 17, pp. 4587–4590, 2013.

46. S. Myung, J. Rollin, C. You et al., “In vitro metabolic engineering of hydrogen production at theoretical yield from sucrose,” *Metabolic Engineering*, vol. 24, pp. 70–77, 2014.

47. J. Woodward, M. Orr, K. Cordray, and E. Greenbaum, “Enzymatic production of biohydrogen,” *Nature*, vol. 405, no. 6790, pp. 1014–1015, 2000.

48. J. A. Rollin, X. Ye, J. M. Del Campo, M. W. Adams, and Y. H. Zhang, “Novel hydrogen bioreactor and detection apparatus,” *Advances in Biochemical Engineering/Biotechnology*, 2014.

49. J. A. Rollin, J. Martin del Campo, S. Myung et al., “High-yield hydrogen production from biomass by in vitro metabolic engineering: mixed sugars coutilization and kinetic modeling,” *Proceedings of the National Academy of Sciences*, vol. 112, no. 16, pp. 4964–4969, 2015.

Table A1. Yields of SHI from different expression systems

Protein	Expression host	Affinity tag	Purification steps	Protein yield (mg)[1]	Reference
Native SHI	*P. furiosus*	-	4	2.5	[6]
Recombinant SHI	*E. coli*	-	3	0.16	[15]
Strep-tag II SHI	*P. furiosus*	Strep-tag II	1	17	[17]
9x-His Dimeric SHI	*P. furiosus*	9x-His tag	2	16	[18]
9x-His SHI	*P. furiosus*	9x-His tag	1	135	[19]

[1]Protein yield from 100 g of cells (wet weight)

Table A2. Strains for SHI expression

Strain designation	Genotype	Deleted or inserted ORF/elements	Reference
MW400	P_{slp} Strep-tag II-*shIβγδα*	P_{slp} Strep-tag II, P_{gdh}-*pyrF*	[17]
MW402	Δ *shIβγδα* P_{slp} 9x-His-*shIδα*	P_{slp} 9x-His-*shIδα*, P_{pdaD}-*pdaD*	[18]
MW430	P_{slp} 9x-His-*shIβγδα*	P_{slp}9x-His, P_{gdh}-*pyrF*	[19]
MW434	P_{slp} 9x-His-*shIβγδα*	P_{slp}9x-His, P_{gdh}-*pyrF*	[19]

Figure A1

Models of tetrameric (a), Ni-free trimeric (b), and dimeric (c) forms of SHI. These are modified from [10] and are based on the cofactor and iron-sulfur cluster contents in sequence analysis. The proposed electron flow from NADPH oxidation to hydrogen evolution is also shown. Four different strains of *P. furiosus* were constructed to obtain the various forms of SHI. They are designated as MW400, MW430, MW434, and MW402 and their properties are listed in Table A2. These were used to prepare PF0891 Strep-tag II SHI [11], PF0891 9x-His tag SHI [12], PF0894 9x-His tag SHI [12], and PF0893 9x-His tag dimeric SHI [13], respectively. SDS PAGE gels show the purity of the different forms: (d) lane 1, Strep-tag II tetrameric SHI; (e) lane 2, 9x-His tag tetrameric SHI; lane 3, 9x-His tag Ni-free trimeric SHI; (f) lane 4, native SHI; lane 5, 9x-His tag dimeric SHI (PF1542 is an unrelated protein that is a persistent contaminant that copurified with dimeric SHI). The SDS PAGE gel data were modified from [11–13].

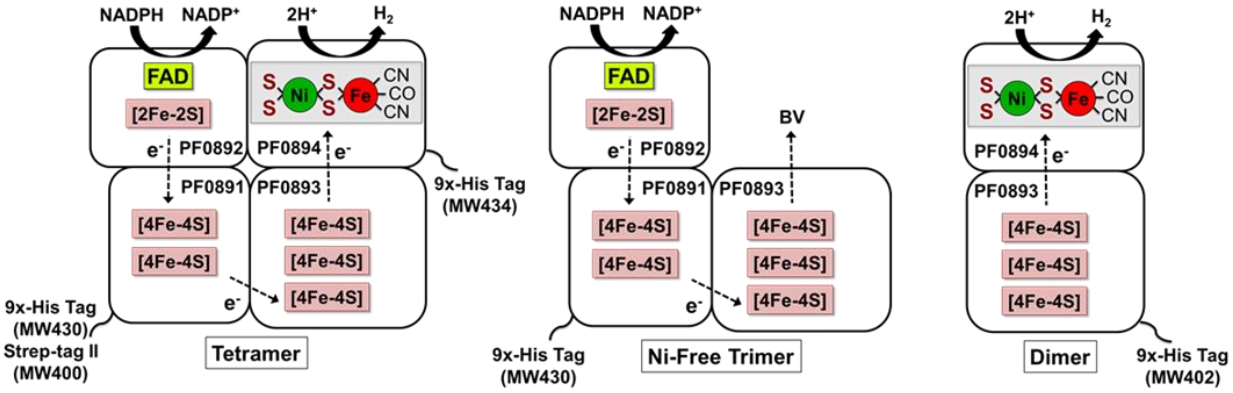
NADPH
NADP+
2H+
H2
FAD
[2Fe-2S]
e-
PF0892
PF0894
e-
PF0891
PF0893
[4Fe-4S]
[4Fe-4S]
[4Fe-4S]
[4Fe-4S]
e-
9x-His Tag
(MW434)
9x-His Tag
(MW430)
Strep-tag II
(MW400)
Tetramer
(a)
NADPH
NADP+
FAD
[2Fe-2S]
e-
PF0892
BV
PF0891
PF0893
[4Fe-4S]
[4Fe-4S]
[4Fe-4S]
[4Fe-4S]
e-
9x-His Tag
(MW430)
Ni-Free Trimer
(b)
2H+
H2
PF0894
e-
PF0893
[4Fe-4S]
[4Fe-4S]
[4Fe-4S]
Dimer
9x-His Tag
(MW402)
(c)

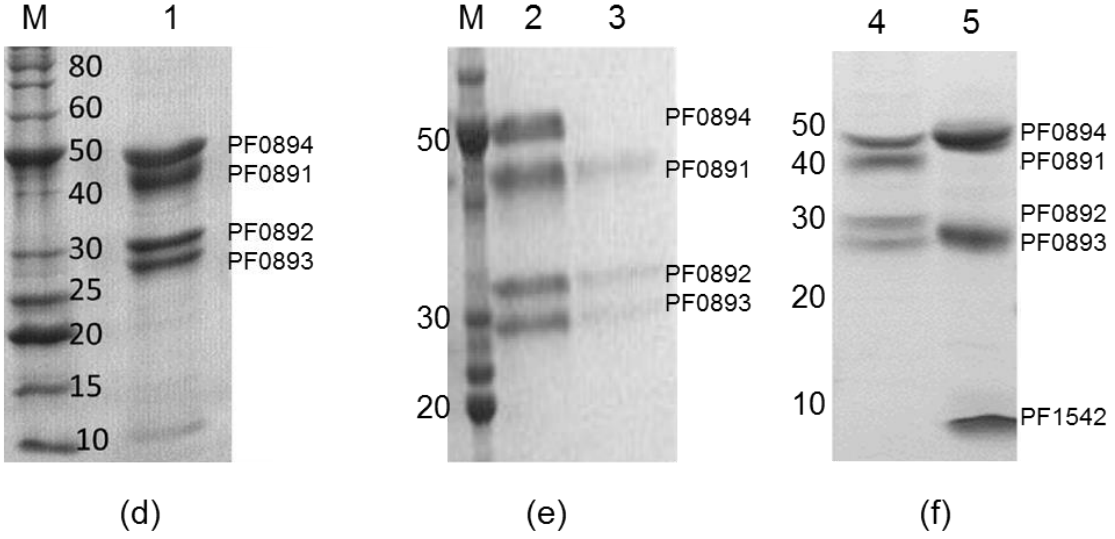
M
1
80
60
50
40
30
25
20
15
10
PF0894
PF0891
PF0892
PF0893
(d)
M
2
3
50
30
20
PF0894
PF0891
PF0892
PF0893
(e)
4
5
50
40
30
20
10
PF0894
PF0891
PF0892
PF0893
PF1542
(f)

Figure A2

Genetic strategy for overexpression of SHI. MW400 is used as the example. The knock in cassette contains upstream flanking region (UFR) and downstream flanking region (DFR) homologous to PF0890 and PF0891, respectively. This cassette also contains a selectable marker *pyrF* with the promoter P_{gdh}, the promoter for the S-layer protein (P_{slp}) to drive expression of the SHI genes, and a Strep-tag II at the N-terminus of PF0891. By homologous recombination, this cassette was inserted into the SHI locus in *P. furiosus* COM1.

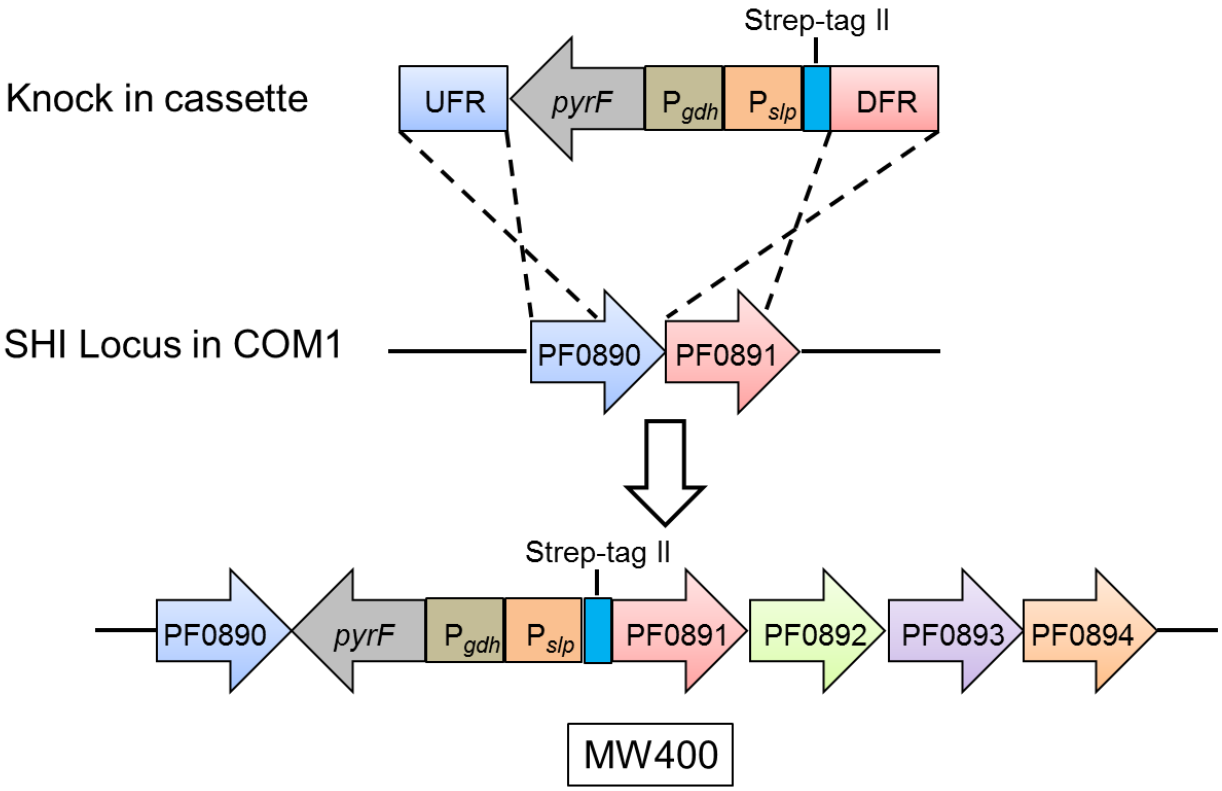
Knock in cassette
Strep-tag II
UFR
pyrF
P gdh
P slp
DFR
SHI Locus in COM1
PF0890
PF0891
Strep-tag II
PF0890
pyrF
P gdh
P slp
PF0891
PF0892
PF0893
PF0894
MW400

Figure A3

Biohydrogen production from glucan and water via SyPaB. SHI is colored in red and the model of tetrameric SHI (see Figure A1) shows how NADPH is oxidized to produce hydrogen. The abbreviations are GNP, glucan phosphorylase; PGM, phosphoglucomutase; G6PDH, G-6-P dehydrogenase; 6PGDH, 6-phosphogluconate dehydrogenase; R5PI, phosphoribose isomerase; Ru5PE, ribulose 5-phosphate epimerase; TKL, transketolase; TAL, transaldolase; TPI, triose phosphate isomerase; ALD, aldolase; FBP, fructose-1,6-bisphosphatase; PGI, phosphoglucose isomerase. g1p, glucose-1-phosphate; g6p, glucose-6-phosphate; 6pg, 6-phosphogluconate; ru5p, ribulose-5-phosphate; x5p, xylulose-5-phosphate; r5p, ribose-5-phosphate; s7p, sedoheptulose-7-phosphate; g3p, glyceraldehyde-3-phosphate; e4p, erythrose-4-phosphate; dhap, dihydroxyacetone phosphate; fdp, fructose-1,6-diphosphate; f6p, fructose-6-phosphate; and Pi, inorganic phosphate. Modified from [14].

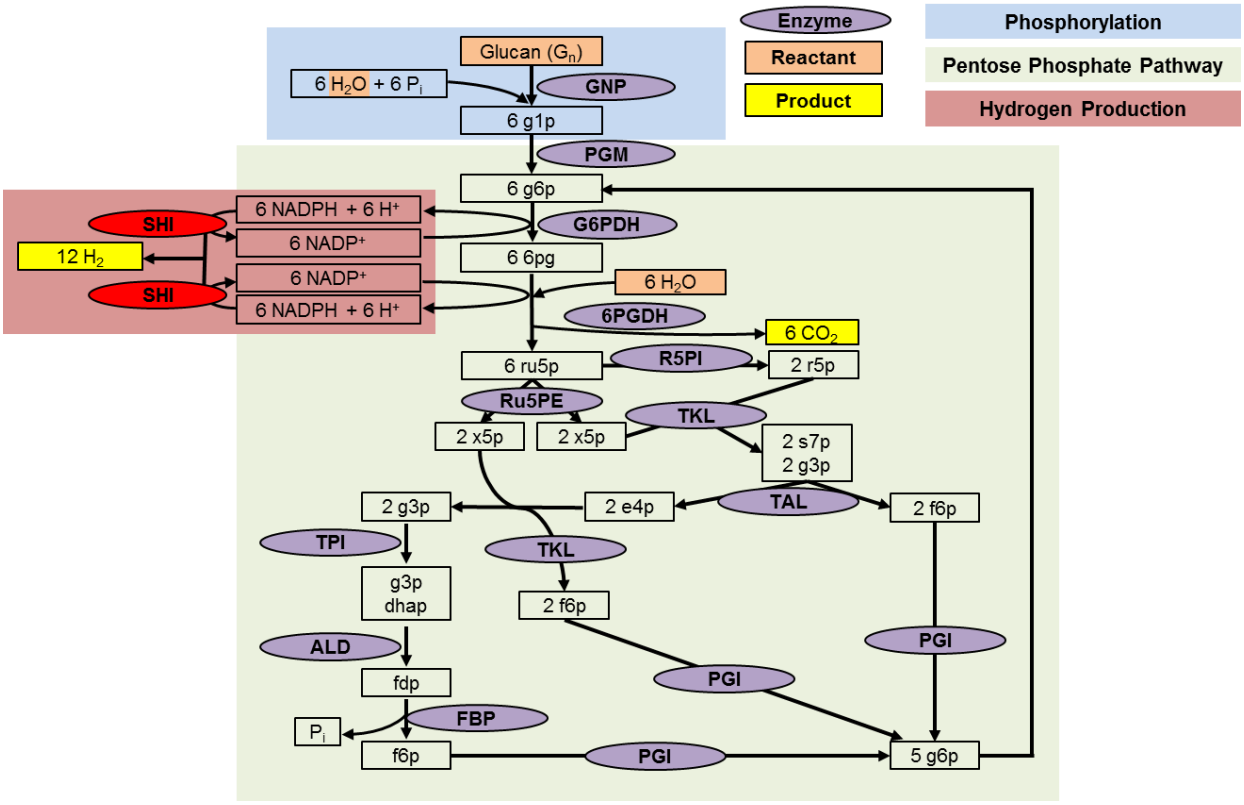
Enzyme
Reactant
Product
Phosphorylation
Pentose Phosphate Pathway
Hydrogen Production
Glucan (G_n)
6 H_2O + 6 P_i
GNP
6 g1p
PGM
6 g6p
SHI
6 NADPH + 6 H^+
G6PDH
6 NADP+
12 H_2
6 6pg
6 NADP+
SHI
6 NADPH + 6 H^+
6 H_2O
6PGDH
6 CO_2
6 ru5p
R5PI
2 r5p
Ru5PE
TKL
2 x5p
2 x5p
2 s7p
2 g3p
2 g3p
2 e4p
TAL
2 f6p
TPI
TKL
g3p
dhap
2 f6p
ALD
PGI
fdp
PGI
FBP
P_i
f6p
PGI
5 g6p

APPENDIX B

STRUCTURE OF AN ANCIENT RESPIRATORY SYSTEM

Yu H, **Wu CH**, Schut GJ, Haja DK, Zhao G, Peters JW, Adams MWW, Li H. (2018) Structure of an ancient respiratory system. *Cell*. DOI: 10.1016/j.cell.2018.03.071

Summary

Hydrogen gas-evolving membrane-bound hydrogenase (MBH) and quinone-reducing complex I are homologous respiratory complexes with a common ancestor, but a structural basis for their evolutionary relationship is lacking. Here, we report the cryo-EM structure of a 14-subunit MBH from the hyperthermophile *Pyrococcus furiosus*. MBH contains a membrane-anchored hydrogenase module that is highly similar structurally to the quinone-binding Q-module of complex I while its membrane-embedded ion-translocation module can be divided into a H^+- and a Na^+-translocating unit. The H^+-translocating unit is rotated 180° in-membrane with respect to its counterpart in complex I, leading to distinctive architectures for the two respiratory systems despite their largely conserved proton-pumping mechanisms. The Na^+-translocating unit, absent in complex I, resembles that found in the Mrp H^+/Na^+ antiporter and enables hydrogen gas evolution by MBH to establish a Na^+ gradient for ATP synthesis near 100°C. MBH also provides insights into Mrp structure and evolution of MBH-based respiratory enzymes.

Keywords

cryo-EM; protein structure; structural biology; membrane protein; complex I; Mrp antiporter; cation/proton antiporter; respiration evolution of respiratory complexes; hydrogen gas; hydrogenase

Introduction

The evolution of complex life from anaerobic ancestors on this planet was driven in part by the high energy yield of aerobic respiration wherein membrane-bound electron transfer from NADH to molecular oxygen is coupled in a highly efficient manner to conserve energy in the form of a proton motive force. NADH oxidation is catalyzed by proton-pumping complex I (or NADH quinone oxidoreductase) (Hirst, 2013, Letts and Sazanov, 2017, Sazanov, 2015). Some anaerobic archaea lacking complex I instead use a sodium-pumping mechanism to provide chemical potential for ATP synthesis (Mayer and Müller, 2014). Typical examples are the 14-subunit membrane bound hydrogenase (MBH) (Sapra et al., 2003, Schut et al., 2016b) of the hyperthermophile *Pyrococcus furiosus* and the closely related 18-subunit formate hydrogen lyase (FHL) (Lim et al., 2014) and 16-subunit carbon monoxide dehydrogenase (CODH) (Schut et al., 2016a) of *Thermococcus* onnurineus. CODH and FHL enable *T. onnurineus* to grow using only formate or CO as its sole energy (ATP) source. MBH, FHL, and CODH all evolve H_2 gas and contain group 4 [NiFe]-hydrogenase modules. They differ mainly in that FHL and CODH have additional subunits that enable formate or CO, respectively, to serve as electron donors (Lipscomb et al., 2014, Schut et al., 2016a, Schut et al., 2016b). Hence, MBH oxidizes reduced ferredoxin generated by sugar fermentation and evolves H_2 gas whereas FHL and CODH oxidize formate or CO to evolve H_2. In all cases, the redox reaction leads to H_2 production and generates a sodium ion gradient across the cell membrane (Kim et al., 2010, Lim et al., 2014, Mayer and Müller, 2014, Sapra et al., 2003). The membrane potential established by these membrane complexes is subsequently utilized by a Na^+-driven ATP synthase (Mayer and Müller, 2014, Pisa et al., 2007). Consistent with the similar mechanism of energy conservation among these complexes, both FHL (Lipscomb et al., 2014) and CODH (Schut et al., 2016a) have been heterologously expressed in

P. furiosus, and the organism is then able to evolve H_2 by oxidizing either formate or CO as a source of energy for growth. Indeed, stimulation of H_2 evolution by Na^+ ions has been experimentally demonstrated both with FHL (Lim et al., 2014) and with MBH (Figure SB1A).

Complex I and these MBH-type respiratory complexes are evolutionarily related and share an ancestral root, which is generally considered to be the Mrp antiporter (multiple resistance and pH antiporter) (Figure B1A) (Efremov and Sazanov, 2012, Hedderich, 2004, Sazanov, 2015). Many of the membrane-embedded ion-translocating subunits of these complexes clearly have a common ancestor (Table B1). For example, the MBH subunits D and E together, G, and H correspond to the *Thermus thermophilus* complex I (NADH:quinone oxidoreductase, Nqo) subunits Nqo10, Nqo11, and Nqo14, and the C-terminal region of MrpA, MrpC, and MrpD of the *Bacillus subtilis* Mrp antiporter, respectively. Interestingly, complex I lack subunits corresponding to the MBH subunits A, B, C, and F and Mrp subunits E, F, G, and B (Table B1) (Schut et al., 2013, Schut et al., 2016b). The Mrp antiporter system belongs to cation:proton antiporter-3 (CPA3) family. It provides resistance to high Na^+ stress through a H^+/Na^+ exchange mechanism and plays an essential role in numerous bacteria, including pathogens, although its molecular mechanism remains a mystery due to lack of a Mrp structure (Kosono et al., 2005, Krulwich et al., 2011, Morino et al., 2008, Morino et al., 2010, Swartz et al., 2005). Notably, except for MrpA, six out of the seven Mrp subunits have homologs in MBH (Table B1), suggesting a shared Na^+ translocation core module between these complexes (Schut et al., 2013, Schut et al., 2016b).

Here, we have used the MBH from the anaerobic hyperthermophilic microorganism *Pyrococcus furiosus.* This grows optimally near 100°C in marine volcanic vents and has been proposed to represent an ancestral life form (Nisbet and Sleep, 2001). MBH accepts electrons from reduced ferredoxin (E_m ~−480 mV) and reduces protons to hydrogen gas (H^+/H_2, $E_o' = -420$ mV,

pH 7) (Mayer and Müller, 2014, McTernan et al., 2014). The energy that is conserved (ΔE = 60 mV; 12 kJ/mol/2e$^-$) is only ∼15% of that conserved by complex I (ΔE = 420 mV; 81 kJ/mol/2e−), which uses NADH as the electron donor (NAD/NADH, $E_o' = -320$ mV) and reduces the much higher potential acceptor ubiquinone (E_m +100 mV) (Efremov and Sazanov, 2012). The 14 MBH subunits are named alphabetically (MbhA–MbhN) and together they make up a molecular mass of ∼300 kDa (McTernan et al., 2014). Like complex I, MBH has peripheral and membrane arms. Four subunits (MbhJ, MbhK, MbhL, and MbhN) are predicted to be exposed to the cytoplasm and form the peripheral arm while the remaining ten (MbhA–MbhI, MbhM) are predicted to be integral membrane proteins forming the membrane arm (Schut et al., 2013, Schut et al., 2016b). The peripheral arm contains the catalytic [NiFe] site (in MbhL) together with three iron-sulfur clusters (in MbhN and MbhJ). MbhL and MbhJ show surprisingly low sequence homology to the corresponding subunits in the other three types of [NiFe] hydrogenase but they are homologous to the quinone-reducing Q-module of complex I (Schut et al., 2013, Schut et al., 2016b). These peripheral arms are involved in coupling electron transfer to hydrogen gas production and ubiquinone reduction, respectively (Schut et al., 2013, Schut et al., 2016b). Structural knowledge of an ancient respiratory complex such as the MBH would be invaluable to understanding the functional relationships among the anaerobic H_2-evolving membrane complexes (MBH, FHL, and CODH) and the path that led to the evolution of complex I of the aerobic respiratory chain. Therefore, we determined the structure of the MBH by cryo-EM single particle reconstruction and derived a 3.7-Å resolution atomic model.

Results

Structure determination

We modified the 14-gene operon encoding MBH with an insert at the N terminus of *mbhJ* encoding an affinity tag (His_9) (Figure B1B). The affinity-tagged MBH complex was natively expressed in and purified from *P. furiosus* (Figures SB1C–SB1E; STAR Methods). Cryo-EM of the MBH resulted in a 3D density map at an average resolution of 3.7 Å; however, the transmembrane region has a better resolution of ~3.3 Å (Figures B1C and SB2). Most loops and many side-chain densities were well resolved in the experimental electron density map allowing *de novo* model building for 2,470 out of the total 2,502 residues of the complex (Figure SB3). A 32-residue flexible loop region of MbhI (residues 42–73) was not as well resolved and only allowed for main chain tracing (Figure SB3I). Like complex I, MBH adopts an L-shaped structure with dimensions of 120 Å *130 Å *60 Å with a peripheral arm and a membrane arm (Figures B1C and B1D). The MBH atomic model represents the first structure of a group 4 [NiFe]-hydrogenase.

Membrane arm

The membrane arm of MBH contains 44 transmembrane helices (TMH) from 10 membrane-embedded subunits, MbhA–MbhI and MbhM (Figures B1D and B2). The largest membrane subunit is MbhH and this features 14 TMH. Its TMH4–TMH8 and TMH9–TMH13 form two inverted folding units (Figures B2A and B2B) and each of these two 5-TMH units features a discontinuous 4^{th} helix, TMH7, and TMH12, respectively. This fold with two discontinuous helices and internal symmetry is typically found in antiporter-like subunits of complex I (Baradaran et al., 2013, Zhu et al., 2016, Zickermann et al., 2015). Indeed, subunit H is

homologous to the antiporter-like subunits *T. thermophilus* Nqo14, Nqo13, and Nqo12 and mammalian ND2, ND4, and ND5 (Figure B2A), which are proposed to translocate protons (Baradaran et al., 2013, Hirst, 2013, Sazanov, 2015, Zhu et al., 2016, Zickermann et al., 2015). Therefore, we suggest a similar role for subunit H in MBH. Loosely packed against the H subunit is the M subunit and this has eight TMH and anchors the peripheral arm. The M subunit also contains a 5-TMH fold: TMH2–TMH6 with a discontinuous 4^{th} α-helix (TMH5). This is similar to subunit Nqo8 of complex I (Figures B2C and B2D), consistent with their predicted homology (Schut et al., 2013). However, it is unclear if subunit M contributes to ion translocation because it is largely separated from the main ion-translocating module by a sizable gap that appears filled by two phospholipid molecules (Figures SB4A–D). Unexpectedly, a bridging subunit I ties together the otherwise separated main ion-translocating module and the subunit M-anchored peripheral module (Figure B3A).

Located at the distal region of the membrane arm of MBH are seven smaller subunits, A–G, that are homologous to Mrp antiporter subunits (Figure B3A; Table B1) (Schut et al., 2016b). Remarkably, MBH subunits B, C, D, and G each fold into a three-helix sheet-like structure and they pack sequentially to form four contiguous layers (Figure B2E). Subunit G is sandwiched between TMH1 and TMH2 of subunit E. Subunit F contains four TMHs; two (TMH3 and TMH4) are exposed to the lipids and the other two (TMH1 and TMH2) are internal, tilted, and contact the four TMH3 of subunits B, C, D, and G. At the distal end of the complex, subunit A starts with two short TMH that pack against TMH3 of subunit C and TMH1 of subunit F, followed by a long lateral helix (HL) (V60-I88), and ends with a cytosolic ferredoxin-like domain that wraps around the three TMHs of subunit C. The subunit F ferredoxin-like domain lacks the Cys residues

necessary to coordinate an iron-sulfur cluster and indeed no such cluster was found in our structure. The function of this domain is currently unknown.

The potential proton translocation subunits in the MBH membrane module

By aligning the homologous antiporter-like MBH subunit H with Nqo14 of complex I, we identified a common core between these two respiratory complexes (Figures B3A–D): subunit H corresponds to Nqo14, G to Nqo11, and D and E combined together correspond to Nqo10 (Figures SB4E–H). Notably, the MBH core is rotated 180° in-membrane with respect to that of complex I (Figures B3A and B3B), giving rise to the apparently distinct architectures of the two complexes: the membrane-bound peripheral module is located to the left of the core in MBH, whereas the peripheral module in complex I is at the right side of the core (Figure B3C). Except for this 180° in-membrane relative rotation, the two common cores are highly similar and share several important structural details: (1) MBH subunit D contains a π-bulge in the middle of TMH3 (Figure SB4H); this is a structural feature observed in the corresponding TMH3 of Nqo10 of complex I from various origins (Efremov and Sazanov, 2011, Zhu et al., 2016, Zickermann et al., 2015); (2) MBH subunit I anchors the discontinuous TMH7 of subunit H via its middle lateral helix and the C-terminal region of TMH2 (Figure B3A); this resembles another important feature observed in the complex I structures—the anchoring of Nqo12 onto Nqo14 (Figures B3D and SB4I) (Baradaran et al., 2013, Zhu et al., 2016, Zickermann et al., 2015); and (3) two chains of polar and charged residues form two putative hydrophilic channels across the membrane arm: one within the antiporter-like subunit MbhH and the other within the small subunits D, E, and G (Figure B3E). They contribute two possible proton translocation pathways, which are connected via a hydrophilic

central axis across the interior of this membrane core. Although there is controversy over the proton path across the small subunits in complex I (the counterparts of MbhD, MbhE, and MbhG) (Baradaran et al., 2013, Efremov and Sazanov, 2011, Kaila et al., 2014, Sazanov, 2015, Zickermann et al., 2015), the proposed proton paths and the central hydrophilic axis within this core MBH module are generally consistent with what has been proposed in complex I (Baradaran et al., 2013, Efremov and Sazanov, 2011, Fiedorczuk et al., 2016, Zhu et al., 2016, Zickermann et al., 2015). In summary, given the structural correspondence described above, we suggest that this core (subunits D, E, G, and H) identified in MBH is a module shared with complex I and likely functions in proton translocation.

Peripheral arm and evolutionary relationship with Complex I

The MBH peripheral arm transfers electrons from ferredoxin to reduce protons to form H_2 gas (Sapra et al., 2003). This arm contains cytosolic subunits J, K, L, and N that are associated with the membrane by docking on integral membrane subunit M. The five subunits together are referred to as the membrane-anchored hydrogenase module (Figures B1B and B4A–E). The MBH subunits L and J are equivalent to the large and small subunits, respectively, of the heterodimeric core present in all known [NiFe]-hydrogenases, but their structural (and sequence) similarity are limited only to the regions that coordinate the [NiFe]-catalytic site and its proximal [4Fe-4S] cluster (Figure SB5A) (Hedderich, 2004). Indeed, the MBH hydrogenase module is much more similar in both sequence and structure to the hydrophilic Q-module and the associated membrane Nqo8 subunit of complex I (Figure SB5B). These observations support the concept of modular evolution of complex I from an H_2-evolving ancestor (Efremov and Sazanov, 2012, Schut et al., 2013, Schut et al., 2016b).

As described above, the hydrogenase module and the proton-translocating membrane module are bridged by MBH subunit I, which is equivalent to a combination of the N-terminal region of Nqo7 and the C-terminal region of Nqo12 of complex I (Figures B3D and SB5B). The TMH1 of subunit I and Nqo7 are superimposable, but their second and third α helices are configured differently: in Nqo7 they are both TMHs whereas in MBH subunit I the second α-helix is amphipathic and horizontal and only the third helix is a TMH (Figure B4D). Both MbhI and Nqo7 feature a long loop adjacent to their respective redox active sites. The MBH subunits L, J, M, and I enclose a chamber that is equivalent to the quinone-binding chamber in complex I (Figure SB5B) (Baradaran et al., 2013, Zickermann et al., 2015). The entry to the chamber is open in complex I for quinone diffusion, but is sealed off in MBH by several bulky residues, such as F47 and F50 of subunit M (Figure SB5C).

The MBH peripheral arm lacks the equivalent of the so-called N-module of complex I, which are the three additional subunits (Nqo1–Nqo3) that oxidize NADH and, via flavin and multiple iron-sulfur clusters, channel electrons to the Q-module (Figure SB6A). The four Q-module subunits of complex I each contains an insertion loop that interacts with the N-module but these loops are not found in the homologous MBH subunits (J, K, L, and N; Figures SB6B–E). These structural features confirm the evolutionary relationship between the MBH and complex I and support the proposal that the N-module is the latest addition in the evolution of complex I from a ferredoxin-oxidizing, hydrogen-gas evolving respiratory complex (Efremov and Sazanov, 2012, Moparthi and Hägerhäll, 2011, Schut et al., 2016b, Schut et al., 2013).

A possible proton reduction mechanism of the hydrogenase module

In the MBH peripheral arm, the three [4Fe-4S] clusters form a chain and extend from the proposed ferredoxin-binding site by ~40 Å toward the interior [NiFe] site that catalyzes proton reduction to generate H_2 gas (Figure B1D, inset). The edge-to-edge distances between the neighboring clusters are smaller than 12 Å thereby allowing efficient electron tunneling (Page et al., 1999). The distal and medial [4Fe-4S] clusters are each coordinated by four Cys in subunit N, in a manner similar to the coordination of N6a and N6b [4Fe-4S] clusters in complex I Nqo9 (Figure SB5D). The [NiFe]-site and its proximal [4Fe-4S] cluster are also individually coordinated by four Cys in subunit L and J, respectively. This coordination scheme resembles the distantly related dimeric hydrogenase core but it is different from that in complex I Nqo4 as this lacks all four of the Cys that coordinate the NiFe cluster in MbhL (Sazanov and Hinchliffe, 2006) (Figures SB5E and SB5F). In the core of dimeric [NiFe]-hydrogenases, the proton is proposed to be transferred between a Cys and a nearby Glu (Dementin et al., 2004, Fontecilla-Camps et al., 2007). In MBH, E21 of subunit L likely plays the role of the Glu and donates a proton to the nearby C374 (Figure B4B). These two residues are invariably conserved among known members of group 4 hydrogenases (Figure B4C). Upstream of E21, the proton is probably taken up from the bulk solvent and transferred via β2 and β3 strands of subunit L, involving residues E23, K24, D38, K40, and Y43 (Figure B4B). Hence, although the overall sequence similarity between the dimeric cores of group 4 MBH and the other three groups of NiFe-hydrogenases is extremely low, their proton pathways may be conserved (Ogata et al., 2015, Shomura et al., 2011).

Two potential sodium-binding sites in MBH and their evolutionary relationship with the Mrp antiporter

The overall sequence identities between the Mrp subunits of the mesophilic bacterium *Bacilus subtilis* and their MBH counterparts range from 22%–28% but there are highly conserved regions between MrpB, MrpC, MrpD, MrpE, MrpF, and MrpG and the MBH subunits F, G, H, A, B, and C, respectively (Figure SB7; Table B1). Interestingly, MBH subunits D and E together appear to correspond to the C-terminal region of MrpA (Figure SB7F). Mrp can be separated into two stable sub-complexes, MrpA–MrpD and MrpE–MrpG (Morino et al., 2008). This organization is consistent with the structure of MBH in which the corresponding MBH subunits D–H and A–C are packed together, respectively (Figure B3A). Notably, we identified two negatively charged cavities in MBH subunits A–C and F (Figure B5A), and these four subunits are equivalent to MrpE-G and MrpB, homologs of which are not present in complex I (Table B1). Moreover, we have experimental evidence that MBH subunits A–C are involved in Na^+ pumping as the deletion strain of *P. furiosus* lacking these three subunits (Δ*mbhabc*) showed diminished Na^+-dependent H_2 evolution (Figure SB1B).

Analyses of the negatively charged cavities in MbhA–MbhC suggest that they likely constitute a sodium ion translocation pathway. The first cavity reaches halfway into the membrane and is lined by the carboxyl group of the invariably conserved D35 of MBH subunit B and by hydroxyl groups of five highly conserved residues: T36 and T72 of B and T39, T42, and T43 of C (Figures B5B, SB7B, and SB7C). Together, these residues could form a six-coordinate site within this cavity, consistent with the binding of a single sodium ion (Kuppuraj et al., 2009). Another structural feature that supports sodium ion binding is the presence of the conserved P88 of subunit C. It is located adjacent to conserved D35 of subunit B and breaks TMH3 of subunit C into two

half-helices (TMH3i and TMH3ii) (Figures B5A and B5B). Such a feature (an aspartate residue near the break in the TMH in the middle of membrane) is often found in H^+/Na^+ antiporters (Coincon et al., 2016, Hunte et al., 2005, Lee et al., 2013, Wöhlert et al., 2014). Indeed, MBH subunit C P88 is equivalent to P81 in MrpG and in a previous study it was demonstrated that the H^+/Na^+ antiporter activity of Mrp was abolished when P81 is substituted by an alanine or a glycine (Morino et al., 2010). Adjacent to and directly interacting with the potential sodium ion-binding cavity in MbhABC is a conserved loop (119-TPGT/S-122) in the subunit A ferredoxin-like domain. Mutations of MrpE T113Y and P114G, equivalent to T119 and P120 of MBH subunit A, were found previously to significantly reduce the Mrp H^+/Na^+ antiporter activity (Morino et al., 2010). Interestingly, this first potential Na^+-binding site in MBH faces the cytoplasm and is closed by a conserved salt bridge between D29 of subunit B and R34 of subunit C (Figure B5B). If the first cavity is truly a Na^+-binding site, one might further speculate that two adjacent aspartate residues, D29 of subunit B and D30 of subunit C, may function to concentrate Na^+ ions. Adjacent to the potential Na^+ concentrator D29 is the conserved R30 of subunit B that stabilizes a loop around the cavity entrance. Mutations D32A and R33A in MrpF, equivalent to D29 and R30 of MBH subunit B, either abolished (D32A) or reduced (R33A) the H^+/Na^+ antiporter activity (Morino et al., 2010).

The second negatively charged cavity in MBH is enclosed by TMH1 of subunit A, TMH3 of subunit B, TMH3 of subunit C, and a loop of subunit F containing the GHxxPGGGF motif that is highly conserved in Mrp antiporters (Figures B5A, B5C, and B5E). Several positively charged residues line the cavity, and because this cavity faces the outside of the cell, we propose that these residues may facilitate the release of Na^+ ions (Figures B5C and B5D). The conserved and potentially Na^+-coordinating D59 of subunit B in the cavity is 15 Å above the exit face and 18 Å below the potential Na^+-coordinating D35 of subunit B in the first cavity. The two Na^+-binding

cavities are separated by several hydrophobic residues. Therefore, if the two cavities are indeed the Na^+ binding sites, a conformational change would be required during a H^+/Na^+ translocation cycle. Interestingly, subunit F contains a pair of tilted helices (TMH1-2) that bridge the potential Na^+-translocating module with the proton-translocation subunit G via hydrophobic interactions, and may just play such a role (Figures B5C and B5E). Consistent with this scenario, mutations that disrupt the interactions in the Mrp system, such as MrpB F41A and MrpC T75A, equivalent to F39 of MBH subunit F and T81 of MBH subunit G, resulted in a reduced tolerance of the microbes to Na^+ (Morino et al., 2010).

As noted above, MrpA is the only Mrp subunit that does not have a homolog in MBH (Table B1). MrpA and MrpD are both homologous to the antiporter-like Nqo12–Nqo14 subunits of complex I (Sazanov, 2015), where the latter are proposed to pump protons in complex I (Baradaran et al., 2013, Fiedorczuk et al., 2016, Zhu et al., 2016, Zickermann et al., 2015). Furthermore, MrpA–MrpD was previously shown to form a stable sub-complex (Morino et al., 2008). On the basis of these analyses, we suggest that the Mrp antiporter has an extra proton path within MrpA, in addition to those within the H^+ translocation module shared with MBH (Figure B6; Table B1). Therefore, from an evolutionary perspective, MrpA appears to have been replaced by the membrane-anchored hydrogenase module—the peripheral arm attached to subunit M in MBH—converting the secondary antiporter system into a system that couples a redox reaction with ion pumping activity, as now found in MBH.

Discussion

How modern-day complex I evolved is a fundamental yet not well understood question. The cryo-EM structure of MBH as we have described above shows that (1) complex I and MBH share a closely related module in their respective peripheral arm that reduces either protons (MBH) or quinone (complex I), which is similarly anchored to one membrane subunit (Figure SB5B); (2) MBH shares a potential proton-translocation module with complex I, despite the fact that the proton translocating module within each of these complexes is turned around with respect to their respective peripheral module (Figures B3A and B3B); and (3) both respiratory systems show bimodular architecture and the two modules are tied together by a similar linking structure at the peripheral arm involving MBH subunit I and complex I Nqo7 (Figures B3A, B3B, and SB5B). However, the linking mechanism is different at the membrane arm: two TMHs of Nqo7 in complex I are replaced by a lateral helix and one TMH of MBH subunit I (Figure SB5B), possibly arising from the different orientation of the proton-translocation module between MBH and complex I (Figures B3A and B3B). A major distinction between the two complexes is a proposed sodium ion translocation unit that is absent in complex I but resides in subunits A–C and F in MBH and is shared with the Mrp antiporter (Figure B6; Table B1). Therefore, it appears that MBH evolved from the Mrp antiporter by acquiring the membrane-bound hydrogenase module with the concomitant loss of MrpA (Figures B6B and B6C). One could imagine that complex I may have evolved from Mrp by acquiring a second proton translocation unit with an additional proton path at the expense of the sodium translocation unit, as well as acquiring the ability to reduce quinone in the peripheral arm rather than reducing protons to hydrogen gas (Figures B6A and B6C). These insights structurally confirm the long-recognized evolutional relationship among MBH, complex

I, and the Mrp antiporter, and supports the hypothesis that they may have evolved by the assembly of prebuilt modules (Efremov and Sazanov, 2012, Hedderich, 2004, Sazanov, 2015).

Because the potential proton-translocation module of MBH is turned around when compared to complex I and is proximal to the redox-reaction site (Figures B3A and B3B), it is likely that the released redox energy of ferredoxin oxidation by the hydrogenase module is coupled to pumping out a proton through the first proton path in the adjacent subunit H. Subsequently, the outside proton may flow back in via the second proton path, driving the outward pumping of a sodium ion through the proposed sodium translocation path (Figures B5 and B6B). Such a scheme is consistent with the Na^+-dependent energy conservation mechanism proposed for certain anaerobic archaea, particularly involving the MBH-family member and closely related FHL of *T. onnurineus* (Kim et al., 2010, Lim et al., 2014, Mayer and Müller, 2014, Sapra et al., 2003).

The structural conservation between MBH and complex I in the redox site is somewhat unexpected, given they utilize very different electron donors and acceptors. We highlight the following three conserved features: (1) three loops near the catalytic [NiFe] center in MBH ($Linker_{\beta1-\beta2}{}^{L}$, $Linker_{TM1-TM2}{}^{I}$, and $Linker_{TM5-TM6}{}^{M}$; Figure B4A) show good agreement with their counterparts in complex I ($Linker_{\beta1-\beta2}{}^{Nqo4}$, $Linker_{TM1-TM2}{}^{Nqo7}$, and $Linker_{TM5-TM6}{}^{Nqo8}$; *T. thermophilus*) (Figures B4D and B4E); (2) the hydrogen gas-evolving catalytic [NiFe]-site of MBH (MbhL E21-C374-[NiFe]) is close to the proposed binding site of the quinone head-group in complex I (Figure B4D) (Baradaran et al., 2013); and (3) the long $Linker_{TM1-2}{}^{I}$ is partially disordered (Figure SB3I), comparable to its counterpart (TMH1-TMH12 loop of ND3) in a structure of the *B. taurus* complex I (Zhu et al., 2016). These conserved structural features may suggest a similar energy transduction mechanism between the peripheral and membrane arms in

the two complexes (Baradaran et al., 2013, Zhu et al., 2016, Zickermann et al., 2015). However, the exact molecular mechanism is currently unknown in either system (Berrisford et al., 2016, Brandt, 2011, Hirst, 2013, Hirst and Roessler, 2016, Letts and Sazanov, 2017, Sazanov, 2015, Wirth et al., 2016). Indeed, the lateral helix linking unit conserved between MBH (helix HL) and complex I is a remarkable feature (Figure B3D). Some have suggested that this helix in complex I may function as a coupling rod to transduce the redox potential to proton translocation (Baradaran et al., 2013, Hunte et al., 2010, Sazanov, 2015, Steimle et al., 2011). However, such a role is debatable based on recent biochemical studies (Belevich et al., 2011, Hirst, 2013, Zhu and Vik, 2015). It is possible that the required energy transduction in MBH is coupled via the lateral helix of subunit I but it may simply play a structural role by cementing the two MBH subcomplexes into a stable molecular machine.

To summarize, the cryo-EM-derived atomic model of MBH represents a first structure of any respiratory complex directly related to complex I. The MBH structure has illuminated several aspects of the evolutionary relationship between Mrp antiporter and complex I, and will serve as a starting point for mechanistic understanding of these fundamental energy-transducing systems that are ubiquitous in biology.

Experimental Model and Subject Details

Pyrococcus furiosus strain MW0414, COM1 and MW0574 were grown in defined maltose medium consisting of 1x base salts, 1x trace minerals, 1x vitamin solution, 2x 19-amino-acid solution, 10 μM sodium tungstate, 0.25 mg/ml resazurin, and 0.5% (wt/vol) maltose, with added cysteine at 0.5 g/liter, sodium sulfide at 0.5 g/liter, and sodium bicarbonate at 1 g/liter; and adjusted to pH 6.8 (Detailed buffer composition was described in the METHODS DETAILS). For protein

purification, large-scale growth of *P. furiosus* strain MW0414 was carried out in a 20-l fermenter at 90°C with constant flushing of 20% (v/v) CO_2 and 80% (v/v) N_2 for 14 hours, while the pH was maintained at 6.8 by the addition of 10% (w/v) sodium bicarbonate.

Method Details

Expression and purification of MBH

The MBH holoenzyme (S-MBH) was solubilized and purified anaerobically from *Pyrococcus furiosus* strain MW0414, in which a His_9-tag had been engineered at the N terminus of the MbhJ subunit. The procedure was as previously described with some modifications (McTernan et al., 2014). Frozen cells were lysed in 25 mM sodium phosphate, pH 7.5, containing 1 mM DTT and 50 μg/ml DNase I (5 mL per gram of frozen cells). After stirring for one hour, the cell-free extract was centrifuged at 100,000 x g for one hour. The supernatant was removed and the membranes were washed twice using 50 mM EPPS buffer, pH 8.0, containing 5 mM $MgCl_2$, 50 mM NaCl, 10% (v/v) glycerol, 1 mM DTT and 0.1 mM PMSF. The membrane pellet was collected by ultracentrifugation at 100,000 x g for one hour after each wash step. The washed membranes were resuspended in 50 mM Tris-HCl, pH 8.0, containing 5 mM $MgCl_2$, 50 mM NaCl, 5% (v/v) glycerol, 1 mM DTT, and 0.1 mM PMSF. MBH was solubilized by adding n-dodecyl-β-D-maltoside (DDM, Inalco) to 3% (w/v) followed by incubation at 4°C for 16 hours. The solubilized membranes were centrifuged at 100,000 x g for 1 hour. The supernatant was applied to a 5 mL His-Trap crude FF Ni-NTA column (GE Healthcare) while diluting it 10-fold with buffer A (25 mM sodium phosphate, 300 mM NaCl, pH 7.5, containing 1 mM DTT and 0.03% DDM). The column was washed with 10 column volumes of buffer A and the bound protein was

eluted with a 20-column volume gradient from 0 to 100% buffer B (buffer A containing 500 mM imidazole). The eluted protein was further purified by applying it to a 1-mL His-Trap HP Ni-NTA column (GE Healthcare) while diluting it 5-fold with buffer A. A 30-column volume gradient from 0 to 100% buffer B was used to elute the bound protein. The MBH sample was concentrated and further purified using a Superose 6 10/300 GL column (GE Healthcare) equilibrated with 50 mM Tris-HCl, pH 8.2, containing 300 mM NaCl, 2 mM sodium dithionite, and 0.03% DDM.

Deletion of MbhABC

The genetically tractable *P. furiosus* strain COM1 was used to delete the three genes PF1423-1425. 500 bp flanking regions were amplified from *P. furiosus* genomic DNA for the UFR and DFR, and the selection marker (*pyrF*-P_{gdh}) was amplified by using pGL021 as the template (Lipscomb et al., 2011). The knock-in cassette was assembled using overlapping PCR (Bryksin and Matsumura, 2010). The genomic DNA was prepared using Zymobead Genomic DNA Kit (Zymo Research).

P. furiosus transformants were grown in defined maltose media as previously described (Lipscomb et al., 2011). The maltose medium was composed of 1x base salts, salts, 1x trace minerals, 1x vitamin solution, 2x 19-amino-acid solution, 0.5% (wt/vol) maltose, 10 μM sodium tungstate, and 0.25 mg/ml resazurin, with added cysteine at 0.5 g/liter, sodium sulfide at 0.5 g/liter, sodium bicarbonate at 1 g/liter, and 1 mM sodium phosphate buffer (pH 6.8). The 5x base salts stock solution contained (per liter): 140 g of NaCl, 17.5 g of $MgSO_4 \cdot 7H_2O$, 13.5 g of $MgCl_2 \cdot 6H_2O$, 1.65 g of KCl, 1.25 g of NH_4Cl, and 0.70 g of $CaCl_2 \cdot 2H_2O$. The 1000x trace mineral stock solution contained (per liter) 1 mL of HCl (concentrated), 0.5 g of Na_4EDTA, 2.0 g of $FeCl_3$, 0.05 g of

H_3BO_3, 0.05 g of $ZnCl_2$, 0.03 g of $CuCl_2 \cdot 2H_2O$, 0.05 g of $MnCl_2 \cdot 4H_2O$ 0.05 g of $(NH_4)_2MoO_4$, 0.05 g of $AlK(SO_4) \cdot 2H_2O$, 0.05 g of $CoCl_2 \cdot 6H_2O$, and 0.05 g of $NiCl_2 \cdot 6H_2O$. The 200x vitamin stock solution contained (per liter) 10 mg each of niacin, pantothenate, lipoic acid, *p*-aminobenzoic acid, thiamine (B_1), riboflavin (B_2), pyridoxine (B_6), and cobalamin (B_{12}) and 4 mg each of biotin and folic acid. The 25x 19-amino-acid solution contained (per liter) 3.125 g each of arginine and proline; 1.25 g each of aspartic acid, glutamine, and valine; 5.0 g each of glutamic acid and glycine; 2.5 g each of asparagine, histidine, isoleucine, leucine, lysine, and threonine; 1.875 g each of alanine, methionine, phenylalanine, serine, and tryptophan; and 0.3 g tyrosine. A solid medium was prepared by mixing an equal volume of liquid medium at a 2x concentration with 1% (wt/vol) Phytagel (Sigma) previously autoclaved to solubilize all chemicals, and both solutions were maintained at 95°C just prior to mixing in glass Petri dishes. Aliquots of *P. furiosus* culture typically grown to mid-log phase (2×10^8 cells/ml) in defined liquid medium were mixed with DNA at a concentration of 2 to 10 ng DNA per μL of culture, spread in 30 μL aliquots onto defined solid medium. Plates were placed inverted in anaerobic jars and incubated at 90°C for approximately 64 hours. Colonies were picked into 4 mL of defined medium in Hungate tubes and incubated anaerobically overnight at 90°C.

Genomic DNA, isolated using the Zymobead Genomic DNA Kit (Zymo Research), was used for PCR screening, which was carried out by using GXL polymerase (Takara, ClonTech). PCR screening was performed using a pair of primers outside the Mbh locus in order to confirm that the transformation cassette recombined into the correct locus.

Preparation of Cell Suspensions

COM1 and the ΔMbhABC strain were grown in the defined maltose medium in 1L culture bottles at 90°C with shaking as described previously (Lipscomb et al., 2011). Cells were harvested by centrifugation at 18,000 x g for 10 minutes in a Beckman-Coutler Avanti J-30i centrifuge. Cell suspensions were created by washing harvested cells with an anaerobic resuspension buffer containing 20 mM imidazole, 30 mM $MgCl_2 \cdot 6H_2O$, 0.5 M KCl, 2 mM cysteine-HCl, pH 6.5 and resuspending them in the same buffer at cell densities equivalent to OD_{600} = 0.6.

H_2 Production Assays

H_2 production assays are modified from (Lim et al., 2014). In brief, 2.0 mL of cell suspensions was added to rubber-sealed glass vials and the headspace was flushed with argon. Samples were incubated at 80°C for 3 minutes and the reaction was initiated by the addition of the desired concentration of NaCl from an anaerobic 2 M stock solution. At various times, gas samples were removed by syringe and the amount of H_2 was determined using a 6850 Network Gas Chromatograph (Agilent Technologies). Protein concentrations were measured using the Bradford Protein Assay Dye.

Cryo-EM data acquisition

For cryo-EM analysis, 3 μL aliquots of the purified MBH complex at 2-3 mg/ml was applied to a glow-discharged holey carbon grids (C-Flat Cu CF-1.2/1.3, 400 mesh). The grids were blotted for 3-4 s at 10°C with 95% humidity and flash-frozen in liquid ethane using an FEI Vitrobot

IV. Cryo-EM data collection was performed on a 300 kV FEI Titan Krios electron microscopy with a K2 camera positioned post a GIF quantum energy filter. Automated data acquisition was performed with SerialEM (Mastronarde, 2005) and FEI EPU package. Micrographs were recorded in super-resolution counting mode at a nominal magnification of 130,000 × , resulting in a physical pixel size of 1.09 Å per pixel. Defocus values varied from 1.2 μm to 3 μm. The dose rate was 10.2 electron per pixel per second. Exposures of 6 s were dose-fractionated into 30 sub-frames, leading to a total accumulated dose of 51.7 electrons per $Å^2$.

Image processing and 3D reconstruction

Two batches of data were collected. Dose fractionated movie frames were motion corrected (globally and locally), dose weighted and binned by 2 fold with MotionCor2 (Grant and Grigorieff, 2015, Zheng et al., 2017), resulting in summed micrographs in a pixel size of 1.09 Å per pixel. Contrast transfer function (CTF) parameters for each micrograph were estimated by CTFFIND4 (Rohou and Grigorieff, 2015). RELION-2.0 was used for further processing steps (Kimanius et al., 2016). Bad micrographs revealed by manual inspection were excluded from further analysis, yielding 2804 and 2155 good micrographs for each dataset. For each dataset, a manually picked sets of particles were subject to 2D classification. This generated templates for reference-based particle picking, which yielded 674,607 and 574,955 automatically picked particles, respectively. Particle sorting and reference-free 2D classification was performed to remove contaminants and noisy particles, resulting in two datasets with 636,689 and 548,230 particles, respectively. Then 3D classification was performed using an *ab initio* map generated by EMAN2 (Tang et al., 2007) as the initial reference model. For each dataset, one out of 4 classes with high-resolution features was obtained. The two identified good classes were combined as a new set of 301,300 particles,

which was subjected to another round of 3D classification. The most populated 3D class (131,679 particles) was subsequently selected for the final 3D auto-refinement with a soft mask including the protein and detergent regions. This generated a map with an overall resolution of 3.7 Å. The resolution was estimated based on the gold-standard Fourier shell correlation 0.143 criterion (Rosenthal and Henderson, 2003). The final map was corrected for the modulation transfer function (MTF) of the detector and sharpened by applying a negative B-factor, estimated by the post-processing procedure in RELION-2.0. Local resolution distribution was estimated using ResMap (Kucukelbir et al., 2014).

Atomic model building

Most regions of the map, especially the transmembrane helices of membrane subunits, exhibit sufficient features for *de novo* model building of MBH, which started from the global assignment of its 14 subunits. Homology models for six subunits (hydrophilic MbhJ-MbhN and membrane MbhH and MbhM) were generated with the SWISS-MODEL server (Arnold et al., 2006) using the structure of *T. thermophilus* complex I as a template (PDB ID 4hea) (Baradaran et al., 2013). They were fitted into the EM map as rigid bodies with CHIMERA (Pettersen et al., 2004). The assignments of remaining 8 membrane subunits were assisted by their predicted secondary structural features and the excellent main chain connectivity of the map. MbhF, the only membrane subunit with 4 TMHs, was assigned first. Although they all contain 2 TMH, the specific structural features of MbhA, MbhE and MbhI helped to individually locate them to the map. MbhA TM2 is followed by a ferredoxin-like fold, which was predicted by I-TASSER (Yang et al., 2015). For MbhI and MbhE, their TM1-TM2 linkers were predicted to be quite different: a long loop and a following long amphipathic helix for MbhI; a loop with a short helix in the middle for MbhE.

Lastly, MbhB, MbhC, MbhD and MbhG all contain 3 transmembrane helices and they form 4 layers of three-helix bundle together. Among them, MbhC has the longest predicted helices and MbhG TM2-TM3 has the longest loop linker, which helped to locate them on the map. The positioning of last two subunits MbhB and MbhD was assisted by their sequence information.

After the subunit assignment, for the six subunits MbhJ-MbhN, MbhH and MbhM, the fitted homology models were improved by manual adjustments and rebuilding using Coot (Emsley et al., 2010). For each of the remaining 8 membrane subunits MbhA-MbhG and MbhI, a polyalanine model was first built with Coot and subsequent sequence assignment was mainly guided by bulky residues such as Arg, Tyr, Phe and Trp. In the final MBH model, 2470 of 2502 residues was assigned with side chains. MbhI loop Aa42-73 only allows the tracing of its main chain, which were built as polyalanine.

The refinement of the MBH complex model against the cryo-EM map in real space was performed using the phenix.real_space_refine in PHENIX(Adams et al., 2010). The final model was assessed using MOLPROBITY (Chen et al., 2010). All figures were prepared using PyMOL (Schrödinger, LLC.) and CHIMERA.

Quantification and Statistical Analysis

Resolution estimations of cryo-EM density maps are based on the 0.143 Fourier Shell Correlation (FSC) criterion (Chen et al., 2013, Rosenthal and Henderson, 2003).

Data and Software Availability

The accession number for the atomic coordinates reported in this paper is PDB: 6CFW. The accession number for the EM density maps reported in this paper is EMDB: EMD-7468.

Acknowledgments

Cryo-EM images were collected at the David Van Andel Advanced Cryo-Electron Microscopy Suite in the Van Andel Research Institute. This work was funded by grants from the Division of Chemical Sciences, Geosciences and Biosciences, Office of Basic Energy Sciences of the U.S. Department of Energy (DOE; DE-FG05-95ER20175 to M.W.W.A.), the Van Andel Research Institute (to H.L.), and the NIH (AI070285 to H.L.). J.W.P.'s contribution to the structural analysis was supported by the Biological and Electron Transfer and Catalysis (BETCy) EFRC, an Energy Frontier Research Center funded by the U.S. Department of Energy Office of Science (DE-SC0012518).

Author Contributions

M.W.W.A. and H.L. conceived and designed experiments. H.Y., C.-H.W., G.J.S., G.Z., and D.K.H. performed experiments. H.Y., G.J.S., M.W.W.A., J.W.P., and H.L. analyzed the data. H.Y., G.J.S., M.W.W.A., and H.L. wrote the manuscript.

References

Adams, P.D., Afonine, P.V., Bunko´ czi, G., Chen, V.B., Davis, I.W., Echols, N., Headd, J.J., Hung, L.W., Kapral, G.J., Grosse-Kunstleve, R.W., et al. (2010). PHENIX: a comprehensive Python-based system for macromolecular structure solution. Acta Crystallogr. D Biol. Crystallogr. 66, 213–221.

Arnold, K., Bordoli, L., Kopp, J., and Schwede, T. (2006). The SWISS-MODEL workspace: a web-based environment for protein structure homology model-ling. Bioinformatics 22, 195–201.

Baradaran, R., Berrisford, J.M., Minhas, G.S., and Sazanov, L.A. (2013). Crystal structure of the entire respiratory complex I. Nature 494, 443–448.

Belevich, G., Knuuti, J., Verkhovsky, M.I., Wikstro¨ m, M., and Verkhovskaya, M.(2011). Probing the mechanistic role of the long a-helix in subunit L of respiratory Complex I from *Escherichia coli* by site-directed mutagenesis. Mol. Micro-biol. 82, 1086–1095.

Berrisford, J.M., Baradaran, R., and Sazanov, L.A. (2016). Structure of bacterial respiratory complex I. Biochim. Biophys. Acta 1857, 892–901.

Brandt, U. (2011). A two-state stabilization-change mechanism for proton-pumping complex I. Biochim. Biophys. Acta 1807, 1364–1369.

Bryksin, A.V., and Matsumura, I. (2010). Overlap extension PCR cloning: a simple and reliable way to create recombinant plasmids. Biotechniques 48, 463–465.

Chen, V.B., Arendall, W.B., 3rd, Headd, J.J., Keedy, D.A., Immormino, R.M., Kapral, G.J., Murray, L.W., Richardson, J.S., and Richardson, D.C. (2010). MolProbity: all-atom structure validation for macromolecular crystallography. Acta Crystallogr. D Biol. Crystallogr. 66, 12–21.

Chen, S., McMullan, G., Faruqi, A.R., Murshudov, G.N., Short, J.M., Scheres, S.H., and Henderson, R. (2013). High-resolution noise substitution to measure overfitting and validate resolution in 3D structure determination by single particle electron cryomicroscopy. Ultramicroscopy 135, 24–35.

Coincon, M., Uzdavinys, P., Nji, E., Dotson, D.L., Winkelmann, I., Abdul-Hus-sein, S., Cameron, A.D., Beckstein, O., and Drew, D. (2016). Crystal structures reveal the molecular basis of ion translocation in sodium/proton antiporters. Nat. Struct. Mol. Biol. 23, 248–255.

Dementin, S., Burlat, B., De Lacey, A.L., Pardo, A., Adryanczyk-Perrier, G., Guigliarelli, B., Fernandez, V.M., and Rousset, M. (2004). A glutamate is the essential proton transfer gate during the catalytic cycle of the [NiFe] hydrogenase. J. Biol. Chem. 279, 10508–10513.

Efremov, R.G., and Sazanov, L.A. (2011). Structure of the membrane domain of respiratory complex I. Nature 476, 414–420.

Efremov, R.G., and Sazanov, L.A. (2012). The coupling mechanism of respiratory complex I - a structural and evolutionary perspective. Biochim. Biophys. Acta 1817, 1785–1795.

Emsley, P., Lohkamp, B., Scott, W.G., and Cowtan, K. (2010). Features and development of Coot. Acta Crystallogr. D Biol. Crystallogr. 66, 486–501.

Fiedorczuk, K., Letts, J.A., Degliesposti, G., Kaszuba, K., Skehel, M., and Sa-zanov, L.A. (2016). Atomic structure of the entire mammalian mitochondrial complex I. Nature 538, 406–410.

Fontecilla-Camps, J.C., Volbeda, A., Cavazza, C., and Nicolet, Y. (2007). Structure/function relationships of [NiFe]- and [FeFe]-hydrogenases. Chem. Rev. 107, 4273–4303.

Grant, T., and Grigorieff, N. (2015). Measuring the optimal exposure for single particle cryo-EM using a 2.6 A˚ reconstruction of rotavirus VP6. eLife 4, e06980.

Hedderich, R. (2004). Energy-converting [NiFe] hydrogenases from archaea and extremophiles: ancestors of complex I. J. Bioenerg. Biomembr. 36, 65–75.

Hirst, J. (2013). Mitochondrial complex I. Annu. Rev. Biochem. 82, 551–575.

Hirst, J., and Roessler, M.M. (2016). Energy conversion, redox catalysis and generation of reactive oxygen species by respiratory complex I. Biochim. Bio-phys. Acta 1857, 872–883.

Hunte, C., Screpanti, E., Venturi, M., Rimon, A., Padan, E., and Michel, H.(2005). Structure of a Na+/H+ antiporter and insights into mechanism of action and regulation by pH. Nature 435, 1197–1202.

Hunte, C., Zickermann, V., and Brandt, U. (2010). Functional modules and structural basis of conformational coupling in mitochondrial complex I. Science 329, 448–451.

Kaila, V.R., Wikstro¨ m, M., and Hummer, G. (2014). Electrostatics, hydration, and proton transfer dynamics in the membrane domain of respiratory complex I. Proc. Natl. Acad. Sci. USA 111, 6988–6993.

Kim, Y.J., Lee, H.S., Kim, E.S., Bae, S.S., Lim, J.K., Matsumi, R., Lebedinsky, A.V., Sokolova, T.G., Kozhevnikova, D.A., Cha, S.S., et al. (2010). Formate-driven growth coupled with H(2) production. Nature 467, 352–355.

Kimanius, D., Forsberg, B.O., Scheres, S.H., and Lindahl, E. (2016). Accelerated cryo-EM structure determination with parallelisation using GPUs in RELION-2. eLife 5, e18722.

Kosono, S., Haga, K., Tomizawa, R., Kajiyama, Y., Hatano, K., Takeda, S., Wa-kai, Y., Hino, M., and Kudo, T. (2005). Characterization of a multigene-encoded sodium/hydrogen antiporter (sha) from *Pseudomonas aeruginosa*: its involvement in pathogenesis. J. Bacteriol. 187, 5242–5248.

Krulwich, T.A., Sachs, G., and Padan, E. (2011). Molecular aspects of bacterial pH sensing and homeostasis. Nat. Rev. Microbiol. 9, 330–343.

Kucukelbir, A., Sigworth, F.J., and Tagare, H.D. (2014). Quantifying the local resolution of cryo-EM density maps. Nat. Methods 11, 63–65.

Kuppuraj, G., Dudev, M., and Lim, C. (2009). Factors governing metal-ligand distances and coordination geometries of metal complexes. J. Phys. Chem. B 113, 2952–2960.

Lee, C., Kang, H.J., von Ballmoos, C., Newstead, S., Uzdavinys, P., Dotson, D.L., Iwata, S., Beckstein, O., Cameron, A.D., and Drew, D. (2013). A two-domain elevator mechanism for sodium/proton antiport. Nature 501, 573–577.

Letts, J.A., and Sazanov, L.A. (2017). Clarifying the supercomplex: the higher-order organization of the mitochondrial electron transport chain. Nat. Struct. Mol. Biol. 24, 800–808.

Lim, J.K., Mayer, F., Kang, S.G., and Mu¨ ller, V. (2014). Energy conservation by oxidation of formate to carbon dioxide and hydrogen via a sodium ion current in a hyperthermophilic archaeon. Proc. Natl. Acad. Sci. USA 111, 11497–11502.

Lipscomb, G.L., Stirrett, K., Schut, G.J., Yang, F., Jenney, F.E., Jr., Scott, R.A., Adams, M.W., and Westpheling, J. (2011). Natural competence in the hyper-thermophilic archaeon *Pyrococcus furiosus* facilitates genetic manipulation: construction of markerless deletions of genes encoding the two cytoplasmic hydrogenases. Appl. Environ. Microbiol. 77, 2232–2238.

Lipscomb, G.L., Schut, G.J., Thorgersen, M.P., Nixon, W.J., Kelly, R.M., and Adams, M.W. (2014). Engineering hydrogen gas production from formate in a hyperthermophile by heterologous production of an 18-subunit membrane-bound complex. J. Biol. Chem. 289, 2873–2879.

Mastronarde, D.N. (2005). Automated electron microscope tomography using robust prediction of specimen movements. J. Struct. Biol. 152, 36–51.

Mayer, F., and Muller, V. (2014). Adaptations of anaerobic archaea to life under extreme energy limitation. FEMS Microbiol. Rev. 38, 449–472.

McTernan, P.M., Chandrayan, S.K., Wu, C.H., Vaccaro, B.J., Lancaster, W.A., Yang, Q., Fu, D., Hura, G.L., Tainer, J.A., and Adams, M.W. (2014). Intact functional fourteen-subunit respiratory membrane-bound [NiFe]-hydrogenase complex of the hyperthermophilic archaeon *Pyrococcus furiosus*. J. Biol. Chem. 289, 19364–19372.

Moparthi, V.K., and Ha¨ gerha¨ ll, C. (2011). The evolution of respiratory chain complex I from a smaller last common ancestor consisting of 11 protein subunits. J. Mol. Evol. 72, 484–497.

Morino, M., Natsui, S., Swartz, T.H., Krulwich, T.A., and Ito, M. (2008). Single gene deletions of mrpA to mrpG and mrpE point mutations affect activity of the Mrp Na+/H+ antiporter of alkaliphilic *Bacillus* and formation of hetero-oligomeric Mrp complexes. J. Bacteriol. 190, 4162–4172.

Morino, M., Natsui, S., Ono, T., Swartz, T.H., Krulwich, T.A., and Ito, M. (2010). Single site mutations in the hetero-oligomeric Mrp antiporter from alkaliphilic *Bacillus pseudofirmus* OF4 that affect Na+/H+ antiport activity, sodium exclusion, individual Mrp protein levels, or Mrp complex formation. J. Biol. Chem. 285, 30942–30950.

Nisbet, E.G., and Sleep, N.H. (2001). The habitat and nature of early life. Nature 409, 1083–1091.

Ogata, H., Nishikawa, K., and Lubitz, W. (2015). Hydrogens detected by sub-atomic resolution protein crystallography in a [NiFe] hydrogenase. Nature 520, 571–574.

Page, C.C., Moser, C.C., Chen, X., and Dutton, P.L. (1999). Natural engineering principles of electron tunnelling in biological oxidation-reduction. Nature 402, 47–52.

Pettersen, E.F., Goddard, T.D., Huang, C.C., Couch, G.S., Greenblatt, D.M., Meng, E.C., and Ferrin, T.E. (2004). UCSF Chimera–a visualization system for exploratory research and analysis. J. Comput. Chem. 25, 1605–1612.

Pisa, K.Y., Huber, H., Thomm, M., and Mu¨ ller, V. (2007). A sodium ion-dependent A1AO ATP synthase from the hyperthermophilic archaeon *Pyrococcus furiosus*. FEBS J. 274, 3928–3938.

Rohou, A., and Grigorieff, N. (2015). CTFFIND4: Fast and accurate defocus estimation from electron micrographs. J. Struct. Biol. 192, 216–221.

Rosenthal, P.B., and Henderson, R. (2003). Optimal determination of particle orientation, absolute hand, and contrast loss in single-particle electron cryomicroscopy. J. Mol. Biol. 333, 721–745.

Sapra, R., Bagramyan, K., and Adams, M.W. (2003). A simple energy-conserving system: proton reduction coupled to proton translocation. Proc. Natl. Acad. Sci. USA 100, 7545–7550.

Sazanov, L.A. (2015). A giant molecular proton pump: structure and mechanism of respiratory complex I. Nat. Rev. Mol. Cell Biol. 16, 375–388.

azanov, L.A., and Hinchliffe, P. (2006). Structure of the hydrophilic domain of respiratory complex I from *Thermus thermophilus*. Science 311, 1430–1436.

Schut, G.J., Boyd, E.S., Peters, J.W., and Adams, M.W. (2013). The modular respiratory complexes involved in hydrogen and sulfur metabolism by heterotrophic hyperthermophilic archaea and their evolutionary implications. FEMS Microbiol. Rev. 37, 182–203.

Schut, G.J., Lipscomb, G.L., Nguyen, D.M., Kelly, R.M., and Adams, M.W.(2016a). Heterologous production of an energy-conserving carbon monoxide dehydrogenase complex in the hyperthermophile *Pyrococcus furiosus*. Front. Microbiol. 7, 29.

Schut, G.J., Zadvornyy, O., Wu, C.H., Peters, J.W., Boyd, E.S., and Adams, M.W. (2016b). The role of geochemistry and energetics in the evolution of mod-ern respiratory complexes from a proton-reducing ancestor. Biochim. Bio-phys. Acta 1857, 958–970.

Shomura, Y., Yoon, K.S., Nishihara, H., and Higuchi, Y. (2011). Structural basis for a [4Fe-3S] cluster in the oxygen-tolerant membrane-bound [NiFe]-hydrogenase. Nature 479, 253–256.

Steimle, S., Bajzath, C., Do¨ rner, K., Schulte, M., Bothe, V., and Friedrich, T.(2011). Role of subunit NuoL for proton translocation by respiratory complex I. Biochemistry 50, 3386–3393.

Swartz, T.H., Ikewada, S., Ishikawa, O., Ito, M., and Krulwich, T.A. (2005). The Mrp system: a giant among monovalent cation/proton antiporters? Extremophiles 9, 345–354.

Tang, G., Peng, L., Baldwin, P.R., Mann, D.S., Jiang, W., Rees, I., and Ludtke, S.J. (2007). EMAN2: an extensible image processing suite for electron microscopy. J. Struct. Biol. 157, 38–46.

Volbeda, A., Garcin, E., Piras, C., DeLacey, A.L., Fernandez, V.M., Hatchikian, E.C., Frey, M., and Fontecilla-Camps, J.C. (1996). Structure of the [NiFe] hydrogenase active site: Evidence for biologically uncommon Fe ligands. J. Am. Chem. Soc. 118, 12989–12996.

Wirth, C., Brandt, U., Hunte, C., and Zickermann, V. (2016). Structure and function of mitochondrial complex I. Biochim. Biophys. Acta 1857, 902–914.

Wo¨ hlert, D., Ku¨ hlbrandt, W., and Yildiz, O. (2014). Structure and substrate ion binding in the sodium/proton antiporter PaNhaP. eLife 3, e03579.

Yang, J., Yan, R., Roy, A., Xu, D., Poisson, J., and Zhang, Y. (2015). The I-TASSER Suite: protein structure and function prediction. Nat. Methods 12, 7–8.

Zheng, S.Q., Palovcak, E., Armache, J.P., Verba, K.A., Cheng, Y., and Agard, D.A. (2017). MotionCor2: anisotropic correction of beam-induced motion for improved cryo-electron microscopy. Nat. Methods 14, 331–332.

Zhu, S., and Vik, S.B. (2015). Constraining the lateral helix of respiratory Com-plex I by cross-linking does not impair enzyme activity or proton translocation. J. Biol. Chem. 290, 20761–20773.

Zhu, J., Vinothkumar, K.R., and Hirst, J. (2016). Structure of mammalian respiratory complex I. Nature 536, 354–358.

Zickermann, V., Wirth, C., Nasiri, H., Siegmund, K., Schwalbe, H., Hunte, C., and Brandt, U. (2015). Structural biology. Mechanistic insight from the crystal structure of mitochondrial complex I. Science 347, 44–49.

Table B1. Homologous counterparts among respiratory Complex I (*Thermus thermophilus*), *Bacillus subtilis* Mrp H^+/Na^+ antiporter, and *Pyrococcus furiosus* MBH

Proposed MBH module	***P. furiosus* MBH complex**	***B. subtilis* Mrp complex**	***T. thermophilus* Complex I**	**Module of Complex I**
-	-	-	Nqo15/Nqo16	-
-	-	-	Nqo1/Nqo2/ Nqo3	N-module
Membrane-anchored hydrogenase module	MbhJ	-	Nqo6	Q-module
	MbhK	-	Nqo5	
	MbhL	-	Nqo4	
	MbhN	-	Nqo9	
	MbhM	-	Nqo8	P-module
-	-	MrpA TM1-16	Nqo12/Nqo13	
-	MbhI N-terminal[a]	-	Nqo7 N-terminal	
-	MbhI C-terminal[b]	-	Nqo12 C-terminal	
Proton translocation module	MbhD[c]	MrpA TM17-21	Nqo10	
	MbhE[c]			
	MbhG	MrpC	Nqo11	
	MbhH	MrpD	Nqo14	
Sodium translocation module	MbhF	MrpB	-	-
	MbhA	MrpE	-	
	MbhB	MrpF	-	
	MbhC	MrpG	-	

[a] MbhI N-terminal TMH1 and its following loop are homologous to Nqo7 N-terminal TMH1 and its following loop (Figure SB5B).

[b] MbhI C-terminal lateral helix and TMH2 is homologous to Nqo12 C-terminal lateral helix and TMH16 (Figures B3D and SB4I)

[c] MbhD and MbhE together are homologous to Nqo10 (Figures B3D and SB4H)

Figure B1

Overall structure of the *Pyrococcus furiosus* MBH. (A) The respiratory MBH complex and complex I are evolutionarily and functionally related to the Mrp H+/Na+ antiporter system. Fd_{ox} and Fd_{red} represent oxidized and reduced ferredoxin, respectively. (B) Operon encoding 14 subunits (MbhA–MbhN) of *P. furiosus* MBH are colored as labeled. Three modules based on the MBH structure are indicated. The operon was genetically modified for complex preparation: a His_9 tag was inserted to the N terminus of *mbhJ* with preceding promoters (P_{gdh} and P_{slp}) and selectable marker (*pyrF*). See STAR Methods for more details. (C) Cryo-EM map of MBH complex segmented by subunits and viewed from the membrane side (left) and cytoplasmic side (right). Subunits are colored as those in (B). (D) Two orthogonal views of the MBH structure in cartoon display. Subunits are colored the same as in (B). Inset: arrangement of three [4Fe-4S] clusters and one [NiFe]-center in the peripheral arm viewed in an orientation as in the right panel. The distance between metal sites, including center-to-center and edge-to-edge distances (in brackets) are indicated in Å. See also Figures SB1–3.

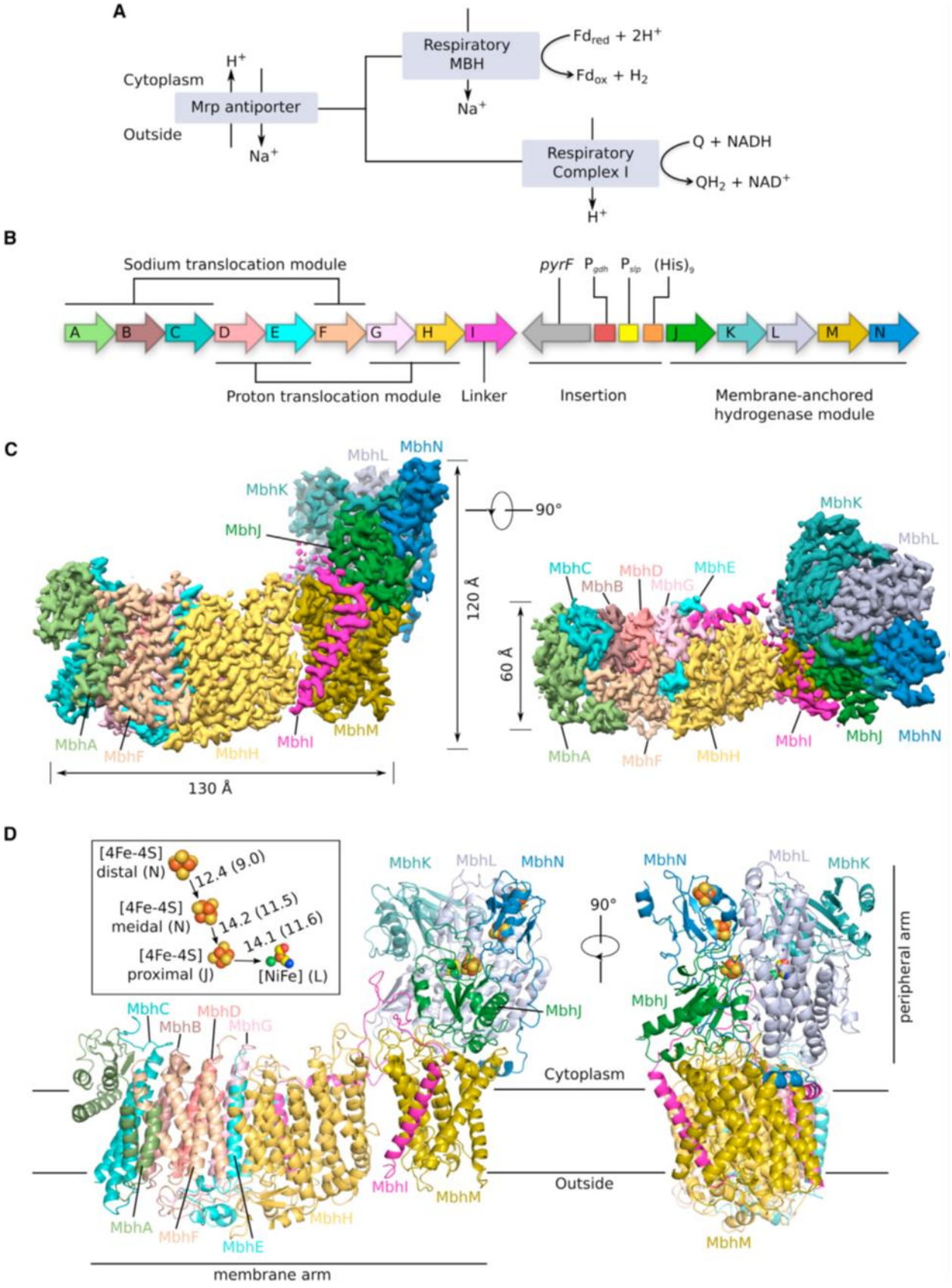
A
Respiratory MBH
Fd_{red} + $2H^+$
Fd_{ox} + H_2
H^+
Cytoplasm
Mrp antiporter
Outside
Na^+
Na^+
Respiratory Complex I
Q + NADH
QH_2 + NAD^+
H^+
B
Sodium translocation module
pyrF
P_{gdh}
P_{slp}
$(His)_9$
A
B
C
D
E
F
G
H
I
J
K
L
M
N
Proton translocation module
Linker
Insertion
Membrane-anchored hydrogenase module
C
MbhL
MbhN
MbhK
MbhJ
90°
120 Å
60 Å
MbhA
MbhF
MbhH
MbhI
MbhM
130 Å
MbhC
MbhD
MbhE
MbhB
MbhG
D
[4Fe-4S] distal (N)
12.4 (9.0)
[4Fe-4S] meidal (N)
14.2 (11.5)
[4Fe-4S] proximal (J)
14.1 (11.6)
[NiFe] (L)
peripheral arm
Cytoplasm
Outside
membrane arm

Figure B2

Structures of the MBH membrane subunits and comparisons with their corresponding subunits in Complex I. (A) Overlay of MbhH (yellow) with Nqo14 (magenta) of *T. thermophilus* complex I (PDB: 4hea) illustrates the common fold of the two antiporter-like subunits. The structures are shown as cartoons in top view—looking down the membrane plane from the cytosol. The number at the end of each helix cylinder refers to the TMH number in the primary sequence. Note that TMH7 and TMH12 are discontinuous, a hallmark of the antiporter-like subunits previously observed in complexI. (B) Left: side view from within the membrane plane showing the detailed fold of the antiporter-like subunit MbhH. The two putative proton-translocating five-helix folding units, TMH4-TMH8 and TMH9-TMH13, are colored in blue and light gray, respectively. The 180° rotation symbol underneath the gray folding unit indicates that the gray unit needs to be flipped upside down to fit the blue folding unit, as shown in the right panel. Right: the good fit between the upside-down flipped gray MbhH TMH9-13 unit with the blue TMH4-8 unit indicates an inverted arrangement of the two folding units in the antiporter-like MBH subunit H. (C) Structure of the membrane subunit MbhM in cartoon presentation as viewed from cytoplasmic side. (D) Overlay of MbhM with the Nqo8 of *T. thermophilus* complex I (PDB: 4hea) shows a conserved fold of the two proteins. TMH9 of Nqo8 (shaded area) is absent in MbhM. (E) Architecture of the seven small MBH subunits. Left: top view from cytoplasmic side with all TMH numbered. Right: side view from membrane side. See also Figure SB4.

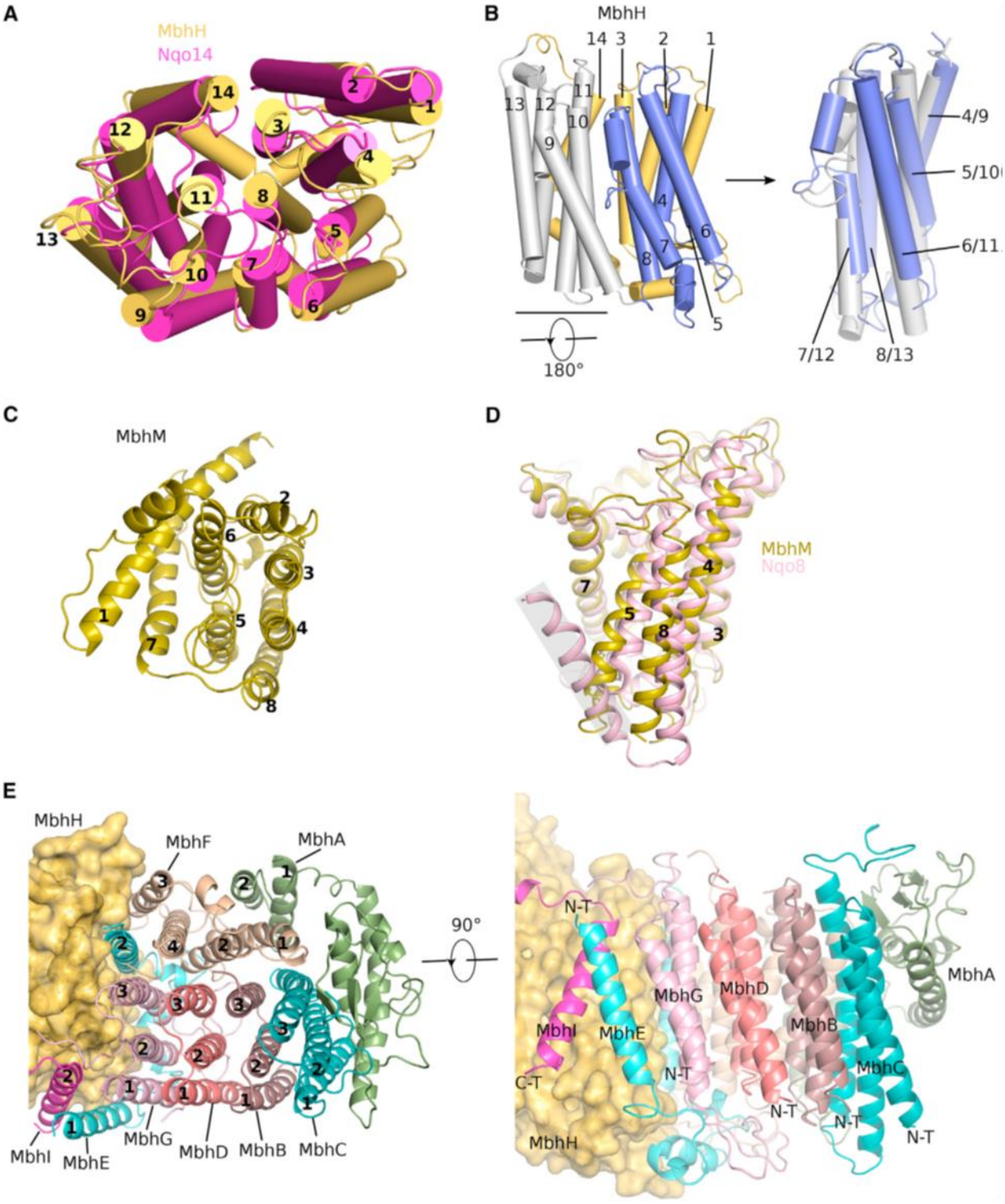
A
MbhH
Nqo14
B
MbhH
180°
4/9
5/10
6/11
7/12
8/13
C
MbhM
D
MbhM
Nqo8
E
MbhH
MbhF
MbhA
90°
MbhI
MbhE
MbhG
MbhD
MbhB
MbhC
N-T
C-T

Figure B3

The MBH membrane arm and its relationship with Complex I. (A) Top view of the MBH membrane arm from the cytoplasm. Subunits are colored as in Figure B1D. Outlined region is the proton-translocation module containing two potential proton pathways. (B) Complex I (*T. thermophilus*; PDB: 4hea) membrane arm is lined up with MBH in (A) through the alignment of their homologous subunits on the proximal end of the membrane domain: Nqo8 (complex I) and MbhM (MBH complex). Subunits are colored as labeled where homologous subunits between complex I and MBH are colored the same. Outlined region is the proton-translocation module shared with MBH but its orientation is reversed compared to that in MBH. (C) Complex I (*T. thermophilus*; PDB ID 4hea) is lined up with MBH via their respective antiporter-like subunits Nqo14 and MbhH. They are shown separately for clarity. The well-aligned proton-translocation modules (as outlined in A and B) are shown as transparent surfaces. MBH subunits are colored as in (A). Complex I Nqo12 is in orange, Nqo13 green, Nqo10, Nqo11, and Nqo14 light gray, and all the other subunits dark gray. (D) Zoomed view of the alignment as in (C). Subunits within the shared proton-translocation module are shown. Complex I Nqo8 and MBH MbhM are shown as a transparent cartoon. Prominent shared features are labeled, including: (1) the discontinuous TMH7 and TMH12 of MbhH/Nqo14, (2) the lateral helix HL and the following TMH of MbhI/Nqo12 anchored to the discontinuous TMH7, and (3) TMH3 of MbhD/Nqo10 with a p-bulge. (E) Two potential proton translocation paths in the MBH. The discontinuous helices of MbhH (TMH7 and TMH12; featured in antiporter-like subunits of complex I) and the p-bulge helix (TMH3 of MbhD) are shown as cylinders. Polar residues lining the proton path are shown as sticks. Protonatable residues along the horizontal central hydrophilic axis are

underlined. A hydrophilic axis across MbhM membrane interior is also identified but it is separated from that in MbhH due to a gap between the two subunits. See also Figure SB4.

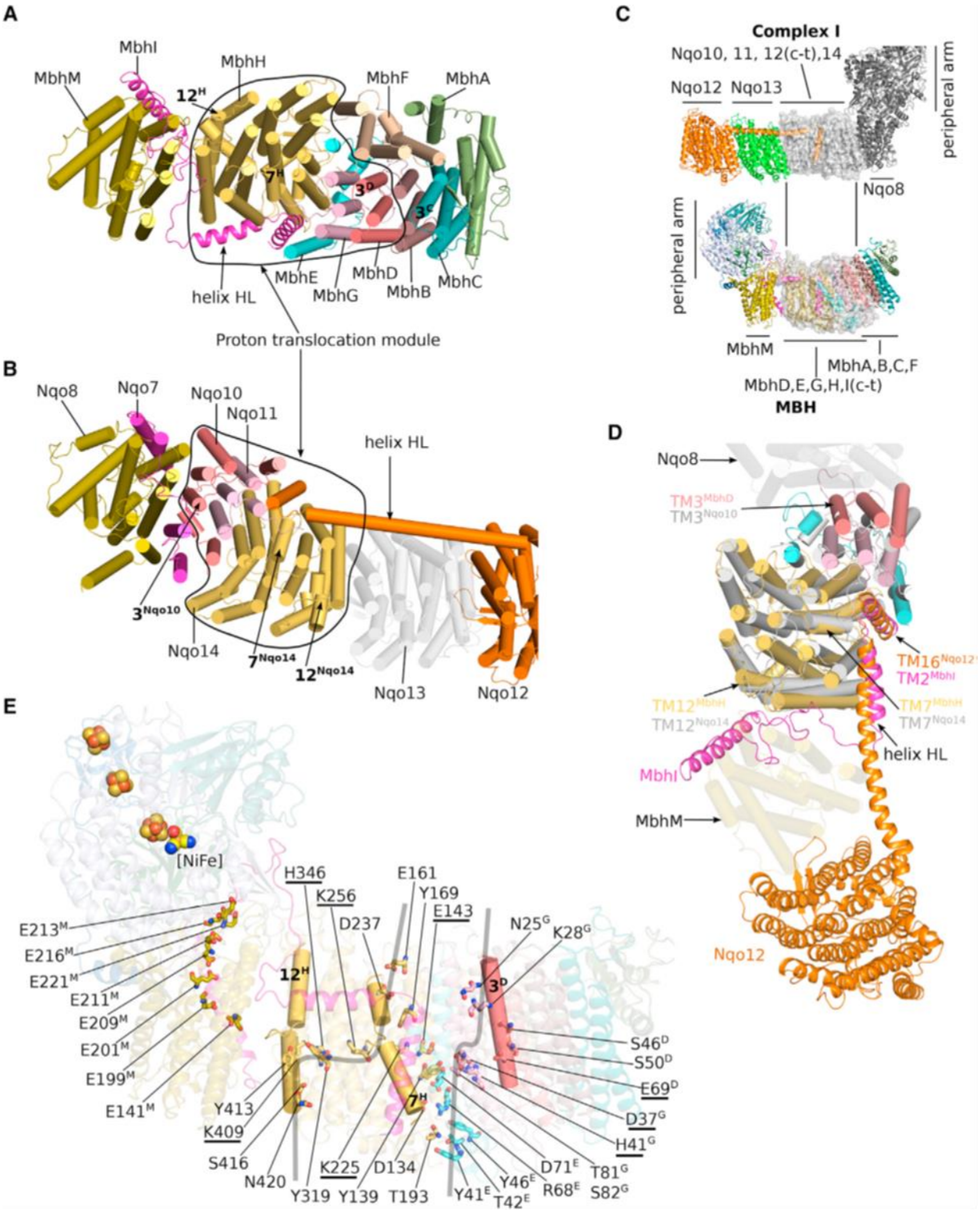
A
MbhI
MbhM
MbhH
MbhF
MbhA
12H
7H
3D
3C
helix HL
MbhE
MbhG
MbhD
MbhB
MbhC
Proton translocation module
B
Nqo8
Nqo7
Nqo10
Nqo11
helix HL
3Nqo10
Nqo14
7Nqo14
12Nqo14
Nqo13
Nqo12
C
Complex I
Nqo10, 11, 12(c-t),14
Nqo12
Nqo13
peripheral arm
Nqo8
peripheral arm
MbhM
MbhA,B,C,F
MbhD,E,G,H,I(c-t)
MBH
D
Nqo8
TM3MbhD
TM3Nqo10
TM16Nqo12
TM2MbhI
TM12MbhH
TM12Nqo14
TM7MbhH
TM7Nqo14
helix HL
MbhI
MbhM
Nqo12
E
[NiFe]
H346
K256
D237
E161
Y169
E143
N25G
K28G
E213M
E216M
E221M
E211M
E209M
E201M
E199M
E141M
12H
3D
S46D
S50D
E69D
D37G
H41G
7H
Y413
K409
S416
N420
K225
D134
T193
Y319
Y139
D71E
T81G
Y46E
R68E
S82G
Y41E
T42E

Figure B4

Peripheral hydrogenase arm. (A) Architecture of the peripheral arm of the MBH complex anchored to the membrane by MbhM, viewed parallel to the membrane. Three loops that link the first two N-terminal b strands (b1-b2) of MbhL, TMH1, and TMH2 of MbhI, and TMH5 and TMH6 of MbhM are at the interface between peripheral and membrane arms. The hydrogen-evolving [NiFe]-center is located right above the three interfacial loops. The MBH subunits are colored as in Figure B1D. (B) Zoomed view of the structure around the hydrogenase catalytic center. The curved dark green arrow marks a possible proton pathway from the bulk solvent to the catalytic [NiFe] center. (C) Sequence alignment of MbhL with its counterparts in selected members of group 4 energy-converting hydrogenases. EcoHycE, *Escherichia coli* hydroge-nase-3 subunit HycE; EcoHyfG, *Escherichia coli* hydrogenase-4 subunit HyfG; MbaEchE, Methanosarcina barkeri hydrogenase subunit EchE. (D) A detailed comparison of the redox active sites of the MBH and *T. thermophilus* complex I. The structures are aligned based on their homologous soluble subunits MBH MbhL and complex I Nqo4. Individual subunits are colored as in Figure SB5B that shows the whole structures. In complex I, the conserved H38 and Y87 of Nqo4 bind the quinone headgroup. The H_2-evolving catalytic site of MBH is defined by MbhL E21, C374, and the [NiFe] center. Importantly, the three interfacial loops (between the peripheral and membrane arms) in MBH and complex I are in a similar configuration to probe their respective active sites. (E) Sequence alignment of the three linker loops of MBH and complex I as shown in (D). The protein sequences are from *Pyrococcus furiosus* (Pfu), *Thermus thermophiles* (Tth), and *Ovis aries* (Ova). See also Figures SB5 and SB6.

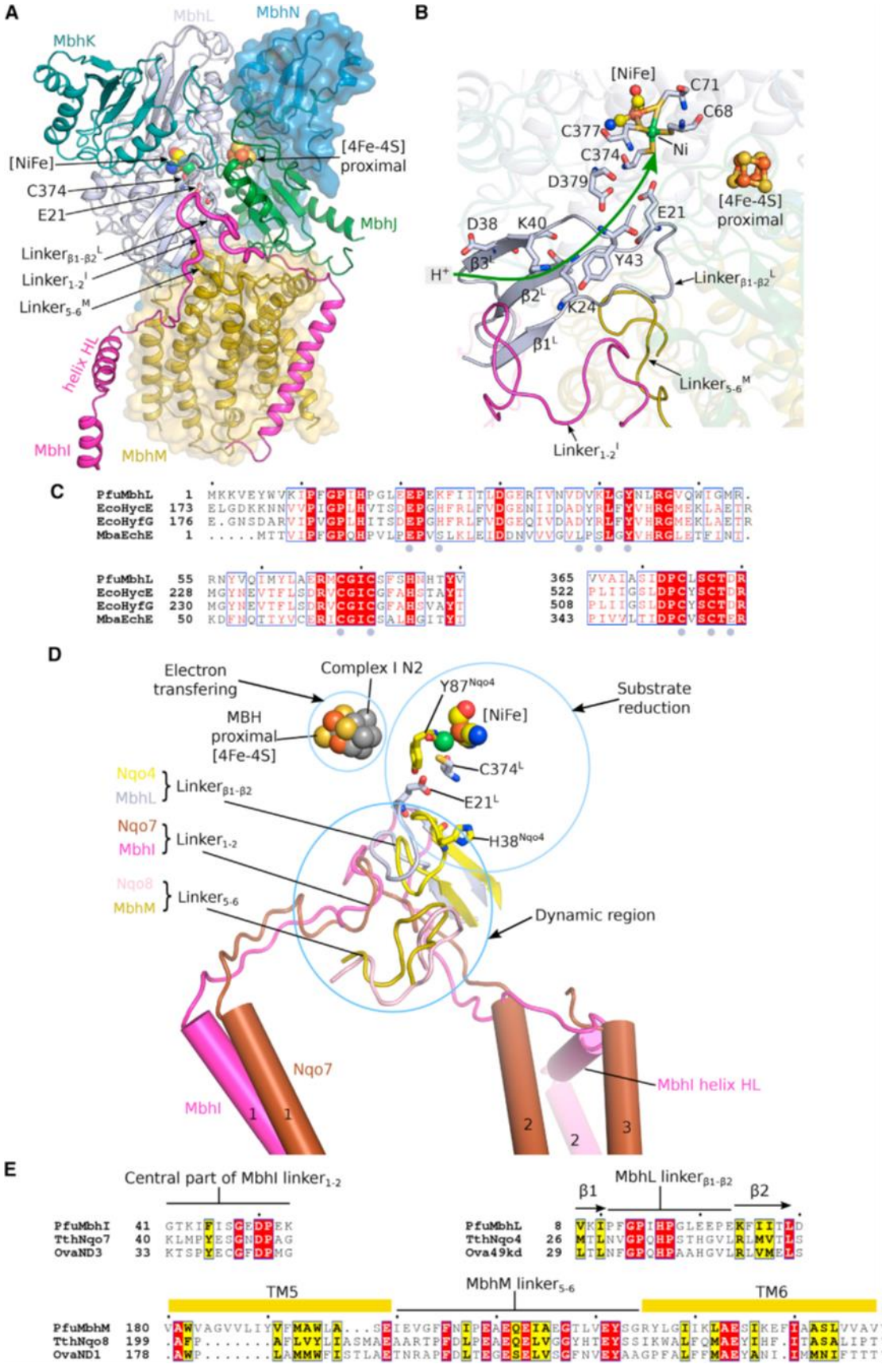
A
MbhL
MbhN
MbhK
[NiFe]
[4Fe-4S] proximal
C374
E21
MbhJ
Linker β1-β2 L
Linker 1-2 I
Linker 5-6 M
helix HL
MbhI
MbhM
B
[NiFe]
C71
C68
C377
C374
Ni
D379
[4Fe-4S] proximal
E21
D38
K40
Y43
H+
β3 I
β2 L
K24
β1 L
Linker β1-β2 L
Linker 5-6 M
Linker 1-2 I
C
PfuMbhL 1 MKKVEYWVKIPFGPHHPGLEEPEKFIITLDGERIVNVDVKLGYNLRGVQWIGMR.
EcoHycE 173 ELGDKKNNVVPIGPLHVTSDEPGHFRLFVDGENIIDADYRLEYVHRGMEKLAETR
EcoHyfG 176 E.GNSDARVIPVGPLHITSDEPGHFRLFVDGEQIVDADYRLEYVHRGMEKLAETR
MbaEchE 1 .....MTTVIPFGPQHPVLPEPVSLKLEIDDNVVVGVLPSLGYVHRGLETFINI.
PfuMbhL 55 RNYVQIMYLAERMCGICSFSHNHTYV
EcoHycE 228 MGYNEVTFLSDRVCGICGFAHGTAYT
EcoHyfG 230 MGYNEVTFLSDRVCGICGFAHGSVAYT
MbaEchE 50 KDFNQTTYVCERICGICSALHGITYH
365 VVAIASIDPCLSCTER
522 PLIIGSLDPCYSCTGR
508 PLIIGSLDPCYSCTGR
343 PIVVLTIDPCVSCTER
D
Electron transfering
Complex I N2
MBH proximal [4Fe-4S]
Y87 Nqo4
[NiFe]
Substrate reduction
C374 L
E21 L
H38 Nqo4
Nqo4
MbhL
Linker β1-β2
Nqo7
MbhI
Linker 1-2
Nqo8
MbhM
Linker 5-6
Dynamic region
Nqo7
MbhI
MbhI helix HL
1
1
2
2
3
E
Central part of MbhI linker 1-2
PfuMbhI 41 GTKIFISGEDPEK
TthNqo7 40 KLMPYESGNDPAG
OvaND3 33 KTSPYECGFDPMG
β1
MbhL linker β1-β2
β2
PfuMbhL 8 VKIPFGPHPGLEEPEKFIITLD
TthNqo4 26 MTLNVGPQHPSTHGVLRLMVTLS
Ova49kd 29 LTLNFGPQHPAAHGVLRLVMELS
TM5
MbhM linker 5-6
TM6
PfuMbhM 180 VAWVAGVVLIYVPMAWLA...SEIEVGFFNIPPAEQEIAEGTLVEYSGRYLGIIKLAESIKEFIAASLVVAV
TthNqo8 199 .AFP.....AFLVYLIASMAEAARTPFDLPEAEQLVGGYHIEYSSIKWALFQMAEYIHF.ITASALIPT
OvaND1 178 .AWP.....LAMMWFISTLAETNRAPFDLTEGESELVSGFNVEYAAGPFALFFMAEYANI.IMMNIFTTT

Figure B5

Putative sodium translocation path in MBH. (A) Two negatively charged cavities are identified as potential sodium-binding sites in MbhA–MbhC and MbhF and are shown as red surfaces. Subunits are colored as in Figure B1D. TMHs are shown as cylinders and the MbhA ferredoxin-like domain is shown as cartoon. (B) The first cavity is halfway through the membrane where the highly conserved D35 of MbhB resides. Residues highly conserved between MBH and Mrp system are underlined. Detailed sequence alignment is shown in Figure SB7. (C) The second cavity is at the extracellular side where the highly conserved MbhB D59 is located. The extracellular linkerTMH1–TMH2 of MbhF packs against MbhG via hydrophobic interactions, shown by the shaded area, and constricts the size of the cavity opening to the solvent. For (B) and (C), Residues highly conserved between MBH and Mrp system are underlined. Detailed sequence alignment is shown in Figure SB7. (D) A cutaway electrostatic surface potential of the second cavity showing that MbhB D59 is located at the tip of a funnel-like opening. (E) Sequences of the interacting structural elements of MbhF and MbhG (shaded in C) are highly conserved in the Mrp system. See also Figure SB7.

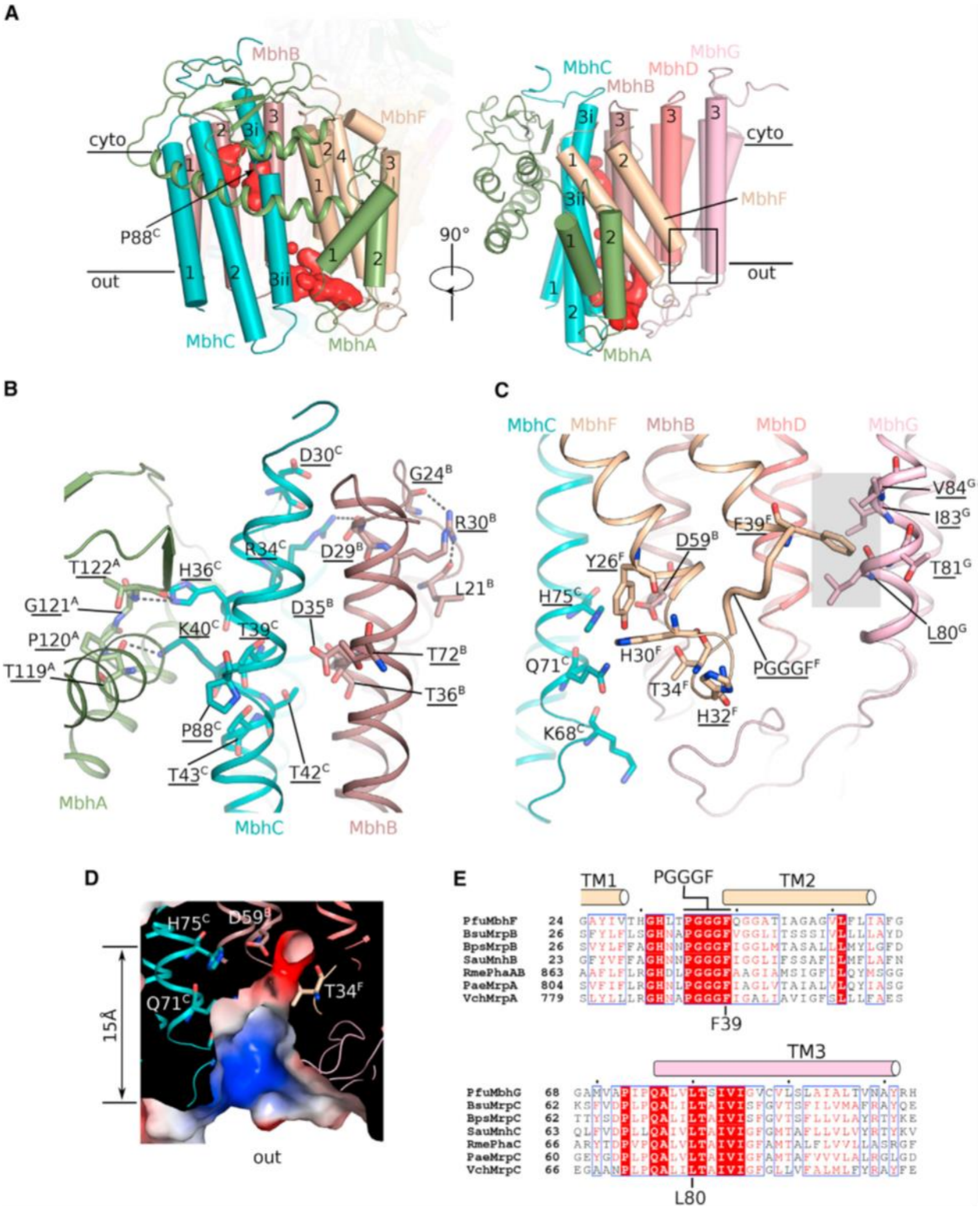
A
MbhB
MbhF
cyto
P88C
out
MbhC
MbhA
90°
MbhC
MbhD
MbhG
MbhB
cyto
MbhF
out
MbhA
B
D30C
G24B
R30B
R34C
D29B
T122A
H36C
L21B
G121A
D35B
K40C
T39C
P120A
T72B
T119A
T36B
P88C
T43C
T42C
MbhA
MbhC
MbhB
C
MbhC
MbhF
MbhB
MbhD
MbhG
V84G
I83G
F39F
D59B
Y26F
T81G
H75C
L80G
H30F
PGGGFF
Q71C
T34F
H32F
K68C
D
H75C
D59B
15Å
Q71C
T34F
out
E
TM1
PGGGF
TM2
PfuMbhF 24 GAYIVTHGHLTPGGGFQGGATIAGAGVLFLIAFG
BsuMrpB 26 SFYLFLSGHNAPGGGFVGGLITSSSIVLLLLAYD
BpsMrpB 26 SVYLFFAGHNNPGGGFIGGLMTASALLLMYLGFD
SauMnhB 23 GFYVFFAGHNNPGGGFIGGLIFSSAFILMFLAFN
RmePhaAB 863 AAFLFLRGHDLPGGGFAAGIAMSIGFILQYMSGG
PaeMrpA 804 SVFIFLRGHNLPGGGFIAGLVTAIALVLQYIASG
VchMrpA 779 SLYLLLRGHNAPGGGFIGALIAVIGFSLLLFAES
F39
TM3
PfuMbhG 68 GAMVRPIPQALVLTSIVIGVCVLSLAIALTVNAYRH
BsuMrpC 62 KSFVDPLPQALILTAIVISFGVTSFILVMAFRAYQE
BpsMrpC 62 TTYSDPLPQALILTAIVISFGVTSFLLVLAYRTYKE
SauMnhC 63 QLFVDPLLQAIVLTAIVIGFGMTAFLLVLVYRTYKV
RmePhaC 66 ARYIDPVPQALVLTAIVIGFAMTALFLVVLLASRGF
PaeMrpC 60 GEYGDPLPQALVLTAIVIGFAMTAFVVVLALRGLGD
VchMrpC 66 EGAANPLPQALILTAIVIGFGLLVFALMLFYRAYFE
L80

Figure B6

Comparison of the working models of Complex I, MBH, and the homologous Mrp H^+/Na^+ antiporter. (A) A putative redox-driven proton pumping mechanism of complex I. Sketched are the prominent features highlighted in previous studies of complex I: three-loop cluster, lateral helix HL, and the four potential proton translocation pathways (gray arrows). Note that the left three antiporter-like subunits are the primary candidates for proton translocation while the fourth proton path within the small subunits is controversial. (B) A working model of MBH. The MBH modules shared with complex I—the membrane-anchored hydrogenase module and H^+ translocation module—are differently arranged, suggesting a mechanism related to complex I but with some variations: the redox reaction may drive the outward flow of proton through antiporter-like subunit MbhH and then the expelled proton may flow inward through the second proton path to drive the export of the sodium ion via the tentatively identified sodium path. (C) The proposed proton- and sodium-translocation paths in MBH may be conserved in the Mrp H^+/Na^+ antiporter. See sequence alignment in Figure SB7 and a list of subunit correspondence among MBH, Mrp, and complex I in Table B1. MrpA, the predicted antiporter-like subunit, may contribute an extra proton path to the antiporter, as illustrated by the left dashed arrow. For (A)–(C), a dashed line within a proton-trans-location module separate the antiporter-like subunits from the other small subunits within the same module. Curved arrows mark the potential proton- or sodium-translocation paths, solid arrows indicate paths with stronger evidence, and dashed arrows mark those with less certainty. See also Figure SB7.

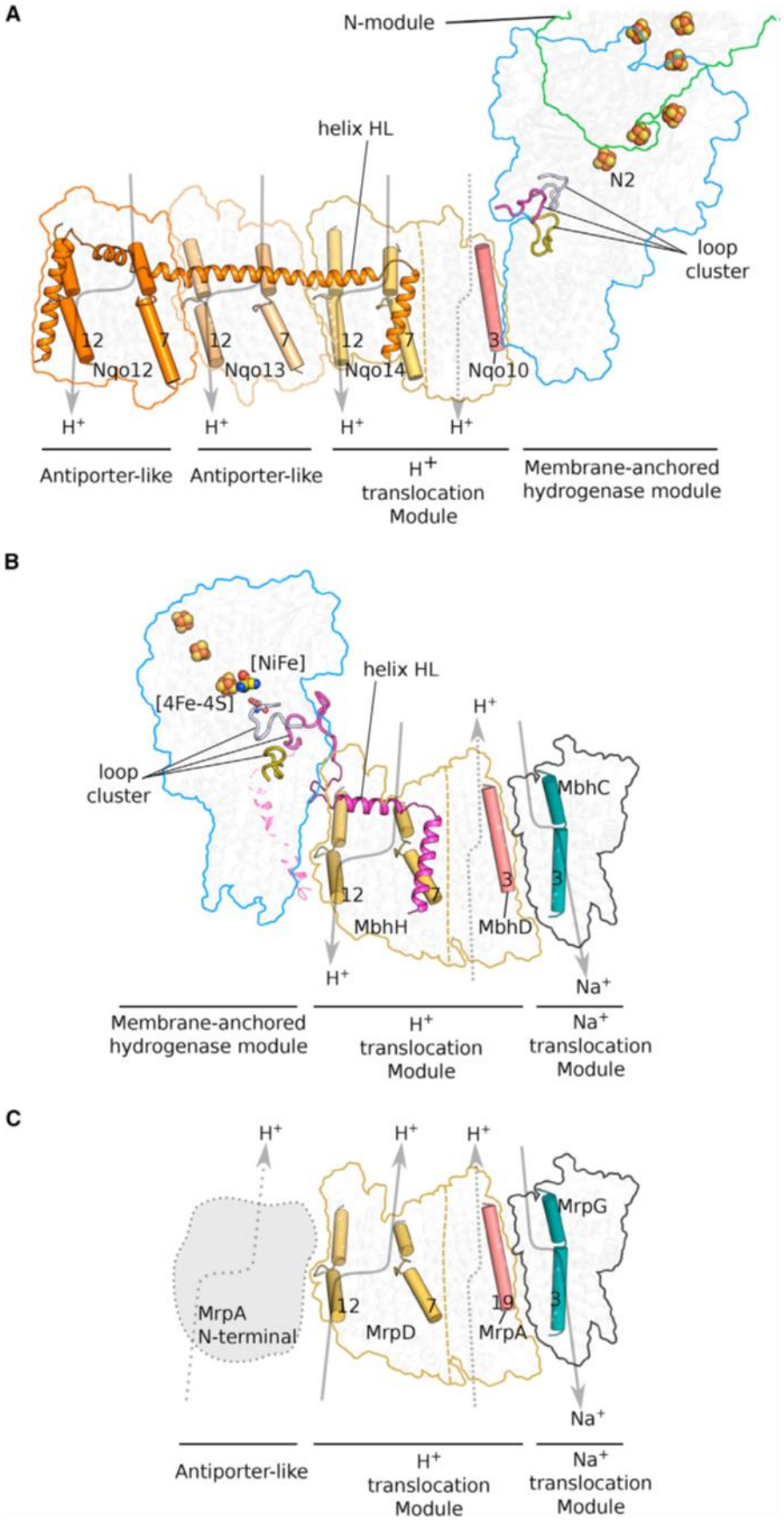
A
N-module
helix HL
N2
loop
cluster
12
7
Nqo12
12
7
Nqo13
12
7
Nqo14
3
Nqo10
H+
H+
H+
H+
Antiporter-like
Antiporter-like
H+
translocation
Module
Membrane-anchored
hydrogenase module
B
[NiFe]
[4Fe-4S]
helix HL
H+
loop
cluster
MbhC
12
7
MbhH
3
MbhD
3
H+
Na+
Membrane-anchored
hydrogenase module
H+
translocation
Module
Na+
translocation
Module
C
H+
H+
H+
MrpG
MrpA
N-terminal
12
7
MrpD
19
MrpA
3
Na+
Antiporter-like
H+
translocation
Module
Na+
translocation
Module

Figure SB1

Biochemical characterization of *Pyrococcus furiosus* MBH complex, related to Figure B1 and STAR Methods. (A and B) Na^+-dependent H_2 production activity of *P. furiosus*. Effect of NaCl concentration (0, 50 or 150 mM) on the H_2 production activity of cell suspensions of the parent (COM1, panel (A) or DmbhABC (B) strains. Data are represented as mean ± SEM. (C–E) Preparation of MBH for single-particle cryo-EM analysis. (C) The predicted molecular weight (kDa) of each of the fourteen MBH subunits. (D) A representative profile of size-exclusion chromatography (Superose 6 10/300 GL column) of the purified MBH complex solubilized in the detergent n-Dodecyl b-D-maltoside. (E) SDS-PAGE of the pooled gel filtration peak fractions shows the presence of all fourteen MBH subunits as labeled to the right. Molecular weight markers in kDa are labeled to the left.

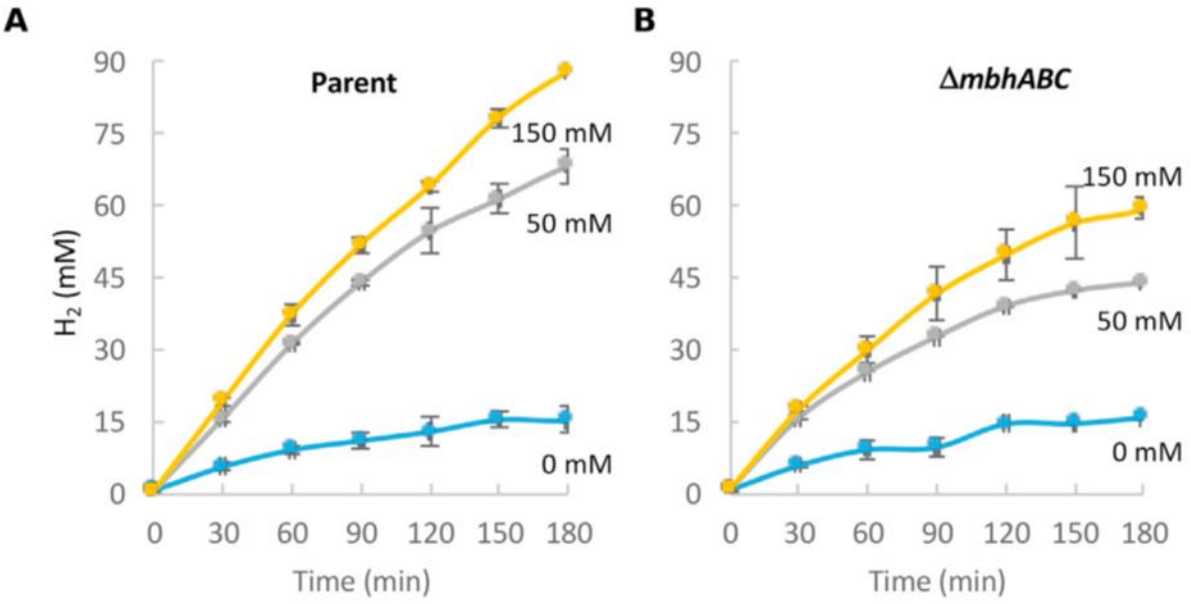

C

MBH Subunit	MW (KDa)
H	54.9
L	47.9
M	35.4
K	20.2
A	18.7
J	18.3
N	15.7
F	15.5
C	13.5
I	13.0
G	12.8
E	11.1
D	10.4
B	9.1

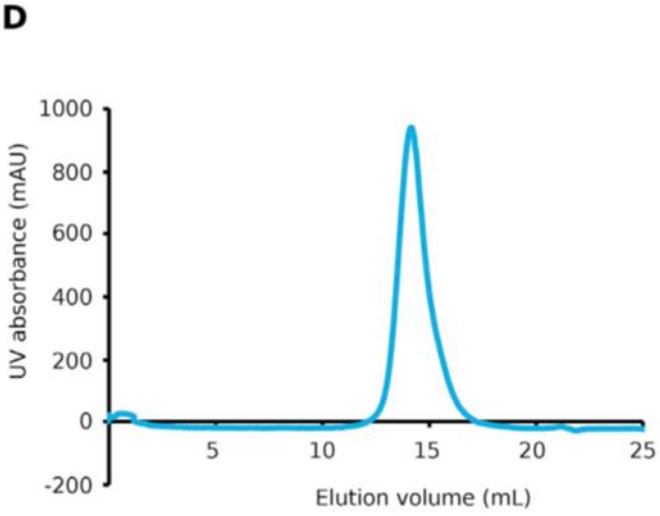

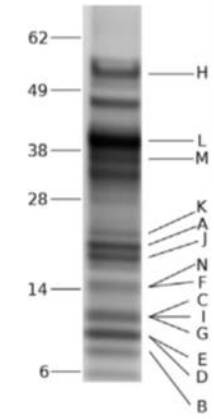

Figure SB2

Cryo-EM analysis of the archaeon *Pyrococcus furiosus* MBH complex, related to Figure B1. (A) Representative cryo-EM micrograph of the MBH particles. (B) Representative 2D class averages of the MBH particles. (C) The workflow of cryo-EM data processing. Two datasets, each contains 2804 and 2155 micrographs, respectively, were collected and processed separately during 2D classification and the first round of 3D classification. The best 3D class from these two datasets were combined for the second round of 3D classification. Then the most populated 3D class (131,679 particles, 44% of total particles) was subjected to the final refinement, which resulted in a 3D density map with an estimated resolution of 3.7 A. See STAR Methods for more details. (D–F) Statistics of the cryo-EM 3D map. (D) Angular distribution of all particles used in the final 3D reconstruction (top panel) is shown with the corresponding view of the 3D map (bottom panel). The number of particles in each orientation is indicated by bar length and color (blue, low; red, high). (E) The gold-standard Fourier shell correlation (FSC) curve of the 3D map. (F) Local resolution of the 3D density map, calculated with ResMap. The range of resolution is color-coded from the higher resolution blue (3 Å) to the lower resolution red (5 Å).

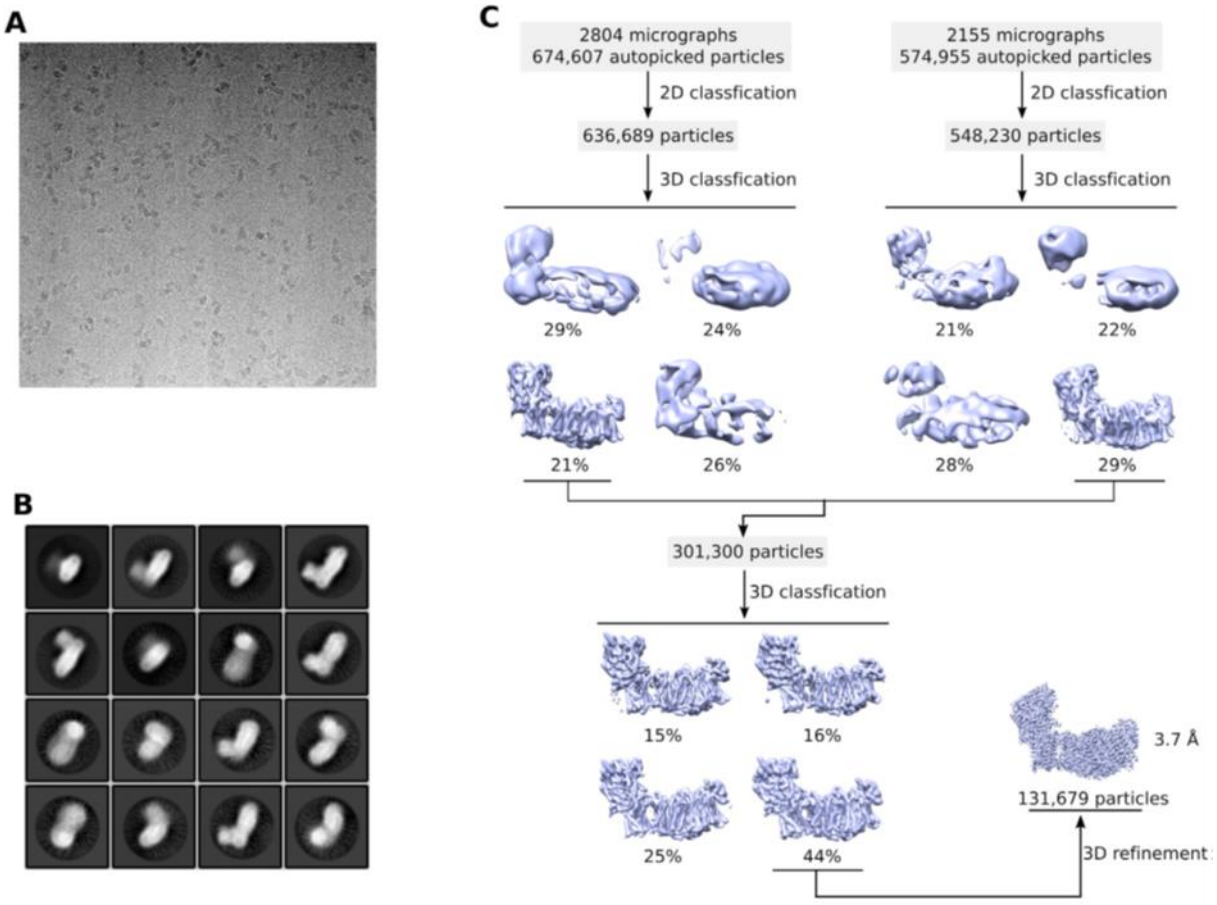
A
B
C
2804 micrographs
674,607 autopicked particles
2D classfication
636,689 particles
3D classfication
29%
24%
21%
26%
2155 micrographs
574,955 autopicked particles
2D classfication
548,230 particles
3D classfication
21%
22%
28%
29%
301,300 particles
3D classfication
15%
16%
25%
44%
3.7 Å
131,679 particles
3D refinement

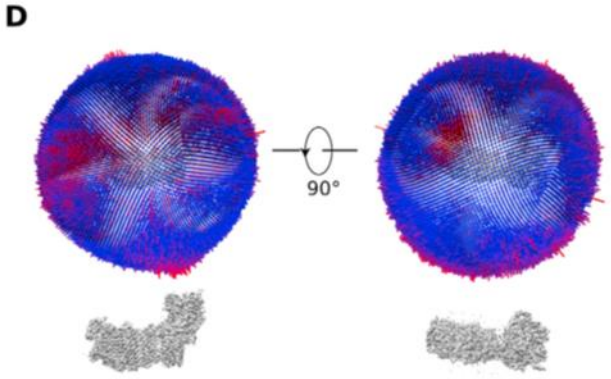
D
90°

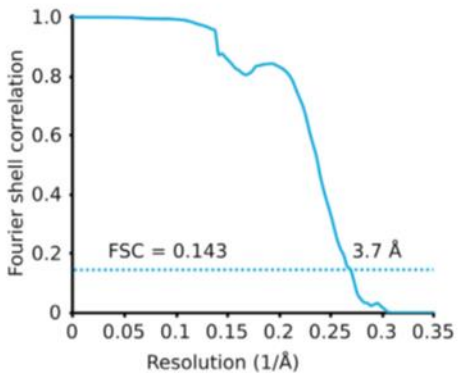
E
Fourier shell correlation
1.0
0.8
0.6
0.4
0.2
0
FSC = 0.143
3.7 Å
0 0.05 0.1 0.15 0.2 0.25 0.3 0.35
Resolution (1/Å)

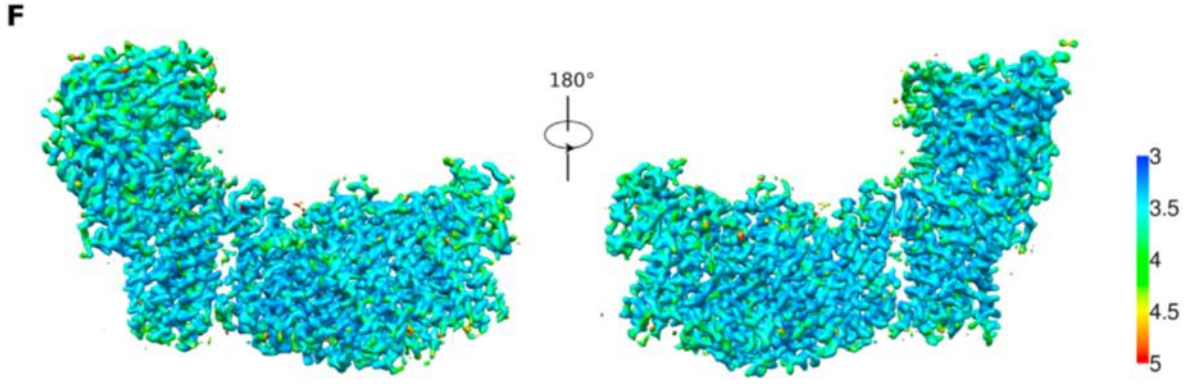
F
180°
3
3.5
4
4.5
5

Figure SB3

A gallery of EM density maps of ten membrane subunits (A–J) and four cytoplasmic subunits (K–N) superimposed with their corresponding atomic models in cartoon and stick views, related to Figure B1. A, MbhA. B, MbhB. C, MbhC. D, MbhD. E, MbhE. F, MbhF. G, MbhG. H, MbhH. I, MbhI. Densities for Aa42-73 were weak and only allowed the tracing of their main-chain atoms. (J), MbhM. K, MbhJ. L, MbhK. M, MbhL. N, MbhN.

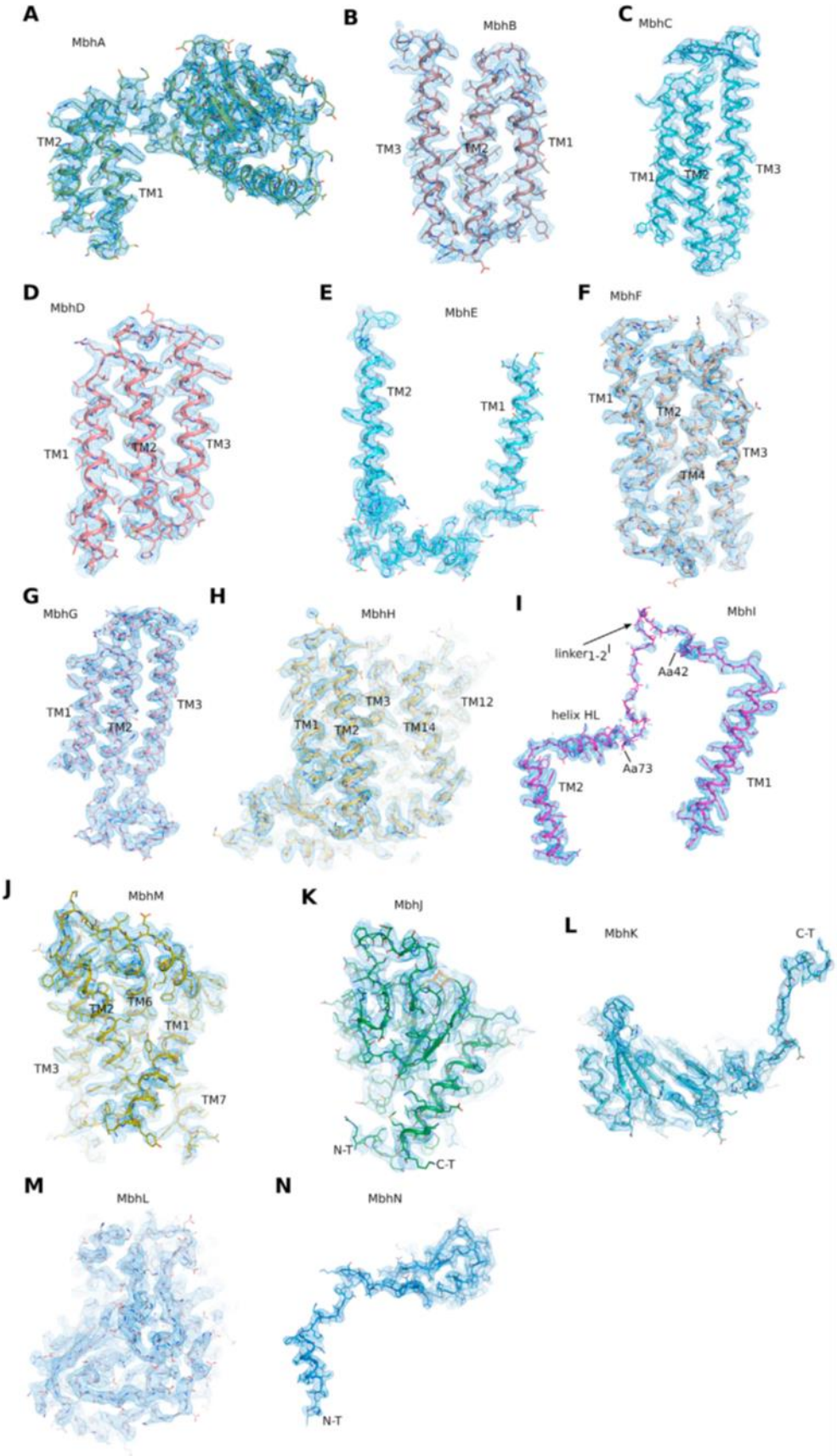
A
MbhA
TM2
TM1
B
MbhB
TM3
TM2
TM1
C
MbhC
TM1
TM2
TM3
D
MbhD
TM1
TM2
TM3
E
MbhE
TM2
TM1
F
MbhF
TM1
TM2
TM3
TM4
G
MbhG
TM1
TM2
TM3
H
MbhH
TM1
TM2
TM3
TM14
TM12
I
MbhI
linker1-2
Aa42
helix HL
Aa73
TM2
TM1
J
MbhM
TM2
TM6
TM1
TM3
TM7
K
MbhJ
N-T
C-T
L
MbhK
C-T
M
MbhL
N
MbhN
N-T

Figure SB4

Comparison of membrane arms between MBH and Complex I, related to Figure B3. (A–D) MBH complex (A and C) and complex I (B and D; *T. thermophilus*; PDB: 4hea) were aligned by the membrane subunits immediately below their respective peripheral arms: Nqo8 of complex I versus MbhM of MBH. Side views of this comparison are shown separately in (A) (MBH) and (B) (complex I). The top views are shown separately in (C) (MBH) and (D) (complex I), respectively. Note the large gap between subunits M and H in MBH (A). There are four elongated densities located to the lower region of the gap (A) inset; marked by blue dashed lines), which stack against several hydrophobic regions of subunits M and H. These densities are likely from two phospholipid molecules that may stabilize the structure and prevent ion leakage across the membrane bilayer. The dashed curves in (C) and (D) highlight the fact that the chain of hydrophilic residues found in complex I is continuous (D), but is discontinuous in MBH (C). (E) Superimposition of the MBH complex and *T. thermophilus* complex I (PDB ID 4hea), aligned based solely on their respective antiporter-like subunit MbhH and Nqo14 (as Figure B3C). By this alignment, the peripheral arm is docked to the right end of the membrane arm of complex I and to the left end of the membrane arm of the MBH. (F–I) Structural alignment shown in (E) revealed a module shared between the MBH complex and complex I. The corresponding subunits are superimposed and show (F) MbhH and Nqo14, (G) MbhG and Nqo11, (H) MbhD and MbhE together are equivalent to Nqo10. Notably, MbhD TMH3 contains a p-bulge that is also present in Nqo10. (I) Similarity between the MbhI C-terminal region (lateral helix HL and TMH2) with the Nqo12 C-terminal region (lateral helix HL and TMH16).

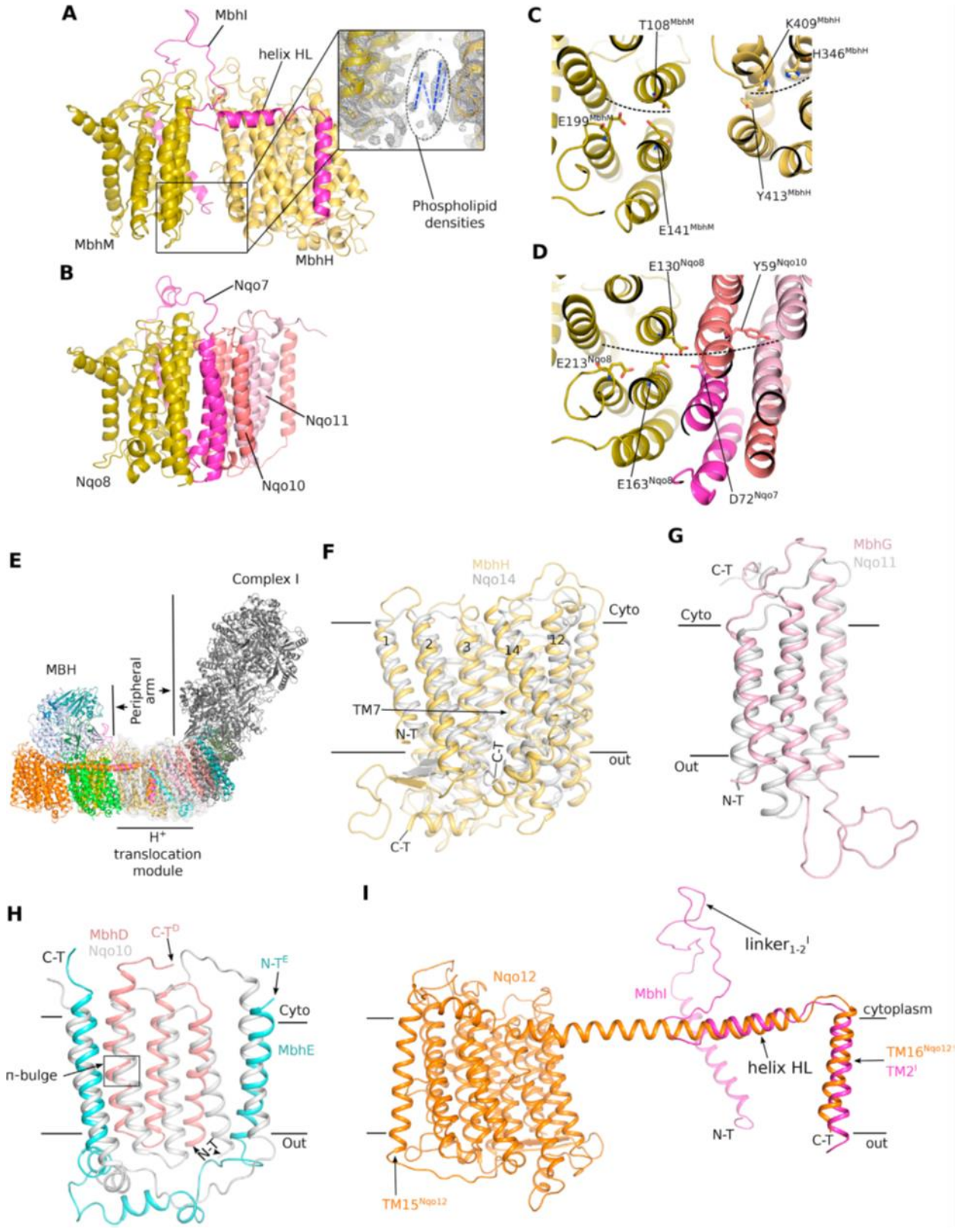
A
MbhI
helix HL
Phospholipid densities
MbhM
MbhH
B
Nqo7
Nqo11
Nqo8
Nqo10
C
T108MbhM
K409MbhH
H346MbhH
E199MbhM
Y413MbhH
E141MbhM
D
E130Nqo8
Y59Nqo10
E213Nqo8
E163Nqo8
D72Nqo7
E
Complex I
MBH
Peripheral arm
H+ translocation module
F
MbhH
Nqo14
Cyto
1
2
3
14
12
TM7
N-T
C-T
out
C-T
G
MbhG
Nqo11
C-T
Cyto
Out
N-T
H
MbhD
Nqo10
C-T
C-TD
N-TE
Cyto
MbhE
n-bulge
Out
N-T
I
linker1-2I
Nqo12
MbhI
cytoplasm
helix HL
TM16Nqo12I
TM2I
N-T
C-T
out
TM15Nqo12

Figure SB5

A comparison of the membrane-anchored hydrogenase module between the MBH complex and Complex I, related to Figure B4. (A) Overlay of MBH peripheral arm with the classic dimeric [NiFe] hydrogenase from *D. gigas* (PDB ID 2frv) by aligning MbhL with the large subunit of the two-subunit classic hydrogenase. Only MbhL and MbhJ are visible here. The membrane subunit MbhM of MBH is also shown, although it is absent in the dimeric [NiFe] hydrogenase. (B) Overlay of MBH peripheral arm plus the membrane Mbh M and I with the corresponding *T. thermophilus* complex I subunits – the Q-module and the membrane Nqo8, Nqo7. The alignment is based on MbhL and Nqo4. The two systems share a similar architecture except for the C-terminal regions of MbhI and Nqo7, suggesting that this sub-complex is well conserved between the MBH complex and complex I. (C) Like in complex I, there is also a chamber at the interface between the peripheral arm and the membrane subunit MbhM in the MBH complex. The internal cavity is shown as a red surface. The entry to the chamber in the MBH complex, which is equivalent to the quinone entry site in complex I, is closed due to the presence of several bulky residues there. Structural alignment was based on MbhM (MBH) and Nqo8 (complex I). (D–F) A comparison of coordinations of the [4Fe-4S] and [Ni-Fe] clusters in the peripheral arm of the MBH complex with those in *D. gigas* hydrogenase and complex I. The structures are colored as in (A) and (B). (D) The coordination of the distal and medial [4Fe-4S] clusters in MbhN (MBH) is highly similar to that in Nqo9 (complex I). (E) The coordination of the proximal [4Fe-4S] cluster is similar between the MBH and D. gigas hydrogenase. In complex I, coordination of the N2 cluster involves an unusual pair of tandem Cys residues (C45 and C46). (F) The side chains coordinating the [NiFe] cluster in MBH are similar to those in the *D. gigas* hydrogenase. The structural elements for coordinating [Ni-Fe] cluster are not present in complex I.

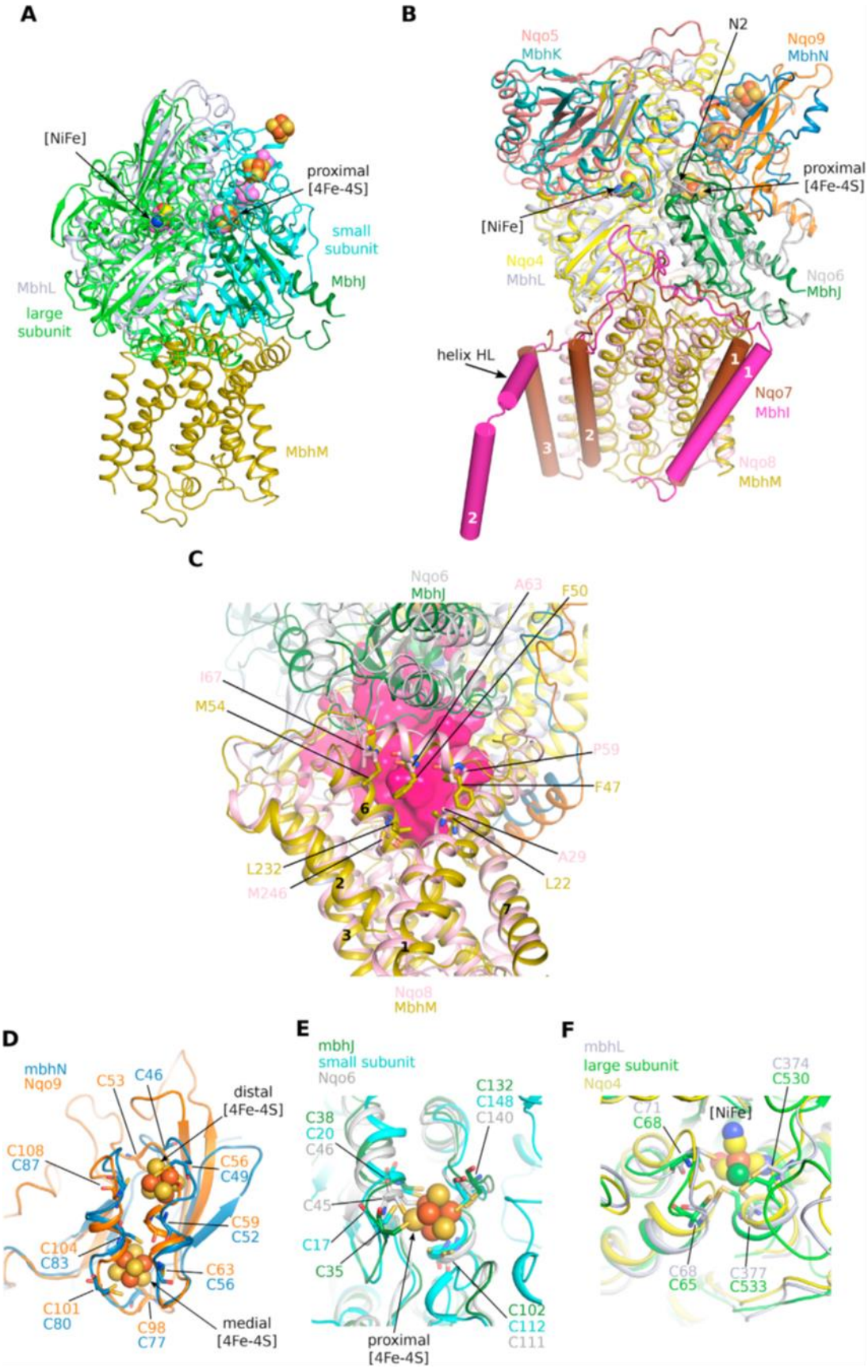
A
[NiFe]
proximal
[4Fe-4S]
small
subunit
MbhJ
MbhL
large
subunit
MbhM
B
N2
Nqo5
MbhK
Nqo9
MbhN
proximal
[4Fe-4S]
[NiFe]
Nqo4
MbhL
Nqo6
MbhJ
helix HL
Nqo7
MbhI
Nqo8
MbhM
C
Nqo6
MbhJ
A63
F50
I67
M54
P59
F47
A29
L22
L232
M246
Nqo8
MbhM
D
mbhN
Nqo9
C53
C46
distal
[4Fe-4S]
C108
C87
C56
C49
C59
C52
C104
C83
C63
C56
C101
C80
C98
C77
medial
[4Fe-4S]
E
mbhJ
small subunit
Nqo6
C132
C148
C140
C38
C20
C46
C45
C17
C35
C102
C112
C111
proximal
[4Fe-4S]
F
mbhL
large subunit
Nqo4
C374
C530
C71
C68
[NiFe]
C68
C65
C377
C533

Figure SB6

Structure and sequence comparison of the peripheral arms of the MBH complex with Complex I revealed several insertions evolved in complex I for anchoring its N-module, related to Figure B4. (A) Overlay of MBH peripheral arm and the membrane MbhM with the *T. thermophilus* complex I N-module, Q-module, and the membrane Nqo8. Alignment was based on MbhL and Nqo4. Individual subunits are colored as in Figure SB5B. The N-module of complex I, shown in cartoon as well as in transparent surface view, is peripheral and evolved later. (B–E) Structural comparisons (top panel) and sequence alignments (bottom panel) of the four N-module-interacting subunits of complex I with their corresponding MBH subunits: B, Nqo4 and MbhL; (C) Nqo9 and MbhN, (D) Nqo6 and MbhJ (E) Nqo5 and MbhK. Protein sequence sources are Pfu, *Pyrococcus furiosus*; Tth, *Thermus thermophilus*; Ova, *Ovis aries*. Major structural differences are marked by gray ovals, and further highlighted by the gray square(s) in the sequence alignment shown below each panel.

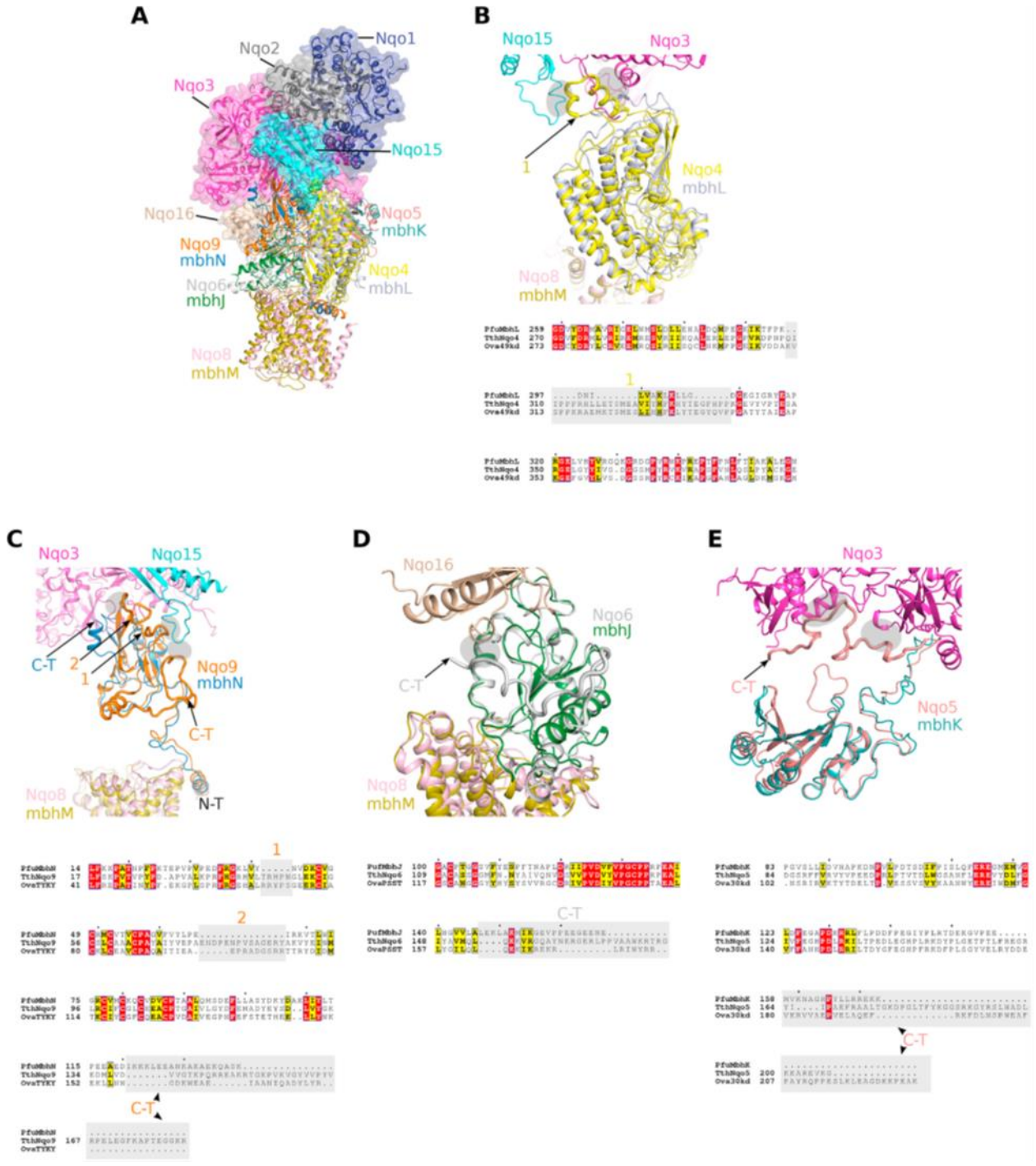
A
Nqo1
Nqo2
Nqo3
Nqo15
Nqo16
Nqo5
mbhK
Nqo9
mbhN
Nqo6
mbhJ
Nqo4
mbhL
Nqo8
mbhM
B
Nqo15
Nqo3
1
Nqo4
mbhL
Nqo8
mbhM
C
Nqo3
Nqo15
C-T
2
1
Nqo9
mbhN
C-T
Nqo8
mbhM
N-T
D
Nqo16
Nqo6
mbhJ
C-T
Nqo8
mbhM
E
Nqo3
C-T
Nqo5
mbhK

Figure SB7

Sequence alignments of individual MBH membrane subunits with their counterparts in the Mrp H^+/Na^+ antiporter, related to Figures B5 and B6 and Table B1. The TMH numbers shown above the primary sequences are based on the MBH structure. The predicted secondary structural elements of Bacillus subtilis Mrp subunits are shown below the sequences. Protein sequence sources are Pfu, *Pyrococcus furiosus*; Bsu, *Bacillus subtilis*; Bps, *Bacillus pseudofirmus*; Sau, *Staphylococcus aureus*; Rme, *Rhizobium meliloti*; Pae, *Pseudomonas aeruginosa*; Vch, *Vibrio cholera*. The filled black triangles mark residues shown in Figure B3E, and the filled black squares mark residues shown in Figures B5B and B5C.

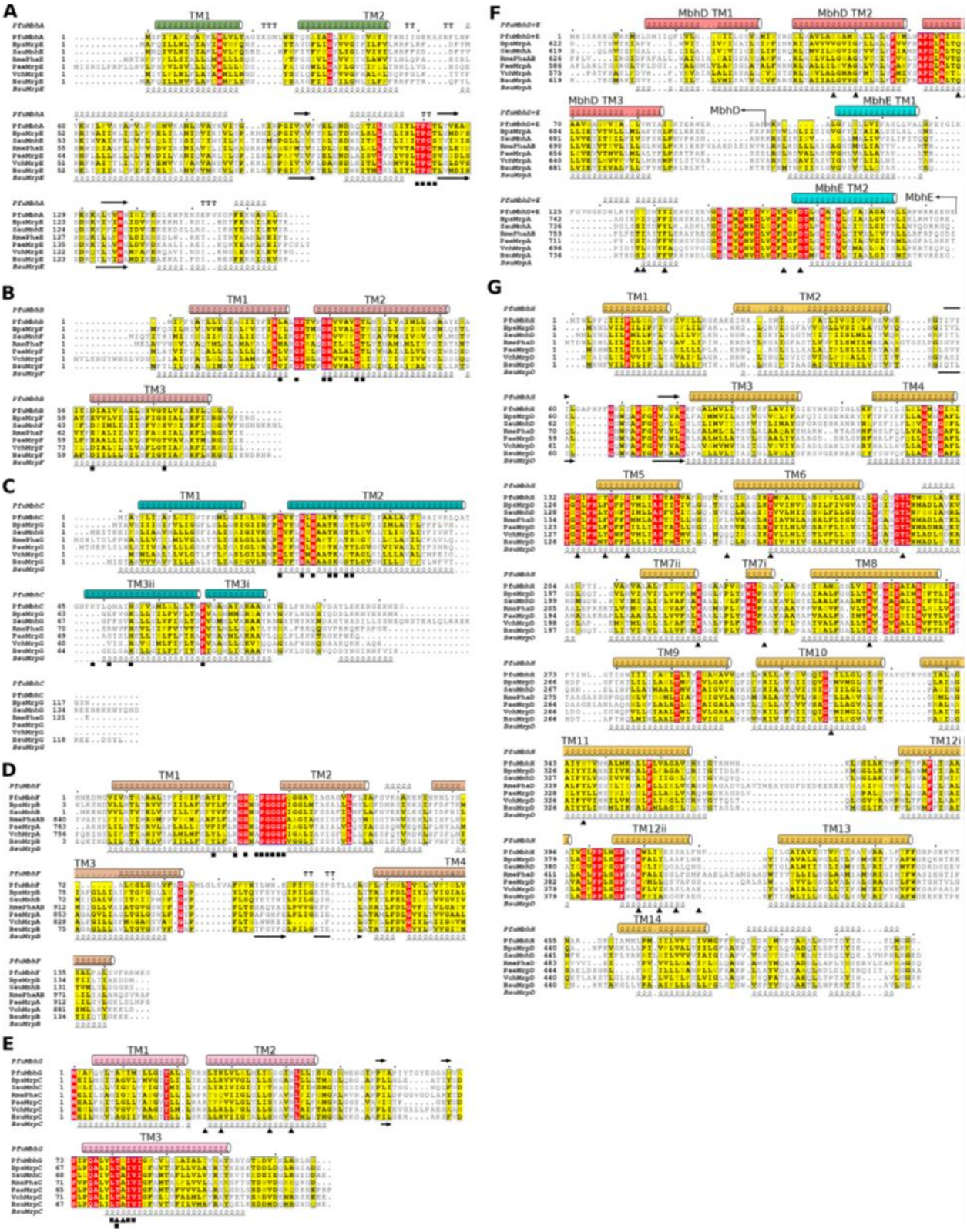
A
TM1
TM2
B
TM1
TM2
TM3
C
TM1
TM2
TM3ii
TM3i
D
TM1
TM2
TM3
TM4
E
TM1
TM2
TM3
F
MbhD TM1
MbhD TM2
MbhD TM3
MbhD
MbhE TM1
MbhE TM2
MbhE
G
TM1
TM2
TM3
TM4
TM5
TM6
TM7ii
TM7i
TM8
TM9
TM10
TM11
TM12i
TM12ii
TM13
TM14

APPENDIX C

PUBLICATIONS OF CHANG-HAO WU

1. **Wu CH**, Haja DK, Adams MWW. (2018) Cytoplasmic and membrane bound hydrogenases from *Pyrococcus furiosus*. *Meths. Enzymol.* (to be submitted 07/2018)
2. Haja DK*, **Wu CH***, Poole FL, Williams S, Jones AK, Adams MWW. (2018) *Pyrobaculum aerophilum* thiosulfate reductase heterologously expressed in *Pyrococcus furiosus* is more active with molybdenum than with tungsten. *Biochemistry* (to be submitted 07/2018)
   *Contributed equally
3. **Wu CH**, Schut GJ, Poole FL, Haja DK, Adams MWW. (2018) Membrane-bound sulfane reductase is a missing link in the evolution of modern day respiratory complexes. *Proc Natl Acad Sci U S A.* (submitted 06/2018)
4. **Wu CH**, Poole FL, Haja DK, Adams MWW. (2018) A new mechanism of arsenic resistance evident from the heterologous expression of a respiratory arsenate reductase in *Pyrococcus furiosus*. *Appl. Environ. Microbiol.* (submitted 06/2018)
5. **Wu CH**, Ponir CA, Haja DK, Adams MW. (2018) Improved production of the NiFe-hydrogenase from *Pyrococcus furiosus* by increased expression of maturation genes. *Protein Eng Des Sel*. (in revision)
6. Yu H, **Wu CH**, Schut GJ, Haja DK, Zhao G, Peters JW, Adams MWW, Li H. (2018) Structure of an ancient respiratory system. *Cell*. DOI: 10.1016/j.cell.2018.03.071.

7. Straub CT, Counts JA, Nguyen DMN, **Wu CH**, Zeldes BM, Crosby JR, Conway JM, Otten JK, Lipscomb GL, Schut GJ, Adams MWW, Kelly RM. (2018) Biotechnology of extremely thermophilic archaea. *FEMS Microbiol Rev*. DOI: 10.1093/femsre/fuy012.
8. Ligaba-Osena A, Jones J,Donkor E, Chandrayan S, Farris Pole FL, **Wu CH,** Rockhold DR, Vieille C, Belknap WR, Adams MWW, Hankoua B. (2018) Novel bioengineered cassava expressing an archaeal starch degradation system and a bacterial ADP-glucose phosphorylase for starch self-digestibility and yield increase. *Front Plant Sci*. **9**, 192.
9. Kim JE, Kim EJ, Chen Hui, **Wu CH**, Adams MW, Zhang YP. (2017) Advanced water splitting for green hydrogen gas production through complete oxidation of starch by in vitro metabolic engineering. *Metab Eng*.**44**, 246-252.
10. Chica B, **Wu CH**, Liu Y, Adams MW, Dyer RB. (2017) Balancing electron transfer rate and driving force for efficient photocatalytic hydrogen production in CdSe/CdS nanorod-[NiFe] hydrogenase assemblies. *Energy Environ Sci*.**10**, 2245-2255.
11. Vaccaro BJ, Clarkson SM, Holden JF, Lee DW, **Wu CH**, Poole Ii FL, Cotelesage JJH, Hackett MJ, Mohebbi S, Sun J, Li H, Johnson MK, George GN, Adams MW. (2017) Biological iron-sulfur storage in a thioferrate-protein nanoparticle. *Nat Commun*. **8**, 16110.
12. Sekar N, **Wu CH**, Adams MW, Ramasamy RP. (2017) Electricity generation by *Pyrococcus furiosus* in microbial fuel cells operated at 90°C. *Biotechnol Bioeng*. **114**, 1419-1427.
13. Sekar N, **Wu CH**, Adams MW, Ramasamy RP. (2016) Exploring extracellular electron transfer in hyperthermophiles for electrochemical energy conversion. *ECS Trans*. **72**, 1-7.
14. Kim EJ, **Wu CH**, Adams MW, Zhang YP. (2016) Exceptionally high rates of biological hydrogen production by biomimetic in vitro synthetic enzymatic pathways. *Chemistry*. **22**, 16047-16051.

15. Greene BL, Vansuch GE, **Wu CH**, Adams MW, Dyer RB. (2016) Glutamate gated proton-coupled electron transfer activity of a [NiFe]-hydrogenase. *J Am Chem Soc*. **138**, 13013-13021.
16. Schut GJ, Zadvornyy O, **Wu CH**, Peters JW, Boyd ES, Adams MW. (2016) The role of geochemistry and energetics in the evolution of modern respiratory complexes from a proton-reducing ancestor. *Biochim Biophys Acta*. **1857**, 958-70.
17. Moustafa HM, Kim EJ, Zhu Z, **Wu CH**, Zaghloul TI, Adams MW, Zhang YP. (2016) Water splitting for high-yield hydrogen production energized by biomass xylooligosaccharides catalyzed by an enzyme cocktail. *ChemCatChem*. **8**, 2898-2902.
18. Greene BL, **Wu CH**, Vansuch GE, Adams MW, Dyer RB. (2016) Proton inventory and dynamics in the Nia-S to Nia-C transition of a [NiFe] hydrogenase. *Biochemistry*. **55**,1813-25.
19. Kwan P, McIntosh CL, Jennings DP, Hopkins RC, Chandrayan SK, **Wu CH**, Adams MW, Jones AK. (2015) The [NiFe]-hydrogenase of *Pyrococcus furiosus* exhibits a new type of oxygen tolerance. *J Am Chem Soc*.**137**,13556-65.
20. **Wu CH**, McTernan PM, Walter ME, Adams MW. (2015) Production and application of a soluble hydrogenase from *Pyrococcus furiosus*. *Archaea.* 2015:912582.
21. Rollin JA, Martin del Campo J, Myung S, Sun F, You C, Bakovic A, Castro R, Chandrayan SK, **Wu CH**, Adams MW, Senger RS, Zhang YH. (2015) High-yield hydrogen production from biomass by in vitro metabolic engineering: Mixed sugars coutilization and kinetic modeling. *Proc Natl Acad Sci U S A*. **112**, 4964-9.
22. Greene BL, **Wu CH**, McTernan PM, Adams MW, Dyer RB. (2015) Proton-coupled electron transfer dynamics in the catalytic mechanism of a [NiFe]-hydrogenase. *J Am Chem Soc*.

137,4558-66.

23. Chandrayan SK, **Wu CH**, McTernan PM, Adams MW. (2015) High yield purification of a tagged cytoplasmic [NiFe]-hydrogenase and a catalytically-active nickel-free intermediate form. *Protein Expr Purif*. **107**, 90-4.
24. McTernan PM, Chandrayan SK, **Wu CH**, Vaccaro BJ, Lancaster WA, Adams MW. (2015) Engineering the respiratory membrane-bound hydrogenase of the hyperthermophilic archaeon *Pyrococcus furiosus* and characterization of the catalytically active cytoplasmic subcomplex. *Protein Eng Des Sel*. **28**, 1-8.
25. McTernan PM, Chandrayan SK, **Wu CH**, Vaccaro BJ, Lancaster WA, Yang Q, Fu D, Hura GL, Tainer JA, Adams MW. (2014) Intact functional fourteen-subunit respiratory membrane-bound [NiFe]-hydrogenase complex of the hyperthermophilic archaeon *Pyrococcus furiosus*. *J Biol Chem*. 289,19364-72.